INVESTIGATION OF CARBONATED WATER INJECTION (CWI) FOR ENHANCED OIL RECOVERY AT THE PORE AND CORESCALE

By

© Sedigheh Mahdavi

A thesis submitted to the

School of Graduate Studies

In partial fulfillment of the requirements for the degree of

Doctoral Research

Faculty of Engineering and Applied Science

Memorial University of Newfoundland

January 2019

St. John's Newfoundland and Labrador

Abstract

Oil recovery by CO_2 injection has been studied in the laboratory and applied in the field, however, for the most part, CO_2 injection lacks acceptable sweep efficiency. Various CO_2 injection strategies such as CO_2 alternating water and gas (CO_2-WAG) and CO_2 simultaneous alternating water and gas (CO_2-SWAG) have been suggested to alleviate this problem and improve oil recovery. The amount of CO_2 required can be a limiting factor especially in offshore applications. Thus, carbonated water injection (CWI) has recently been given considerable attention as it requires less CO_2 for the injection and increases the sweep efficiency. This study provides an overview of previous work on the topic and outlines the results of an integrated experimental, theoretical, and simulation investigation of the CWI for enhanced oil recovery (EOR). The effect of carbonated water injection on vertical displacement (gravity effect) at both the pore-scale and core-scale was investigated in this study. ***The novelty of this research is to investigate the performance of water flooding (WF) and CWI in the presence of gravity using homogeneous and heterogeneous (fractured) porous media.***

The first phase of this research investigates the pore-scale displacement phenomena which occurs in the presence of CWI in a glass micromodel. Although the effects of many parameters have been studied, an investigation of the effect of gravity displacement and heterogeneous porous media on trapped oil extraction using CWI, is deficient in the current literature. To evaluate the potential use of CWI for vertical displacement and oil extraction, a series of experiments in medium pressure homogeneous and heterogeneous (fractured) micromodels were designed at 2.1 MPa (305 psi) and 21°C (69.8 °F). The oil saturation profile, fluid flow pattern, pore-scale mechanisms, and trapped oil mobilization were analyzed during the experiments. The results of CWI showed an increased

vertical sweep efficiency compared to water flooding. The fluid flow pattern in both water flooding and CWI showed that the carbonated water phase has a better sweep efficiency. Secondary CWI resulted in 16.8% additional oil recovery compared to water flooding.

After a visual investigation of the impact of CWI on oil recovery and oil distribution in micromodels, core flooding experiments were designed to qualify and compare the effectiveness of water flooding, water alternating CO_2 gas (CO_2-WAG), and CWI at reservoir conditions considering the solubility of CO_2 in seawater and oil. The results of the core flooding experiments were evaluated using a simulation study. The results of core flooding experiments showed that secondary CWI obtained the highest recovery factor of 74.8% compared to 66.5% in CO_2-WAG and 64.2% in tertiary CWI processes.

The third phase the research was to simulate and predict the experimental results using Computer Modeling Group (CMG version 2014) software. The fluid model was constructed using CMG-WinProp^{TM} to create the compositions and properties of the CO_2-oil and CO_2-brine mixtures. The fluid model was incorporated into the compositional and unconventional reservoir simulator, CMG-GEM^{TM}, in order to reproduce the CWI and CO_2-WAG flooding tests conducted in this study. The simulation results indicated that CWI had a higher oil recovery factor compared to water flooding and CO_2-WAG. In summary, this comprehensive study highlights the CWI applicability for vertical oil sweep efficiency and enhanced oil recovery in homogeneous and heterogeneous porous media.

Acknowledgement

I would like to thank my supervisor, Dr. James, for all her support and her helpful thoughts. I must thank the technical services team and the faculty of Engineering and Applied Science for showing me what it means to be a dedicated person during my PhD, each one in their own unique way.

I also thank the Hibernia Management and Development Company (HMDC), Chevron Canada, and the Petroleum Research Newfoundland and Labrador (PRNL) for the financial support.

Thanks to my great friend, José Hernández, for teaching me that my job in life is to be happy, to help others, and to understand myself. I am grateful to all my friends who supported me in difficult moments.

Dedication

To my beloved father and mother,

His word of inspiration and encouragement in pursuit of excellence are always with me. He always whispered this famous poem for me:

If your tree of human being gets the fruit of knowledge

You can understand the whole universe

This journey would not have been possible without the support of my mother. I always knew that she believed in me and wanted the best for me. I would like to thank my siblings for their support and great patience throughout years of my graduate studies.

Table of Contents

List of Figures

List of Tables

List of Abbreviations

API	American Petroleum Institute gravity
BT	Breakthrough (PV)
Ca^{2+}	Calcium ions
$CaCO_3$	Calcium carbonate
CH_4	Methane
CO_2	Carbon dioxide
CEP	Critical point
CMG	Computer modeling group
CO_3^{2-}	Carbonate
CW	Carbonated Water
CSW	Carbonated seawater
CWI	Carbonated water injection
D	Diffusion coefficient (m^2/s)
EOR	Enhanced oil recovery
E	Efficiency (%)
GOR (cm^3/cm^3)	Gas oil ratio
H_i	Henry's constant
HCl	Hydrochloric acid
HF	hydrofluoric acid
HRZ	Horizontal
H_2CO_3	Carbonic acid
$H_2CO_3^-$	Bi carbonic
HC	Hydrocarbon
Hz	Hertz
K	Permeability (mD)
k_r	Relative permeability
L	Length (cm)
log	Logarithm
M	Mobility
Mg^{2+}	Magnesium ion
$MgCO_3$	Magnesium carbonate
μ	Viscosity (cP)
MMP	Minimum miscibility pressure (psi)
MW	Molecular weight (g/mol)
N_2	Nitrogen
N_{ca}	Capillary number
NH_4F	Nitrate fluoride
NL	Newfoundland
n_w	Exponent in water relative permeability
n_o	Exponent in oil relative permeability
O_2	Oxygen
OOIP	Original oil in place
P	Pressure (MPa)
PV	Pore volume

PVT	Pressure volume temperature
ppm	Part per million
R	Constant gas (J/mol.K, ft^3.psi/lb mol.R)
RF	Recovery factor (%)
SWF	Seawater flooding
SCFcar	Supercritical carbonic fluid
SCM	Scheme
SCWI	Secondary CWI
SWAG	Simultaneous alternating water and gas
S_{or}	Residual oil saturation (%)
S_{wc}	Connate water saturation (%)
T	Temperature (°C)
TADB	Thermal assisted direct bonding
TCWI	Tertiary CWI
TDS	Total dissolved solid (ppm)
u	Velocity (m/s)
VRT	Vertical
v	Molar volume (cm^3/g)
W	watt
WF	Water flooding
WAG	Water alternative gas
ρ	Density (g/cm^3)
σ	Interfacial tension (mN/m)
φ	Porosity (%)
δ	Solubility (mol solute/mol solvent)

Chapter 1 **Introduction**

1.1. Oil Resources and Global Energy Demand

The International Energy Outlook forecasts that global demand for energy is expected to increase 48% from 2012 to 2040 as economies in both developed and developing countries continue to grow. World energy consumption by fuel source was: oil 31%, coal 29%, natural gas 21%, biofuels and waste 10%, nuclear 5%, hydro 2%, and other (solar, wind, geothermal, heat) 1% until 2013 (Key World Energy Statistics, 2015). Figure 1-1 reported by International Energy Agency shows that oil and coal are expected to remain the most widely-used fuel sources until 2030 and beyond.

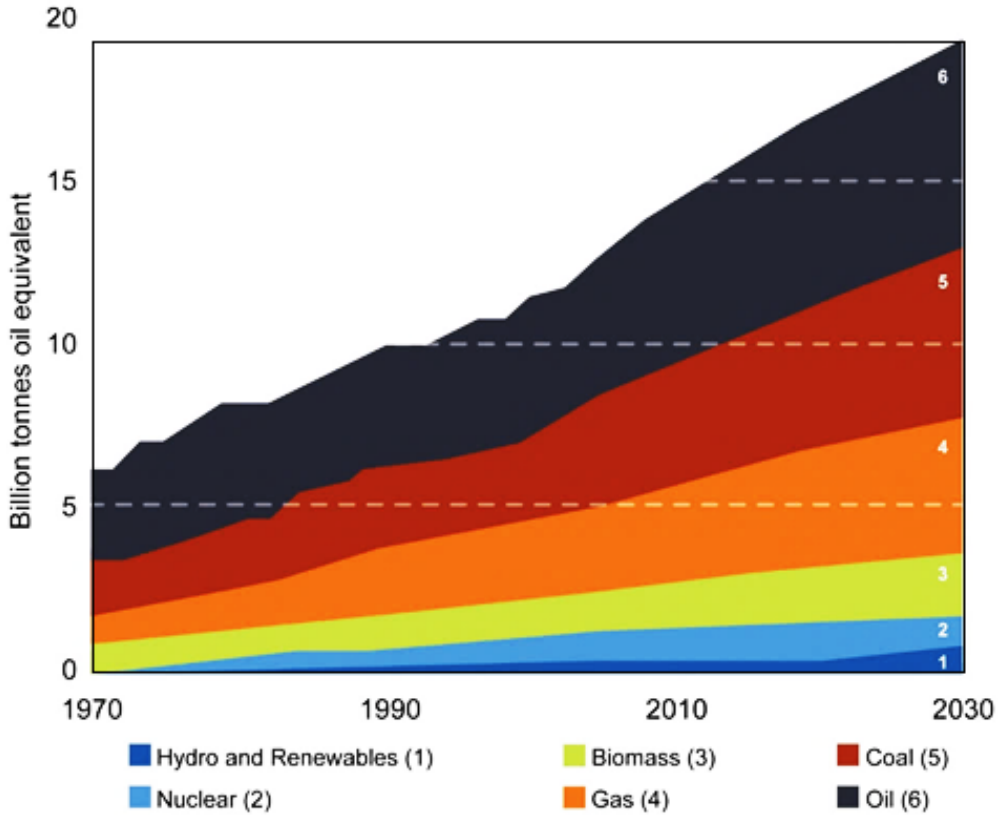

Figure 1–1: World Energy consumption by fuel type (IEA: World Energy Outlook, 2006)

1.2. Enhanced Oil Recovery (EOR)

Oil production can be categorized into three distinct phases: primary, secondary, and tertiary recoveries (Lake, 2010). In primary production, the natural pressure depletion of the reservoir drives the oil into the wellbore and then the surface. Approximately 10% of oil in the reservoir is typically produced during primary production. Secondary recovery techniques extend a field's life by injecting water or gas into the reservoir to maintain the pressure resulting in 20 to 40% recovery of the original oil in place (OOIP). However, EOR techniques increase the ultimate oil recovery to 30-60% of the OOIP (Mahendra, 2015). EOR processes are categorized as solvent flooding, chemical flooding, and thermal recovery. Enhanced oil recovery (EOR) is crucial to achieve the highest recovery factor (RF) and reduce environmental pollution and gas emission. Figure 1-2 summarizes both onshore and offshore EOR processes. For onshore fields, thermal EOR processes (mainly steam injection, but also hot water injection and combustion) are the most common EOR applications, followed by CO_2 miscible, hydrocarbon (HC) gas miscible, and polymer flooding. In offshore applications, hydrocarbon miscible gas is the most commonly used EOR method.

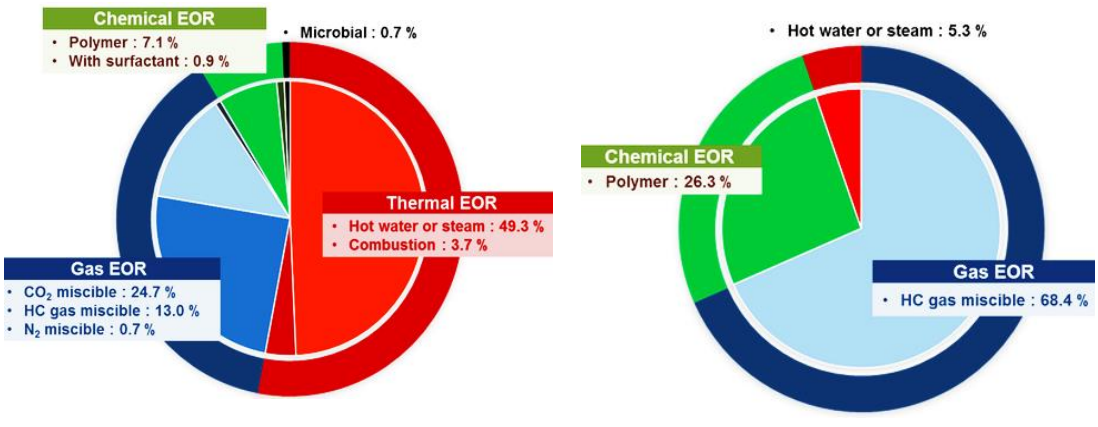

a) b)

Figure 1–2: Successful EOR processes, a) onshore and b) offshore (Kang et al., 2016)

Applying of EOR processes in an offshore environment is challenging due to the required supply of injection fluid, environmental conditions, space limitation on offshore platforms, and increased cost. Hence, the application of EOR processes in an offshore environment warrants comprehensive evaluation.

1.2.1. Gas Based EOR Processes

Gas injection may improve recovery factor but sweep efficiency during CO_2 flooding is a typical challenge. Due to the low viscosity and density of gas, the sweep efficiency of gas injection in reservoirs is reduced by viscous fingering and gravity override, respectively. Additionally, the presence of high permeability streaks in the formation gives rise to bypassing of oil by injected gas (Belgrave and Win, 1993). Additionally, gas injection is useful over a wider range of crude oil properties. There are different gas injection schemes: immiscible, near-miscible, and fully miscible. Immiscible gas injection is conducted when insufficient reservoir pressure is available, the gas is too lean, and/or there is a gas cap (Thomas et al., 1994).

CO_2, natural gas, nitrogen, or a mixture of these gases can be used as an injection gas. Immiscible CO_2 increases oil recovery by reducing the oil viscosity and swelling due to the higher solubility of CO_2 in oil than water. The swelling helps to remobilize trapped oil, which can be useful in mature oil reservoirs (Orr et al., 1980). Miscible flooding is a general term for gas injection EOR mechanisms when the gas is miscible with the oil. The most commonly used fluid for miscible displacement is CO_2 because it has a lower minimum miscibility pressure (MMP) and it is less expensive than other gases. In a miscible displacement, multi-contact miscibility is achieved, and intermediate and heavier oil components are extracted (Klins and Farouq, 1982; Belgrave and Win, 1993; Ghasemzadeh et al., 2011). In CO_2 miscible process, which is a common onshore EOR

method (Orr, 2009), CO_2 causes the oil to swell, reduces the viscosity of the oil, and increases the density of the oil as the oil becomes saturated with CO_2 at the increased pressure (Skjærveland and Kleppe, 1992; Srivastava and Dong, 2000). However, there are other studies that show when CO_2 is dissolved in oil results in oil density reduction (Miller and Jones, 1981). The MMP of CO_2 with oil is lower than hydrocarbon gases, hence CO_2 injection is more applicable over a wider range of reservoir conditions (Srivastava and Dong, 2000; Ela et al., 2014). It should be mentioned that in some oils, CO_2 injection may cause asphaltene precipitation and deposition in the reservoir, however, Hamouda et al. (2009) showed that a minimum amount of CO_2 (CO_2 critical content in the liquid phase) is required to disturb the equilibrium, resulting in asphaltene precipitation. The asphaltene precipitation increases when the CO_2 fraction in the fluid exceeds a critical point. No precipitation occurs below the critical content CO_2 (below the critical content of CO_2 in liquid, the solubility capacity of oil may increase). Two crude oil samples (30 ºAPI) with 0.35 and 10% wt asphaltene were studied and modeled under 50ºC, and 9 and 14 MPa (1305 and 2030 psi). It was found that the CO_2 critical content in the liquid phase (the liquid in equilibrium with asphaltene phase (solid)) is between 17 and 42 mol%.

CO_2 injection is a promising method in the oil industry for EOR purposes. The process has increased recovery from some oil reservoirs by an additional 4 to 15% beyond primary and secondary recovery. The CO_2 injection schemes include continuous injection of CO_2, CO_2-based water alternating gas (CO_2-WAG), and simultaneous injection of CO_2 gas and water (CO_2-SWAG). In an immiscible CO_2 injection scheme, the oil swelling phenomenon plays an important role in reducing oil viscosity (Khatib et al., 1981). CO_2 solubility in oil is dependent on pressure, oil composition, and temperature (Simon, 1964; Klins and Farouq, 1982). Oil displacement by

CO_2 injection relies on the phase behavior of the CO_2 and the oil, which are both strongly dependent on reservoir temperature, pressure and oil composition. Although continuous gas injection (e.g. CO_2, N_2, and HC), WAG, and SWAG improve the sweep efficiency the gas fingering and fluid segregation occurs due to the high mobility ratio of oil and gas that promotes an early breakthrough (Srivastava and Dong, 2000). In offshore reservoirs, the transportation of a large volume of CO_2 is technically difficult and expensive (European Technology Platform, 2010; Mohd Noh et al., 2014; Kang et al., 2016). Developing methods such as carbonated water injection (CWI) that use lower quantities of CO_2 is promising.

The petroleum industry is interested in CO_2 injection as an environmentally friendly method for both increasing oil recovery and capturing for storage and/or use (Majlaton, 2012). The important factors affecting the performance of CWI are CO_2 dissolution in water/brine, CO_2 transfer from water/brine phase to oil phase, and CO_2 solubility in the oil phase. Dissolution of CO_2 in water/brine is a function of pressure, temperature, and salinity of the aqueous phase, which determines the quantity of available CO_2 that needs to be transferred to oil.

1.2.2. CO_2 Dissolution in Water

The accurate prediction of CO_2 solubility over a wide range of temperatures, pressure, and ionic strength (salinity) is vital to understand the phase behavior and the advantages of using CO_2 in petroleum applications (Khatib et al., 1981; Duan et al., 1992a). To trace the mechanisms involved in EOR processes, there have been many experimental studies on the solubility of CO_2 in water and brine solutions (Enick et al., 1990; Carroll et al, 1991; Dhima et al., 1999, Duan et al., 2006; Li et al., 2014). In gas injection processes, CO_2 injection for EOR is a well-established technology (Taber et al., 1997). The solubility of CO_2 in oil results in improving oil recovery by swelling the

oil, reducing the oil viscosity and possibly the vaporization and extraction of intermediate components (Orr et al., 1981). Dissolved CO_2 in water (CWI) is a promising method to enhance oil recovery (Martin 1951). A comparison of CO_2 solubility in water to other gases at ambient conditions and high temperature conditions shows that CO_2 solubility is higher than other potential gases (i.e., N_2, CH_4, and O_2) for injection. Although increasing the temperature (e.g. reservoir temperature) reduces the solubility of CO_2 in water, it still has the highest solubility in water (Figure 1-3), except for H_2S.

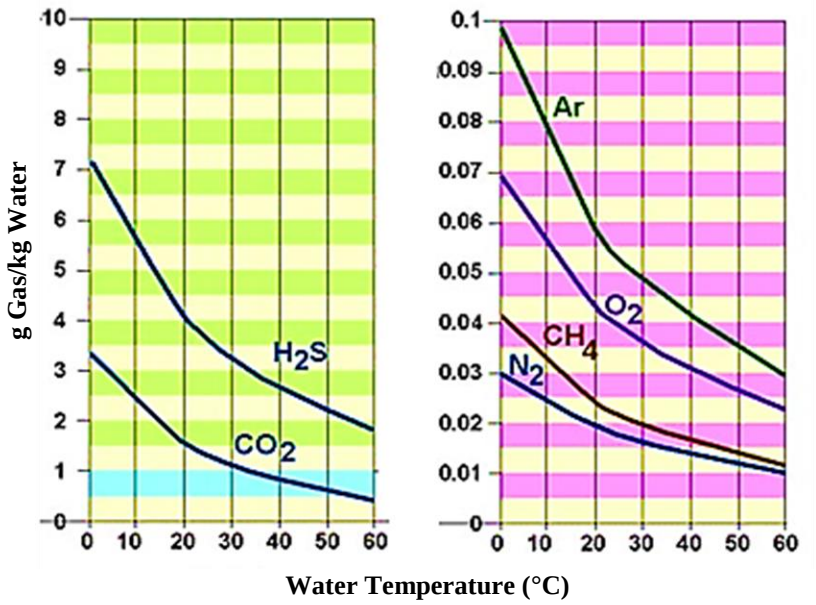

Figure 1–3: Solubility of gases in water at atmospheric pressure (http://geologycafe.com/oceans/chapter7.html)

CO_2 solubility in water/brine is a very important consideration for preparing a carbonated water solution. In offshore reservoirs, seawater is the most accessible source to prepare the carbonated water solution. The salinity of seawater (e.g., Atlantic Ocean seawater salinity is 35,987 ppm) affects the solubility of CO_2 in seawater. The solubility of CO_2 in brine and seawater directly impacts the amount of CO_2 in the water phase available to transfer to the oil phase impacting oil swelling and CWI performance

1.2.3. CO_2 Dissolution in Brine

The solubility of CO_2 in water and oil under reservoir conditions (high pressure/high temperature conditions) needs to be considered for CWI applications, where it is assumed the higher CO_2 concentration dissolved in water, the greater the recovery potential. Duan and Sun (2003) and Duan et al. (2006) collected data and proposed a model to predict the solubility of CO_2 in temperatures from 273.15 to 533 K (0 to 260°C), for pressures ranging 0 to 29,007 psi (0 to 200 MPa), and for ionic strength ranging 0 to 4.3 molality. Figure 1-4 illustrates that the solubility of CO_2 increases with increasing pressure and decreases with increasing in salinity. Dissolution of CO_2 in water or brine changes the physical properties of the water phase (i.e., viscosity and density of water and interfacial tension between oil and carbonated water), which directly affects the mobility and improves microscopic displacement efficiency.

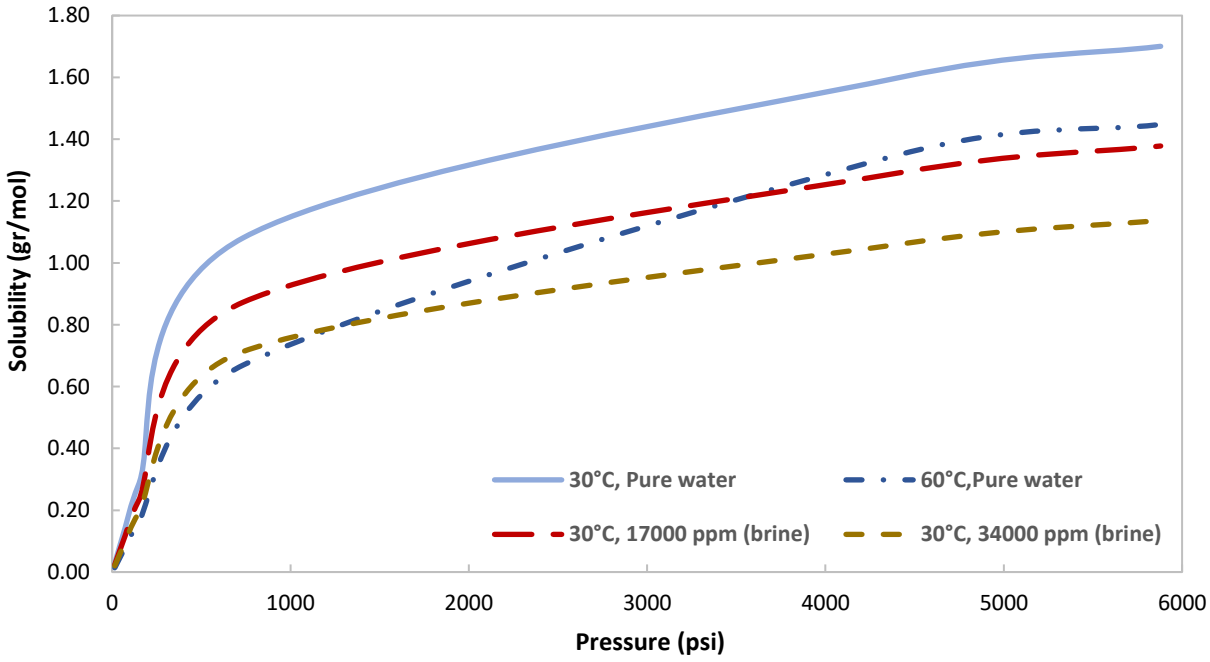

Figure 1–4: Solubility of CO_2 in water at different P, T, and salinity (NaCl) (Duan and Sun, 2003)

1.2.4. CO_2 Dissolution in Oil

To understand the effect of CO_2 solubility on oil properties, it is necessary to explain the relationship of CO_2 solubility in crude oil as a function of oil saturation pressure, temperature, oil composition, and oil °API gravity. CO_2 solubility increases with increasing pressure and oil °API gravity and decreases with increasing temperature (Simon and Graue, 1965; Emera and Sarma, 2007; Ilieva et al., 2016). The literature shows that oil composition and CO_2 concentration affect CO_2 solubility in oil (Emera and Sarma, 2007). The effect of CO_2 solubility on oil density is not significant with oils containing heavy components (Grigg, 1995; DeRuiter et al., 1994). Regarding changes in viscosity, oil viscosity decreases dramatically with increasing CO_2 concentration, resulting in increased oil mobility and oil recovery (Rojas and Farouq Ali, 1988). Mosavat et al. (2014) conducted a series of CWI experiments at 25ºC and 6.9 MPa in a sand-pack column (the detail of flooding will be discussed in section 2.4.1). The solubility measurements showed that the solubility of CO_2 in brine (salinity of 20,000 ppm) and oil (44.1 ºAPI) was 0.057 g CO_2/g brine and 0.013 g CO_2/g oil, respectively.

In the micromodel experiments conducted in this research at 21°C and 2.1 MPa, the CO_2 solubility was obtained to be 0.096 mol CO_2/mol oil (0.016 g CO_2/g oil) for oil with 29.8 °API and 0.0124 mol CO_2 /mol deionized water (0.030 g CO_2/g deionized water). In core flooding experiments (85°C and 31 MPa), the CO_2 solubility was calculated to be 0.448 mol CO_2/mol oil (0.076 g CO_2/g oil) and 0.0188 mol CO_2/mol seawater (0.046 g CO_2/g seawater). Details of the calculations and measurements are explained in section 4.2.1.1.

1.2.5. Carbonated Water Injection (CWI)

Carbonated water injection (CWI) has several benefits compared to other CO_2-EOR processes. Although CO_2-EOR processes are widely considered to be a useful method for immature and mature oil reservoirs (Ferguson et al., 2009), continuous CO_2 gas injection, WAG, and SWAG injection require large volumes of CO_2 and may have poor sweep efficiency. Water-blocking can also cause problems in CO_2-WAG and CO_2-SWAG processes due to gravity underride. Since CO_2 solubility in water is higher compared to other hydrocarbon gases (Figure 1-3) (e.g., methane and ethane), an effective injection strategy may be CWI. Swelling of the oil phase helps oil droplets join each other and move easily, favorably affecting oil mobility.

In CWI, CO_2 is dissolved in water or brine prior to injection. Several laboratory studies have shown the high performance of CWI in light and heavy oil samples (section 2.4). Field application of CWI demonstrates the high potential of CWI due to improvement of injectivity. The first carbonated water injection was applied on November 1960 in Oklahoma at the Dewey-Bartlesville Field (Christensen, 1961; Hickok and Ramsay, 1962). The oil had the 33 °API and a viscosity of 6.4 cP. The permeability and porosity of the rock was reported to be 56 mD and 17.2%, respectively. After 90% depletion, an additional 43% of residual oil was recovered using CWI compared to water flooding. Subsequent studies showed that secondary CWI achieved a higher recovery factor due to direct interaction between the carbonated water phase and the oil phase. CO_2 is transferred from the water to the oil phase, changing the reservoir fluid properties, and consequently, oil mobility and oil physical properties. In addition, tertiary CWI is more effective than water flooding. Results showed higher efficiency because oil mobility is improved due to oil phase swelling and oil viscosity reduction (Section 1.2.5.1).

1.2.5.1. Recovery Mechanisms

Oil trapping and EOR mechanisms in the swept region strongly depend on the physical properties of the displacing fluid (gas/water), displaced fluid (oil), porous media geometry, and their mutual interactions. The viscosity and density of CWI is improved in comparison to water and CO_2. Islam and Carlson (2012) studied the viscosity of carbonated water (deionized water) and carbonated seawater (brine with salinity of 35,000 ppm) solutions at the pressure and temperature ranges of 0.1 to 60 MPa and 20 to 105ºC. It was found that the viscosity of carbonated water varies from 0.28 to 1.05 cP and the viscosity of carbonated seawater changes from 0.35 to 1.4 cp. The density of carbonated water is increased compared to water. Bavier (1991) showed that the CO_2 dissolution in water at experimental conditions of 25ºC, and 10 MPa and 15 MPa increases the density of carbonated water by 18.9% and 27.3%, respectively.

In the CWI process, dissolved CO_2 is transferred from the injected carbonated water to the oil phase and reduces the oil viscosity and oil density. Reduction of oil viscosity under CO_2 injection was studied by Holm and Josandel (1974). Core flooding experiments were performed at 135 ºF (57.2ºC) using an oil with 41 ºAPI and CO_2 saturation pressures ranging from 0 to 9.6 MPa (1400 psi). Oil viscosity varied from 1.82 to 0.2 cP as the CO_2 saturation pressure was increased. Nevers (1964) showed that the high performance of CWI is due to oil viscosity reduction. The calculation of oil viscosity using the developed model showed that viscosity reduction due to CO_2 transfer from aqueous phase to oil phase is the main mechanism in oil recovery under the CWI process. The change in oil viscosity from 1,100 to 350 cP was reported under the CO_2 saturation pressure ranging from 0 to 13.7 MPa (2000 psi). The injected carbonated water sweeps considerably more oil than both water flooding and continuous CO_2 injection because of the lower mobility and density contrasts between oil and the carbonated water phase. Dissolution of CO_2 in oil reduces

the oil viscosity (Srivastava et al., 2000). A laboratory study was performed by Srivastava et al. (2000) using Weyburn oil to determine the properties of the mixture of CO_2 and oil. It was shown that oil viscosity reduction by CO_2 occurred from 3.01 to 0.2 cP under the experimental conditions of 59ºC and CO_2 saturation pressure ranges from 2.9 to 19.7 MPa (2857 psi).

Lower mobility enhances the horizontal sweep efficiency and eliminates the risk of viscous fingering. Lower density contrast between the carbonated water phase and oil provides a stable frontal displacement in vertical direction, which reduces the risk of gravity segregation and poor vertical sweep efficiency (Araktingi and Orr, 1993). The other effective mechanism is reconnection of oil ganglia due to oil swelling by CO_2 mass transfer from carbonated water phase into the oil phase (Riazi et al., 2011). Dead-end oil trapping and by-passed zones in water flooded reservoirs is the main challenge at the end of flooding. Dissolved CO_2 in water can gradually diffuse to the invaded zones and reach any trapped oil in the dead-end pores and by-passed zones, potentially mobilizing the oil. These properties of carbonated water injection as well as lower amounts of required CO_2 compared to the other gas-based EOR processes, make dissolved CO_2 in water (CWI) a promising EOR process for oil reservoirs especially offshore fields where it may be possible to capture constrained volume of CO_2 from offshore electrical generations. More than 70% of oil and gas production comes from mature reservoirs which have already been water flooded. Increasing recovery from mature fields requires extending the life and EOR, especially CO_2-based methods like CWI can help. An increase of approximately 1% could add two extra years to hydrocarbon supply and help to provide enough energy for current demands (Reinertsen, 2004). Hence, application of a process that is feasible in mature oil fields is another effective parameter for choosing CWI.

1.3. Research Objectives

The main objective of this study is to answer the question, "***What is the effect of carbonated water injection (CWI) as an enhanced oil recovery method on oil production and vertical oil displacement in both homogeneous and heterogeneous porous media*?"** The flowchart below shows the objectives of the current PhD research in more detail.

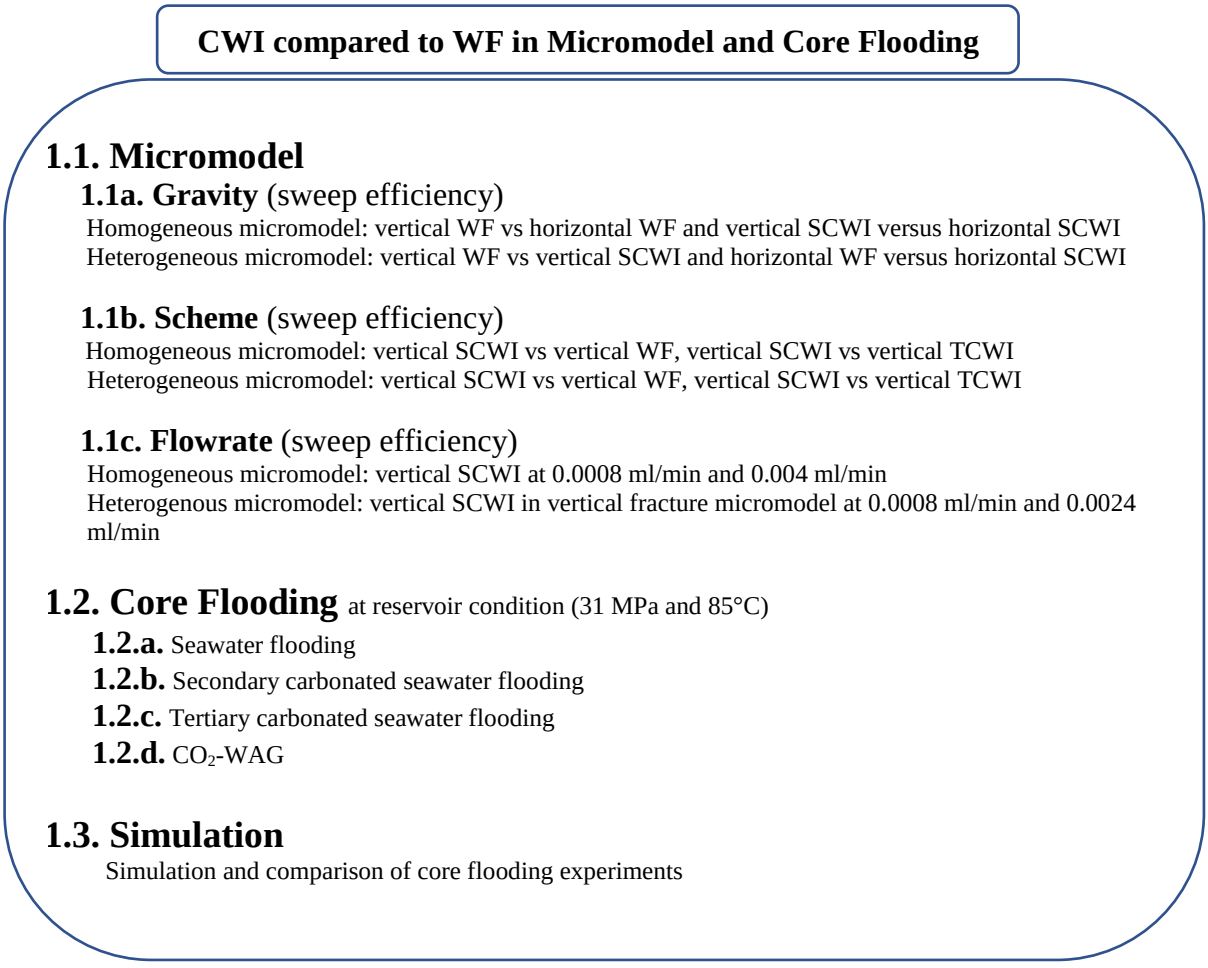

Figure 1–5: Objective of the current PhD research

As shown in Figure 1-5, the research objectives are met by considering pore-scale recovery using micromodels, core-scale recovery, and simulation to consider compositional phase behavior.

Part 1: To visually study the pore-scale (micromodel) performance of water flooding and CWI, we fabricated a medium pressure glass micromodel which endured the maximum pressure of 5 MPa (725 psi) without overburden pressure. Then, two different porous media (homogeneous and heterogeneous) were designed to visually investigate fluid displacement, oil-carbonated water interaction at the pore-scale, trapped oil extraction and vertical and horizontal sweep efficiencies during CWI. The homogenous micromodel was designed to understand the effectiveness of CWI on vertical sweep efficiency and oil redistribution in the presence of gravity. Oil recovery from heterogenous reservoirs is always challenging due to the presence of different permeability zones. We especially considered the effect of fractures on oil recovery. Hence, two heterogeneous micromodels were designed: horizontally-oriented to flow fractures and fractures perpendicular to flow in order to evaluate the performance of CWI on oil extraction and fluid distribution. This approach resulted in a qualitative analysis of the dominant mechanisms in the CWI process. Oil and water saturation were measured and calculated using an in-house image analysis software. After visually investigating the effect of CWI on oil recovery at the pore-scale, part 2 of this study was designed.

Part 2: In the second part of this study, the vertically-oriented core (core flooding) experiments using Newfoundland offshore reservoir conditions were conducted. Several schemes were tested: simple seawater flooding, CO_2-WAG, secondary carbonated seawater injection (secondary CWI) and tertiary carbonated seawater injection (tertiary CWI). These were performed to qualify the effectiveness of CWI on enhanced oil recovery and vertical oil displacement at reservoir conditions, 4,500 psi (31 MPa) and 185 °F (85°C). In the core flooding experiments, carbonated water was prepared using Atlantic seawater with a salinity of 35,987 ppm at 3,500 psi (24 MPa)

and 85°C (185 °F). In this series of experiments, cumulative oil, water and gas, inlet and outlet pressures were recorded to calculate the recovery factor (RF), cumulative gas to oil ratio (GOR), and cumulative water to oil ratio (WOR).

Part 3: To evaluate the performance of CWI, a phase behavior study of CO_2-deionized water, CO_2-seawater, and phase interactions were used to calculate the solubility and equilibrium ratios of carbonated water (CW)/oil and carbonated seawater (CSW)/oil. Mixtures were modeled using CMG-WinProp^{TM} (version 2014.10) and OLI Studio software. The simulation of simple water flooding, CWI, and CO_2-WAG processes were then conducted to evaluate the results of vertical core flooding experiments. A model was built using CMG-GEM^{TM} (version 2014.10) compositional software. In the simulation model, the exact properties of the core samples, injection rate, and bottom hole pressure were defined to match the experimental conditions.

1.4. Research Motivation

CWI is an alternative injection process that requires less CO_2 compared to continuous CO_2 injection. Hence, this process is particularly attractive for reservoirs with limited access to CO_2, such as offshore reservoirs. Storage of CO_2 using CWI eliminates the risk of buoyancy-driven leakage opposed to CO_2 gas phase injection (Burton and Bryant, 2007). Carbonated water is denser than water at different conditions. For example, at 69.8 °F (21°C) and 305 psi (2.1 MPa), ρ_{CW} = 1003.4 kg/m^3 (62.7 lbm/ft^3) vs ρ_{water} = 998.0 kg/m^3 (62.30 lbm/ft^3). At reservoir conditions (185 °F (85°C) and 4,500 psi (31 MPa)), the density changes to ρ_W = 968.6 kg/m^3 (60.47 lbm/ft^3) and $\rho_{seawater}$ = 994.3 kg/m^3 (62.1 lbm/ft^3) vs ρ_{CW} = 1.0152 kg/m^3 (63.34 lbm/ft^3). Furthermore, CWI is beneficial in a thick reservoir. It can displace most of the oil in the reservoir because of stable frontal movement. The higher solubility of CO_2 in water allows us to achieve high CO_2-enriched

water at lower temperatures and pressures. Due to the higher solubility of CO_2 in oil than in water in both micromodel conditions (0.096 mol CO_2/mol oil vs 0.0124 mol CO_2 /mol deionized water) and core flooding conditions (0.076 g CO_2/g oil vs 0.046 g CO_2/g seawater), dissolved CO_2 in the water can transfer from water to oil and improve oil recovery (section 1.2.4). Additionally, CWI can be used for water flooded reservoirs (i.e. tertiary recovery). Offshore Eastern Canada has very light oil and high permeability reservoirs. EOR processes in offshore reservoirs are challenging. Despite the recent downturn in price, the demand for oil continues and is forecasted to increase in the following years. To meet this demand, it is important that oil exploration and drilling continues soon as current alternative energy sources are unable to fully replace fossil fuels. Newfoundland's oil and gas industry is based on offshore fields. Drilling offshore wells are more expensive than onshore wells (International Energy Agency, 2016). Therefore, it is important that oil recovery is maximized and enhanced oil recovery (EOR) methods can help.

The challenge facing Newfoundland offshore fields, being 310-350 km off the coast, is the supply of any fluids to inject for EOR and the associated processing/facilities' space. Natural gas offshore NL is economically stranded and regulations require minimum flaring. Produced natural gas is currently injected for pressure support and has started being used in water alternating gas (WAG) EOR. The produced natural gas and diesel (for startup and during shutdowns) are used in co-fired steam generators to produce electricity on offshore production facilities producing CO_2 in the combustion process. This CO_2 can be captured using different technologies such as absorption and adsorption towers and more recently membrane separation units generating a solvent that can be used for EOR while sequestering a greenhouse gas. Unlike onshore or near shore fields where large sources of CO_2 can be captured and sequestered or used in CO_2 floods, the distance from

shore and lack of major CO_2 sources limits this potential. The lower volumes CO_2 captured from the offshore electrical generators can be used in EOR techniques such as CWI and CO_2 WAG. This thesis examines the pore and core scale recovery of CWI as one potential EOR using the low volumes of captured CO_2. Additionally, it focuses on CWI recovery from a fractured reservoir, applicable to certain fields offshore NL. Besides which, increasing demand for oil requires new and unconventional techniques to produce problematic matrix oil from challenging fractured reservoirs. This thesis not only is important in finding a way to capture and use CO_2 for EOR but also addresses increasing oil recovery from fractured reservoirs that has always been an issue.

1.5. Research Contribution

This study outlines the results of my PhD thesis to study the applicability of CWI process for oil extraction. The effectiveness of an EOR process depends on the vertical, horizontal, and pore-scale sweep efficiencies. Vertical displacement is an important indicator of every EOR flooding performance. Although the effects of many parameters in CWI have been studied, there is no documented study on the effect of gravity displacement, geometry of the porous media and production rate on trapped oil extraction and fluid flow pattern in the current literature. This work investigates pore-scale displacement phenomena occurring in CWI in a homogeneous glass micromodel in the presence of gravity. To evaluate the potential use of CWI for vertical displacement, a series of experiments in a medium pressure glass micromodel have been designed accounting for phase behavior and solubility of CO_2 in the water and oil.

Heterogeneity is an important factor that affects the performance of CWI process which has not been investigated in previous work. Heterogeneous glass micromodels were designed to

investigate the vertical displacement in horizontal fracture, vertical fractures, and non-fracture porous media. The oil saturation profile, fluid flow pattern, pore-scale mechanisms, trapped oil mobilization, and fracture-matrix interaction were analyzed during the experiments. Core flooding experiments were designed to quantify the effect of CWI in Berea core samples. In micromodel and core flooding experiments, the production rate also was changed to investigate the effectiveness of CWI with different schemes (i.e. secondary and tertiary CWI). Figure 1-6 shows my contributions to pore-scale and core-scale CWI experiments. Finally, a compositional simulation study using CMG simulator (computer modeling group) was conducted to predict the core flooding experimental results at high pressure and high temperature.

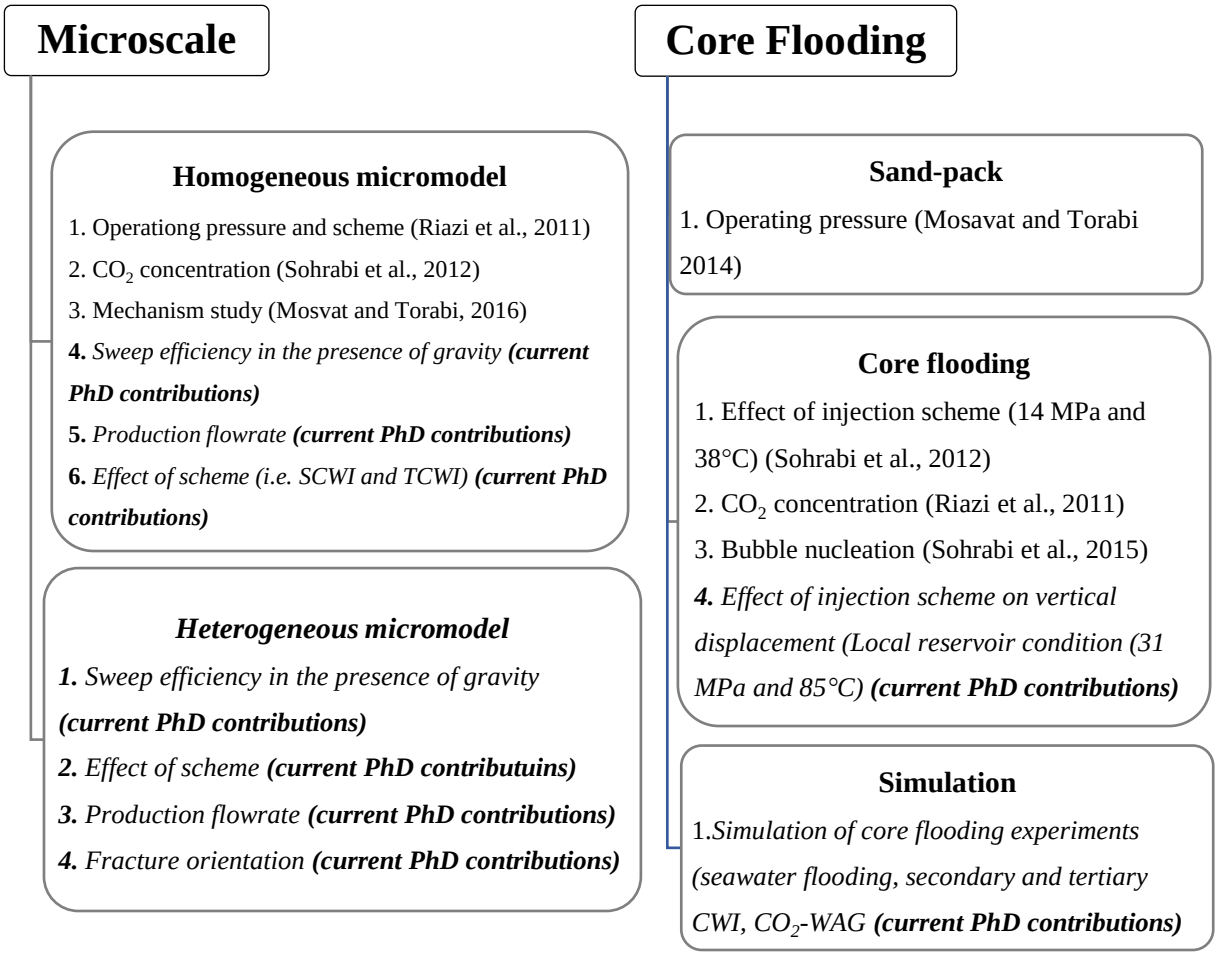

Figure 1–6: Contribution of the current PhD research compared to other studies

1.6. Thesis Content

The aim of this study is to investigate the effectiveness of carbonated water injection (CWI) as an EOR method on oil production and vertical oil displacement in the presence of gravity. This study is divided into seven chapters which are described below. Chapter 1 is an introduction to the EOR processes. Chapter 2 comprehensively reviews the literature of CWI in micromodel, core flooding, and sand-pack experiments. In Chapter 3, the micromodel fabrication for different geometries is explained. The experimental methodology and flooding setups are then described in Chapter 4. This is followed by the experimental results in pore-scale experiments in Chapter 5. The experimental and simulated results of the core flooding are discussed in Chapter 6. Finally, in Chapter 7, the conclusions and recommendations are presented.

Chapter 2 **Literature Review**

2.1. Oil Recovery Fundamentals

Natural depletion of an oil reservoir generally allows for very limited recovery of original oil in place (OOIP). Recovery factor under natural depletion is approximately 20%. Secondary recovery may yield an additional 15-20% recovery factor (Carcoana, 1992). Recovery can vary significantly depending on many factors. To understand the significance of enhanced oil recovery, we need to study the mechanisms limiting primary and secondary recovery. There are two main reasons why oil cannot be swept completely from a reservoir when displacing it with another fluid. First, we have trapping of oil on the pore-scale, which is described by capillary number (Lake 1989). The second phenomena affecting recovery is described by another dimensionless number, the mobility ratio. The mobility ratio is given as the ratio of the displacing phase mobility to the displaced phase mobility. In essence, enhanced oil recovery methods aim to overcome these pore-scale and sweep efficiency limitations.

In this chapter, the mechanisms limiting oil recovery are discussed in order to highlight the significance of enhanced oil recovery methods. Previous studies on carbonated water injection (CWI) are also comprehensively reviewed and the research plan for the current study is proposed.

2.1.1. Mobility Ratio

The mobility of a fluid is the effective relative permeability of that fluid divided by its viscosity. Mobility ratio (M) is the ratio of the mobility of the displacing fluid (gas/water) behind the flood front to that of the displaced fluid (oil) ahead of the flood front. The most common mobility ratio definition used for an oil-water system is (Dake, 1978):

$$M = \left(\frac{\mu_D}{\mu_I}\right).\left(\frac{k_{rI}}{\mu_D}\right) \quad (1)$$

where μ_D (cP) and μ_I (cP) are the viscosities of the displaced and injected fluids and k_{rI} and k_{rD} are relative permeabilities of water and oil, respectively.

If M > 1, such as when the viscosity of the displacing fluid is lower than the displaced fluid, the displacing fluid will pass the displaced fluid and viscous fingering will occur. The mobility ratio M can be reduced by decreasing the viscosity of the displaced fluid (oil), increasing the viscosity of displacing fluid, increasing the effective permeability to oil or decreasing the effective permeability to the displacing fluid.

2.1.2. Capillary Number

Reservoir fluid flow is usually dominated by capillary forces. Therefore, although the macroscopic flow is driven by gravity or viscous forces, the fluid flow at the pore-scale is determined by the capillary forces. The capillary number is the ratio of viscous forces over interfacial tension, which is given by:

$$N_{ca} = \left(\frac{u\mu_I}{\sigma}\right) \quad (2)$$

where, u is the Darcy velocity (m/s), μ_I (Pa.s) is the injected fluid viscosity, and σ (N/m) is the interfacial tension between the fluids. For low capillary numbers (a rule of thumb says less than 10^{-5}) (Lenormand et al., 1988; Kulkarni, 2004 and 2005), fluid flow in porous media is dominated by capillary forces, whereas for high capillary numbers the capillary forces are negligible compared to the viscous forces (Chatzis and Morrow 1984; Ding and Kantzas, 2004). The capillary

number indicates the flow regime and residual oil saturation after flooding. Figure 2-1 shows the relation between the residual oil saturation to the capillary number.

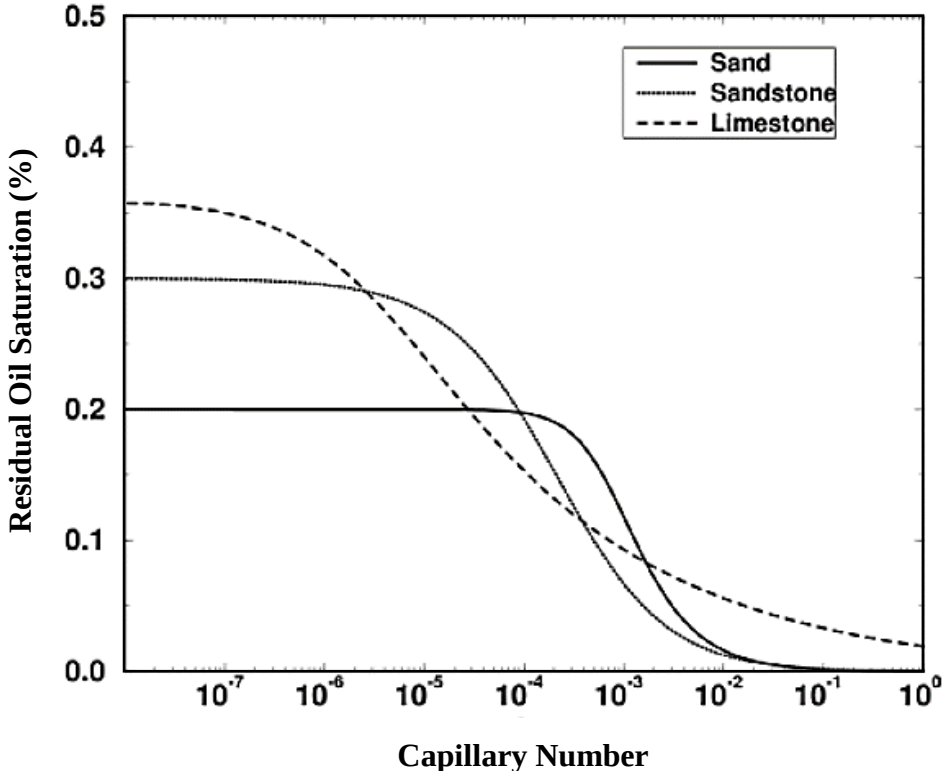

Figure 2–1: Residual oil saturation as a function of capillary number (Hilfer, 1996)

Figure 2-1 highlights that higher capillary numbers result in lower residual oil saturation. Total recovery efficiency is calculated using residual oil saturation. Oil displacement recovery and performance in any EOR method is a function of gravity, capillary, and viscous forces.

2.2. Displacement Mechanisms in Porous Media

Gravity, capillary, and viscous forces determine the sweep efficiency of every EOR method. Different flow regimes occur depending on competition between gravity force, capillary force, and viscous force. In the absence of gravity, for slow displacements, the displacement is controlled by capillary pressures (Lenormand and Zarcon, 1984). For fast displacements, where viscous forces

overcome capillary effects, a viscous fingering regime occurs (Chen and Wikinson, 1985). The total recovery efficiency (E) of the fluid displacement process is calculated by the macroscopic (volumetric) efficiency $(E_s \times E_i)$ and the microscopic displacement efficiency (E_d):

$$E = E_s \times E_i \times E_d \tag{3}$$

2.2.1. Macroscopic Displacement Mechanisms

The macroscopic displacement efficiency (volumetric sweep efficiency) is made up of two terms, the areal, (E_s) and vertical (E_i). The schematic of areal and vertical sweep efficiencies is shown in Figure 2-2. The macroscopic displacement efficiency is a measure of how well the displacing fluid encounters the oil in the reservoir. Many factors affect macroscopic displacement efficiency such as heterogeneity, mobility of the displacing, and pattern of the injection and production wells. The movement of fluids through the reservoir will not be uniform if there are large variations in properties such as porosity and permeability (Dullien, 1979).

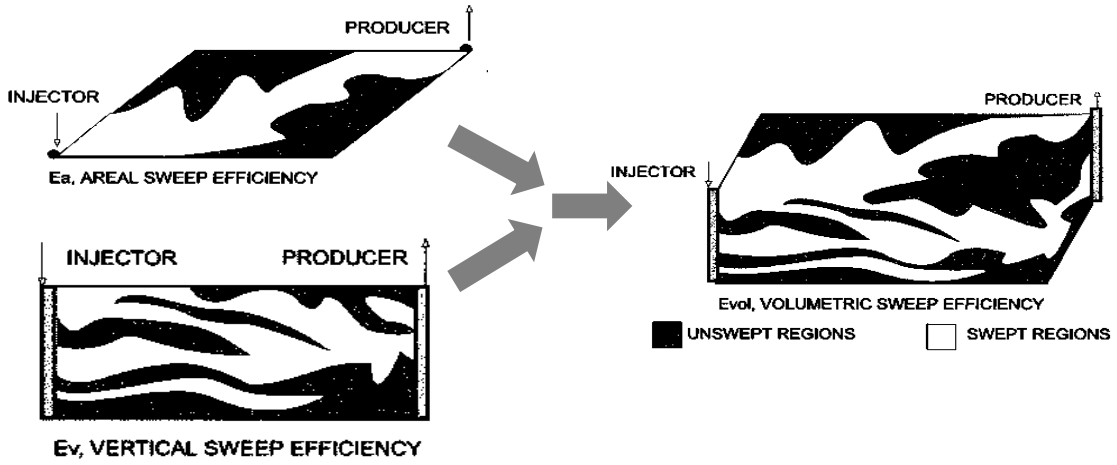

Figure 2–2: Schematic of areal, vertical, and volumetric sweep efficiencies (Baker, 1998)

2.2.1.1. Viscous Fingering

Viscous fingering is an important physical phenomenon that determines the macroscopic displacement efficiency and it occurs during unstable displacement. Viscous fingering occurs at the interface of two fluids in reservoirs when a high viscosity oil is displaced by a low viscosity fluid such as water. Viscous fingering is a function of mobility of the displaced and displacing fluids, and fluid properties including viscosity and relative permeability. The viscous fingering in porous media is one of the most typical issues of oil recovery by water flooding (Gupta and Greenkorn, 1974; Tang and Koscek, 2011). Local fluctuation in permeability and high injection rate cause viscous fingering (Araktingi and Orr, 1993; Doorwar and Mohanty, 2015). CO_2 dissolution in oil results in lower oil viscosity (Lohrenz et al., 1964; Barclay and Mishra, 2016). During CWI, CO_2 is transferred from the carbonated water to the oil and oil viscosity is reduced (Riazi et al., 2011). Therefore, the viscosity difference between the injected carbonated water (CW) and oil is decreased, and thus reduces the risk of viscous fingering, so better oil sweeping is expected.

2.2.1.2. Gravity Segregation

Gas injection processes have been practiced since the last century (Cotter, 1962), however the low volumetric sweep efficiencies of gas injection have always been an issue. In general, the viscosity of the injected gases such as (e.g. CO_2, hydrocarbons, and N_2) is approximately one-tenth of the reservoir oil viscosity. High viscosity contrast between the gas and oil results in highly unfavorable mobility, and high-density difference between the gas and oil results in gravity segregation. Gravity segregation causes large un-swept areas resulting in poor volumetric sweep efficiencies (Green and Willhite, 1998; Kulkarni, 2004). In water flooding, water underride is caused by gravity which causes a poor sweep efficiency in the upper part of the reservoir.

For a homogeneous reservoir that is gas flooded, vertical sweep efficiency and oil recovery at breakthrough have been found to increase with increasing gas injection rates (Belgrave and Win, 1993). Reservoirs with low heterogeneity results in higher oil recovery at higher injection rates. Vertical sweep efficiency is affected by vertical heterogeneity (Belgrave and Win, 1993).

As we discussed before there are challenge in sweep efficiency of water flooding and gas-based EOR processes such as continuous gas injection, CO_2-WAG, and SWAG. Mosavat and Torabi (2014 and 2016) believed that CWI is a beneficial strategy for oil recovery because it reduces the mobility contrast between the injected and displacing fluids. Carbonated water may reduce the gravity segregation; hence the sweep efficiency is improved. Figure 2-3 compares water flooding, CO_2 injection, WAG, and CWI processes.

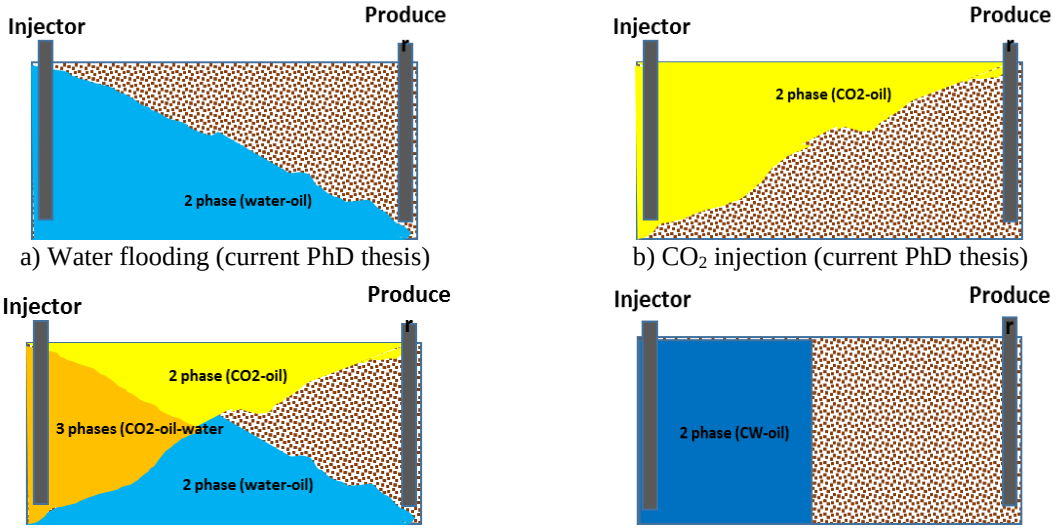

a) Water flooding (current PhD thesis)

b) CO_2 injection (current PhD thesis)

c) WAG (current PhD thesis)

d) CWI, Mosavat and Torabi (2016)

Figure 2–3: The schematic of water flooding, CO_2 injection, WAG, and CWI

2.2.2. Microscopic Displacement Mechanisms

Microscopic displacement efficiency is a measure of how well displacing fluid mobilizes residual oil. Interfacial tension and wettability are the parameters that change microscopic displacement efficiency (Dake, 1978). During immiscible flooding, two mechanisms may occur, snap-off or pore-doublet. The snap-off mechanism is the result of heterogeneity caused by aspect ratio and pore diameter (Figure 2-4). In water flooding, high water saturation will create a film flow causing discontinuous trapped oil leading to a poor sweep efficiency. Snap-off occurs when the film flowing increases and traps the oil (Lenormand and Zarcone, 1983; Chatzis and Morrow, 1984).

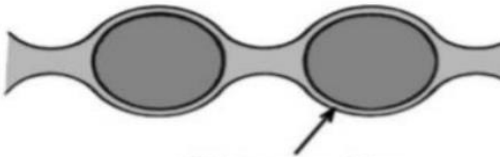

Oil trapped by snap-off

Figure 2–4: The schematic of snap-off mechanism in oil trapping (Brownell and Katz, 1947)

Blunt and Scher (1995) investigated the effect of flow rate on immiscible fluid displacement. They determined that the dominant fluid displacement mechanism changes depending on flow rate due to fluid competition at the pore-scale. Nguyen et al. (2006) reported that snap-off is more possible at low flowrates, high aspect ratios, and small contact angles. However, Juanes and Blunt (2006) reported that snap-off increases residual trapping at faster injection rates due to the increased capillary pressure in small pores. The other factor that affects microscopic efficiency is the wettability of the porous media.

Wettability is a function of the chemical composition of both the fluids and the rock. Surfaces can be either oil-wet or water-wet, depending on the chemical composition of the fluids and the rocks.

Large polar compounds in the oil phase can adsorb onto the solid surface; this leaves an oil film that may alter the wettability of the surface (Anderson, 1986; Muñoz et al., 2015; Sripal and James, 2016). The concept of wettability leads to another significant factor in the recovery of residual oil. This factor is capillary pressure, which in a porous medium depends on pore size distribution, the chemical composition of the rock and fluids, and the saturation of the fluids in the pores. Rock wettability alteration may occur under different processes such as water flooding depending on the composition of injected water and rock. For instance, an injected water containing sulfate and magnesium changes the wettability of a surface containing calcite (section 2.3.3) such as carbonated rock to more water wet (Gomari et al., 2006).

Seyyedi et al. (2015) investigated the effect of carbonated water on the wettability of three different minerals: quartz, mica, and calcite. For each mineral, two aging conditions were considered: an unaged (clean) rock and an aged rock. The observed change in the measured contact angles was a function of pressure. For the unaged substrates, the change in wettability by carbonated water was moderate, with a maximum change of 6° for quartz. The results of the aged minerals revealed a much higher change in wettability compared to the unaged substrates. For example, in the aged quartz sample, the contact angle changed from 76° to 61°; for the aged mica, the contact angle changed from 89° to 63°, and for the calcite, the contact angle changed from 144° to 97°. Therefore, wettability change was considerable under CWI.

2.2.2.1. Drainage

The immiscible displacement in porous media is in general affected by capillary and viscous forces. A minimum of two parallel pores is considered in pore displacement mechanisms. Drainage

occurs when a non-wetting phase displaces a wetting phase and imbibition occurs when a wetting phase displaces a non-wetting phase. In drainage, for example, gas as a non-wetting phase displaces the liquid (wetting phase). As the non-wetting phase arrives at point A, displacement of the wetting phase in the wider throat takes place first, and then the gas-liquid interfaces are established at the inlets of the narrow throats (Figure 2-5).

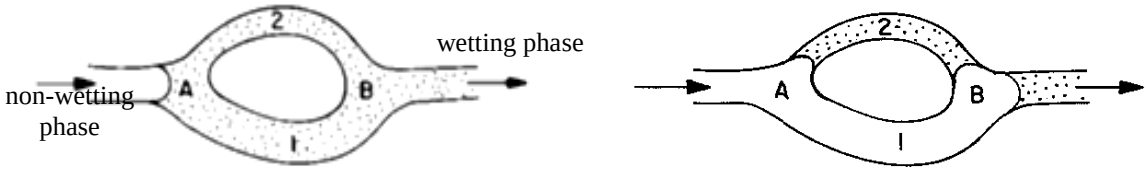

Figure 2–5: The schematic of drainage mechanism (Chatzis and Dullien, 1982)

2.2.2.2. Imbibition

If the rock is water-wet, the displacement of oil by water is known as imbibition, which is divided into two types: free imbibition and forced imbibition. In free imbibition, the wetting phase only flows by spontaneous capillary pressure without any applied pressure, whereas an external pressure is applied in forced imbibition. The wetting phase moves into the smaller pore due to higher capillary pressure, resulting in oil trapping in the larger pore (Figure 2-6). It is known that a reduction of capillary forces and local heterogeneity will reduce the amount of trapped oil by this mechanism (Laidlaw and Wardlaw, 1983; Chatzis and Dullien, 1983; Lake, 1989; Rose, 2001).

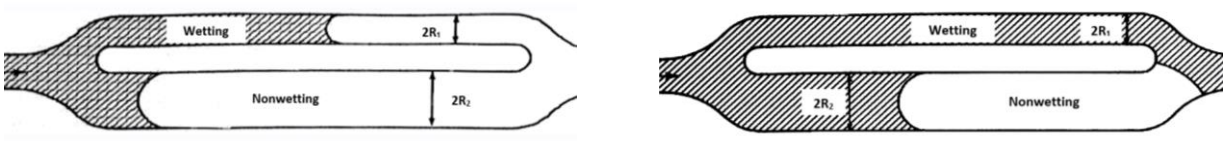

a) before trapping b) after trapping

Figure 2–6: Schematic of imbibition (Lake, 1989)

2.2.2.3. Dead-end Extraction

In porous media trapped oil occurs in two different types; the continuous non-wetting phase and the discontinuous non-wetting phase. Displacement of the trapped phase is possible by several different techniques: i) decreasing the interfacial tension, ii) increasing the viscous forces, iii) or the two phases can be made miscible so that the trapped phase will be dissolved by the flooding phase.

In pore network micromodels, observations of displacements led to an understanding of the phenomenon of dead-end oil extraction (Campbell and Orr, 1985). Recovery of oil from dead-end pores, with and without water barriers shielding the oil, was investigated by Peksa et al., (2013). Visual observations of pore-level displacement events indicate that CO_2 displaces the oil more efficiently in both first-contact and multiple-contact miscible displacements when water is absent. Experiments in dead-end pores blocked by water also demonstrate that CO_2 can reach trapped oil where a solvent insoluble in water cannot reach. Figure 2-7 shows the process of recovering oil from a dead-end pore.

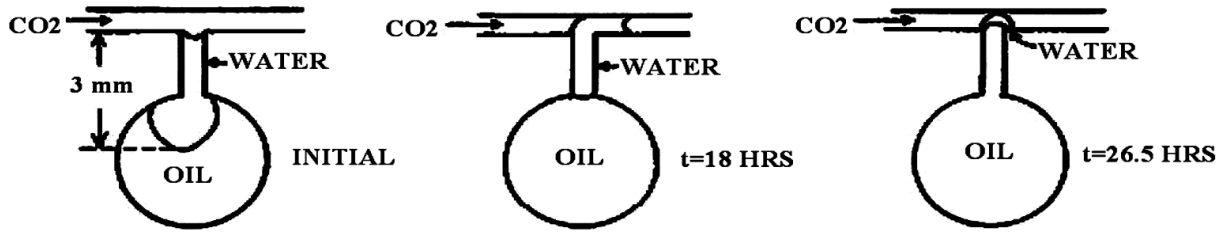

Figure 2–7: Swelling of trapped oil in a dead-end pore in CO_2 injection (Campbell and Orr, 1985)

It is expected that the performance of CWI, due to its CO_2 content, is dependent on pore structure and pore-throat connectivity. Oil trapping and dead-end trapping mechanisms are affected by the

nature of CWI. The degree of the reservoir's complexity in terms of layering and the presence of fractures will affect the CW-oil interactions resulting in the amount of CO_2 transfer. The effect of CWI on oil extraction in a fractured porous media (horizontal fracture and vertical fracture pore network) is investigated in this study.

2.3. Phase Behavior of CO_2

CO_2 can be found in a solid, gas, liquid, and supercritical liquid state depending on the combination of pressure and temperature. Figure 2-8 is a phase diagram, displaying how the state of CO_2 is connected to temperature and pressure.

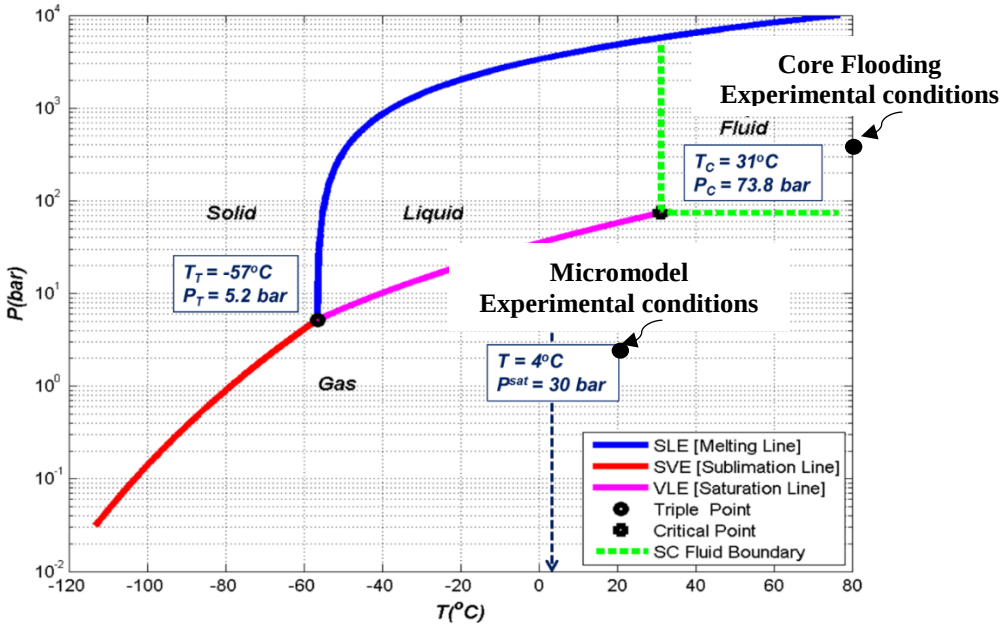

Figure 2–8: CO_2 phase diagram as a function of pressure and temperature (Picha, 2007)

The solid lines represent the equilibrium between the two phases. CO_2 is supercritical at temperatures and pressures higher than 31°C (87.8 °F) and 7.4 MPa (1,070.4 psi). Supercritical CO_2 exists in both gaseous and liquid phases, where it is not possible to distinguish between the two phases. The density of supercritical CO_2 is similar to liquid CO_2, and the viscosity is similar to

the viscosity of gaseous CO_2. In this research, the CO_2 is considered a gas during the micromodel studies (21°C (69.8 °F) and 2.1 MPa (305 psi)) and supercritical at core flooding conditions (85°C (185 °F) and 31 MPa (4,500 psi)) as illustrated in Figure 2-8.

2.3.1. Solubility of CO_2 in Water/Brine

The thermodynamic properties of aqueous solutions containing CO_2 and salts are very important for the petroleum industry. CO_2-based EOR processes are dependent on the phase behavior of CO_2 and its interaction with other fluids in the reservoir including brine, oil, and gas.

Several models of the CO_2-H_2O-brine system, at different pressure and temperature conditions, have been developed. Duan and Sun (2003) developed a thermodynamic model for the solubility of CO_2 in pure water and brine solutions with different salinities for temperatures from 0 to 260°C (0 to 450 °F), for pressures under 200 MPa (29,000 psi), and salinity between 0 to 77,000 ppm.

The solubility of CO_2 in pure water/brine has been measured over a wide range of pressures and temperatures. This is also reported by Bamberger et al. (2000), Kiepe et al. (2002), Koschel et al. (2006), and Mao et al. (2013). Figure 2-10 shows the dependency of CO_2 solubility (g/mol H_2O) on pressure, temperature, and salinity. As Duan and Sun, (2003) showed, CO_2 solubility increases when the pressure increases and decreases as the temperature increases. Duan and Sun (2003) showed that the CO_2 solubility is reduced from 1.7 g/mol to 0.71 g/mol for pure water to 58,000 ppm and a temperature of 30 to 90°C (86 to 194 °F), and a pressure of 0 to 40 MPa (5,800 psi) (Figure 2-9).

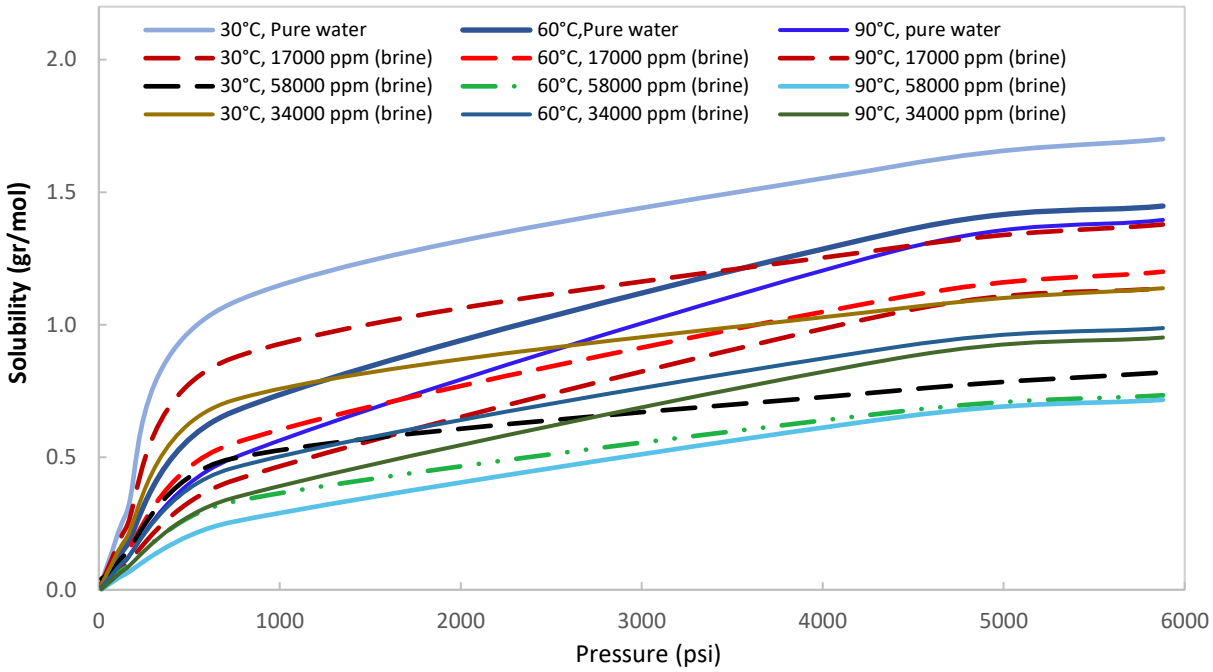

Figure 2–9: CO_2 solubility in water/brine as a function of P and T (Duan and Sun, 2003)

2.3.2. Phase Behavior of Carbonated Water

In Figure 2-10, the phase diagrams of the CO_2-H_2O (carbonated water) and CO_2-brine (carbonated brine) systems up to 100°C (212 °F) and 100 MPa (14,504 psi) are depicted. Figures 2-10a to d, show the phase diagram for zero salinity, 18,000, 54,000, and 108,000 ppm salinity (0 to 4.3 molality). The fields between phase boundaries are the stable regions. The three-phase curve involving the aqueous liquid (Laq), the carbonic liquid (Lcar), and the carbonic vapor run diagonally through the center of Figure 2-10a from the critical point (CEP) at 31.5°C and 7.4 MPa (Wendland et al., 1999), down to -25°C and 1.68 MPa (Span and Wagner, 1996; Span et al., 2013). Above this curve, the carbonic liquid is the phase that saturates the aqueous liquid. At the pressure and temperature conditions above CEP, the aqueous liquid is in equilibrium with the supercritical carbonic fluid (SCFcar). The red curves display the solubility (molality%) of CO_2 in pure water (a) and brine (b,c, and d). Each contour represents a bubble curve of the system. Continuous

contours indicate solubilities in P-T regions where the aqueous solution is at a stable equilibrium in the ternary CO_2-H_2O-brine system (Akinfiev and Diamond, 2010).

The phase diagram for this research depicts the carbonated deionized water (zero salinity) and the carbonated seawater (Atlantic seawater, 35,987 ppm salinity). The carbonated water solutions were prepared at 21°C (69.8 °F) and 1.5 MPa (220 psi) for the micromodel study, and 85°C (185 °F) and 24 MPa (3,500 psi) for the core flooding study. After the preparation of carbonated water (CW) and the carbonated seawater (CSW), the experimental conditions for the carbonated water injection were set at 21°C (69.8 °F) and 2.1 MPa (305 psi) for the micromodel study and 85°C (185 °F) and 31 MPa (4,500 psi) for the core flooding study.

The reason for partially saturating the carbonated solutions in both micromodel and core flooding is that we do not want to have a three-phase system composed of gas (CO_2), aqueous (CW or CSW), and liquid (oil). We are interested in having a two-phase system that includes CW or CSW, and liquid (oil). There are three ways to make sure the carbonated water is single phase. a) visual observation, that there is not any bubble in the micromodel besides the oil phase and single-phase carbonated water (which looks like water). b) the saturation pressure of carbonated water phase was lower than the experimental pressure, because if the experimental pressure fluctuates during the experiment, there is enough difference between the carbonated water saturation pressure and experimental pressure that does not allow any gas comes out of the solution. c) the sampling of the carbonated phase using back pressure, if there is any gas phase besides the carbonated water, initially gas is produced from the top side of the accumulator containing carbonated water.

The solubility of CO_2 in seawater (35,987 ppm) at 85ºC and 31 MPa was interpolated using Figure 2-10b and c to be 0.976 mol CO_2/kg water (0.01746 mol CO_2/mol water). The solubilities change between approximately 0.8 mol CO_2/kg water (0.0144 mol CO_2/mol water) and 1.15 mol CO_2/kg water (0.0207 mol CO_2/mol water).

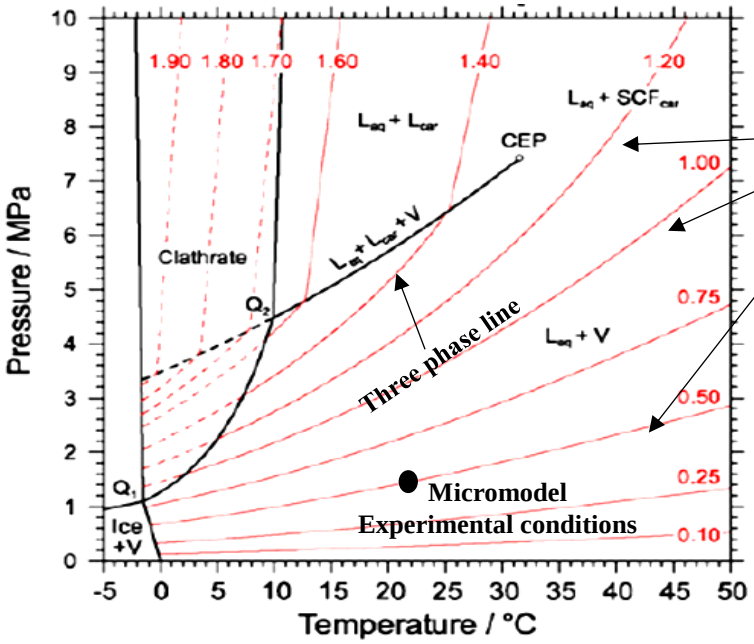

Solubility curves (red) at different pressures and temperatures

a) 0 ppm salinity

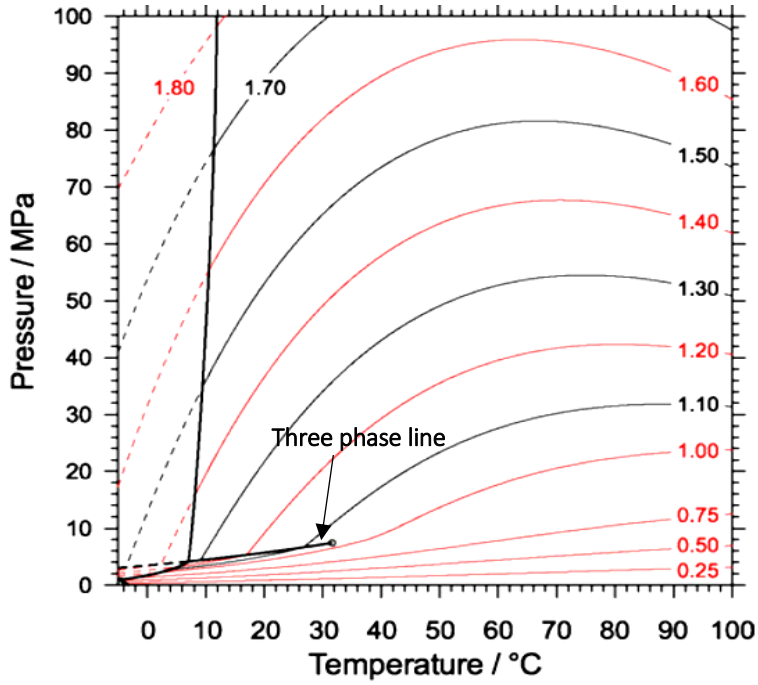

b) 18,000 ppm

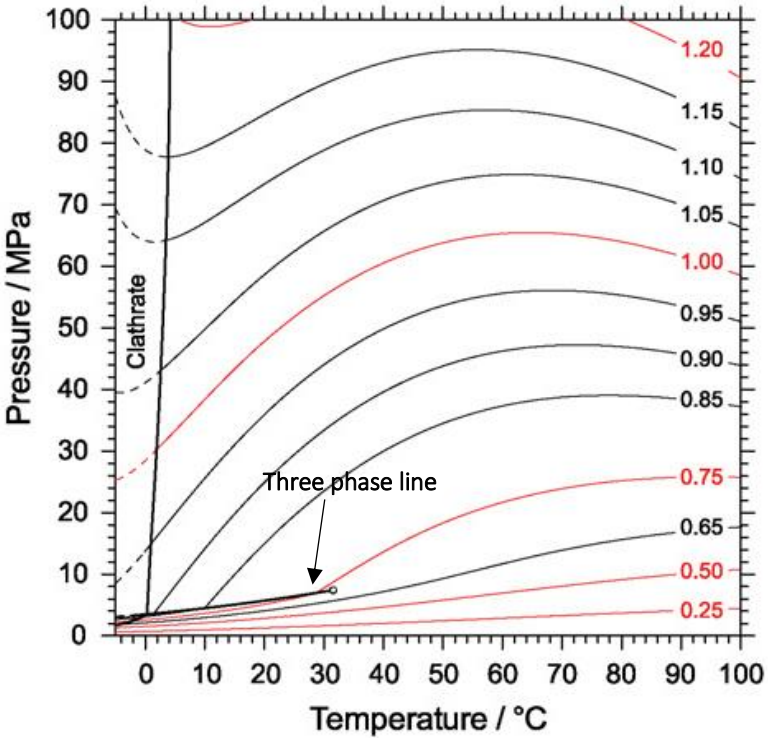

c) 54,000 ppm

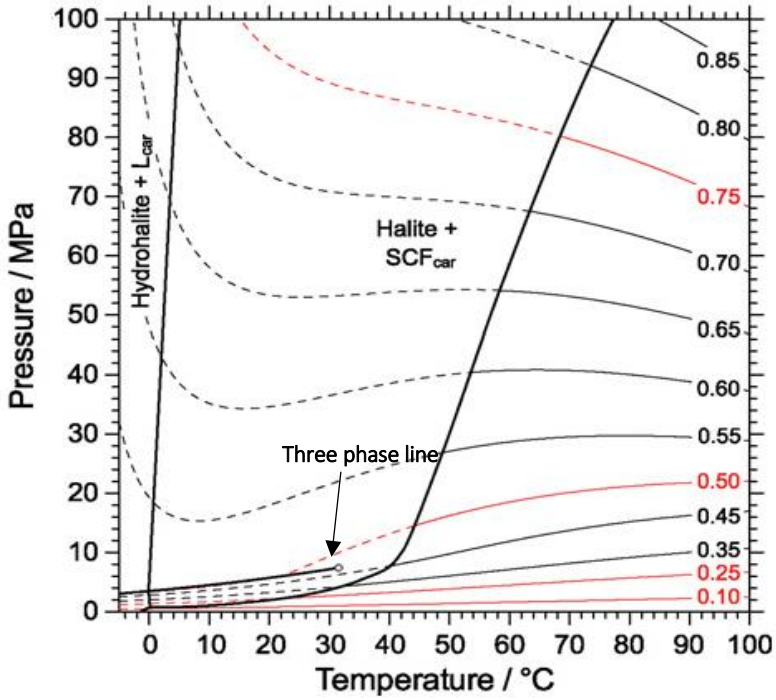

d) 108,000 ppm

Figure 2–10: Carbonated water phase diagram as a function of P, T, and salinity (NaCl) a) zero salinity, b) 18,000 ppm, c) 54,000 ppm, and d) 108,000 ppm (Akinfiev and Diamond, 2010)

2.3.3. Effect of CO_2 on pH of Water/Brine

The dissolution of CO_2 in water/brine reduces the pH of the injection water which may affect the wetting characteristics of the rock (Hirasaki, 1991; Seyyedi et al., 2015). When CO_2 dissolves, it interacts with water molecules until an equilibrium is established. Equation 4 shows the reaction between dissolved CO_2, water (H_2O), and H_2CO_3 (carbonic acid).

$$CO_2\ (aq) + H_2O\ (l) \longleftrightarrow H_2CO_3\ (l) \quad (4)$$

This reaction is kinetically slow, and a small fraction of dissolved CO_2 is converted to H_2CO_3. Carbonic acid is a weak acid that dissociates in two steps (Lide, 1990). Therefore, most of the CO_2 remains as dissolved molecular CO_2 in water (equilibrium ratio is 1.7×10^{-3} at room temperature).

$$H_2CO_3 + H_2O \longleftrightarrow H_3O^+ + H_2CO_3^- \quad (5)$$

$$H_2CO_3^- + H_2O \longleftrightarrow H_3O^+ + CO_3^{2-} \quad (6)$$

In water/brine the pH of dissolved CO_2 decreases with an increase in pressure and a decrease in temperature. This behavior follows a similar trend found for CO_2 solubility in H_2O/brine. Pressure and temperature affect the pH as CO_2 dissolves in water/brine (Park et al., 1999; Hou et al., 2013). By increasing pressure, the dissolution of CO_2 in water/brine is increased and by increasing temperature the dissolution of CO_2 is decreased (Figure 2-10). For example, by increasing pressure from 0 to 5,880 psi at constant temperature of 30ºC, the solubility varies from 0 to 1.7 g/mol. By increasing the temperature to 90ºC, the solubility of CO_2 in water decreases to 1.37 g/mol.

Note that carbonate anions interact with the cations present in the brine to form insoluble carbonates. For instance, if Ca^{2+} is present in carbonate rocks, $CaCO_3$ is formed and if Mg^{2+} is

present, $MgCO_3$ is formed. The formation of these deposits can move the equilibrium to the right resulting in acidification of the water (Lide, 1990).

$$Ca^{2+} + CO_3^{2-} \longleftrightarrow CaCO_3 \quad (7)$$

$$Mg^{2+} + CO_3^{2-} \longleftrightarrow MgCO_3 \quad (8)$$

2.3.4. CO_2 Solubility in Oil

In CO_2 injection, CO_2 solubility is the main mechanism in oil recovery. Oil and CO_2 are in direct contact, resulting in the CO_2 transfer from the CO_2 phase to the oil phase. When the reservoir pressure is below the MMP or the reservoir oil composition is not favorable, the CO_2 and oil do not form a single phase and are not miscible. However, CO_2 will still dissolve in the oil causing oil swelling and viscosity reduction that both help to improve sweep efficiency, which leads to an increase in oil mobility (Martin and Taber, 1992). The saturation pressure, temperature, and oil gravity are the main factors that affect the CO_2 solubility in oil (Simon and Graue, 1965). CO_2 solubility in oil increases with pressure and decreases with temperature and also increases with oil API gravity (Simon and Graue, 1964; Welker and Dunlop, 1963). Emera and Sarma (2006) studied the physical properties of CO_2 in oil and proposed a new genetic algorithm-based correlation to predict CO_2 solubility, oil swelling factor, and density and viscosity of CO_2/oil mixtures.

In the current study, the physical properties of CO_2/oil mixture were calculated by the generated correlations by Emera and Sarma (2006). The correlations to calculate the solubility of CO_2 ($\delta_{CO2-oil}$) and the swelling factor (SF) for dead oil, $MW_{oil} < 300$ g/mol, and T > $T_{critical,CO2}$ (all pressure ranges) and T < $T_{critical,CO2}$ (pressure less than equilibrium pressure) are listed below:

$$\delta_{CO2-oil} = 2.238 - 0.33y + 3.235y^{0.6474} - 4.8y^{0.25656} \quad (9)$$

where $y = \gamma \left(\frac{T^{0.8}}{P_{sat}}\right)^{exp\left(\frac{1}{MW}\right)}$

$$SF = 1 + 0.48411Y - 0.9928Y^2 + 1.6019Y^3 - 1.2773Y^4 + 0.48267Y^5 - 0.06671Y^6 \quad (10)$$

where $Y = 1{,}000 \times \left(\left(\left(\frac{\gamma}{MW}\right) \times \delta_{CO2-oil}^2\right)^{exp\left(\frac{\gamma}{MW}\right)}\right)$

The density and viscosity of CO_2-oil mixture were estimated based on the correlations (Emera and Sarma, 2006) as described below:

$$\rho_{CO2-oil} = \rho_i + 0.0008z - 0.0008z^{0.157} \quad (11)$$

where $z = \gamma\rho_i \frac{(P_{sat}-14.7)}{T}$

$$\mu_{CO2-oil} = w\mu_i - 10.8\left(\frac{\delta_{CO2-oil}}{\mu_i}\right) \quad (12)$$

where $w = x^{-0.74}$ and $x = \left(\mu_i \left(\frac{P_{sat}}{T}\right)^{0.2}\right)^{(\gamma \times \delta_{CO2-oil})}$

where in all the above-mentioned correlations, $\delta_{CO2-oil}$ is the solubility of CO_2 in oil (mole fraction), SF is the swelling factor, γ is the specific gravity of oil, MW is the molecular weight of oil (g/mol), P_{sat} is the saturation pressure of CO_2/oil mixture (psia), ρ_i is the initial oil density at the specified temperature (g/cm^3), μ_i is the initial oil viscosity at the specified temperature (cP), and T is the temperature (°F). The physical properties of CO_2 and oil mixture were calculated and

reported in Tables 2-1 for micromodel experimental conditions and Table 2-2 for core flooding experimental conditions.

Table 2-1: Physical properties of the CO_2/oil mixture at 21°C (69.8 °F) and 1.5 MPa (220 psi)

Prop.	Calculated solubility (*) (mol CO_2 /mol oil)	Calculated solubility (**) (mol CO_2 /mol oil)	SF (*) (cm^3/cm^3)	$\boldsymbol{\rho}$ (*) (g/cm^3)	$\boldsymbol{\mu}$ (*) (mPa.s)
Value	0.096	0.102	1.014	0.878	6.23

(*) correlation: Emera and Sarma (2006), (**) CMG-WinProp

Table 2-2: Physical properties of the CO_2/oil mixture at 85°C (185 °F) and 24 MPa (3,500 psi)

Prop.	Calculated solubility (*) (mol CO_2 /mol oil)	Calculated solubility (**) (mol CO_2 /mol oil)	SF (*) (cm^3/cm^3)	$\boldsymbol{\rho}$ (*) (g/cm^3)	$\boldsymbol{\mu}$ (*) (mPa.s)
Value	0.448	0.452	1.162	0.887	3.76

(*) correlation: Emera and Sarma (2006), (**) CMG-WinProp

When two or more fluid phases are present, the saturation of one phase affects the permeability of the other(s), and relative permeabilities must be considered. Relative permeability has been studied since 1939 (Leverett, 1938) and is a function of pore geometry, wettability, fluid distribution, viscosity, flowrate, and fluid saturation history. In carbonated water injection, CO_2 is transferred to the oil from the carbonated water phase and there is not any free CO_2 gas phase (Riazi, 2011).

The residual oil saturation is an important point in oil relative permeability which affects the mobility of oil. When CO_2 is dissolved in oil, swelling occurs. CO_2 dissolution in oil extracts the trapped oil droplets in dead-ends. This event causes the trapped oil droplets that cannot move under the present pressure gradient to move toward the production well. Oil swelling is considered as an increase in oil saturation, which in turn enhances the oil relative permeability (Li et al., 2015). In this work, the calculation of solubility of CO_2 in water and oil ($\delta_{CO2-oil} = 0.096$ mol CO_2/mol oil

compared to $\delta_{CO2-water} = 0.0128$ mol CO_2/mol water) showed that CO_2 from water phase was transferred to oil phase and no CO_2 bubble was observed.

$$M_{oil} = \frac{k_{ro}}{\mu_o} \tag{13}$$

Where M_{oil} is the mobility of oil, k_{ro} (fraction) is the relative permeability of oil and μ_o (cP) is the viscosity of oil. An understanding of the physical properties of oil during CO_2 injection is important to analyze the process and the effects of CO_2 on the oil recovery factor. In the CWI process, CO_2 mixed with water gives water a lower interfacial tension, which can give a lower residual oil when water displaces the oil (Honarvar et al., 2017).

2.3.5. CO_2 Diffusion in Oil

CO_2 injection may improve oil recovery through three mechanisms: swelling, reducing viscosity, and decreasing residual oil saturation. Mixing between CO_2 and oil improves displacement efficiency in CO_2 injection processes. Diffusion is responsible for mass transfer at the pore scale. Diffusion is defined as the movement of molecules from regions of high concentration to low concentration to achieve equilibrium in chemical potential (Darvish, 2007). As for a solvent-assisted recovery process, the mass transfer rate is important to evaluate the feasibility for recovering heavy oil (Luo and Kantzas, 2008), while the diffusion coefficient is a key parameter required to quantify the mass transfer process.

The impact of CO_2 diffusion in CO_2 injection has been investigated by several researchers (Laidlaw and Wardlaw, 1983; Majlaton, 2012). The partial solubility of CO_2 as a result of CO_2 diffusion is a parameter that determines the performance of the CO_2 injection process. Mass

transfer in porous media depends on molecular diffusion and convection. Molecular diffusion can be defined as the movement of molecules from high concentration region to low concentration region. Convection is mechanical mixing resulting from velocity variations (Perkins, 1963). Mass transfer phenomena for a gas-liquid system in porous media is a time-dependent process and highly depends on the molecular diffusion in the absence of convection mechanism (Abedini et al., 2014; Kavousi et al., 2013).

Diffusion in liquids is slower than in gases, because the distance between the molecules is substantially smaller than in gases, and free mobility of the molecules is strongly reduced by intermolecular forces (Al-Rawajfeh, 2004).

Yang and Gu (2008) developed a dynamic interfacial tension method to determine the diffusion coefficients of an oil-CO_2 system at high pressure and constant temperature. The diffusion coefficient in an oil sample from the Weyburn oil field was measured. The density and viscosity of the Weyburn oil are 0.877 g/cm^3 (29.8 °API) and 13.0 cP, respectively. The diffusion coefficient changed from 0.47 to 2.49×10^{-9} m^2/s as the pressure increased from 0.1 to 5.0 MPa at 27°C. The measured diffusion coefficient (0.47 to 2.49×10^{-9} m^2/s) are close to the literature data values of 2.0×10^{-9} m^2/s for the Maljamar oil-CO_2 with the viscosity of 3 cP. However, they are larger than the CO_2 diffusion coefficients in Lloydminster heavy oil (0.20 to 0.55×10^{-9} m^2/s) of which viscosity is several orders of magnitude higher. Diffusivity of the gas differs with changing temperature and pressure, and oil composition. Increasing pressure increases the diffusion coefficient of CO_2 in oil. CO_2 diffusivity in oil increases with increasing temperature. This is expected since diffusion is a viscosity dependent mechanism and oil viscosity decreases when

temperature increases. Therefore, it facilitates the mass transfer of CO_2 into oil phase (Unatrakarn et al., 2011).

There is little data on CO_2 diffusion in light oil and most of the studies are focused on CO_2 diffusion in heavy oil reservoirs. Araujo et al., (2013) studied the CO_2 diffusion in a light oil (28 °API). They carried out experiments at pressure of 28.9 MPa using pressure decay and CT scanning methods. The diffusion coefficient was found to be 2.91×10^{-8} m^2/s at a temperature of 20°C (68 °F). The molecular diffusion of an oil-gas system is a key factor in determining the mass transfer rate. The actual mass transfer between oil and gas is an unsteady-state process. Guo et al., (2009) studied CO_2 diffusion in an oil sample (17 °API) at 20 MPa (2,900 psi) and 60°C (140 °F) by a developed mutual diffusion model to be 1.08×10^{-11} m^2/s. Results of the coefficient measurements showed that the presence of transit zone is one of the major characteristics of the gas-oil diffusion processes. In order to obtain molecular diffusion of CO_2 in oil, the diffusion coefficient was calculated using the following equation (Renner, 1988):

$$D_{CO_2,oil} = \left(\mu_o{}^{-0.4562} M_{CO_2}{}^{-0.6869} v_{CO_2}{}^{-1.706} P^{-1.831} T^{4.524}\right) \times 10^{-9} \quad (14)$$

where D is the diffusivity coefficient of CO_2 in the crude oil (m^2/s), μ_o is the viscosity of oil (cP), M_o is the molecular weight of the oil (g/mol), v_{CO_2} is the molar volume of CO_2 (cm^3/g) at the experimental condition, P(Psi) is the pressure of the system at equilibrium condition, and T(K) is the temperature of the system.

Bagalkot and Hamouda (2017) studied the diffusion coefficient of CO_2 in n-decane, n-heptane, and n-hexane at experimental conditions of 25 to 45°C (77 to 113 °F) and 2.5 to 6.5 MPa (363 to

943 psi) using dynamic pendant drop volume analysis (DPVA). The diffusion coefficients of CO_2 in n-hexane (1.7 to 3.5×10^{-9} m^2/s), n-heptane (1.3 to 2.7×10^{-9} m^2/s), and n-decane (1.2 to 2.4×10^{-9} m^2/s) were obtained. It was observed that the diffusion coefficient increased as the hydrocarbon was lighter. The higher diffusion coefficient of CO_2 in the lighter hydrocarbon (n-hexane) compared to the heavier hydrocarbon (n-decane) was attributed to the viscosity of CO_2 plus the hydrocarbon phase. An increase in the diffusion coefficient was observed by increasing the pressure. Additionally, it was concluded that the dependency of IFT to temperature is related to the density difference in drop phase (CO_2+hydrocarbon) and the surrounding gas phase (CO_2). In the current work, the physical properties of oil are listed as 6.82 cP, 257 g/mol, 1.362 cm^3/g, 4500 psi (31 MPa), and 358.15 K (85°C). Using the mentioned physical properties, $D_{CO_2,oil\ (85°C,4500\ psi)}$ was calculated to be 2.10×10^{-9} m^2/s. And $D_{CO_2,oil\ (21°C,305\ psi)}$ at the micromodel experimental conditions was calculated to be 9.43×10^{-10} m^2/s. All the physical properties were calculated using CMG-WinProp™.

In displacements where contact times are short (laboratory coreflood) or where diffusion paths are long (field-scale floods), and for systems where diffusion rates are low, non-equilibrium effects may reduce displacement efficiency under a diffusion mechanism (Grogan and Pinczewski, 1987).

2.3.6. CO_2 Diffusion in Aqueous Phase

In CO_2 injection, when CO_2 is injected into the reservoir, it interacts with oil and formation brine. The amount of CO_2 that is mixed with oil and formation brine phases is controlled by the rate of CO_2 diffusion. Because CO_2 is soluble with formation brine it can easily reach the interface between oil and brine.

Lu et al. (2013) studied the diffusivity of CO_2 in pure water in a high-pressure capillary optical cell. They reported that the diffusion coefficient of CO_2 to be 5.39×10^{-9} m^2/s at a temperature of 80°C and a constant pressure of 20 MPa. Azin et al. (2013) studied the diffusivity of CO_2 in brine with salinity of 115,000 ppm. It was found that the CO_2 diffusion coefficient changes in the range of 3.52 to 6.16×10^{-9} m^2/s at the pressure range of 6 to 7 MPa (870 to 1,015 psi) and the temperature range of 32 to 50°C.

Zarghami et al., (2017) studied the diffusivity of CO_2 in the formation water at high temperatures of 50 to 70°C (122 to158 °F) and a pressure of 17.2 MP (2,500 psi) using the pressure decay method in a PVT cell. The results indicated that the rate of CO_2 diffusion in the formation water increased with an increase in temperature. The results showed that the rate of CO_2 diffusion decreased with increasing salt concentration in the formation water. The presence of salt in the formation water increases the viscosity of the water, which results in a higher resistance for the movements of CO_2 molecules in the water. The CO_2 diffusion coefficient was measured to be 7.8×10^{-9} in pure water, 6.4×10^{-9}, 5.9×10^{-9}, and 3.8×10^{-9} m^2/s in 20,000, 40,000, and 80,000 ppm salinity, respectively.

The diffusivity of CO_2 in the brine was estimated using the following equations (McLachlan and Danckwerts, 1972; Al-Rawajfeh, 2004):

$$\log\left(D_{CO_{2,}w}\right) = -4.1764 + \frac{712.52}{T} - \left(\frac{2.5907\times10^5}{T^2}\right) \quad (15)$$

$$\log\left(\frac{D_{CO_{2,}b}}{D_{CO_{2,}w}}\right) = -0.87\log\left(\frac{\mu_{SW}}{\mu_w}\right) \quad (16)$$

where D_{CO_2-w} (m^2/s) and D_{CO_2-b} (m^2/s) are the diffusion coefficients of CO_2 in distilled water and brine, respectively, and T (K) is the experimental temperature. In the current study, the $D_{CO_2-w(21°C,305\,psi)}$ and $D_{CO_2-b(85°C,4500\,psi)}$ were calculated to be 1.78×10^{-9} and 3.10×10^{-9} m^2/s regarding the viscosity of water and brine at specified experimental conditions. The viscosity of water, 0.978 cP at 21°C and the viscosity of brine, 0.364 cP at 85°C were obtained using the developed correlation and graph by El-Dessouky and Ettouny (2002).

2.4. Laboratory Scale CWI Investigation

Martin (1951) studied the effect of CWI on oil recovery using core samples. He found a 12% improvement in oil recovery compared to water flooding. He showed that oil recovery enhancement increases with the CO_2 saturation in water. Additionally, the effect of CWI in heavy oil recovery was more than that in light oil recovery.

Holm (1959) conducted a series of core flooding experiments using carbonated brine with a salinity of 10,000 ppm at pressures of 6.2 MPa (900 psi), 12.4 MPa (1,800 psi), and a temperature of 51°C (125 °F). Berea sandstone cores were used with a porosity of 16 to 25% and permeabilities from 100 to 200 mD. The crude oil had a 37.5 °API gravity. Oil recovery for CWI ranged from 60 to 80% of the OOIP compared to waterflooding recovery of 30 to 45% after 8 PV injection. At pressures higher than 1,800 psi, oil recovery was more than 80%. In this work, the core flooding experiments were performed at lower pressures using low salinity brine, however, pressure and salinity has a considerable effect on the solubility of CO_2 in brine and consequently less CO_2 is available to be transferred to oil phase.

Nevers (1964) studied the effect of CWI in core flooding experiments using sandstone core samples at 60 °F (21°C) and 800 psi (5.5 MPa). Two crude oil samples, a viscous, low-gravity San Joaquin Valley crude and a mobile, high-gravity mid-continent crude. the viscosity of oil at reservoir pressure was 400 cP. The properties of rock sample were not reported. Carbonated water solution was prepared using fresh water at the saturation pressure of 800 psi (solubility of CO_2 in water, 0.019 mol CO_2/mol water). The calculations of viscosity and swelling during the CWI experiments indicated that viscosity reduction was the most effective parameter to increase oil recovery. By increasing the concentration of dissolved CO_2 in deionized water, more oil was recovered. However, increasing pressure did not increase the oil production. In other words, by increasing the pressure, the rate of produced oil was reduced. Nevers (1964) reported that the oil recovery factor for water flooding and CWI at 1 PV were almost the same (46%). Recovery factors after 2.6 PV injection were calculated to be 50% and 57% (two different CO_2 concentration in water) for CWI compared to 48% in water flooding. The conducted core flooding experiments in this study were performed at pressures up to a maximum of 800 psi and 21°C. Both pressure and temperature are shown to affect the solubility of CO_2 in water and brine (refer to Figure 2-9) so there is a need to understand recovery at offshore NL conditions.

Khatib et al. (1981) analyzed the research that was done by two companies. The initial work in the 1940's was done by Montclair Research, New Jersey on sand-pack for the Oil Recovery Corporation. Fresh cores from waterflooded fields in the Mid-Continent, Illinois, and Pennsylvania were used. Results indicated that residual oil saturation (S_{or}) could be reduced by as much as 15% by displacement with carbonated brine after water flooding (tertiary CWI). In another study, Sohio Petroleum Company ran many tests in its laboratory in Oklahoma City under an agreement with

the Oil Recovery Corporation. Tertiary CWI core flooding experiments were conducted at high pressures of 800 to1,000 psi (5.5 to 6.9 MPa). The gravity of oil was 28 to 50 °API. The residual oil saturation after carbonated brine injection were 2 to 26% PV less than for water individually. Additionally, Khatib et al. (1981) reported an investigation of CWI experiments in the 1970's by the Institute France du Petrole (IFP). They performed core flooding experiments with Bati Raman oil (14.8 °API) and Dodan gas in a series of injection cycles with plain water, CO_2, and carbonated brine. At the experimental conditions of 149 ºF (65ºC) and 406 psig (2.8 MPa). An improvement of 14% to 15% in the oil recovery was reported. The performance of CWI is dependent to the pressure and temperature (as previously explained) and this work again confirms the need to examine CWI at offshore NL conditions since we expect the phase behavior to strongly influence the effectiveness of CWI. In the next study by Khatib et al., (1981), pressure is increased but temperature remains constant.

Khatib et al. (1981) investigated the effect of CWI using a series of core displacement experiments at 15 MPa (2,175 psi) and 65°C (149 °F). The density and viscosity of oil were reported as 0.967 g/cm^3 and 290 cP, respectively. The experiments were conducted using a rock sample with the porosity of 17.1% and air permeability of 24 mD. They showed that additional recovery of heavy oil, and in some experiments light oil, was possible with carbonated brine. They injected carbonated water as a tertiary CWI, the recovery factor increased from 33.2% to 48.1% from water flooding to CWI. Mayers et al. (1988) listed two groups of core flooding experiments done in 1981 and 1985 with oil 13.5 and 12.3 °API, respectively. The average oil recovery improvement was 17% PV for the core samples in 1981 and 19.4% PV for the core sample in 1985 (PV=83.7 cm^3).

Perez et al. (1992) investigated the effect of CWI at different CO_2 concentrations in a sandstone fractured porous media at 13.7 MPa (2,000 psi) and room temperature. Limestone rock samples with the porosity ranging from 19.5 to 27% and the permeability ranging from 7 to 68 mD were used. Deionized water was enriched with CO_2 at different pressures from 50 to 500 psi (solubility of CO_2 in fresh water from 50 to 500 psi, 0.002 to 0.014 mol CO_2/mol water). Nuclear Magnetic Resonance (NMR) method was used to study the effects of carbonated water imbibition on oil recovery rate and recovery factor. They observed that oil mobility and permeability were increased. They found that oil recovery is increasing especially in the low matrix permeability due to an increase in oil mobility. The recovery rate and ultimate recovery increased as a function of the amount of CO_2 dissolved in the water. Oil recovery increased after 50 hours injection from 10% to almost 16% of OOIP for the oil with 38.9 °API and oil recovery increased from 7% to 20% for the oil with the 39.6 °API. In this work, although the experimental pressure was high (2,000 psi) the carbonated water was equilibrated at low pressures (50 to 500 psi) thus the water was severely undersaturated.

Nasehi and Asghari (2010) studied the application of carbonated brine (1 wt% brine) through a sand-pack (porosity of 36.5% and permeability of 16 D) column at 1,000 psi (6.8 MPa) and 30°C (86 °F). The CWI was equilibrated at experimental conditions and the solubility of CO_2 in brine was calculated to be 0.016 mol CO_2/mol water. They found that CWI significantly improves the incremental recovery of heavy oil (1,000 cP) to 27.5% OOIP at 12 PV injection. It was also found that the increase in the operating pressure resulted in increased oil recovery. This is a meaningful study for heavy oil and heavy oil reservoir conditions. Since the authors did find that oil recovery

increased with pressure, we confirm the need to examine the effectiveness of CWI at offshore NL conditions.

Dong et al. (2011) found that CWI recovered more oil compared to water flooding from sand-packs in the secondary and tertiary CWI schemes. The porosity of 30% and permeability of 1,700 to 3,700 mD were reported for sand-packs columns. The experimental conditions were 4.1 MPa (600 psi) and 40ºC (104 ºF). Carbonated water was prepared using deionized water at experimental conditions with the CO_2 solubility of 0.013 mol CO_2/mol water. The density and viscosity of oil were reported to be 70.7 cP and 0.936 g/cm^3. Higher flooding rates gave an optimal recovery factor. The mass transfer of CO_2 from water into oil is substantial because CO_2 has higher solubility in oil than in water. They stated that the efficiency of CWI process is not dependent on achieving miscibility, so it has less restrictive requirements for reservoir conditions and fluid composition, and it is more practical for the water flooded fields. Ultimate recovery factor at 1 PV varied from 30 to 58% and the ultimate recovery factors of 60 to 90% at 12 PV were achieved during CWI with different sand-pack columns. This work in a sand-pack column provides a good understanding of CWI at low pressure and intermediate temperature.

Riazi et al. (2011) compared CWI with water flooding using a horizontal homogeneous glass micromodel (porosity of 62% and permeability of 3D) at 13.7 MPa (2,000 psi), 38°C (100 °F) using n-decane (viscosity of 0.83 cP at the experimental conditions). Carbonated water was prepared using deionized water at the experimental conditions (solubility of CO_2 in water, 0.019 mol CO_2/mol water). The recovery factor after injecting 6 PV was obtained to be 33%, 36%, and 51% for water flooding, secondary and tertiary CWI, respectively. The main mechanisms of oil

recovery that were observed during CWI were the swelling and subsequent coalescence of trapped oil ganglia, local flow diversion, and reduction of the oil viscosity. In this work, although the experimental pressure was reasonable, a synthetic oil (n-decane) was used. Using a multicomponent oil may affect the compositional behavior of the fluids and CO_2 transfer. Kechut et al. (2011) conducted core flooding experiments using n-decane and dead oil (0.844 g/cm^3) in secondary and tertiary schemes at the same experimental conditions. A sandstone core sample from North Sea with a porosity of 35% and permeability of 4,580 mD was used. It was found that 45 to 51% of the injected CO_2 was stored in the core at the end of the core flooding tests indicating the high potential of CWI not only for EOR, but also as a CO_2 storage injection strategy. The recovery factor of 42% and 50% was reported at 1 PV. The recovery factor of secondary CWI reached 60% at 4 PV injection which gave 19% additional recovery factor compared to water flooding.

In another study, Sohrabi et al. (2012) examined the application of CWI in a Clashach sandstone core using light and heavy oil samples (62.3 and 20.3 °API) at 13.7 MPa (2,000 psi) and 38°C (100 °F). Experiments was performed using a sandstone rock sample with the porosity of 18.5% and permeability of 1,300 mD. Carbonated water was prepared at the same experimental conditions using seawater with the salinity of 35,380 ppm (solubility of CO_2 in seawater, 0.015 mol CO_2/mole water). Water breakthrough was observed in CWI later than in plain water injection. The recovery factor of 42% and 51% were obtained after 1 PV injection for water flooding and secondary CWI, respectively. They showed that there was a higher incremental oil recovery of 20.5% and 13.3% after 5 PV in both the secondary and tertiary schemes than in water flooding. The results proved CWI performance was influenced by oil viscosity, core wettability and brine

salinity. A higher oil recovery was obtained with the mixed-wet core rather than the water-wet core, with light oil rather than with viscous oil, and low salinity carbonated brine rather than high salinity carbonated brine. This study gave a good understanding of the performance of CWI at medium pressure and temperature using light and heavy oil samples. Performing experiments at higher temperature may reveal a more realist observation of CWI performance a core-scale.

Mosavat et al. (2014) investigated the effect of injection schemes in a sand-pack column (average porosity of 27.6% and permeability of 7,184 mD) at various operating pressures. Synthetic brine with a salinity of 20,000 ppm was used to prepare carbonated water solution (solubility of CO_2 in brine, 0.017 mol CO_2 in water). Experiments were performed using a crude oil with 45 °API and viscosity of 2.76 cP. The recovery factor after 1 PV injection was 66.5% and 59.7% for secondary CWI and water flooding, respectively. It was found that ultimate oil recovery factors for secondary CWI was 78.8% while that for conventional water flooding was 59.7%. It was found that at a pressure of 10.3 MPa (1,494 psi) and a temperature of 25°C (77 °F), oil recovery from tertiary CWI increased 12.5% more than simple water flooding after 6 PV injection. It was reported that increasing operating pressure in CWI enhances the oil recovery, which was mainly affected by higher CO_2 solubility in the injected brine. This work was done in a sand-pack column with high permeability, which may inversely impact the oil-carbonated water interaction compared to a lower permeability porous media where there is more interfacial area between the phases.

Shu et al., (2014) studied the effect of pre-flooding using carbonated water. The experimental conditions were designed at 18 MPa (2,610 psi) and 21°C (69.8°F). The porosity and permeability of Berea core samples were reported to be 16 to 23% and 51.5 to 84.8% mD, respectively. A crude

oil with 45.2 °API and viscosity of 2.17 cP were used. The carbonated water was activated by adding a nonionic surfactant (0.075 wt% IGEPAL CO430 + 0.15 wt% Stepan C2024 AOS + 0.075 wt% Hacros HDP 909-127-2 in a brine of 3.0 wt % salinity) to reduce the IFT between oil and water. The MMP of oil and CO_2 was calculated to be 7.5 MPa using CMG-WinProp software. The experimental results showed that pre-injection of carbonated water before CO_2 injection enhanced the oil recovery by 35.5% compared to 16.6% in pure CO_2 injection. It was found that pre-injection of carbonated water did not increase the recovery factor immediately, however, the increase in oil recovery appeared in tertiary CO_2 injection. Recovery factor (~ 53%) was almost the same at 1 PV injection for pure CO_2 injection and different schemes of tertiary CO_2 injection with pre-injection of active carbonated water (different slug sizes for carbonated water). The ultimate recovery factor of 71.2%, 72.5%, 70.2%, 89.4%, 87.6%, 85.3%, and 87.5% at 4.8 PV injection were obtained for pure CO_2 injection, pre-carbonated water-0.2 slug CO_2 injection, pre-carbonated water-0.4 slug CO_2 injection, pre-carbonated water-0.6 slug CO_2 injection, pre-carbonated water-0.8 slug CO_2 injection, pre-carbonated water-1.0 slug CO_2 injection, and pre-carbonated water-1.4 slug CO_2 injection. It was reported that 0.6 slug size carbonated water injection gave the highest recovery factor among all the schemes. They believed, at 0.6 PV enough contact occurred between residual oil and injected fluid. The solubility of CO_2 is inversely related to temperature. These experiments were performed at ambient temperature of 21°C and medium pressure of 2,610 psi begging the question still as to how does CWI perform at higher reservoir pressures and temperatures.

Sohrabi et al. (2015) investigated the effect of CWI in a pore network micromodel and core flooding at 38°C (100 °F) and 17.2 MPa (2,500 psi). The porosity and permeability of core samples were reported to be 22% and of 1.2 D, respectively. A crude oil with 28 °API and brine with a

salinity of 35,380 ppm were used. Carbonated water was prepared using brine at the above-mentioned experimental conditions (solubility of CO_2 in brine, ~ 0.017 mol CO_2/mol water). Recovery factor was almost constant after 1 PV injection while the recovery factor for secondary CWI was 45%. The results of core flooding experiments showed the recovery factor of 41% and 62% at 5.5 for water flooding and secondary CWI, respectively. The results showed that pore-scale interaction between oil and carbonated water were different from the known dominant mechanisms. Viscosity reduction and oil swelling were considered the two main recovery mechanisms for recovering oil during CWI.

In addition to the previuos study, Sohrabi et al., (2015) found that the formation of a new phase within the oil is another mechanism to recover oil by CWI. In the micromodel experiments, after injection of carbonated water, they noticed the nucleation of a new phase within the crude oil. The new phase was colorless, and it was formed in the crude oil next to the carbonated water path. The recovery factor in both secondary and tertiary CWI in micromodel and core flooding showed that the performance of CWI was a function of the concentration of light and intermediate hydrocarbons in oil.

Mosavat and Torabi (2016) investigated the performance of CWI through a series of horizontal homogeneous micromodel (porosity of 52%) experiments. A very light oil sample with 44.7 °API and brine with a salinity of 20,000 ppm at 2.1 MPa (300 psi) and 19°C (66 °F) was used. The micromodel had the dimension of 12.3 cm by 4 cm. Wettability, contact angle, and residual oil trapping mechanisms were studied during water flooding and CWI. It was observed that viscous fingering was a dominant oil recovery mechanism up to breakthrough. They found that the main

oil trapping mechanism was wettability trapping due to the oil-wet nature of the micromodel. Snap-off and bypassing pores were also observed. The oil recovery at breakthrough was reported to be 70.4% of the original oil-in-place (OOIP), which was 8.1% higher than the water flooding recovery factor at breakthrough. The ultimate recovery factor of 91.1% in secondary CWI was obtained compared to 81.7% in water flooding. Carbonated water changed the wettability of the mixed-wet or oil-wet micromodel to water-wet. CWI was successfully used to recover oil for a longer period.

Shakiba et al. (2016) investigated the carbon storage and oil recovery aspects of CWI in a series of core flooding experiments using oil with 28 °API at 40°C (104 °F) and 13.7 MPa (2,000 psi). The rock sample was carbonated with an average porosity and a permeability of 24% and 11.6 mD, respectively. The results showed 31.5% and 19.7% oil recovery at 1 PV, and 40.5% and 56.7% oil recovery after 7 PV injection during tertiary CWI and secondary CWI compared to the corresponding water flooding. However, the CO_2 storage capacities for both tertiary and secondary CWI schemes were almost the same. Secondary CWI resulted in a 16.2% additional oil recovery compared to tertiary CWI flooding.

Seyyedi et al. (2017) conducted a series of multiple-contact tests in the micromodel (this micromodel was used in Riazi et al., 2011) and slim-tube (porosity of 30% and permeability of 6 D) at 17.2 MPa (2,500 psia) and 38°C (100 °F) using a synthetic live oil (20.9 °API) and seawater (salinity of 54,540 ppm) to understand the interaction between oil and carbonated water. The solubility of CO_2 in seawater was calculated to be 0.014 mol CO_2/mol water. The live oil was brought into contact with carbonated water in a PVT cell. The compositional analysis of each contact period showed that a new gas phase is formed. At the early stage, the new phase was

composed of CH_4 and CO_2. However, as more contact was made between oil and CW, the new phase was richer in CO_2. They also performed a slim-tube experiment to mimic the CW-live oil phase behavior and displacement in porous media. The water breakthrough in CWI occurred at 0.31 PV with the recovery factor of 32.8% compared to breakthrough in water flooding at 0.29 PV with the recovery factor of 26.2%. The recovery factor at 1 PV was reported to be 42% and 54% for water flooding and secondary CWI, respectively. The results of the slim tube tests showed that CWI led to an additional oil recovery of 24.0% compared to water flooding at 5 PV (ultimate recovery factor for secondary CWI ~ 93%). Formation of the new phase improved the oil recovery through reconnection of the trapped oil and oil displacement, creating a favorable three-phase flow region with less residual oil saturation, restricting the flow path of CW and diverting it toward un-swept areas of the porous medium. Formation of the new phase occurred faster and stronger when CW was injected as secondary CWI rather than tertiary CWI. In this work, the effect of live oil is considered and shown to affect the compositional behavior of oil and carbonated water.

2.4.1. Numerical Simulation of CWI

Laboratory observations and numerical simulation studies have confirmed the potential use of gas-based EOR processes for oil recovery in homogeneous and heterogeneous reservoirs. There are several studies related to the simulation of CO_2 injection and related mechanisms. However, there are few carbonated water injections numerical simulation in the literature.

Nevers (1964) proposed a calculation method based on the Buckley-Leveret theory for the performance of CWI process. The effect of oil viscosity reduction and oil swelling due to CO_2 transfer from the carbonated water phase to the oil phase were included. It was shown that CO_2 concentration and carbonated water slug size were the most effective parameters on the

performance of CWI. Additionally, viscosity reduction was the most effective parameter compared to oil swelling. It was found that increasing the CO_2 concentration and carbonated water slug size will increase recovery, but this effect is less pronounced as the pressure increases.

Shenawi and Wu (1994) numerically modeled the CWI process using a compositional simulator (COMABS). They used laboratory CWI core flooding experiments. The COMABS considers the partitioning of CO_2 between the water and oil phases. They selected two different number of grid blocks of 3 and 15. The model could simulate the experimental data very well. They found that the oil viscosity is reduced, and oil density is increased under CWI.

Riazi et al. (2011) mathematically modeled the dependency of oil swelling on CO_2 concentration in a dynamic process of carbonated water injection. They considered two situations; firstly, the swelling of an oil drop, separated from a CO_2 source by a water layer (oil/W/CO_2 source), and secondly, direct contact of oil drop with CW (oil/CW). The simulation of the swelling of the viscous oil showed that the water layer did not have a significant impact on the diffusion rate. This is due to the lower CO_2 diffusion coefficient in oil than that in water for the viscous oil. It was found that the water layer significantly affected the performance of CWI. The available simulation studies investigated the interaction of single drop of oil and CW in a sand-pack porous media.

In the current study, a lab-scale numerical simulation model was built to match the experimental data. A fluid model was built using CMG-WinProp^{TM} considering the effect of CO_2 solubility in the water/brine phase and the performance of seawater flooding, secondary CWI, tertiary CWI, and CO_2-WAG. A vertically-oriented sandstone core sample was simulated using CMG-GEM^{TM} compositional simulator.

2.4.2. Summary and Gaps of the Previous Studies

Table 2-3 outlines the literature review on laboratory CWI experiments. The type of porous media, the experimental conditions, the fluid characteristics, the solubility of CO_2 in water and brine, the fluid flow regime, the injection scheme, the recovery factor at breakthrough, and the ultimate recovery factor are reported.

As the summary of the laboratory experiments shows, experiments are divided into three types: i) sand-pack, ii) micromodel, and iii) core flooding. For example, some sand-pack flooding experiments were performed at different conditions of 600 to 1,500 psi and 20 to 40°C. Several micromodel studies examined the effect of simple water flooding and CWI on oil recovery. However, all the micromodel experiments were performed horizontally and the effect of gravity force on the performance of the injection scheme (water flooding (WF), secondary CWI (SCWI), and tertiary CWI (TCWI)) was ignored. In all of the micromodel studies, homogenous micromodel patterns were designed, and permeability did not vary at different parts of the porous media. Heterogeneity and the presence of low permeable-high permeable zones impacted the fluid flow pattern (Laroche et al., 1999). The presence of gravity and different permeability zones may or may not improve the displacement efficiency, which has not been investigated thus far.

The reported core flooding experiments were performed horizontally at temperatures ranging from atmospheric to 40°C and pressures ranging from 600 psi (4.1 MPa) to 2,500 psi (17.2 MPa). The performance of CWI at higher pressures and higher temperatures has not been studied. In this study, seawater flooding, carbonated seawater injection, and CO_2-WAG were performed at 85°C and 31 MPa, which represents the conditions of offshore reservoirs in Newfoundland.

Table 2-3: Summary of the Previous CWI Laboratory Experiments

Study	Media	ORT	L*W*H (cm*cm*µm)	ϕ (%)	K	P (psi)	T (°C)	Oil (°API)	TDS (ppm)	SCM	Rate (ml/min)	RF at BT (%)	RF (%)
Nevers, 1961	CModel (sandstone core)	HRZ	NA	NA	NA	800	21	NA	NA	WF-SCWI	NA	NA	58
Riazi, 2011	HM-MModel	HRZ	4*0.7*5	62	3D	2,000	38	25.9	10,000	CO_2, SCWI, TCWI	0.01	49	49
Sohrabi et al., 2012	CModel (sandstone core)	HRZ	8*3.7 (d)	22	1,370 mD	2,000	38	28	35,000	WF, SCWI, TCWI	0.01	50	55.5 SCWI 50 TCWI
Mosavat and Torabi 2014	SModel (glass bed)	HRZ	30*2.54 (d)	27	4,500 mD	600, 1,500	25, 40	22	20,000	WF, SCWI, TCWI	1	64.1, SCWI 61.1, TCWI	71.5 SCWI 61.8 TCWI
Shu et al., 2014	CM (sandstone)	HRZ	13.5*3.8 (d)	21	~75	2,610	21	45.2	-	CO_2, WF-CWI CO_2-CWI	0.5	-	71. to 87.5
Sohrabi et al., 2015	CModel (sandstone core)	HRZ	32*5 (d)	22	1.2D	2,500	38	28.5	35,000	WF, SCWI, TCWI	0.01	47	60
Fatholahi and Rostami, 2015	CModel, outcrop (clay core)	HRZ	16*4 (d)	18	57 mD	2,000	30	nC_{10}	35,000	WF, SCWI, TCWI	0.1	39.4, SCWI	SCWI 42.73 TCWI 39.39
Mosavat and Torabi, 2016	HM-MModel	HRZ	12*4*123	52	NA	300	19	22	20,000	WF, SCWI, TCWI	0.05	70.4, SCWI	91.1 SCWI 89.0 TCWI
Shakiba et al., 2016	CModel (carbonate)	HRZ	76*37.8	24	11.6 mD	2,000	40	28	10,000	WF, SCWI, TCWI	0.2	-	88.4 SCWI 72.2 TCWI, 32 WF
Seyyedi et al., 2017	Slim-tube and PVT cell	HRZ	182*3.8 (d)	30	6D	2,500	38	20.9	54,000	WF, SCWI	0.01	32.7, SCWI	93 SCWI
Shu et al., 2017	Mass transfer study	Static test	-	-	-	2,440 to 2,900	20	NA	-	-	-	-	-

d: diameter, D: Darcy, HRZ: horizontal, VRT: vertical, HM: homogeneous, HT: heterogeneous, MModel: micro model, CModel: core model, SModel: sand-pack model, ORT: orientation, SCM: scheme, TDS: water salinity, NA: not available.

2.4.3. Summary of the Current Study

Table 2-4 summarizes the designed laboratory experiments in micromodel flooding and core flooding. Although the effects of many parameters have been studied, the effect of gravity displacement on sweep efficiency and trapped oil extraction, using CWI, is deficient in the current literature. In this study, experiments were performed at 2.1 MPa (305 psi) and 21°C (69.8 °F) using an oil with the 29.8 °API from an offshore Newfoundland reservoir. The geometry of the porous media is an important factor on the ultimate efficiency of EOR processes. Experiments were performed in the homogeneous, horizontally-oriented fractures, and vertically-oriented fractures, and without fracture micromodels. The experiments were conducted under different experimental conditions including in the absence and in the presence of gravity, scheme (i.e., simple water flooding, and secondary and tertiary CWI), and production flowrate. Additionally, a sandstone core plug and oil sample at 85°C (185 °F) and 31 MPa (4,500 psi) were selected to evaluate the performance of CWI on oil recovery.

Table 2-4: Summary of the Current CWI Laboratory Experiments

Media	ORT	L*W*H (cm^2* µm)	ϕ (%)	K	P (psi)	T (°C)	TDS (ppm)	δ_{CO2} (mol CO_2 /mol H_2O)	SCM	N_{ca}	Rate (ml/min)	Comment
HM-MModel	HRT VRT	20×4×56	30	200-450 D	305	21	DI	0.0124	WF, SCWI, TCWI	2.0E-7	8E-4	Effect of gravity, scheme and flowrate
HT-VF MModel	HRT VRT	20×4×56	39		305	21	DI	0.0124		2.0E-7	8E-4	
HT-HF MModel	HRT VRT	20×4×56	38		305	21	DI	0.0124		2.0E-7	8E-4	
CModel	VRT	10.8×3.8 (d)	19-22	314-381 mD	4,500	85	35,897	0.0188	WF, SCWI, TCWI, CO_2-WAG	3.5E-6	2E-1	Reservoir conditions and scheme

d: diameter, D: Darcy, DI: deionized water, HRZ: horizontal, VRT: vertical, HM: homogeneous, HT: heterogeneous, MModel: micro model, CModel: core model, ORT: orientation, SCM: scheme, TDS: water salinity, NA, not available.

The current research plan is a scale study of CWI which includes: pore-scale, core-scale, and simulation.

2.5. Field-Scale CWI Application

Commercial carbonated water floods (Orcofloods) were started in Oklahoma, Texas, and Kansas. Three of these unique floods were initiated in the Dewey-Bartlesville Field, Washington County, Northeast Oklahoma (Hickok et al., 1960). The only other documented CWI field experience occurred in a field located 16 km north of Bartlesville, Oklahoma in 1958. A substantial improvement in water injectivity was reported in all injection wells in this field during CWI. It was further reported that the additional oil production obtained in 1959 was more than the oil production during the entire primary production life of the field which was 29 years. Corrosion and emulsion were not noticed in the steel piping in the production facilities (Hickok et al., 1960).

2.6. Naturally Fractured Reservoirs

Heterogeneities of porous media (fractures) have a significant effect on the recovery efficiency of a reservoir. Fractured reservoirs represent over 27% of the world's oil and gas reserves. However, they are among the most complicated class of reservoirs to produce efficiently (Saidi, 1996). In the case of fractured reservoirs, high residual oil saturation and bypassing zones are common. Conventional EOR methods such as gas injection and water flooding have a low recovery factor in fractured porous media (Allan and Sun, 2003). The petrophysical analysis of the core thin sections of offshore Newfoundland reservoirs showed that the presence of fractures is evident in rock samples (White Rose Oilfield Development Application, 2001).

Offshore Newfoundland production history shows that oil production is declining (https://www.cnlopb.ca/information/statistics/). Considering how difficult and expensive it is to

produce from offshore reservoirs, it makes sense for oil companies to look to EOR methods to recover more oil.

Fractures cause an earlier breakthrough and an unstable frontal displacement in EOR applications which leads to a lower recovery (Laroche and Kalayadjian, 1999; Kamari et al., 2012). Poor sweep efficiency is common in a fractured porous medium (Conn et al., 2014). Fracture networks contain a significant amount of remaining oil. In gas injection processes in fractured reservoirs, fractures conduct the gas and they extend the exposure of the injected gas with oil in the reservoir rock, which is more effective compared to conventional reservoirs. However, high gas mobility compared to water and oil causes the risk of by-passed oil and gravity override, which can lead to an early gas breakthrough (Van Dijkum and Walker, 1991). Waterflooding in such reservoirs may not be applicable if the matrix is not water-wet, very tight and heterogeneous, and oil viscosity is high. Solvent injection in homogeneous porous media yields very low residual oil saturation behind the front (Hatiboglu and Babadagli, 2005). In the water flooding experiment, no oil is displaced from the low-perm region. In WAG flooding, water or gas are not able to displace oil from low permeability regions. Additionally, the presence of micro-fractures is another limiting factor in WAG flooding (Conn et al., 2014). Fractures have high permeability which causes higher conductivity. Fractures can carry a higher volume of injected fluid (gas, water, and carbonated water) and improve the fracture-matrix interaction resulting in residual oil displacement.

2.6.1. Fracture Matrix Recovery Mechanisms

Initially, Mattax and Kyte (1962) studied water flooding in a fractured glass micromodel. They were pioneers in analyzing water flooding mechanisms. They found that when there is flow in the fractured porous media, the matrix and fracture interact with each other. Imbibition is the main

mechanism that describes the fluid interaction between the matrix and fracture in a water-wet porous media. Capillary imbibition is controlled by capillary forces and forced imbibition is controlled by viscous forces.

Capillary imbibition and forced imbibition (wetting phase displacing non-wetting phase by viscous forces) in a homogeneous and fractured porous media were studied by several researchers (Lenormand and Zarcone, 1984; Haghighi et al., 1993; Firoozabadi and Markeset,1994; Babadagli, 2000; Rose, 2001). They found that permeability of the matrix and flowrate in the fracture determine the type of imbibition process. When the permeability contrast between the fracture and matrix is high enough, fluid prefers to follow the fracture and viscous flow occurs. Meanwhile, the interaction between fracture and matrix occurs due to capillary imbibition. Imbibition is characterized into co-current and counter-current flow based on the fluid flow exchange between matrix and fracture (Saidi, 1987). Driving mechanisms in fractured reservoirs are divided to water-oil imbibition, gas-oil gravity drainage, water-oil gravity drainage in oil-wet rock, molecular diffusion, and convection which determine the performance of a fractured reservoir under an EOR process (Aguilera, R., 1980; Qasem et al., 2008; Bourbiaux, 2009).

If a block is surrounded by water, oil is forced to flow in the opposite direction of water flow which is called counter-current imbibition. If the block is partially covered by water, water is imbibed into the matrix and oil flows ahead of the water front. In this case, water and oil flow in the same direction and the process is called co-current imbibition (Pooladi-Darvish and Firoozabadi, 1988). Stoll et al., (2008) and Delshad et al., (2009) investigated the capillary imbibition process and they found that the imbibition process is a very slow and diffusion limited mechanism. The imbibition

process is only economically feasible when forced imbibition under buoyancy or viscous forces occur. However, most of the studies primarily investigated the effect of imbibition in single fracture or single block surrounded by fractures and not a total flow pattern and mechanisms in the fracture-matrix network (Manrique et al., 2006). One factor to improve the performance of an EOR process in a fractured reservoir is controlling the mobility. Sweep efficiencies are strongly dependent on the mobility ratio. Viscous fingering can take place if the mobility of the displacing phase is greater than the mobility of the displaced phase (Terry, 2001). Displacing fluid (gas/water) often has a lower viscosity than the displaced fluid (oil). It tends to flow through high-permeability zones (fractures) and by-passes oil in neighborhood low permeability zones (matrix) resulting in trapped oil zones. Carbonate reservoirs with low matrix permeability and a fracture network are suitable for CO_2 injection processes (Moritis, 2004). Gas has high mobility and may cause an early breakthrough. If a reservoir has a low permeability matrix, gas cannot find an easy path to breakthrough and will stay in contact with the residual oil. Gas-based EOR processes and solvent are the most favorable mechanisms for fractured carbonated reservoirs (Manrique et al., 2006).

The effect of capillary and forced imbibition in a fractured porous media has not been completely studied in the presence of gravity force. According to the literature, there are not any documented studies about the application of CWI in a heterogeneous porous media (fractured). In this study, the performance of CWI in fractured porous media was investigated. The effect of gravity and fracture orientation on oil displacement pattern and oil recovery were also studied.

Chapter 3 **Micromodel Fabrication**

The chapter is based on a paper that was published as described below:

***A Quick and Low-Cost Method to Fabricate Glass Micromodel Networks** (2018) was published in the journal of Microsystem Technology, Issue 5. Mahmoodi, M., Mahdavi, S., and James, L. A.*

The contribution of S. Mahdavi was to establish the idea of using CO_2 laser engraving to etch the substrate on the glass followed by the traditional wet etching method, optimize the thermal bonding procedure, and pressure testing procedure. The first author assisted in the trial and error procedures and drafted the manuscript.

3.1. Overview

In this chapter, a novel fabrication method for a glass micromodel is presented. The challenges with common fabrication methods (wet etching) including time and expenses are addressed. To overcome these challenges, recent advances in chemical etching were modified and combined to decrease the process time and expenses. Generally, the chemical etching process includes masking, etching, and bonding. First, the common masking step was simplified by engraving the glass plates with a CO_2 laser. This new technique eliminated the required facilities for photoresist layer deposition and UV lithography. Next, the general composition of the solution used in the etching step, and the operating conditions of thermal bonding step, were modified based on recent investigations in the literature to improve the pressure threshold (breaking pressure) of the micromodel. The pressure threshold for a glass micromodel was obtained at 5 MPa (720 psi). Finally, the visualization study of water flooding and carbonated water injection (CWI) was

performed at 305 psi (2.1 MPa) and 69.8 °F (21°C) using one homogeneous and three heterogeneous glass micromodels.

The developed fabrication methodology for pressurized glass micromodel was used in a master's thesis at Memorial University.

3.2. Micromodel Fabrication Background

There are several parameters that affect the properties of a micromodel including pore geometry, the roughness of the surface, surface wettability, and corrosion of the grain's edge. The earliest micromodels were fabricated using glass (Mattax and Kyte, 1961). Micromodel studies play a very important role in understanding fluid flow mechanisms (Chatzis, 1982; McKeller and Wardlaw, 1983; Javadpour and Fisher, 2008; Buchgraber et al., 2012). The growing number of multidisciplinary studies that use microfluidic devices to have a better understanding of ongoing mechanisms have required further developments and modifications of micromodel types based on process conditions. The prototyping procedure for micromodels can be categorized as follows: Hele-Shaw and glass-bead models (Chuoke et al., 1959), optical lithography (Thompson et al., 1983 and 1994), etching method (Mattax and Kyte, 1961), stereolithography (Hull, 1986) and soft lithography (Quake and Scherer, 2000). Karadimitriou & Hassanizadeh (2011) extensively investigated and summarized different micromodel fabrication and reported that etching techniques mostly include an acid solution as a chemical agent which etches the silicon-based materials like borosilicate glass, quartz, or silicon wafers (Wegner and Christie, 1983) and create flow channels (<1 mm) in unmasked areas. Hydrofluoric acid (HF) is the core component in an etching solution which diffuses into the surface and dissolves the silicon oxide substrate. The general steps in wet etching process are masking, etching and bonding the used material plates.

The masking procedure and coating substrates are the main expensing and quality controller factors.

There are different materials and technologies that can be used for micromodel fabrication. In chemical etching, hydrofluoric acid (HF) and hydrochloric acid (HCl) are used as etchants to etch the glass surface (Wegner and Christie, 1983; Upadhyaya, 2001; Lago et al., 2002). Chemical etching is a very popular way of making micromodels; however, this method has some limitations. One is that the pore walls are sloped rather than vertical wall, also, there is a curvature at the bottom of pores, which does not happen in a real porous media (Davis and Jones,1968). This happens because liquid acids are isotropic and thus erode glass in all directions. The depth of penetration depends on the concentration of acid and the time of exposure to the etchant (Buchgraber et al., 2012). Basov et al. (1970) used a laser to create the pattern on the glass substrate.

Mohammadi et al. (2012) proposed the application of laser technology for engraving the porous media on glass. In this work, a CO_2 laser device was used to construct porous media patterns on the soda lime glass surfaces, and they optimized the parameters of the laser engraving including fractional power, engraving speed, and resolution.

3.3. Pore Network Micromodel Fabrication

In this work, a soda lime glass plate (thickness, 10 mm) was engraved by a CO_2 laser machine to simplify the masking step by reducing time and cost expenses compared to chemical etching. The available advances in etching buffer composition along with a novel thermal assisted direct

bonding technique were employed to enhance the quality of the final product. This method reduced the previously mentioned problems of traditional micromodel etching (e.g. sloped pore walls). The steps used in the fabrication process are summarized as follows: i) sketching the pattern, ii) laser engraving on glass, iii) chemical etching, iv) making inlet and outlet ports, and v) thermal bonding the two plates.

3.3.1. Pattern Sketching

Initially, the flow pattern was generated using Corel Draw X7 at a magnification of 1:1 and the resolution of 600 dpi. Inlet and outlet ports were added to the drawing, and then the pattern was transferred to a computer which was loaded with the interface program.

3.3.2. Laser Engraving

The CO_2 laser machine (Trotec SP300) was used to engrave the pattern on the glass. The laser machine has a laser beam size of <150 micrometers. The method for laser engraving on glass used carbon dioxide laser radiation at the wavelength of 10.6 μm with the large ratio of the major-to-minor axes to heat the glass along the entire cutting lines enabling every specific throat, pore and grain to be accurately designed. Initially, one side of the glass was covered by laminate (acid resistant layer). Four pore networks of homogeneous and heterogeneous patterns were engraved for this work. It should be mentioned that in this method, the geometric feature of the designed throats was more flexible in laser engraving (≤150 microns). However, the size of the throat in the conventional UV/photoresist masking procedure is limited to the technical complication of photoresist layering and the UV projection process. Additionally, using laser engraving directly on the glass causes micro-fractures which affect the image analysis. An appropriate laser power, speed, and resolution were chosen based on the visibility of glass after removing the laminate and also the sharpness of edges (Table 3-1). Resolution was kept at the maximum number of 1,000 Hz

and then different combinations of speed and power were tried. We noticed that a lower speed was better in terms of less microfractures on the glass. At higher speed, the channels left lots of debris and even after soft brushing and using air, still the glass surface of the edges of channels was fragile. Finally, power was optimized.

Table 3-1: Laser machine optimized engraving settings

Parameter	Mode	Power (W)	Speed (m/min)	Frequency (Hz)
Value	Engraving	16-18 W	10-12	1,000

The micromodel was composed of two plates: one plate contained the pore network pattern and the other plate, which was featureless, was used as a cover. The size of the plate was 12×30 cm^2. The size of the pore network in this study was designed with dimensions of 4.1×20 cm^2 and 3.5×19.9 cm^2, which provided sufficient time for effective contact between the phases and the porous surface. The edges were 2×2 cm^2. This optimized edge distance was achieved through several tries to avoid breakage. The inlet and outlet holes were drilled in predefined locations. The homogeneous micromodel is shown in Figure 3-1. In the heterogeneous micromodel including horizontal fractures, there are five horizontal fractures which oriented parallel to fluid flow direction. Additionally, in the heterogeneous micromodel including vertical fracture there are four fractures perpendicular to flow. The fracture aperture's width is 1 mm; all fractures were designed to have equal aperture (Figure 3-2 and 3-3). The last micromodel was designed to evaluate the vertical flooding with the same direction of core flooding (Figure 3-4). Figure 3-5 shows the detailed and dimensions of the homogeneous and heterogeneous patterns. The micromodel was flooded by water at a very flowrate to obtain the volume of void spaces. The porosity was obtained using the volume of void spaces and the bulk volume of micromodel.

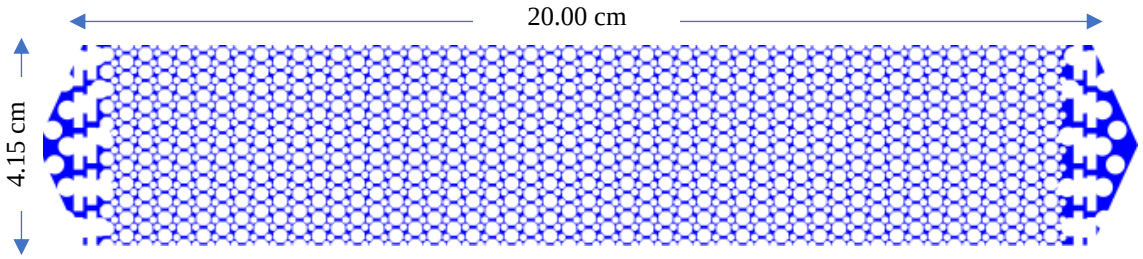

Figure 3–1: Schematic of the homogenous micromodel

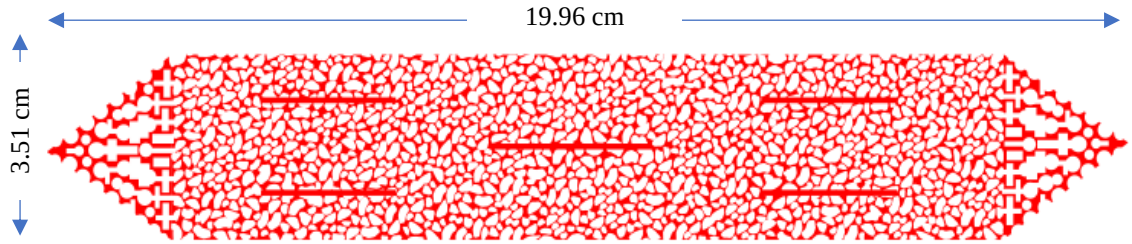

Figure 3–2: Schematic of the heterogeneous micromodel with horizontal fractures

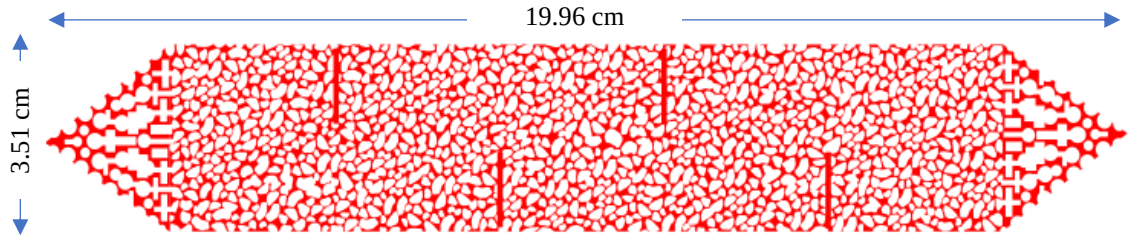

Figure 3–3: Schematic of the heterogeneous micromodel with vertical fractures

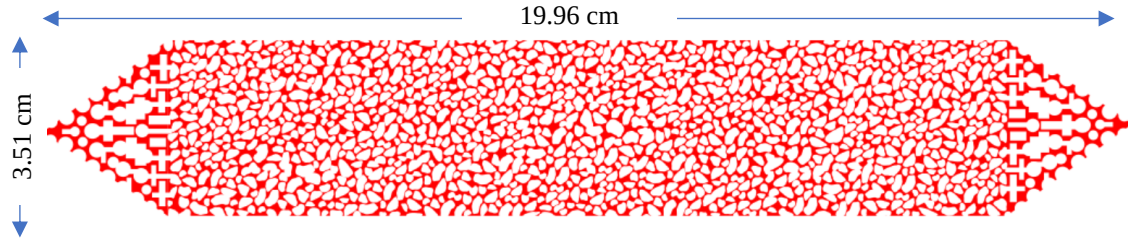

Figure 3–4: Schematic of the heterogeneous micromodel without fractures

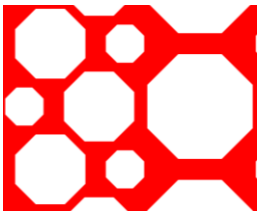

Homogenous pattern

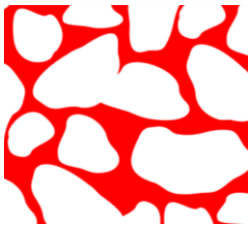

Heterogeneous pattern

The pore-scale characteristics, including pore body size, pore throat size, and grain size are the same in homogeneous and heterogeneous micromodels. Besides, there are dead-ends and fractures in the heterogeneous micromodels.

Grain size, radius (mm): 1.01, 2.02 and 3.00
Throat size, radius (mm): 0.26, 0.37 and 0.60
Pore size, radius (mm): 0.650, 0.77 and 0.99

Figure 3–5: Detailed characteristics of homogeneous and heterogeneous micromodels

Table 3-2 summarizes the physical properties of the four fabricated glass micromodels (homogeneous, horizontal fracture, vertical fracture, and non-fracture).

Table 3-2: Physical properties of fabricated micromodels

Properties	HM	HRZ	VRT	HTN
Length (cm)	20.00	19.96	19.96	19.96
Width (cm)	3.50	3.50	3.50	3.50
Average depth (µm)	56	56	56	56
Permeability (D)	450	320	280	200
Porosity (%)	30	39.2	38.0	30
Length of fracture (cm)	0	2.5	1.5	-
Fracture aperture (mm)	0	1	1	-

HM: Homogeneous micromodel, HRZ: Heterogeneous micromodel with horizontal fractures, VRT: heterogeneous micromodel with vertical fractures, HTN: heterogeneous micromodel without fracture

3.3.3. Chemical Etching

The chemical etching procedure used in this work was different than the conventional etching procedure in which various chemicals, masks, and laminate are used. The conventional chemical etching procedure does not allow the required level of accuracy in the engraving depth provided by the laser method. The process of image analysis and the physical accuracy of the entire process

was enhanced when the laser machine was used to engrave the micropattern on the glass surface. The pattern was then etched using chemical etching. The concentration of HF and exposure time was optimized by measuring the depth of channels and later the results of thermal bonding. It should be mentioned that thermal bonding blocked the narrow and low superficial channels. The base solution in this research was adopted and optimized from Wegner and Christie (1983). Through their research, it was shown that the smoothness of etched channel walls in soda lime glass is enhanced by the addition of HCl acid (48-51% purity form Cole-Parmer) and buffer NH_4F (98+% from Cole-Parmer). The laminate in the etching process prevented the acid from contacting the rest of the glass and only the engraved area by the laser was in contact with the acid solution. The concentration of acid and buffer were also optimized. The etching was performed in a well-stirred aqueous solution of 5% buffered HF (7:1 NH_4F (40%)-HF (49%) and 9.25% HCl)) for 60 min under a fume hood. Due to the precipitation of insoluble silica during the reaction, the glass was placed faced down in a standard etching plastic container. The etched depth of the micromodel was measured using scanning electron microscopy (SEM, FEI, MLA 650 FEG), which varied between 52.51-60.19 microns (Figure 3-6).

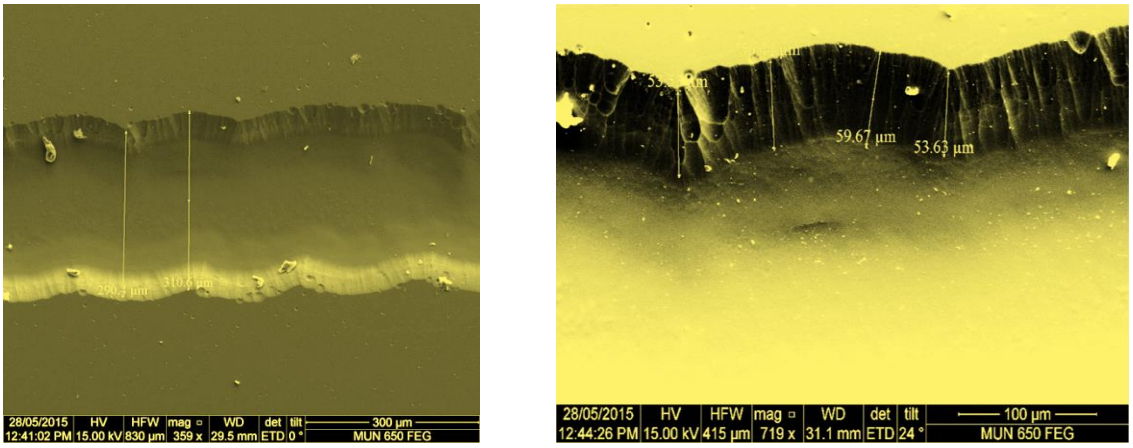

Figure 3–6: SEM images of etched channels, (a) top view, (b) tilted view

3.3.4. Thermal Bonding

The bonding of the two plates was performed using an oven from Euclid Kilns, model CST-708F, USA. In this study, an optimized thermal assisted direct bonding technique (TADB) (Chen et al., 2009) was designed to seal together the attached plates. This process and temperature ramp were optimized. Initially, the featureless glass plate was cleaned with alcohol (Fisher Scientific, 99.8%) and acetone (Fisher Scientific, 99.5%), as the contamination and dust particles on soda lime glass prevent perfect bonding between two plates of glass. This issue can arise when the micromodel is under pressure, resulting in leaking and detachment of some grains. For bonding, the glass plates in these experiments were then placed on top of each other by tape from four directions and placed in the oven. They heated up by 5^{o}C/min and held at 610^{o}C for 240 min. It should be noted that the etched plate was placed on the top and the featureless plate on the bottom, because when the featureless plates receive heat, they melt and may fill etched channels.

No articles document the details for processing a micromodel that can withstand pressure without overburden. In this work, after making the micromodel, a pressure test was performed. The fabricated micromodel, after thermal bonding, was pressure tested using water. Figure 3-7 below shows the pressure change over time. The outlet of the micromodel was closed, and water injection was started at the same rate as the actual experiments (0.0008 ml/min). Figure 3-7 shows the pressure change at a constant injection rate for which the pressure threshold for the glass micromodel was obtained at 5 MPa (720 psi). At 720 psi, breakage occurred without overburden, however, we performed experiments at 2.1 MPa (305 psi).

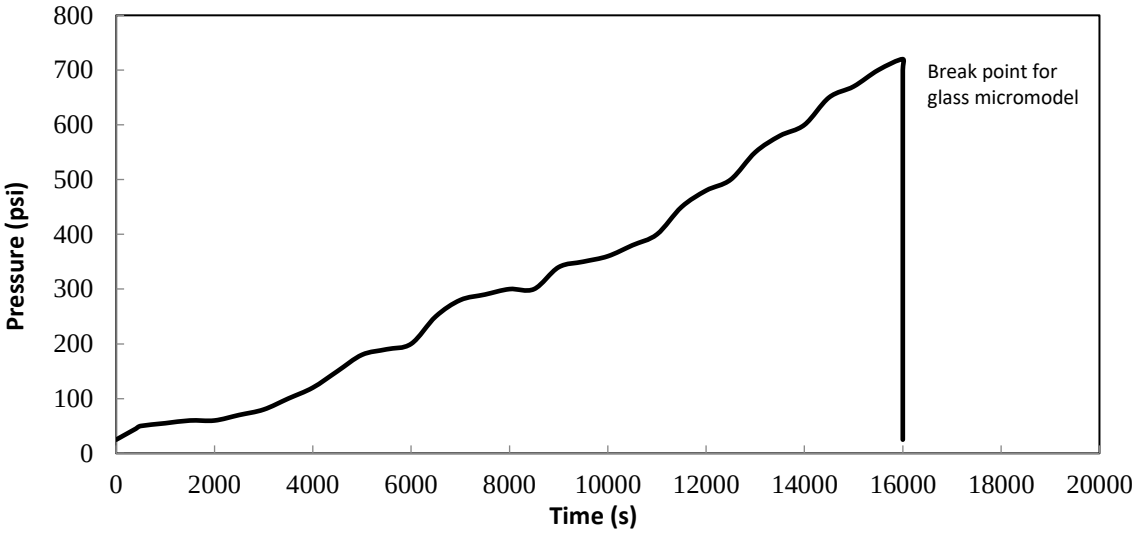

Figure 3–7: Pressure test for the glass micromodel

3.3.4. Porous Media Characterization

In this study, four medium pressure glass etched micromodels were fabricated by utilizing the new technique including laser engraving and chemical etching as described. One homogeneous micromodel and three heterogeneous micromodels were designed. The homogeneous micromodel was designed to investigate the effect of gravity and omit the effect of heterogeneity on fluid flow and displacement. Effects of flow rate, scheme, and gravity were studied. In the next step, four heterogeneous micromodels, including horizontal fractures, vertical fractures, and no fractures, were designed. The heterogeneous matrix pattern was designed based on the pore size distribution of the SEM images of sandstone rock from Newfoundland offshore reservoirs (Figure 3-8).

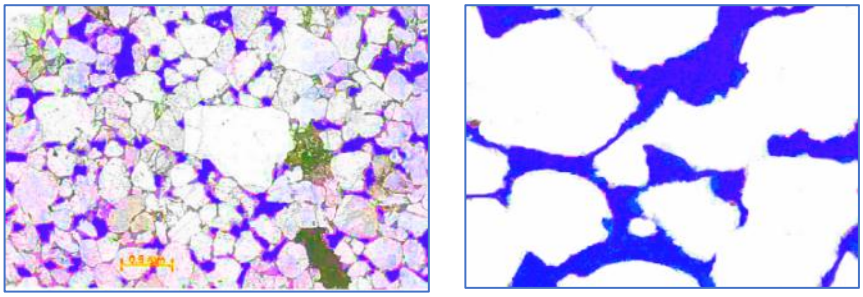

a) close-up of SEM **b) more details**

Figure 3–8: SEM image of a thin section of a sandstone rock sample (a and b)

Initially, the matrix was designed for the dimension 1×2 cm^2, which was then repeated for the whole micromodel. To ensure a continuous pattern, the edges and overlapped region had to be redesigned and modified. Also, regarding the limitation of the etching process (i.e. rounded edges under chemical etching and laser beam width), the shapes of the grains were modified.

3.3.4.1. Fracture Network

Two heterogeneous micromodels were designed to study the effect of high and low permeable areas on fluid flow and fracture-matrix interaction under simple water flooding and CWI. The overall length (distance between inlet and outlet of fracture) of each horizontal fracture was 2.5 cm.

3.3.4.2. Micromodel Orientations

In this section, the orientation of micromodels is sketched. In the horizontally-oriented micromodel, the effect of gravity on fluid flow was negligible due to horizontal orientation and low depth of the etched channels (Figure 3-9). Figure 3-10 shows the vertically-oriented micromodel.

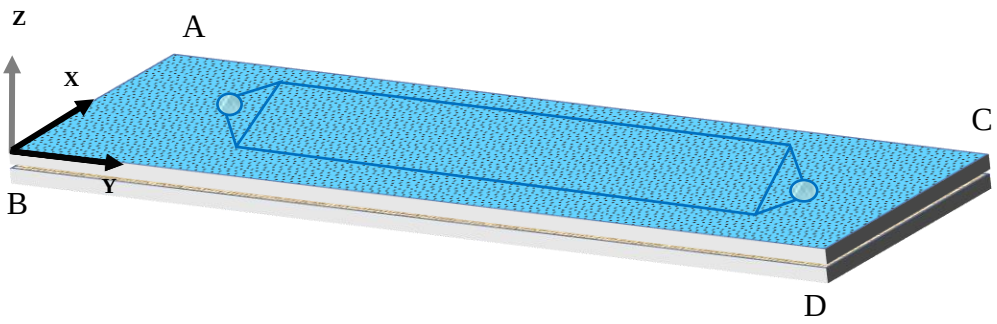

Figure 3–9: Schematic of the horizontal micromodel (X-Y orientation)

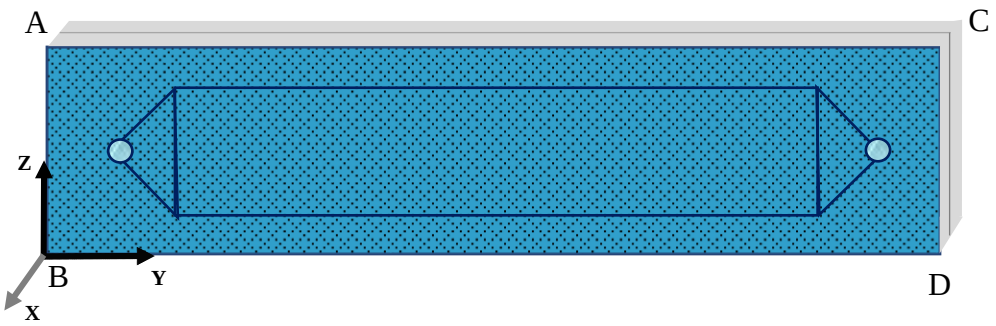

Figure 3–10: Schematic of the vertical micromodel (Z-Y orientation)

In this work, it should be noted that term “vertical” (standing up in landscape) is meant to include the effect of gravity and the term “horizontal” (laid flat on table) is meant without the effect of gravity. Horizontal orientation is considered to be without gravity because the micromodel pattern is only one pore deep (60 μm). When the micromodel is stood up or vertical the height of porous media in the vertical direction is 4 cm (40,000 μm) with approximately 40 pores.

Chapter 4 **Experimental Methodology**

4.1. Research Methodology

In this chapter, the methodology of the laboratory experiments is explained. Our review of previous studies revealed a lack of pore-scale studies on CWI in the presence of gravity and different geometries. It also showed that the performance of CWI has not been experimentally studied at high pressures and high temperatures during core flooding. Hence, a medium pressure glass micromodel was fabricated and characterized for different geometries, after which several experiments were performed. Following the core flooding experiments, a core model was built to predict the experimental results. A summary of the methodology used in this research is shown in Figure 4-1.

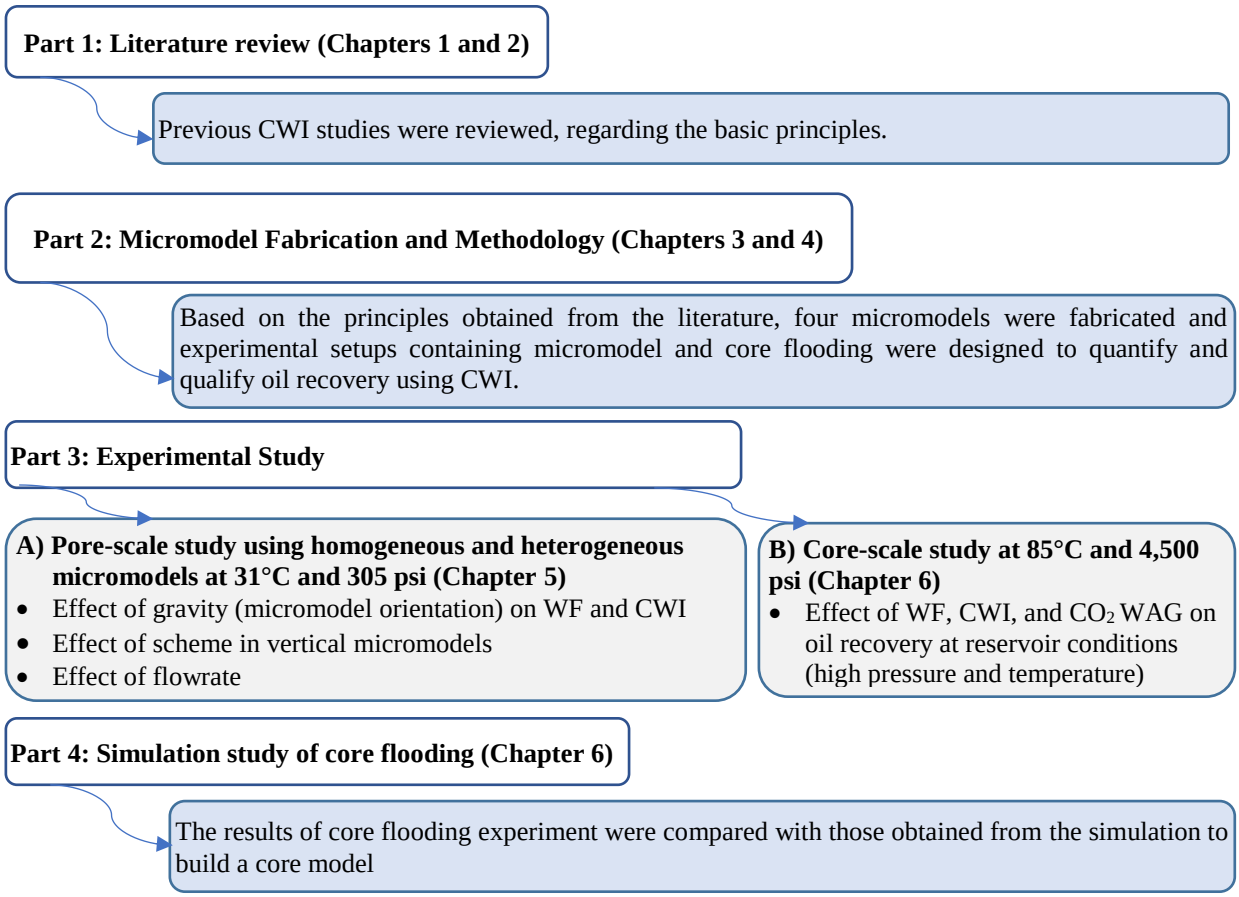

Figure 4–1: Flowchart of the current PhD research

The design of experiments in pore-scale micromodels included the following factors: orientation (horizontal and vertical), scheme (water flooding, secondary CWI, and tertiary CWI) for three porous media (homogeneous, horizontal fracture, and vertical fracture), and flow rate. The experiment objectives, as indicated in the figure above, were to examine the effect of gravity (micromodel orientation), scheme (secondary vs tertiary CWI and water flooding), and flow rate. The design of experiments was based on factorial interest where some factors were constrained depending on practicality and previous literature. Firstly, flow rate was considered only in homogenous and horizontal fractures to determine the effect of Capillary number within the Darcy flow range. The effect of gravity was considered comparing only secondary CWI and water flooding but in all three porous media (homogeneous, vertical and horizontal fractures). Given the effect of gravity, we compared EOR schemes (secondary and tertiary CWI and water flooding) only in the vertically oriented micromodels.

4.2. Material

The oil in this study is a light oil with 29.8 ºAPI from Canada's East Coast region. To overcome the issue of asphaltene and wax precipitation, the oil was filtered for subsequent experiments. The physical properties of the oil are listed in Table 4-1. The CO_2 used in this research, supplied by Praxair, had a purity of 99.99%. Deionized water (DI) was used to make the carbonated water (CW) solution (Table 4-2). We measured and calculated all the physical properties at 305 psi (2.1 MPa) and 21°C (69.8 °F). The viscosity of the oil and DI were measured by the VISCOlab PVT apparatus high-pressure viscometer, to 6.8 ± 0.01 cP and 0.970 ± 0.01 cP, respectively. We found the density of oil, and the DI water by using the Anton Paar densitometer to 0.877 ± 0.001 g/cm^3, 0.997 ± 0.001 g/cm^3, respectively. Methylene blue, which is a water-based dye, was used to

differentiate between the water and carbonated water phases (CW). The density of carbonated water at micromodel experimental conditions of 21°C (69.8 °F) and 2.1 MPa (305 psi) was calculated using CMG-WinProp^{TM} to be 1.003 g/cm^3. It should be noted that the density of deionized water under the same conditions was obtained to be 0.998 g/cm^3. The density of the carbonated seawater at 85°C (69.8 °F) and 24 MPa (3,500 psi) was calculated to be 1.0152 g/cm^3 (Table 4-4).

The pH for the experimental conditions of this research was calculated using OLI Studio software. At a temperature of 21°C and a pressure of 2.1 MPa, the pH of water and carbonated water were calculated to be 7.06 and 3.26, respectively. The pH of seawater and carbonated seawater, at 85°C and 24 MPa, were obtained to be 7.60 and 3.95, respectively, which are higher than those of water and carbonated water due to the lower solubility of CO_2 in brine (salt in solution) in comparison to pure water. The obtained amounts were compared with the reported graphs of Crawford et al. (1963). Gas chromatography, Agilent G2887BA, 7890A/6890N GC was used to identify the oil compositions.

Table 4-1: Physical properties of the oil

Property	**Molecular weight** (g/mol)	**Density** (g/cm^3)	**^{o} API Density** (calculated)	**Viscosity** (mPa.s)
Value	257	0.877 ± 0.001	29.8	6.82 ± 0.01

Table 4-2: Physical properties of the deionized water at different conditions

Property	**Pressure and Temperature**	**Molecular weight** (g/mol)	**Density** (g/cm^3)	**Viscosity** (mPa.s)
Value	21^{o}C and 0.1 MPa	18.015	0.997 ± 0.001	0.97 ± 0.01

Atlantic seawater with a salinity of 35,987 ppm was used to prepare the carbonated seawater (CSW) solution. The salinity and compositional analysis of Atlantic seawater, as reported in Table 4-3, was obtained through Central Testing Laboratory LTD. Carbonated seawater was prepared by mixing seawater and pure CO_2 at the same temperature at which the experiments were conducted. We calculated all the physical properties of the carbonated water at 305 psi (2.1 MPa) and 21°C (69.8 °F) and carbonated seawater at 3,500 psi (24 MPa) and 85°C (185 °F). The viscosity of carbonated water solutions was obtained based on Islam and Carlson Correlation (2012). The viscosity of carbonated solutions was obtained to be 1.008 cP for carbonated water (viscosity of pure water is 0.978 cP) and 0.438 for carbonated seawater (viscosity of seawater is 0.364, Islam and Carlson 2012; Sündermann, Landolt-Börnstein, 1986). The below-developed correlation is based on experimental data and it shows a slightly increase in viscosity with rising the CO_2 concentration in water.

$$\mu_{cw} = \mu_r \times \mu_w \tag{1}$$

$$\mu_r = 1 + \frac{7.632609 \times 10^2 \times w_{water}^{CO2} - 9.460776 \times 10^3 \times (w_{water}^{CO2})^2}{-1.047187 \times 10^4 + 3.683255 \times 10 \times T} \tag{2}$$

$$\mu_{csw} = \mu_{sw} \times (1 + 4.65\ (w_{water}^{CO2})^{1.0134}) \tag{3}$$

where μ_{cw} is the viscosity of the carbonated water (zero salinity) at experimental conditions (cP), μ_{water} is the viscosity of water at experimental conditions (cP), μ_{csw} is the viscosity of carbonated seawater at experimental conditions (cP), μ_{sw} is the viscosity of seawater at experimental conditions. T is the temperature (K), and w_{water}^{CO2} is the weight fraction of dissolved CO_2 in seawater.

Table 4-3: Salt composition of the Atlantic Ocean (measured by this work)

Component	mg/L	Component	mg/L
$CaCl_2$	379,32	**CuCl**	0.00
$MgCl_2$	1,322.49	**Fe_2SO_4**	0.04
KCl	421.65	**Zn**	0.01
NaCl	10,886.90	**Mn**	0.01

4.2.1. Carbonated Water/Seawater Preparation

In this section, the preparation of carbonated water (CW) and carbonated seawater (CSW) is explained. An important part of the CWI experiments is the preparation of the carbonated water/seawater. For this purpose, we must be careful to keep the pressure high enough to avoid any CO_2 gas coming out of the solution. CW is used for micromodel experiments and CSW is used for core flooding experiments. The process of mixing CO_2 with DI water under micromodel experimental temperature-pressure as well as mixing CO_2 with seawater under core flooding conditions was conducted. The step by step carbonated water preparation is shown in the Figure 4-2.

Initially, CO_2 is transferred to an accumulator (Figure 4-2a) to be pressurized (if the pressure of the CO_2 cylinder is much less than required pressure for carbonated water preparation). The CO_2 was injected from a high-pressure piston accumulator into a piston accumulator that held deionized water (for micromodel) or seawater (for core flooding) at constant temperature (Figure 4-2b). Temperature was applied by a heating tape. There was a ball inside the accumulator of water/seawater to homogenize the mixture. Afterwards, the mixture was homogenized for at least 48 hours using an agitator until reaching an equilibrated pressure (constant pressure). We observed the three following situations: i) the same gauge pressure as the expected pressure, ii) a lower pressure than the expected pressure, and iii) a higher pressure than the expected pressure. We

considered the expected pressures of 1.5 MPa (220 psi) for CW in micromodel experiments and 24 MPa (3,500 psi) for CSW in core flooding experiments.

If (i) occurred, the CW/CSW is a saturated CW solution which could be a single phase or two phases (extra gas phase on the top). If the equilibrated pressure (gauge pressure) was greater than the pressure we expected, the CO_2 dissolution was complete, and potential extra gas was not dissolved in the water/seawater. Hence, the accumulator containing CW/CSW was connected to a back-pressure regulator (BPR) to release the gas cap (extra undissolved gas) from the top of the accumulator, while the pump was pushing upward the piston of the accumulator at a constant pressure. If (ii) occurred the CW/CSW is a partially saturated solution, so we must have connected the accumulator to the CO_2 gas accumulator and injected more CO_2. Finally, if (iii) occurred, the solution was oversaturated, and the extra pressure was released.

For micromodel experiments, after the required action in any of the above cases (i, ii, and iii), a high-pressure transparent tube (800 psi) was connected between the accumulator containing CW and BPR to check the single-phase carbonated water solution. The back pressure was set at 220 psi and then the piston of the accumulator containing CW solution was pushed by the Quizix pump upward into the transparent tube. If the single phase was observed and checked by the outlet of BPR it indicates the carbonated water solution is a single phase. Otherwise, the fluid coming out of the accumulator is gas phase and is produced by BPR. Production was continued until a single phase was observed in the tubing. When the first drop of water comes out of BPR it confirms that the free CO_2 gas was removed, and the mixture was in saturated liquid phase in the accumulator. The tubing after BPR was also directed to a graduated cylinder containing water to observe the

produced gas (Figure 4-2c). For the core flooding experiments, after the required action in any of the above cases (i, ii, and iii), the accumulator containing CSW was connected to the back-pressure regulator (BPR). The back-pressure regulator was set at 3,500 psi and the piston of the accumulator containing CSW solution was pushed upward by the pump. When the first drop of water emerges from the BPR, it indicates that the free CO_2 gas was removed, and the mixture was in saturated liquid phase in the accumulator. During all steps, the accumulators were vertically-oriented to make sure any possible free gas will migrate to the top of the solution.

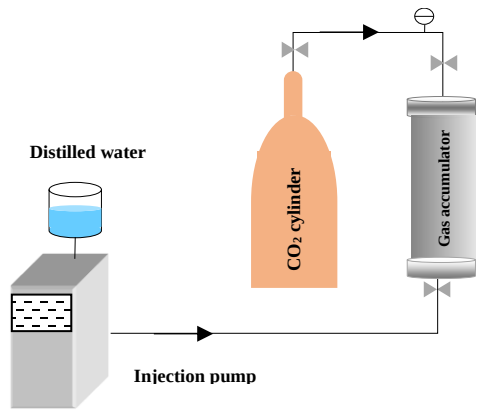

a) transfer CO_2 to accumulator and pressurizes it

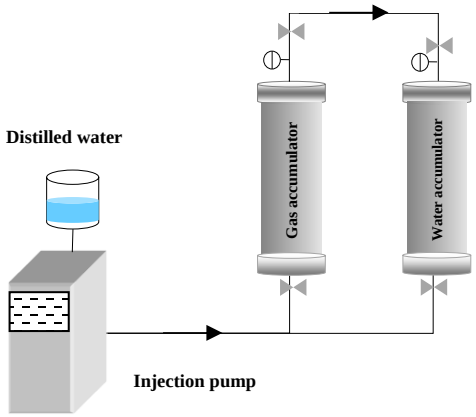

b) transfer CO_2 to water accumulator

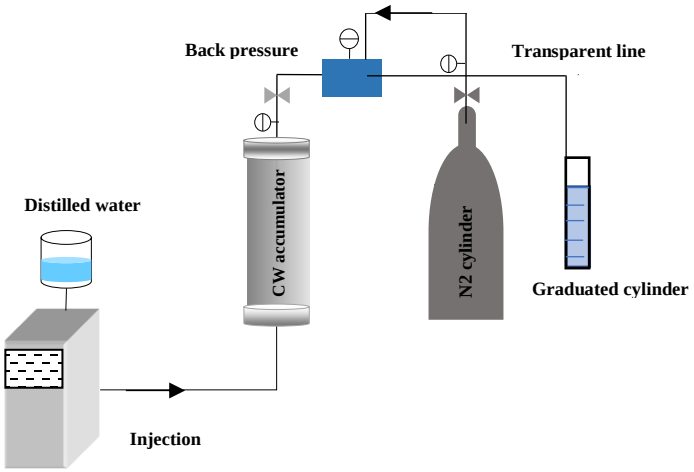

c) carbonated water/seawater sampling

Figure 4–2: Setup of the carbonated water preparation
a) transfer of CO_2 to accumulator and pressurize it, b) transfer of CO_2 to the water accumulator, and c) carbonated water sampling

4.2.1.1. CO_2 Solubility Measurement in Water/Seawater

The solubility of CO_2 is a function of pressure, temperature, and salinity. The accumulator containing a certain amount CW/CSW was connected to a BPR while, the piston was pushed upward by a Quizix pump under constant pressure mode (i.e., 220 psi for CW and 3,500 psi for CSW). The solution passed through the BPR into a graduated cylinder to measure the volume of water and the separated CO_2 was directed to the gasometer using a plastic tube. The ratio of gas volume to water/seawater volume gave the solubility of CO_2 in water/seawater at standard condition (21°C and 14.7 psi).

$$x_{CO2-water} = \frac{Volume_{\ CO2}}{Volume_{\ water}} \times \frac{\rho_{CO2}}{\rho_{Water}} \times \frac{M_{water}}{M_{CO2}} \quad (4)$$

where $x_{CO2-water}$ is the solubility of CO_2 in water (%), $Volume_{\ CO2}$ is the volume of produced CO_2 from gasometer at atmospheric conditions (cm^3), $Volume_{\ water}$ (cm^3) is the volume of collected water in the graduated cylinder , ρ_{CO2} is the density of CO_2 at atmospheric conditions (g/cm^3), ρ_{water} is the density of water at atmospheric conditions (g/cm^3), and M_{CO2} and M_{water} are the molecular weight of CO_2 and water (g/mol), respectively. The measured solubility was compared to the solubility of CO_2 in water and seawater reported in Duan et al. (2003 and 2006). Tables 4-4 and 4-5 show the solubility of CO_2 in water and seawater at the current experimental conditions.

Table 4-4: Physical properties of the carbonated water at 21°C (69.8 °F) and 1.5 MPa (220 psi)

Prop.	Measured solubility (mol CO_2 /mol H_2O)	Duan's solubility (mol CO_2 /mol H_2O)	Calculated solubility (**) (mol CO_2 /mol H_2O)	MW (g/mol)	ρ (*) (g/cm^3)	μ (**) (mPa.s)
Value	0.0124	0.0118	0.0128	18.34	1.003	1.008

Table 4-5: Physical properties of the carbonated seawater at 85°C (185 °F) and 24 MPa (3,500 psi)

Prop.	Measured solubility (mol CO_2 /mol seawater)	Duan's solubility (mol CO_2 /mol seawater)	Calculated solubility (**) mol CO_2 /mol seawater)	MW (g/mol)	$\boldsymbol{\rho}$ (*) (g/cm^3)	$\boldsymbol{\mu}$ (**) (mPa.s)
Value	0.0188	0.0170	0.0182	19.01	1.0152	0.438

(*) CMG-WinProp, (**) Correlation discussed in section 4.2.

4.3. Micromodel Experiment

4.3.1. Design of Experiments

In the experimental design of this research, effective parameters such as flowrate, pressure, temperature, concentration of solvent (CW), scheme, and geometry regarding the displacement efficiency were selected. We set the temperature and pressure at 21°C (69.8 °F) and 2.1 MPa (305 psi), respectively, because we wanted the maximum concentration of CO_2 in the water regarding the functionality of micromodel.

We know that the solubility of CO_2 in water is a function of temperature and pressure (discussed in sections 1.2.2 and 1.2.3). Higher solubility of CO_2 in water is obtained at lower temperatures and higher pressures. Hence, the minimum ambient temperature and the highest possible pressure were selected with respect to the micromodel's functionality. Therefore, the concentration of CO_2 is fixed (section 4.2.1). The literature indicates that the effect of certain parameters in CWI experiments such as production rate, heterogeneity of porous media (high permeability-low permeability zones, e.g. fractures), and the type of injection scheme in the presence of gravity have not been previously investigated.

In this series of experiments, the effect of different parameters including the orientation of the micromodel (gravity), the scheme and flowrate, as well as the geometry, were studied. The purpose of such micromodel experiments is to investigate the active mechanisms of CWI in pore-scale as well as fluid flow pattern under the effects of gravity. Table 4-6 shows the experimental design of micromodel experiments.

We designed pore network micromodel experiments to visualize the displacement phenomena using a medium-pressure micromodel setup. We performed simple water flooding in both vertically and horizontally-oriented micromodels as the base schemes. Afterwards, CWI experiments were conducted at the same temperature and pressure to compare the efficiency of CWI.

In the next stage, effective factors, like flowrate and scheme, were added to optimize the performance of CWI on vertical and horizontal displacement efficiencies at different experimental conditions. Later, to examine the response of the geometry of the porous media (high permeable-low permeable porous media) to simple water flooding and CWI, we changed the variables (e.g. flowrates and scheme) within two heterogeneous micromodel experiments. The flowrate was calculated based on the capillary number which is in the range of 10^{-6}. Finally, to visually mimic the core flooding experiments, a heterogeneous pattern without fracture was designed. Then, second type of vertically-oriented micromodel experiments was performed. Some of the experiments were replicated to ensure the results. Note that in the macro and micro shots in the following figures, the oil is brown, the carbonated water solution is white, and the water is blue.

Table 4-6: Experimental design of micromodel experiments

Experiment	Porous media	Rate (cc/min)	Recovery stage	Orientation
Vertical Water Flooding				
1	HM (r)	0.0008	WF	Vertical homogenous
2	HT_HF	0.0024	WF	Vertical, horizontal fractures
3	HT_VF (r)	0.0024	WF	Vertical, vertical fractures
Vertical SCWI				
4	HM (r)	0.0008	SCWI	Vertical homogenous
5	HT_HF (r)	0.0024	SCWI	Vertical, horizontal fractures
6	HT_VF (r)	0.0024	SCWI	Vertical, vertical fractures
7	HM	0.004	SCWI	Vertical homogenous
8	HT_HF	0.0008	SCWI	Vertical, horizontal fractures
Vertical Tertiary CWI				
9	HM	0.0008	TCWI	Vertical homogenous
10	HT_HF	0.0024	TCWI	Vertical, horizontal fractures
11	HT_VF	0.0024	TCWI	Vertical, vertical fractures
Horizontal WF				
12	HM	0.0008	WF	Horizontal homogeneous
13	HT_HF (r)	0.0024	WF	Horizontal, horizontal fractures
14	HT_VF	0.0024	WF	Horizontal, vertical fractures
Horizontal SCWI				
15	HM	0.0008	SCWI	Horizontal homogeneous
16	HT_HF (r)	0.0024	SCWI	Horizontal, horizontal fractures
17	HT_VF	0.0024	SCWI	Horizontal, vertical fractures

HM: homogeneous micromodel, HT: heterogeneous micromodel, HF: horizontal fracture, VF: vertical fracture, WF: water flooding, SCWI: secondary CWI, TCWI: tertiary CWI, r: replicate.

4.3.2. Micromodel Experimental Setup

The micromodel setup consisted of an oven, glass micromodel, pumps, three double-cap accumulators (for DI water, oil, and carbonated water), amplified pressure transducers, and a computer and imaging system (Figure 4-3). A high-resolution camera (Canon EOS 6D, 100 mm focal length), a digital microscope (Dino-Lite 5MP Edge AM7915MZT, magnification: 2592×1944 pixels), 1/8 in Hastelloy tubing, autoclave valves, a lightbox, and we used two dual-cylinder micro flow piston Quizix™ -20K pumps (flowrate of 0-7.5 ml/min and accuracy of +0.1% of set flow rate). There were two high-precision Quizix model micro flow piston pumps in the system. The first pump injected the displacing fluid and the second pump was responsible for the back pressure in the system. Hence, we used these two pumps, so we could have precise pressure control over the injection pressure and the back pressure. There were two pressure transducers from Honeywell FP2000 (0.1% accuracy) to record the inlet and outlet pressures. To improve the image capturing, a white plexy-plastic matte sheet (diffuser) was placed in front of the lightbox. This plate provided a homogeneous light intensity background.

To run each flooding test, the micromodel was first cleaned using solvents such as toluene, acetone and water (10 PV for each solvent was gradually injected with a syringe), and a high vacuum air pump. After cleaning, the micromodel was fully saturated with oil. The experimental conditions were set at a pressure of 2.1 MPa (305 psi) and an average temperature of 21°C (69.8 °F). In this series of experiments, connate water saturation was not considered ($S_{wc} = 0$). The reason for not having connate water saturation was the experimental conditions of micromodel. The amount of CO_2 dissolved in water at micromodel conditions is low. We believed that when we inject carbonated water, some portion of CO_2 is dissolved in connate water, hence, lower amount of CO_2

is transferred to oil which may affect the mechanisms of oil recovery by carbonated water. We performed simple water flooding, secondary, and tertiary CWI schemes. During the injection process, a camera was used to capture images for analysis using an in-house image software (LabView). The saturation of fluids at the injected pore volume and details of the fluid interactions such as pore-scale recovery, mechanisms, and fluid flow patterns were reported.

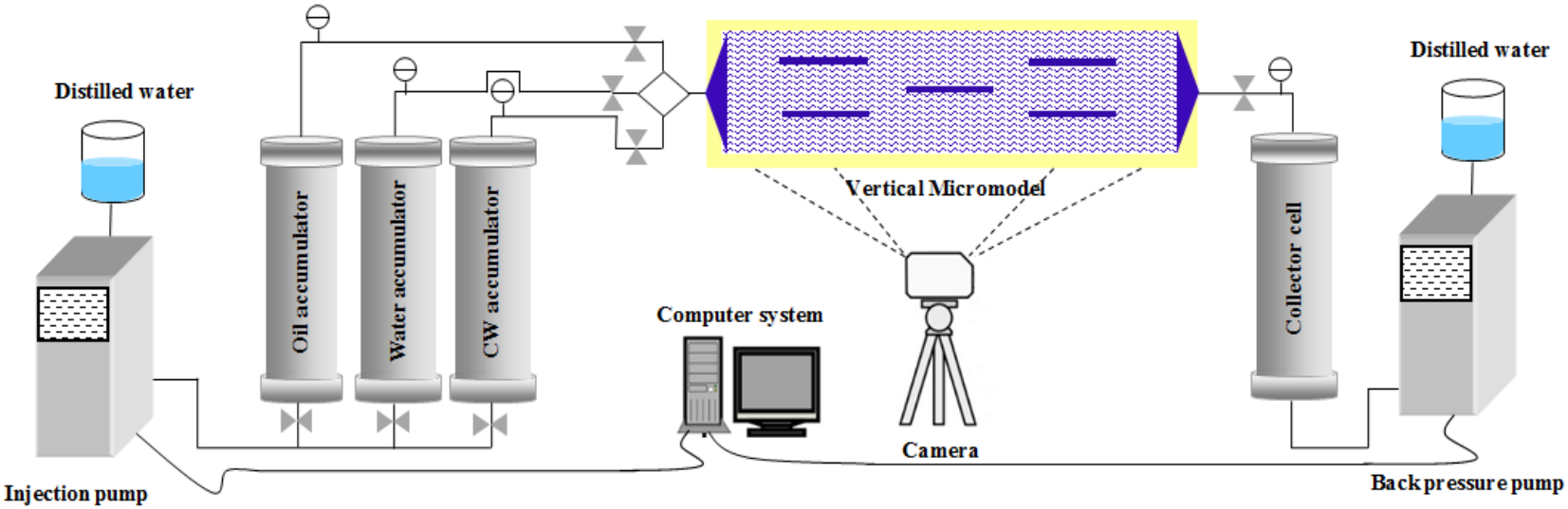

Figure 4–3: Schematic of the pressurized micromodel setup

4.3.3. Micromodel Experimental Procedure

In this study, experiments were performed using the etched glass micromodels. Three accumulators were filled with dyed DI water, carbonated water, and oil. Oil injection started with a low flowrate rate of 0.00009 ml/min (0.2 ft/d). We started the experiments after saturating and pressurizing the micromodel with oil. The injection of water flooding and CWI in a pore network micromodel with and without gravity were examined. The injection pressure and temperature were kept constant at 2.1 MPa (305 psi) and 21ºC (69.8 ºF). Then, based on the defined scheme, either simple water flooding, secondary, or tertiary CWI was conducted. For every scheme, the tubing and fittings were first flooded by oil, then, we switched the fluids and flooded the tubing with water or carbonated water. This reduces the risk of instability in pressure and mixing of fluids before entering the micromodel. All the required equipment was available in the EOR laboratory at Memorial University.

4.4. Core Flooding Experiments

4.4.1. Design of Experiments

After evaluating the mechanisms and performance of CWI in pore-scale experiments, core flooding experiments were designed to evaluate the effectiveness of CWI in real reservoir conditions. Pressure, temperature and fluid represent the fluid model of the reservoir, and geometry and rock type represented the porous media of the reservoir.

The pressure, temperature, and geometry of a reservoir's rock affect the efficiency of EOR processes, especially in gas-based processes (CO_2 injection, WAG, SWAG, and CWI). The studied offshore reservoir in Canada's East Coast region has the conditions of 85°C (185 °F) and 31 MPa

(4,500 psi), and the porous media is high-porosity and high-permeability sandstone rock. In this study, a sandstone rock sample was saturated with a dead oil sample. Carbonated water was prepared using CO_2 and Atlantic seawater at 85°C (185 °F) and 24 MPa (3,500 psi). In the core flooding series of experiments, the effect of different schemes, including simple water flooding, secondary and tertiary CWI, and CO_2-WAG were investigated. Table 4-7 shows the experimental design for the core flooding experiments. The physical properties of core samples were measured three times. The purpose of core flooding experiments was to evaluate the performance of CWI in realistic conditions.

Table 4-7: Physical properties of core samples

Experiment	Rock	L (cm)	D (cm)	Porosity	PV (ml)	Permeability (mD)
Seawater flooding	Sandstone, Berea	9.80	3.0	0.20 ± 0.0002	14.5 ± 0.04	380.6 ± 6.48
Secondary CWI		10.88	3.0	0.22 ± 0.0001	16.9 ± 0.04	381.6 ± 10.07
Tertiary CWI		11.80	3.0	0.21 ± 0.0004	17.4 ± 0.05	314.3 ± 6.82
CO_2-WAG		10.88	3.0	0.19 ± 0.0002	15.0 ± 0.04	360.3 ± 8.39

4.4.2. Core Flooding Experimental Setup

Experimental facilities for the High Pressure-High Temperature (HPHT) core flooding setup included the oven, core holder, back pressure regulator, amplified pressure transducers, three double-caps piston accumulators (for seawater, oil, and carbonated seawater), gasometer, O-rings, and sleeve (Figures 4-4 and 4-5). Core flooding experiments were performed in a tri-axial Hassler-type core holder. All circumstances of a core in the core holder experienced a compressive load in three axes (two radial, and one longitudinal). In this core holder, the axial and radial pressures were independently controlled. A different axial loading was achieved by use of a piston arrangement loaded by a pressure source independent of the pressure surrounding the core (overburden). Independent pressures were used to give more accurate representations of pore

conditions when the rock loading in the reservoir was known to be non-isotropic. In the core flooding setup, there were three dual-cylinder Quizix™ pumps with the rate of 1.5×10^{-4} ml/min, in which one provided the overburden pressure and two other pumps were for the injection of the fluids (i.e. oil, seawater, and carbonated seawater). A back pressure from Equilibar EB1ULF1 (up to 10,000 psi), which operates for carbonated water injection, was used to confine the pressure. A new diaphragm was used to modify the BPR to meet both the low flow rate, high pressure, and potential phase change conditions encountered in carbonated water injection. We also used a gasometer from Emdyne Inc., model MK 2000 (up to 30 liters/hr, ± 0.1 ml). All parts of the apparatus exposed to fluids were made of Hastelloy™, and all the O-rings (Viton) for the core holder and accumulators were specifically for CO_2 application to avoid any leakage due to CO_2 swelling, permeation, and explosive decompression.

Figure 4–4: High pressure-high temperature (HPHT) core flooding apparatus

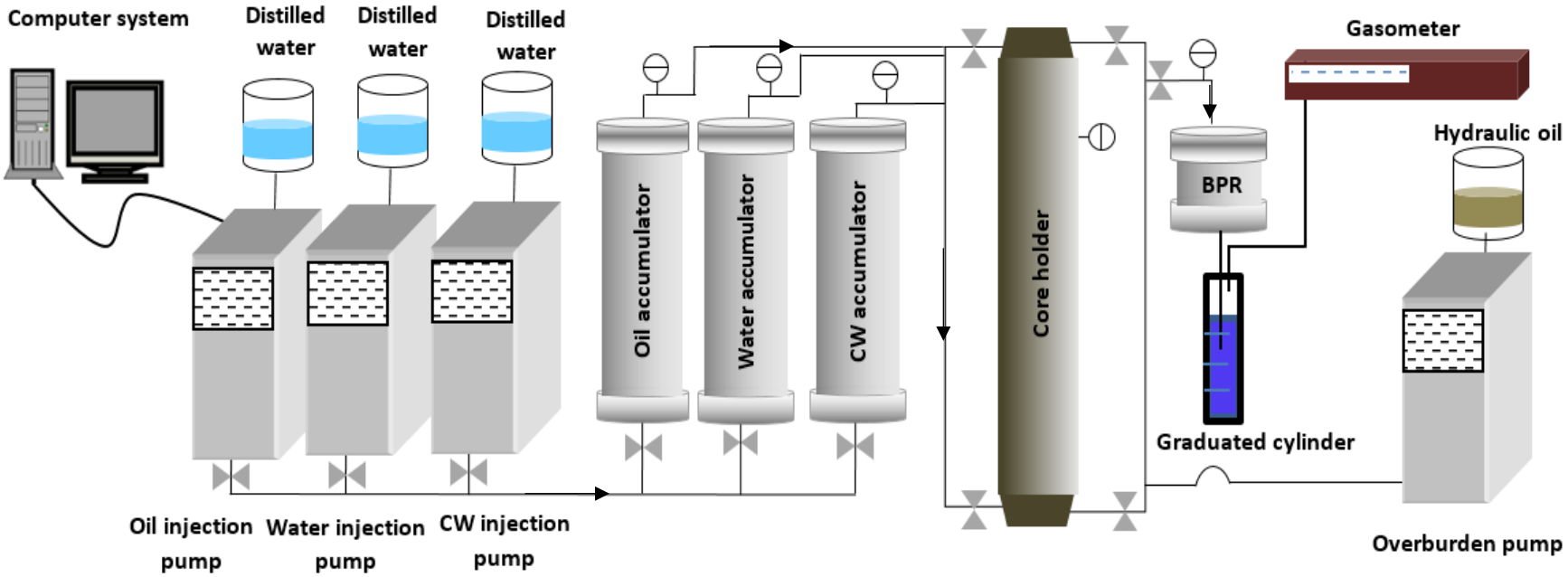

Figure 4–5: Schematic of the core flooding setup

4.4.3. Core Flooding Experimental Procedure

In this study, seawater flooding, secondary carbonated seawater, tertiary carbonated seawater, and CO_2-WAG schemes were performed in a vertically-oriented core holder at reservoir temperature and pressure of 85°C (185 °F) and 31 MPa (4,500 psi).

Experiments were performed using sandstone core samples; cores were saturated with formation brine with a salinity of 100,000 ppm. To run each flooding experiment, the core holder, cores, and tubing were cleaned using solvents (toluene, acetone, methanol, and water) and dried using an oven. After placing the saturated core in the core holder and assembling all the pieces of the core holder, the overburden pressure of 35.8 MPa (5,200 psi) was applied on the placed core in the sleeve to find any potential leakage before starting the experiments. Brine saturation using prepared formation brine was done with a vacuum pump, oil saturation was achieved using a Vinci Rotosilenta 630RS refrigerated centrifuge (Memorial University, EOR laboratory) and connate water saturation was obtained at the average of 27%.

After placing the core holder in the oven, oil flooding then commenced at a rate of 0.01 ml/min to establish a stabilized pressure difference between the core inlet and outlet (graphs of pressure difference are reported in Chapter 6). When the pressures stabilized, the seawater flooding experiment was conducted at a constant flowrate of 0.2 ml/min (~ 0.012 PV/min, considering the average PV of all the core samples ranges from 14.5 to 17.4 ml). Injection flowrate was selected in the range of Darcy's flow (1 ft/day) with a capillary number of 3.5×10^{-6}. Rapoport and Leas (1953) reported the scaling criterion (equation 5) based on laboratory water flooding experiments to diminish the inlet and outlet capillary end-effects, and unstable frontal displacement.

$$LV\mu_w \geq 1 \quad (5)$$

where L is the length of porous media (cm), V is the injection flowrate (ml/min), and μ_w is the viscosity of injected fluid (cP). During the injection process, produced fluids were collected using a high precision graduated cylinder and gasometer; core inlet and outlet pressures, overburden pressure, and injection pressure were monitored using amplified pressure transducers. Some of the experiments were replicated to ensure accuracy of the results. In the tertiary schemes, water flooding was performed until no more oil was produced then tertiary CWI or CO_2-WAG were performed.

4.5. Error Analysis

There are always errors in any measurement. The degree of the closeness of a measurement to a reference value is defined by the accuracy of the system (systematic error). The precision (random error) of a measurement system dictates the reproducibility and repeatability of the measurements.

4.5.1. Mean Value, Standard Deviation, Some of the Square of Errors

The mean value is the average value and is calculated as the sum of all the observed outcome values from the sample divided by the total number of repeated experiments. The mean value ($\bar{x}$) is expressed as below (Taylor, 1982):

$$\bar{x} = \frac{1}{n}\sum_{i=1}^{n} x \quad (6)$$

The standard deviation is a measure of the distribution of the data. The standard deviation of x is given by:

$$s = \sqrt{\frac{1}{n-1}\sum_{i=1}^{n}(x-\bar{x})^2} \quad (7)$$

Sum of squared error (SSE) is the sum of the squared differences between each observation and its group's mean. It can be used as a measure of variation within a cluster. If all cases within a cluster are identical, the SSE would then be equal to 0.

$$SSE = \sum_{i=1}^{n}(x_i - \bar{x_l})^2 \quad (8)$$

where n is the number of the measurements and the x corresponds to the observed values.

4.5.2. Error in Micromodel Experiments

In order to verify the performance of the optimized image analysis, the volumetric oil and water saturations were calculated by the material balance in the micromodel and compared with calculated optimized image-based saturation. Oil and water saturation from the experiments were calculated as follows:

$$Oil\ saturation = \frac{PV_T\ -\ (t \times rate_{\ pump})}{PV_T} \quad (9)$$

$$Water\ saturation = \frac{t \times (rate_{\ pump})}{PV_T} \quad (10)$$

where PV_T is the total pore volume of the micromodel (ml), t is the injection time period and $rate_{pump}$ is the pump flowrate (cm^3/min). The image analysis software used is an in-house software that can calculate the oil and water saturation upon taking pictures at each frame. By comparing the experimental measurement and image analysis calculation, we can then determine the error of image analysis.

$$Error_{oil\ saturation} = \frac{oil\ saturation_{Material\ balance} - oil\ saturation_{Image\ analysis}}{oil\ saturation_{Material\ balance}} \quad (11)$$

$$Error_{water\ saturation} = \frac{water\ saturation_{Material\ balance} - water\ saturation_{Image\ analysis}}{water\ saturation_{Material\ balance}} \quad (12)$$

4.5.3. Error in Core Flooding Experiments

To confirm the results of core flooding experiments, both seawater flooding and secondary CWI, were performed twice. We monitored parameters including core inlet and outlet pressures, overburden pressure, injection pressure and produced fluids (oil, water, and gas). In order to verify the results, the volumetric injected seawater/carbonated seawater is available based on the injection pump rate.

The initial oil in place, dead volume (outlet line (Tee connections, valve, BPR, and tubing): from the outlet of core holder to the tip of production tubing), connate water saturation, and produced fluids were also measured. After calculating the dead volume (Figure 4-6), we know that the initial produced fluid (oil) comes from the dead volume, not from the core. It should be noted that the injection rate was 0.2 ml/min and the dead volume was 6.07 ml. Hence, the required time to

observe the first produced fluid from the core was calculated to be 30.4 mins. All the data that was used in calculations was considered after 30.4 mins of injection. In each core flooding experiment, by material balance calculation, measured values were compared with calculated values versus pore volume injection (the recorded data are available in Appendix C).

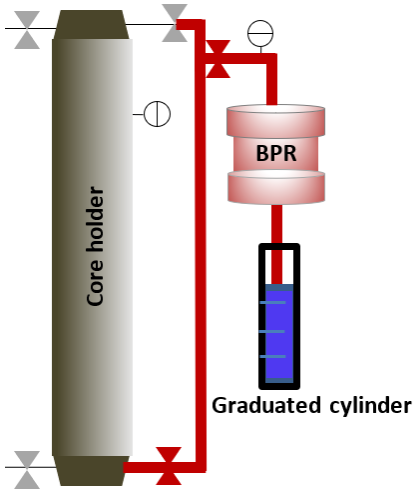

Figure 4–6: Core flooding setup, production section

Chapter 5 **Micromodel Experimental Results**

The chapter is based on the three papers that were published as described below:

1. ***Pore Scale Investigation of Carbonated Water Injection with and without Gravity*** *(2016) was published for presentation at the International Symposium of the Society of Core Analysts (SCA), Snow Mass, Colorado, USA, 21-26 August, Mahdavi, S., James, L. A., and Johansen. T.*
2. ***Investigation of Water Flooding and Carbonated Water Injection (CWI) in a Fractured Porous Media*** *(2017) was published for presentation at the International Symposium of the Society of Core Analysts (SCA), Austria, 27 August-1 September, Mahdavi. S., and James, L.A.*

5.1. Overview

This chapter is part of a comprehensive study on CWI in different geometries. Although the effects of many parameters have been studied previously, the effect of gravity on vertical sweep efficiency, oil recovery, and trapped oil extraction using CWI is absent in the current literature. Micromodel experiments were performed at a pressure and temperature of 2.1 MPa (305 psi) and 21°C (69.8 °F). In the first stage of the experiments, a 2D homogenous glass micromodel was designed to visually investigate the pore-scale phenomena during CWI. To evaluate the potential use of CWI for vertical oil displacement and oil extraction, a series of horizontally-oriented (without gravity) and vertically-oriented (with gravity) pore network micromodel experiments were conducted. The geometry of the porous media is an important factor on the ultimate efficiency of every EOR process. It was motivated from the results of the homogeneous micromodel where additional oil recovery under CWI compared to water flooding was observed. Hence, in the second stage of micromodel experiments, the effect of horizontally and/or vertically-oriented fractures,

and without fractures on the performance of water flooding and CWI were studied in the presence and absence of gravity. Experiments were conducted under different injection schemes (i.e. simple water flooding, secondary CWI, and tertiary CWI) in the presence of gravity. The fluid flow displacement pattern, breakthrough recovery, pore-scale recovery, fluid interactions, trapped oil mobilization, the dead-end oil extraction, and matrix-fracture fluid interaction were visually investigated. We studied the effect of flowrate on the performance of secondary CWI in both homogeneous and heterogeneous micromodels. Following the obtained results, extended secondary and tertiary CWI experiments were conducted in the homogeneous and vertical fracture micromodels to observe the potential of CWI in the deformation of by-passed zones. An in-house image analysis software was employed to qualify and quantify the experimental results. In this chapter, the effect of gravity, scheme, flowrate, and extended CWI scheme, pore scale mechanisms in homogeneous and heterogeneous micromodels are presented.

5.2. Effect of Gravity

The effect of gravity on vertical displacement efficiency is investigated in this section, including simple water flooding in both homogeneous and heterogeneous pore network micromodels. Two heterogeneous micromodels were designed with different geometries: horizontal fractures and vertical fractures. Please note that 1) the injection is from left to right, and 2) vertical means standing up in landscape orientation (Z-X orientation) while horizontal means laid flat on a table (Y-X orientation). Initially, the micromodel was saturated with the oil and the pump pressure was set at 2.1 MPa (305 psi). The production rate was set at a flowrate of 0.0008 ml/min for the homogeneous micromodel, and 0.0024 ml/min for the heterogeneous micromodels (vertical and horizontal fracture). The pressure difference between the inlet and outlet was gradually stabilized

to 1.97 MPa (287 psi) and 1.96 MPa (285 psi), respectively. Then the micromodel was flooded with deionized water.

In this section, the results of simple water flooding in vertically-oriented (with gravity) pore network micromodels are presented. For understanding the effect of gravity on vertical oil sweep efficiency in different geometries, the captured images at different pore volumes were divided to 9 sections in both vertical and horizontal directions as is shown in Figures 5-1 to 5-3. The saturation profiles for each section were obtained at pore volume injection. Sections S1, S4, and S7 are the closest ones to the injection port of the micromodel to (left side of the picture), the middle sections of S2, S5, and S8 are situated in the center part of the micromodel, and sections S3, S6, and S9 are the closest to the production port (right side of the picture).

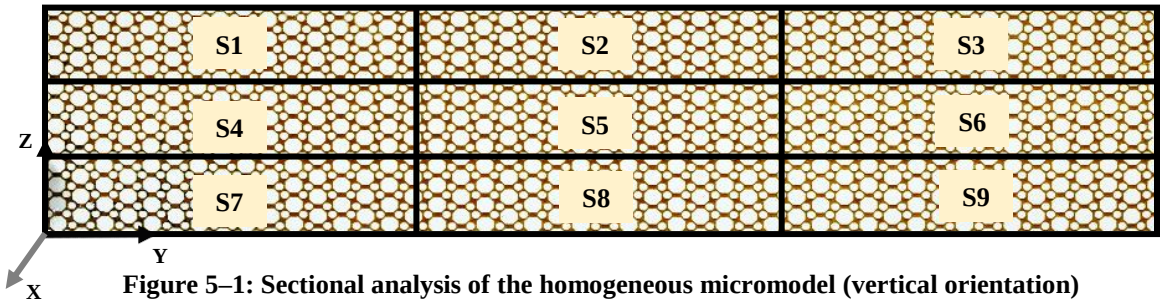

Figure 5–1: Sectional analysis of the homogeneous micromodel (vertical orientation)

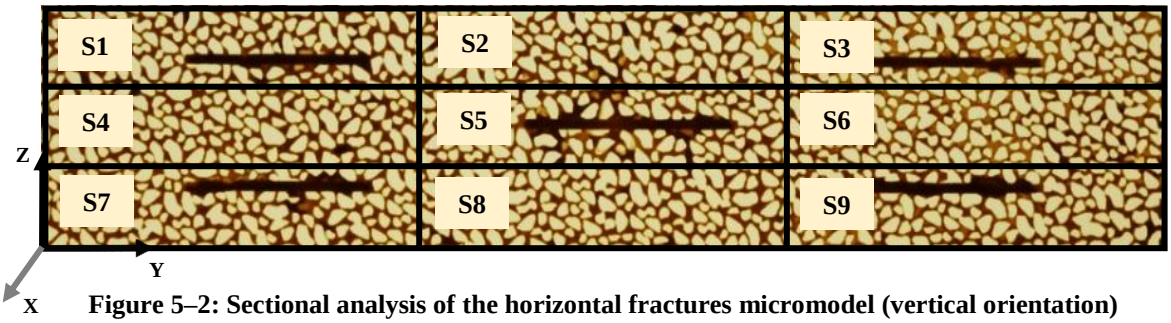

Figure 5–2: Sectional analysis of the horizontal fractures micromodel (vertical orientation)

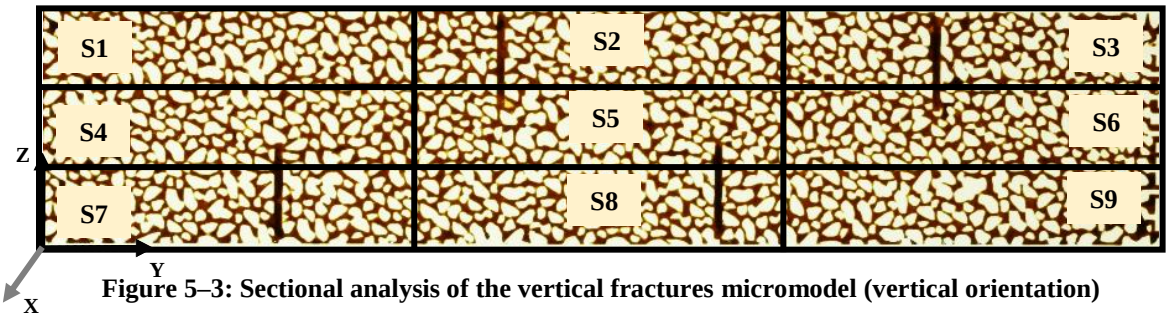

Figure 5–3: Sectional analysis of the vertical fractures micromodel (vertical orientation)

5.2.1. Water Flooding in the Homogeneous Micromodel

Figure 5-4 shows the average saturation profile of water flooding in the homogeneous micromodel in the presence of gravity (vertically-oriented micromodel). The oil saturation immediately started to change for the three sections S1, S4, and S7. Water displaced the oil in the micromodel's lower sections (S4 and S7) more than in its upper section (S1). By continuing injection, the oil displacement in sections S4 and S7 slowed down and the oil displacement in section S7 was continued up to 3.6 PV. Residual oil saturation at 1 PV reached 68.9 ± 0.03%, 43.2 ± 0.05%, 56.8 ± 0.08% for sections S1, S4, and S7. Residual oil saturation of 66.0 ± 0.02%, 44.4 ± 0.02%, and 43.0 ± 0.02% were obtained for sections S1, S4, and S7 after 7 PV water injection, respectively. The difference in residual oil saturation of S1, S4, and S7 showed that the gravity displaced the injected water downward and there was a higher pore-scale recovery in the lower sections (S4 and S7) compared to the upper section (S1).

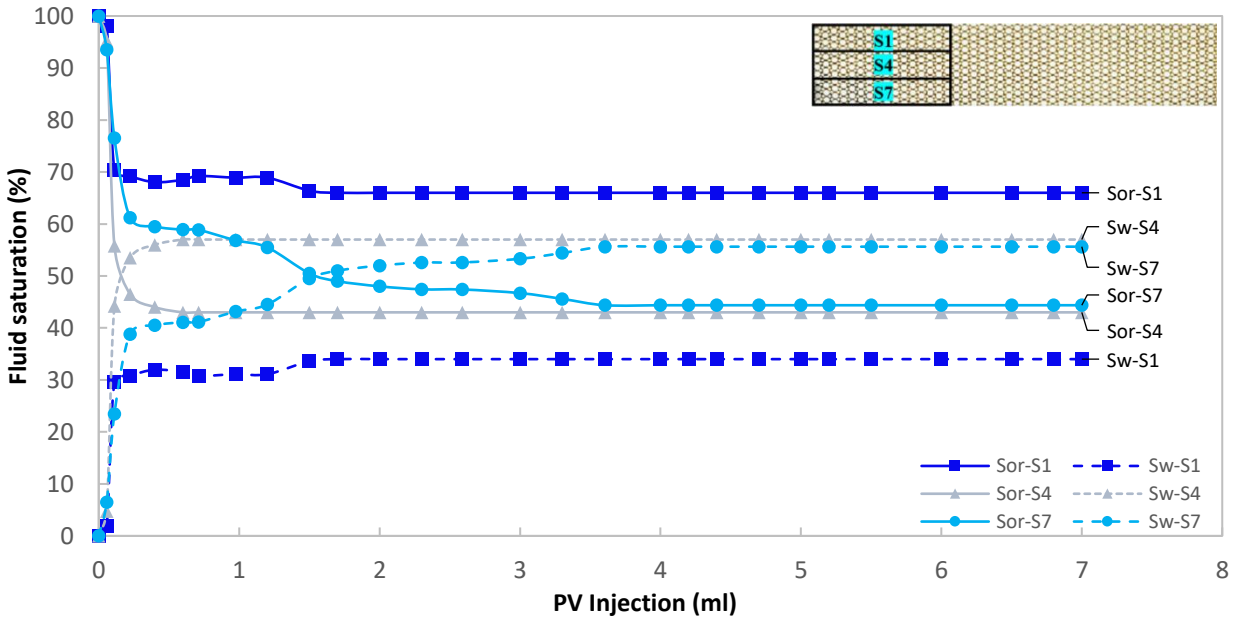

Figure 5–4: Average fluid saturations in the homogeneous micromodel, sections S1, S4, and S7

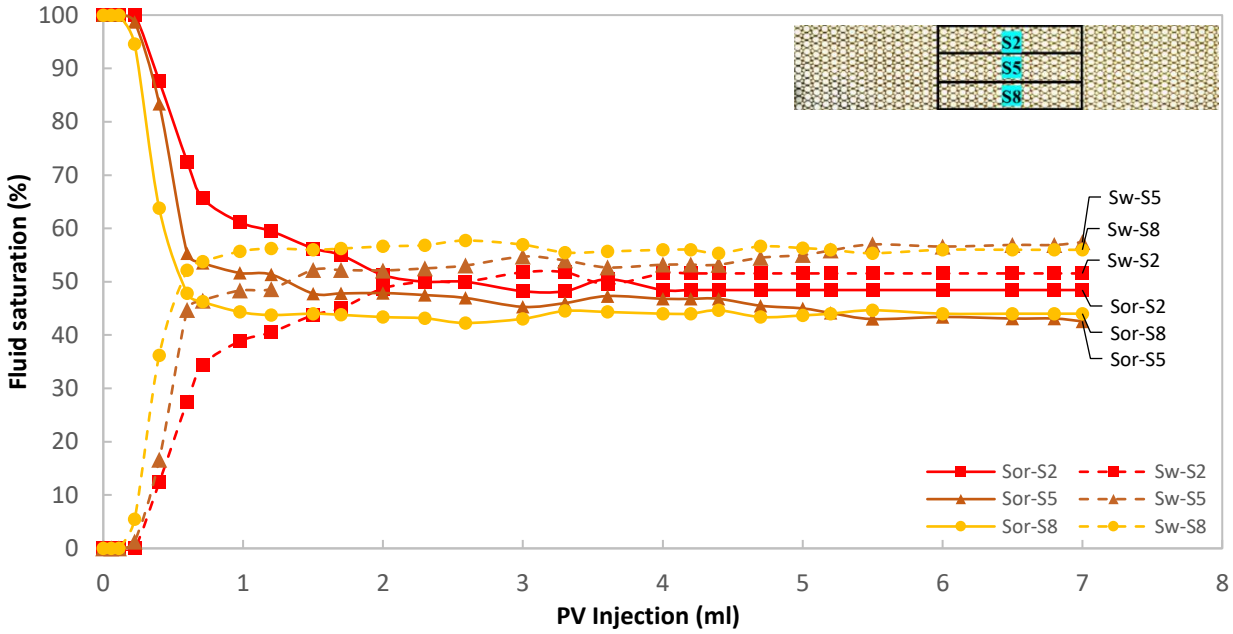

Figure 5–5: Fluid saturations in the homogeneous micromodel, sections S2, S5, and S8

As it is illustrated in Figure 5-5, the oil displacement in the middle sections (S2, S5, and S8) started at 0.1 PV compared to the immediate displacement in the previous sections (S1, S4, and S7). By continuing water flooding, the oil saturation decreased in all the middle sections. Residual oil saturation is lower in section S8 compared to sections S5 and S2, which shows that the effect of gravity in the middle sections (S2, S5, and S8) is more noticeable than in the previous sections (S1, S4, and S7). The higher oil saturation in the most upper and lower sections (S1, 68.5 ± 0.06% and S7, 58.9 ± 0.04%) compared to S2, 72.5 ± 0.09% and S8, 47.9 ± 0.06% at the initial stage of injection (e.g. 0.6 PV) might be due to the effect of localized capillary end-effect. However, as is shown in Figure 5-4 at 1 PV, the oil saturation in S1 did not change and in S7 was decreased to 56.8 ± 0.07% which might be due to the effect of gravity on lower section (S7) compared to upper section (S1). Residual oil saturation at 1 PV reached 61.2 ± 0.05% (S2), 51.7 ± 0.08% (S5), and 44.3 ± 0.04% (S8) compared to 68.9 ± 0.03% (S1), 43.2 ± 0.05% (S4), and 56.8 ± 0.08% (S7).

Monitoring the residual oil saturation in the furthest sections to the injection port (S3, S6, and S9) is depicted in Figure 5-6, which shows that the oil production from these sections began at 0.6, 0.4, and 0.1 PV for S3, S6, and S9, respectively. This difference illustrated that the lower most section (S9) is displaced by water before S6, and section S6 before S3 (upper most section). The different slopes in the residual oil saturation profiles show that gravity pushes the water downward causing oil displacement in the lower sections (S7, S8, and S9) earlier than the upper sections (S1 to S6).

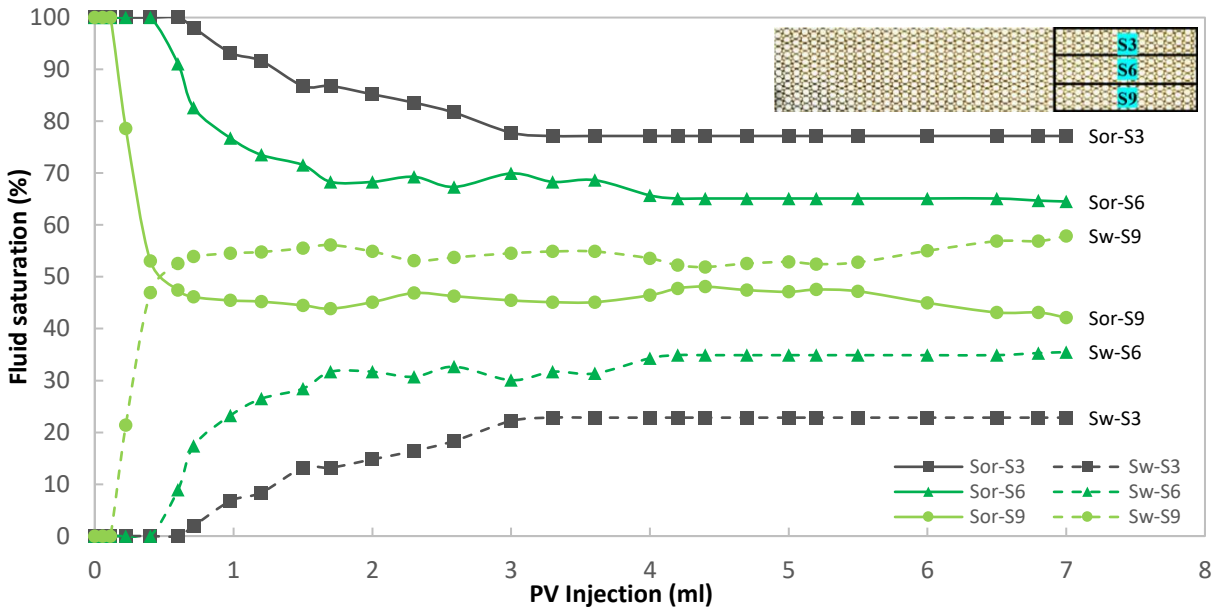

Figure 5–6: Fluid saturations in the homogeneous micromodel, sections S3, S6, and S9

Residual oil saturation of 48.5 ± 0.07%, 44.0 ± 0.06%, and 44.1 ± 0.08% for sections S2, S5, and S8 were obtained compared to 77.2 ± 0.05%, 64.5 ± 0.04, and 42.1 ± 0.06% for sections S3, S6, and S9, respectively.

5.2.1.1. Water Flooding with and without Gravity in Homogeneous Micromodel

To better understand the effect of gravity on oil displacement, breakthrough, and ultimate oil recovery, water flooding in horizontally-oriented (without gravity) micromodels (homogeneous

and heterogeneous) were conducted and compared with vertically-oriented (with gravity) micromodels. In the section 5.2.1, sectional analysis of water flooding showed that there is a difference in fluid saturations (oil and water) of vertical sections at the same pore volumes, which demonstrates the effect of gravity on the oil saturation profile.

The results of simple water flooding in the horizontally-oriented micromodel (without gravity) showed that water pushed the oil forward (from inlet to outlet) in a more stable frontal displacement rather than in the vertically-oriented micromodel (with gravity). However, by continuing injection, the water fingers started to grow until breakthrough in the center part of the micromodel (Figure 5-7, BT in horizontal flooding). The breakthrough occurred at 0.35 PV in the horizontal and 0.3 PV in the vertical displacements resulted in recovery factors of 37.1 ± 0.04% and 29.4 ± 0.02% for the horizontal and vertical displacements at breakthrough, respectively.

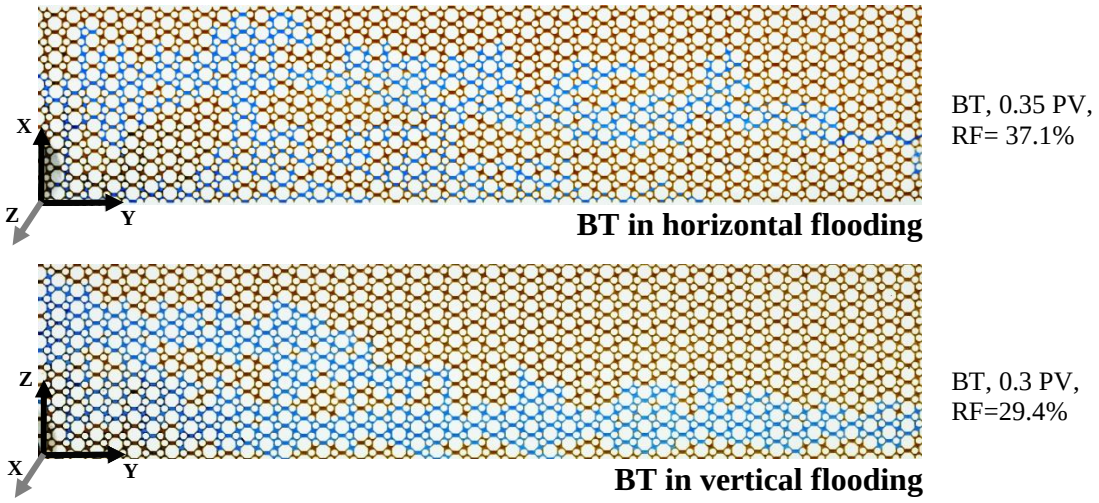

Figure 5–7: BT for waterflooding in the horizontal and vertical homogeneous micromodel

An overview of the entire micromodel is depicted in Figure 5-8, which illustrates that water could not displace the oil in porous media next to the walls and a big un-swept area remained, which resulted in 42.7 ± 0.04% and 36.6 ± 0.02% ultimate oil recovery for the horizontal and vertical micromodels, respectively.

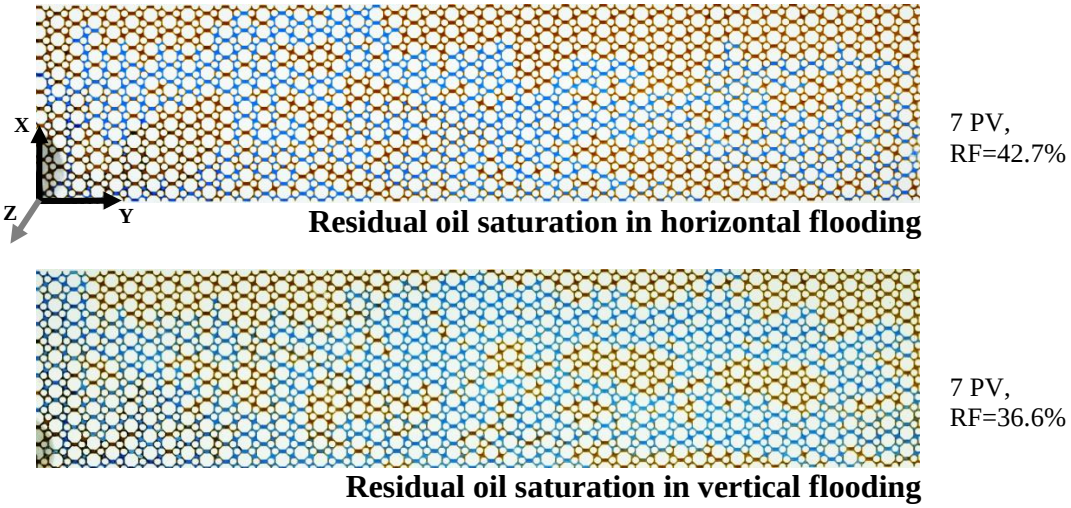

Figure 5–8: S_{or} for WF in the horizontal and vertical homogeneous micromodel

5.2.2. Water Flooding in Heterogeneous Micromodels

In these experiments, the micromodel was oriented vertically to observe the potential of water flooding for vertical sweep efficiency in a heterogeneous porous media containing horizontal and vertical fractures. Initially, the micromodel was saturated with oil and then injection pressure was gradually increased to 305 psi and the production rate was set to 0.0024 ml/min.

5.2.2.1. Effect of Horizontal Fractures

The residual oil saturation profile at different pore volumes and sections in the heterogeneous micromodel including horizontal fractures are displayed in the Figures 5-9 to 5-11. It was observed that high permeability fractures enhanced more oil displacement in the fractures than in the surrounded matrix. Figure 5-9 shows the residual oil saturation for sections S1, S4, and S7. As is shown, the residual oil saturation in sections S1 and S7 is lower compared to section S4 due to high permeability of fractures in both sections S1 and S7. The residual oil saturation at 1 PV reached 43.5 ± 0.05%, 61.8 ± 0.08%, and 49.2 ± 0.05% for sections S1, S4, and S7, respectively.

By continuing water injection up to 7 PV, the residual oil saturation in sections S1, S4, and S7 reached 45.2 ± 0.04%, 59.3 ± 0.07%, and 48.5 ± 0.02%, respectively.

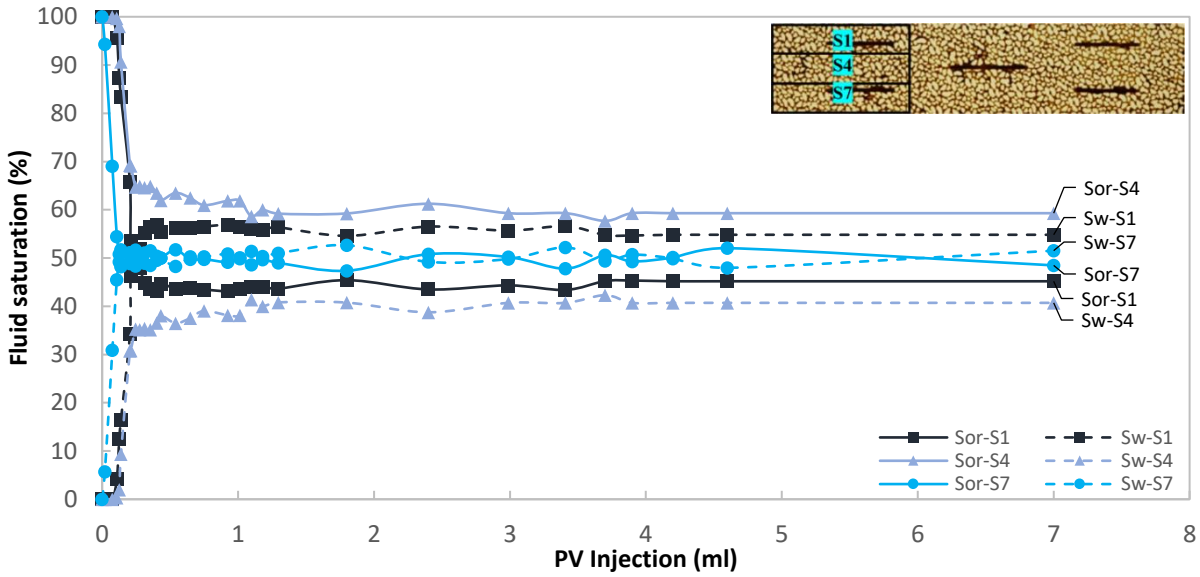

Figure 5–9: Average fluid saturations for WF in the horizontal fracture micromodel, sections S1, S4, and S7

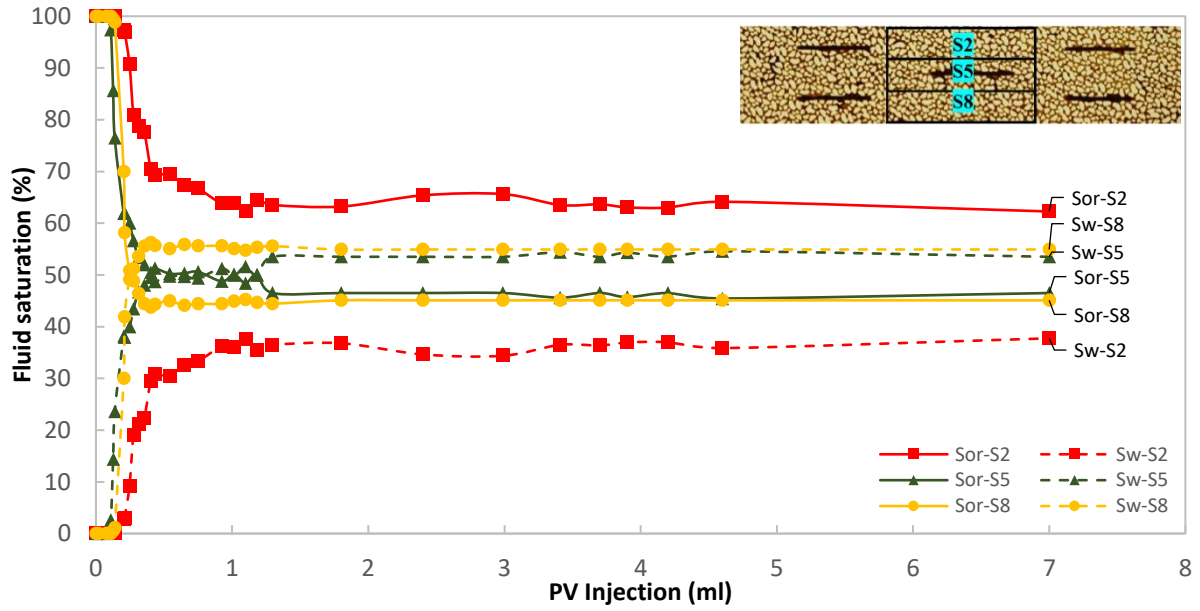

Figure 5–10: Average fluid saturations for WF in the horizontal fracture micromodel, sections S2, S5, and S8

The residual oil saturation profile for the middle section (S2, S5, and S8) is shown in Figure 5-10. The comparison of the saturation profile for sections S5 and S8 shows that the presence of fracture

in the middle section (S5) impacted the effect of gravity which resulted in almost the same residual oil saturation of 45.0 ± 0.02% for both section S5 and S8 from 1.3 to 7 PV injection.

As it is observed in Figure 5-11 the presence of fractures in sections S3 and S9 did not have the same effect on residual oil saturation. Although both sections S3 and S9 have one horizontal fracture, section S9 has lower residual oil (42.8 ± 0.08%) compared to section S3 (60.9 ± 0.05%) after 7 PV. This event might be due to the force of gravity, which pushed the water downward to mostly displace the oil in the lower part of the micromodel (section S9). The residual oil saturation at 1 PV reached 61.9 ± 0.2% (S3), 53.5 ± 0.07% (S6), and 40.9 ± 0.08% (S9) compared to 62.4 ± 0.04% (S2), 50.0 ± 0.08% (S5), and 45.0 ± 0.03% (S8). By continuing water injection up to 7 PV, the residual oil saturation changed to 60.9 ± 0.08% (S3), 49.6 ± 0.05% (S6), and 42.9 ± 0.04% (S9) compared to 62.3 ± 0.03% (S2), 46.5 ± 0.09% (S5), and 49.4 ± 0.04% (S8). The average of oil saturation changed from the inlet to the outlet from 52.0 ± 0.04% to 61.3 ± 0.06% at BT, 51.8 ± 0.08% to 53.0 ± 0.05% at 1 PV, and 51.0 ± 0.07% to 51.3 ± 0.09% at 7 PV.

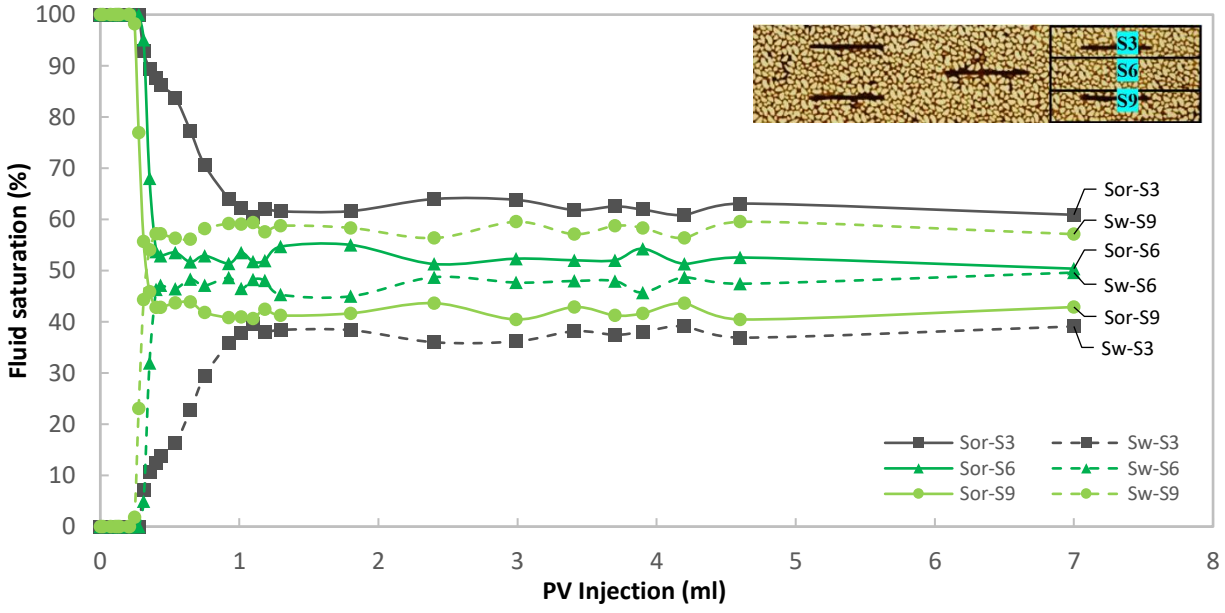

Figure 5–11: Average fluid saturations for WF in the horizontal fracture micromodel, sections S3, S6, and S9

5.2.2.2. Effect of Vertical Fractures

In this experiment, the micromodel is oriented vertically to observe the effect of fractures on vertical sweep efficiency under water flooding.

Sectional analysis of residual oil saturation at different pore volumes and sections are displayed in Figure 5-12. As shown, oil saturation decreased for sections S1 and S7 up to 73.6 ± 0.05% after 0.2 PV. However, the oil saturation was dramatically decreased to 33.7 ± 0.08% in section S4. This might be due to the high permeability of fracture located in section S7 which caused the water to displace the oil in section S4 to reach to the fracture in the lower section (S7). Water preferred to follow the path that led to the high permeability fracture and at the same time gravity reinforced the oil displacement by water in the lower section, S7.

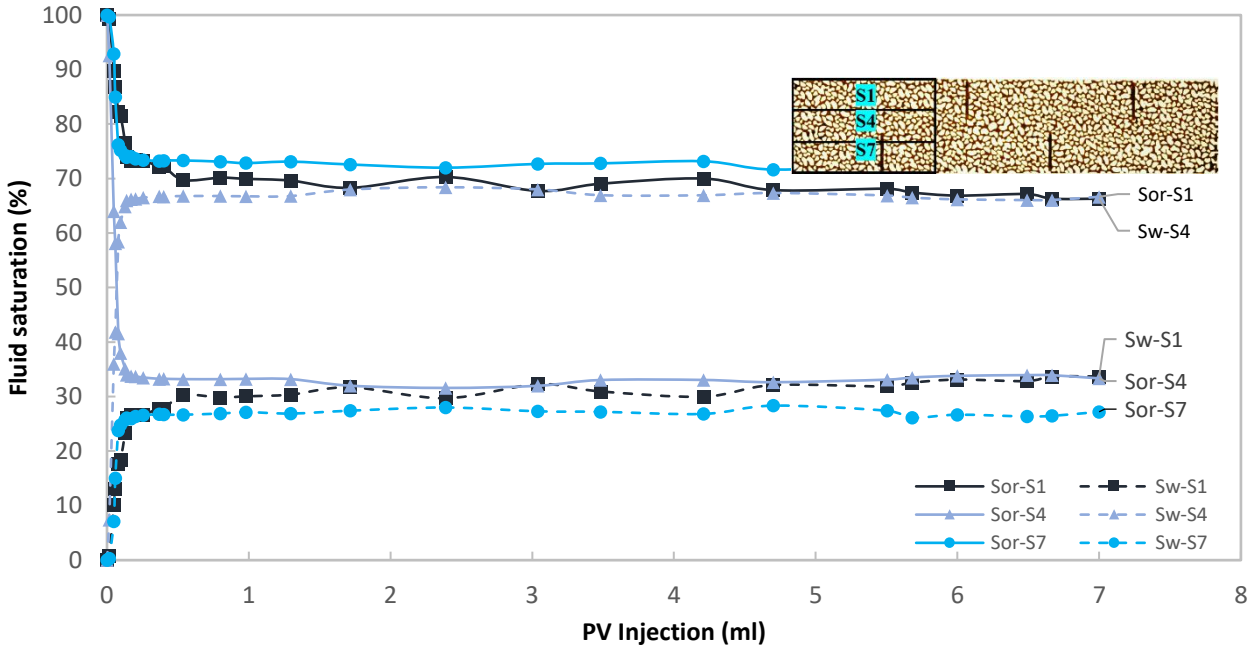

Figure 5–12: Average fluid saturations for WF in the vertical fracture micromodel, sections S1, S4, and S7

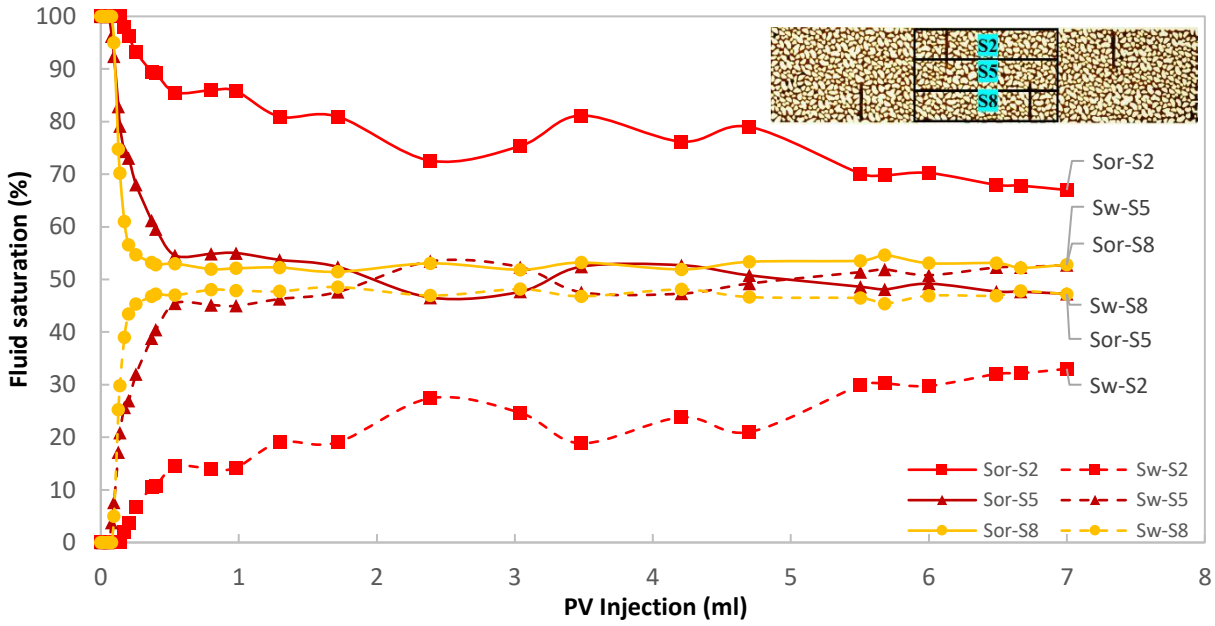

Figure 5–13: Average fluid saturations for WF in the vertical fracture micromodel, sections S2, S5, and S8

Figure 5-13 shows the residual oil saturation for sections S2, S5, and S8 in the vertical fracture micromodel. As is shown, oil saturation in sections S5 and S8 dropped to 54.5 ± 0.07% and 53.0 ± 0.11% at 0.54 PV, respectively, and remained constant at 7 PV. However, oil saturation in section S2 amounted to 85.5 ± 0.08% and kept decreasing, because the presence of fracture in the upper part resulted in gradual oil displacement at different PV injections. The residual oil saturation at 1 PV reached 86.0 ± 0.06% (S2), 55.3 ± 0.08% (S5), and 52.1 ± 0.08% (S8) compared to 69.9 ± 0.08% (S1), 33.3 ± 0.03% (S4), and 72.8 ± 0.08% (S7). By continuing water injection until 7 PV, the residual oil saturation of S2, S5, and S8 reached 67.0 ± 0.08%, 47.3 ± 0.07%, and 53.0 ± 0.11% compared to 66.7 ± 0.04%, 33.3 ± 0.12%, and 72.8 ± 0.03% for S4, S1, and S7, respectively. The comparison of oil saturation at 1 and 7 PV shows that it takes longer for sections S2 and S5 to reach a minimum oil saturation due to the effect of fractures.

The effect of gravity on residual oil saturation is shown in the sections of S3 and S6 compared to S9, which produces at a later point (Figure 5-14). As it is observed, there is a delay in oil recovery close to the producer where residual oil saturation started to decrease at 0.17 PV, 0.98 PV, and 3.48 PV for the sections of S9, S6, and S3, respectively. Oil displacement in the section S9 demonstrated the combination of effects of two fractures in the previous sections S7 and S8, and gravity, which facilitated the oil displacement in the lower part of the micromodel, and finally oil displacement in section S9 reached 39.9 ± 0.06% at 7 PV. Meanwhile, residual oil saturation continued to decrease and reached 83.74 ± 0.02% at 7 PV in other sections (S3 and S6).

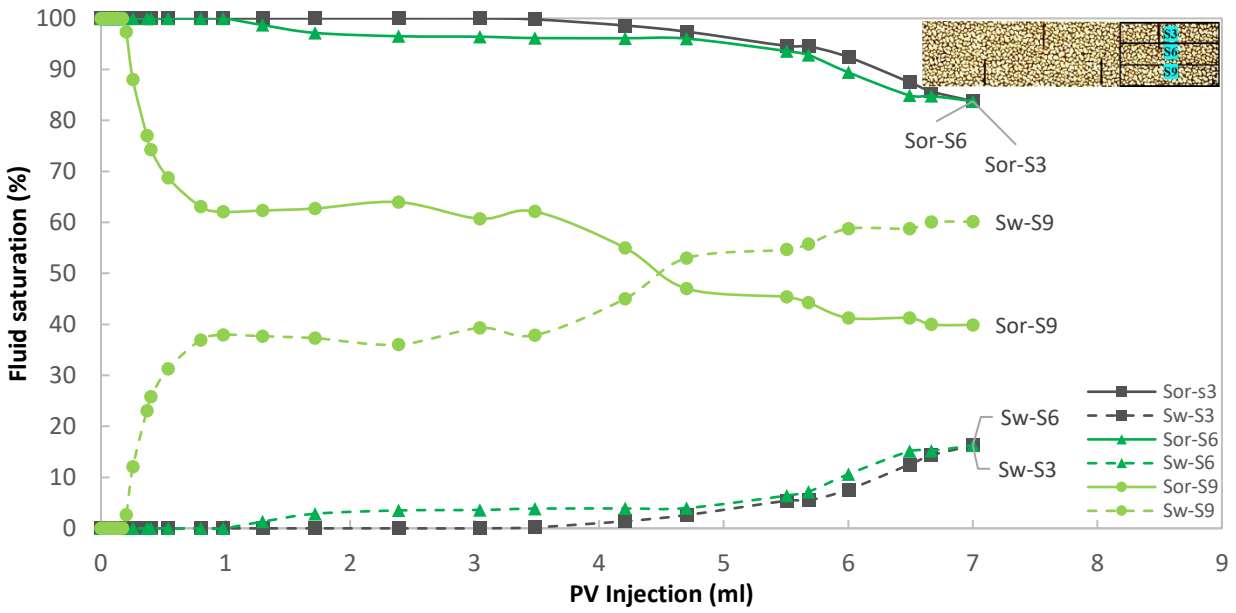

Figure 5–14: Average fluid saturations for WF in the vertical fracture micromodel, sections S3, S6, and S9

5.2.3.2. Water Flooding with and without Gravity in Heterogeneous Micromodels

To understand the simultaneous effect of gravity and heterogeneity on fluid flow pattern and oil recovery, a simple water flooding was performed with the micromodels oriented horizontally (laying flat) and vertically (standing on its side) in both heterogeneous types of micromodels (vertical fractures and horizontal fractures). It was observed that water preferred to enter into

horizontal fractures (parallel to flow) and displaced the oil toward the fractures in both vertical (with gravity) and horizontal (without gravity) flooding. However, in vertical flooding, gravity altered the water path and oil displacement occurred mainly in the lower part of the micromodel until breakthrough (Figure 5-15). Breakthrough occurred at 0.36 PV in horizontal and 0.31 PV in vertical water flooding, which resulted in the recovery factor of 34.3 ± 0.05% and 32.1± 0.03%, respectively.

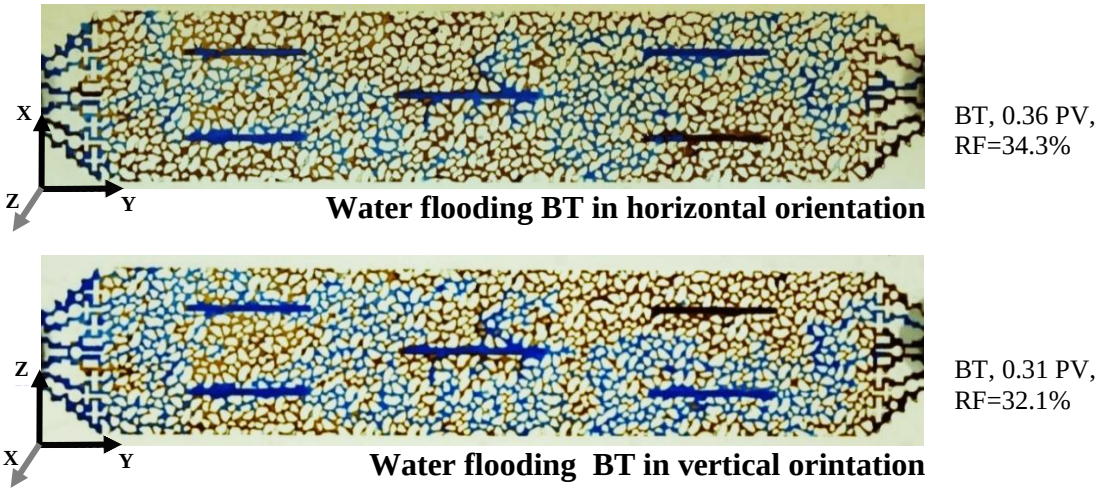

Figure 5–15: Saturation distribution at water flooding BT in horizontal and vertical orientations, horizontal fracture micromodel

In the micromodel with vertical fractures, water flooding experiments were performed in both horizontal and vertical orientations. As is shown in Figure 5-16, oil was displaced evenly in the horizontal micromodel; however, in the vertical orientation, gravity dominated, and sweep was higher in the lower half of the micromodel. Water breakthrough occurred later in the horizontally oriented micromodel at 0.35 PV compared to 0.24 PV in the vertically oriented micromodel, which resulted in 38.6 ± 0.1% and 25.2 ± 0.08% recovery at breakthrough, respectively.

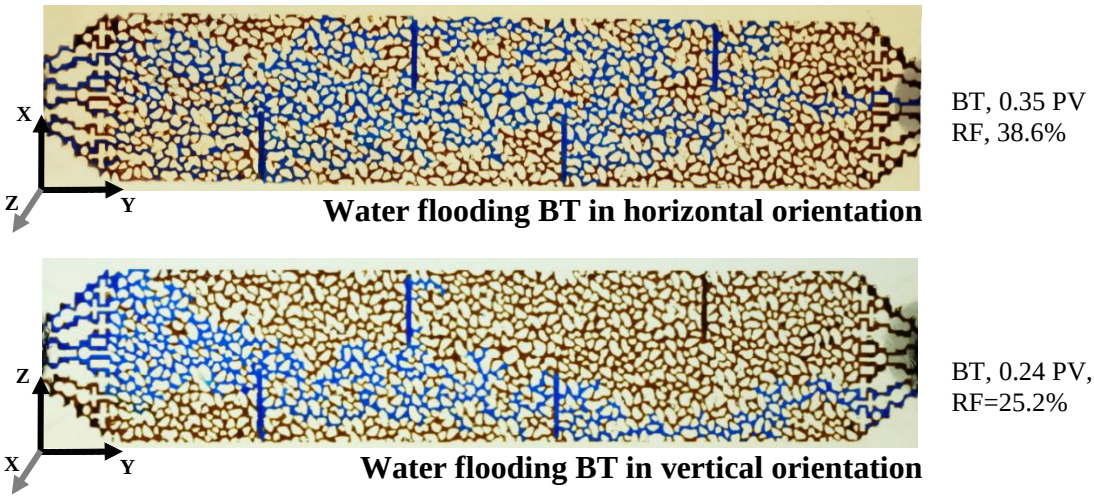

Figure 5–16: Saturation distribution at water flooding BT in horizontal and vertical orientation, vertical fracture micromodel

There was no significant difference in the horizontal fracture micromodel when oriented vertically or horizontally in the configuration of by-passed zones. Oil displacement occurred after breakthrough. However, oil saturation was mostly local, even at higher pore volume injections due to the presence of horizontal fractures parallel to the direction of flow (Figures 5-17 and 5-18).

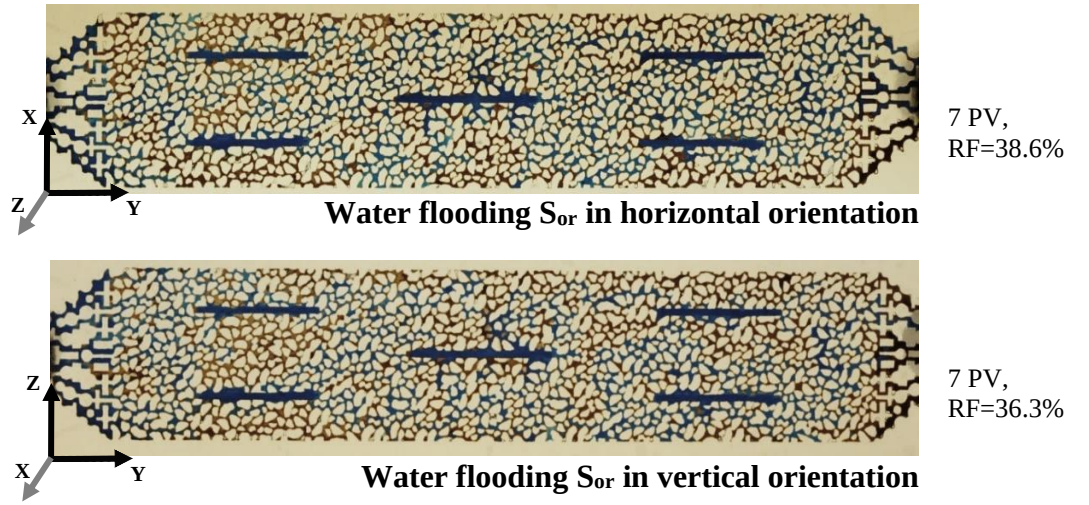

Figure 5–17: S_{or} after 7 PV water flooding in horizontal and vertical orientations, horizontal fracture micromodel

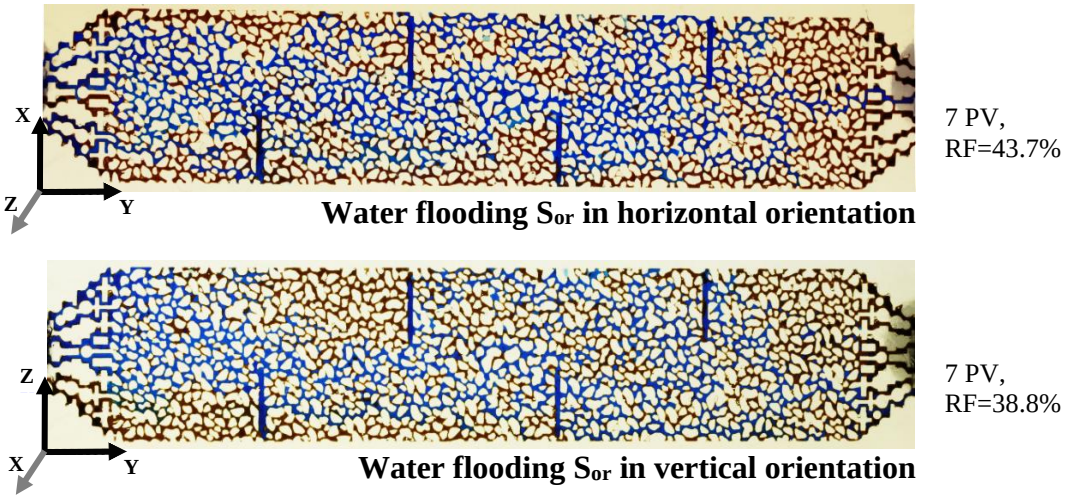

Figure 5–18: S_{or} after 7 PV water flooding in horizontal and vertical orientations, vertical fracture micromodel

Overall, although we expected a stable frontal displacement in the horizontally-oriented micromodels (homogeneous and heterogeneous), water did not show a stable displacement, which might be due to a higher mobility ratio of water/oil compared to CW/oil, as is shown later in sections 5.3.1 and 5.3.2. Additionally, the presence of fractures in the heterogeneous micromodel reinforced the unstable fontal displacement. The recovery factors at BT in vertically-oriented micromodels were obtained 29.4 ± 0.02%, 32.1 ± 0.03%, and 25.2 ± 0.08% for homogeneous, horizontal fracture, and vertical fracture patterns, respectively. Monitoring the oil saturation profiles at 1 PV showed the recovery factor of 32.7 ± 0.05% in the homogeneous, 33.0 ± 0.07% in the horizontal fracture, and 33.0 ± 0.03% in vertical fracture micromodels.

The effect of gravity was neglected in the horizontally-oriented micromodel. This helped the distribution of water all over the porous media, which resulted in higher ultimate oil recovery factors of 42.5 ± 0.02% compared to 36.2 ± 0.03% (homogeneous), 38.6 ± 0.08% compared to 36.3 ± 0.04% (horizontal fracture), and 43.7 ± 0.1% compared to 38.8 ± 0.08% (vertical fracture) in horizontally compared to vertically-oriented micromodels.

5.2.4. Summary of the Effect of Gravity

The results of simple water flooding at different pore volumes is shown and summarized in Figure 5-19 and Table 5-1. As shown, the recovery factor of water flooding in the vertically-oriented micromodels, irrespective of the type of micromodel, does not exceed 39%, which shows the low performance of water flooding in any of the three geometries (homogeneous, horizontal fracture, and vertical fracture micromodels). The comparison of horizontal flooding (dashed line) compared to vertical flooding (solid line) for each micromodel (homogeneous, horizontal fracture, and vertical fracture) showed that, horizontal flooding could displace more oil which resulted in higher oil recovery. The difference in recovery factor between vertical and horizontal flooding for horizontal fracture micromodel was less than the other two geometries (homogeneous and vertical fracture micromodels) due to the orientation of fractures to flow which caused an earlier breakthrough and lower recovery factor.

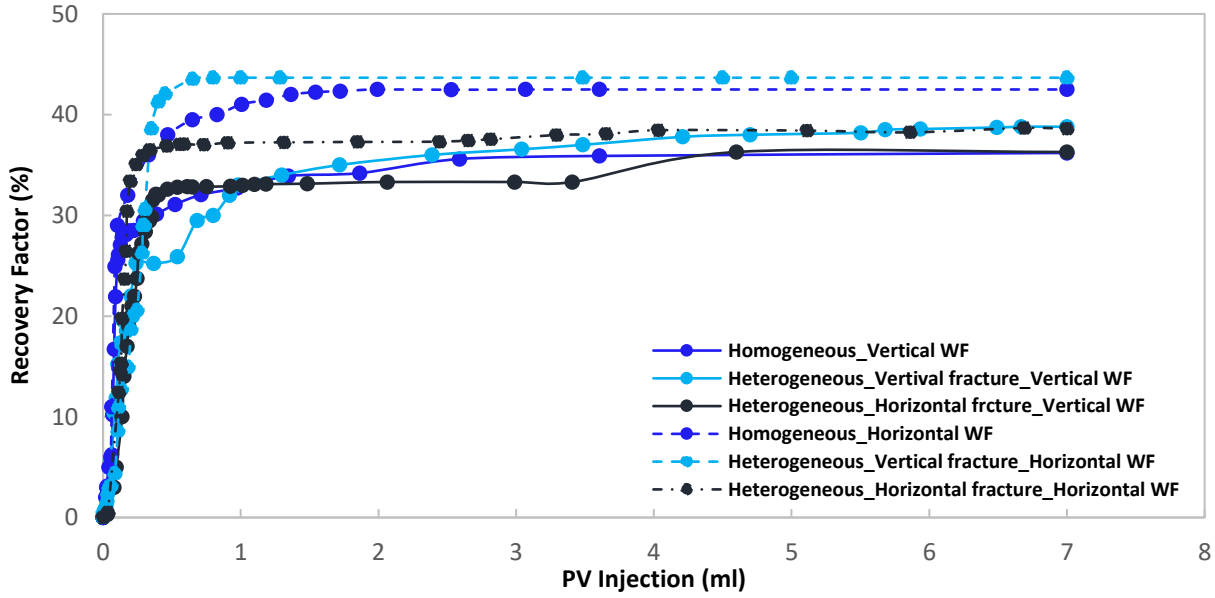

Figure 5–19: RF of WF in horizontal and vertical orientations in the homogeneous, horizontal and vertical fracture micromodels

Table 5-1: Effect of gravity on water flooding in homogeneous and heterogeneous micromodels

Exp.	Micromodel Orientation	BT (PV)	RF (%) at BT	RF (%) (0.8 PV)	RF (%) (1 PV)	RF (%) (1.2 PV)	RF (%) (2 PV)	RF (%) (3 PV)	RF (%) (~7 PV)
WF	HM_V	0.30	29.4	32.3	32.7	33.4	33.9	35.7	36.2
WF^r	HM_V	0.28	29.5	32.1	32.8	33.5	34.1	34.6	35.6
WF	HT_VF_V	0.24	25.2	30.0	33.0	33.7	35.4	36.6	38.8
WF	HT_HF_V	0.31	32.1	32.9	33.0	33.1	33.3	33.3	36.3
WF	HM_H	0.35	37.1	40.0	41.3	41.4	42.5	42.5	42.5
WF	HT_VF_H	0.35	38.6	43.6	43.6	43.6	43.7	43.7	43.7
WF	HT_HF_H	0.36	34.3	37.3	37.6	37.6	37.6	37.6	37.6

WF: water flooding, HM: homogeneous, HT_VF: heterogeneous including vertical fracture, HT_HF: heterogeneous including horizontal fractures, ^{r}: replicate, H: horizontal flooding, V: vertical flooding, BT: breakthrough, PV: pore volume, RF: oil recovery factor

The results of water flooding at BT, 1 PV, and 7 PV for the homogeneous and heterogeneous micromodels in the presence of gravity (vertically-oriented micromodel) are summarized below. Figure 5-20 shows the oil saturation profile of water flooding in the homogeneous micromodel. As is observed (Figure 5-20a), the oil saturation at breakthrough (BT) in upper sections (S1 to S3) is higher than middle sections (S4 to S6) and lower sections (S7 to S9). There is an exception in residual oil saturation for S4 (45.3 ± 0.04%) and S7 (60.3 ± 0.03%) due to the location of the inlet port which is in the left-middle part of S4.

The oil saturation at 1 PV (Figure 5-20b) decreased for all the sections especially for the middle sections (S4 to S6) with the minimum oil saturation at S7 (43.2% ± 0.03). Figure 5-20c illustrates the oil saturation profile at 7 PV. Not only the oil saturation decreased compared to oil saturation at 1 PV but also the lower part on the micromodel (S7 to S9) reached a constant oil saturation of ~ 43% which is the lowest oil saturation compared to other sections.

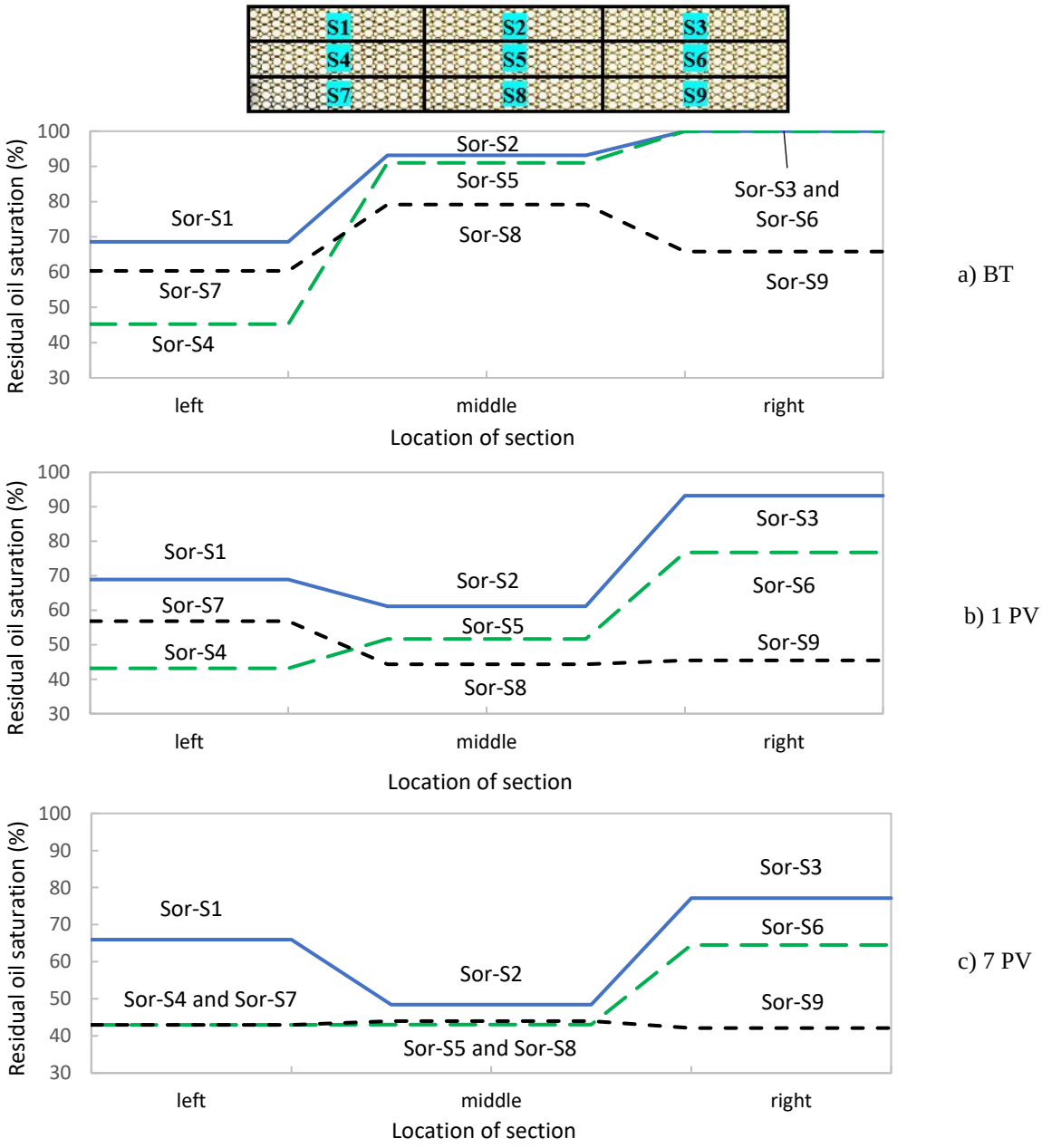

Figure 5–20: S_{or} in the homogeneous micromodel, sections S1 to S9 at BT, 1 PV, and 7 PV

The oil saturation in the closest sections to the inlet (S1 to S7) was lower compared to the middle sections (S2 to S8) at BT (Figure 5-20a). However, the oil saturation profile for the same sections in Figure 5-20b shows that section S2 to S5 were displaced while the oil saturation in sections

S1 to S7 did not change except for S7which was affected by gravity force. The results of water flooding at BT, 1 PV, and 7 PV for the horizontal fracture heterogeneous micromodel in the presence of gravity (vertically-oriented micromodel) are depicted in Figure 5-21. As is observed (Figure 5-21a), the oil saturation at breakthrough (BT) in the upper sections (S1 to S3) is not following the same trend as the lower sections (S4 to S6 and S7 to S9). For example, S1 and S7 have the lower oil saturation of 43.5 ± 0.05% and 48.9 ± 0.07% compared to S4, 64.6 ± 0.04%.

The oil saturation in S5, 53.8 ± 0.05% is lower than adjacent sections S4, 64.6 ± 0.04% and S6, 95.0 ± 0.06% due to the presence of fracture in S5. Figure 5-21b shows that the oil saturation at 1 PV changed considerably for the upper sections (S2 to S3 and S5 to S6) which demonstrated the effect of fracture on oil distribution and competing with the force of gravity in the upper section, S3 and middle section, S5.

The oil saturation in the lower sections (S7 to S8) with the exception of S9 (from 55.7 ± 0.06% to 40.6 ± 0.04%) may be due to the effect of oil distribution in the neighbor sections (S5) that deviate the oil to other sections (S3 and S6). The oil saturation at 7 PV (Figure 5-20c) illustrates that oil saturation changes slowly in most of the section. However, the oil saturation in S3 increased from breakthrough to 7 PV (62.3 ± 0.04% to 69.5 ± 0.02%), because the presence of fracture provides a path for the oil even though it is located at the most upper part of the micromodel resulting in neutralizing the effect of gravity.

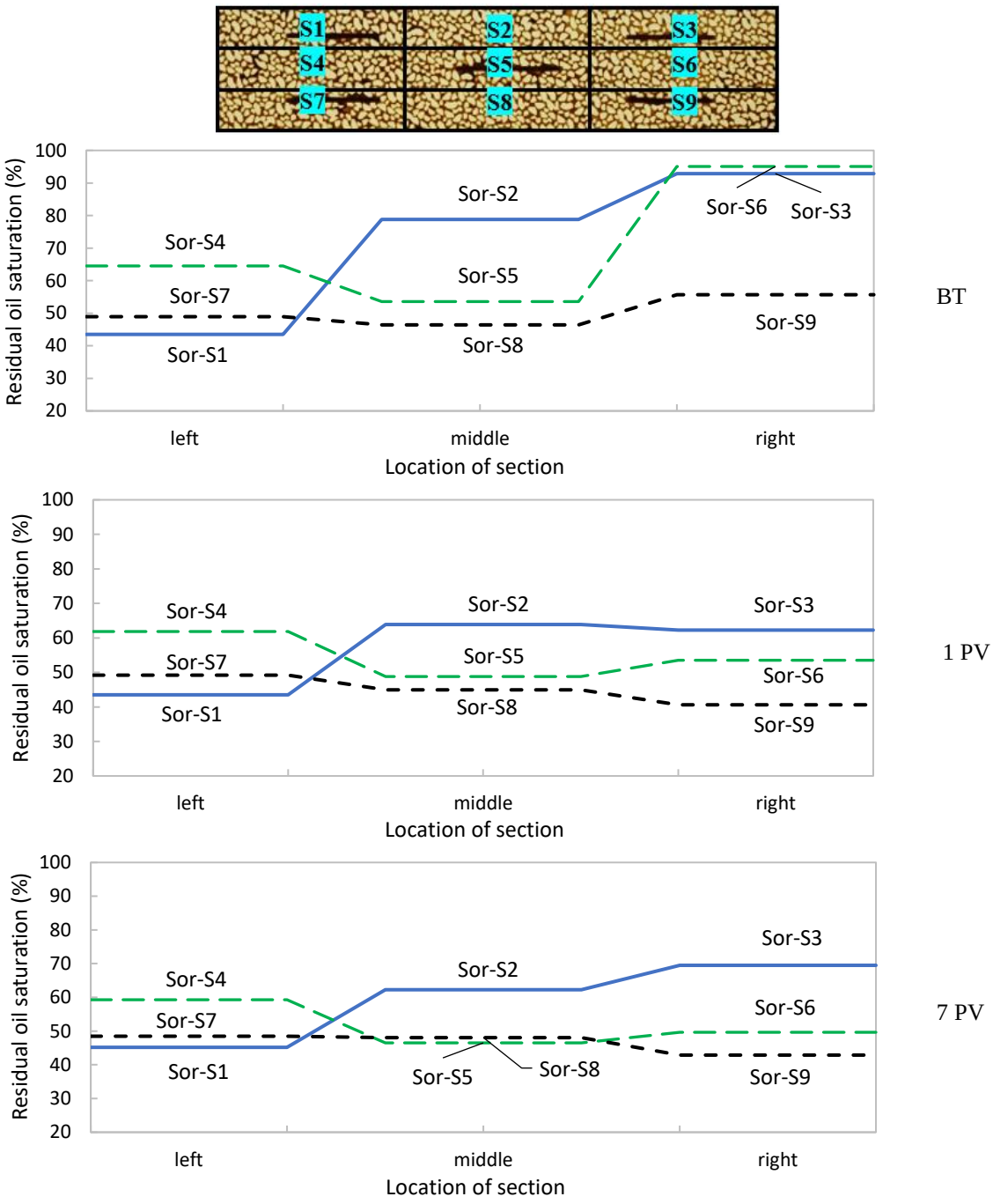

Figure 5–21: S_{or} in horizontal fracture micromodel, sections S1 to S9 at BT, 1 PV, and 7 PV

The oil saturation profile for the closest sections to the inlet port (S1 to S7) from BT to 7 PV shows that the oil saturation did not change considerably which might be due to the effect of capillary end-effect. Initially, the oil displacement occurred in S1 to S7, however, at 1 PV and 7 PV, the oil

saturation became constant. The oil saturation in other sections, S2 to S9 was reduced from BT to 7 PV. The results of water flooding at BT, 1 PV, and 7 PV for the vertical fracture heterogeneous micromodel in the presence of gravity (vertically-oriented micromodel) are summarized in Figure 5-22. The decreasing oil saturation in sections, S1 to S3 (73.4 ± 0.04% to 100 ± 0.02%) and section, S4 to S6 (33.5 ± 0.04% to 100 ± 0.01%) is observed at BT (Figure 5-22b). Contrary to this, the oil saturation in S7, 73.4 ± 0.06% is higher than the next section, S8, 54.7 ± 0.08%, because S7 was impacted by the inlet port which was located in the S7.

The oil saturation in S3 and S6 (100 ± 0.02% and 100 ± 0.03%) did not change at BT. The oil saturation in all section became constant from BT to 1 PV, however, S5 and S9 showed the maximum change in oil saturation (68.1 ± 0.04% to 55.0 ± 0.03% and 88.0 ± 0.03% to 62.0 ± 0.02%). Monitoring the oil saturation profiles at 7 PV (Figure 5-22c) shows S1 to S3, S4 to S6, and S7 to S9 are shifting down compared to their profile at 1 PV which illustrates that water was actively and continuously sweeping the oil at higher pore volume than 1 PV due to the interactive effect of fracture's location and gravity.

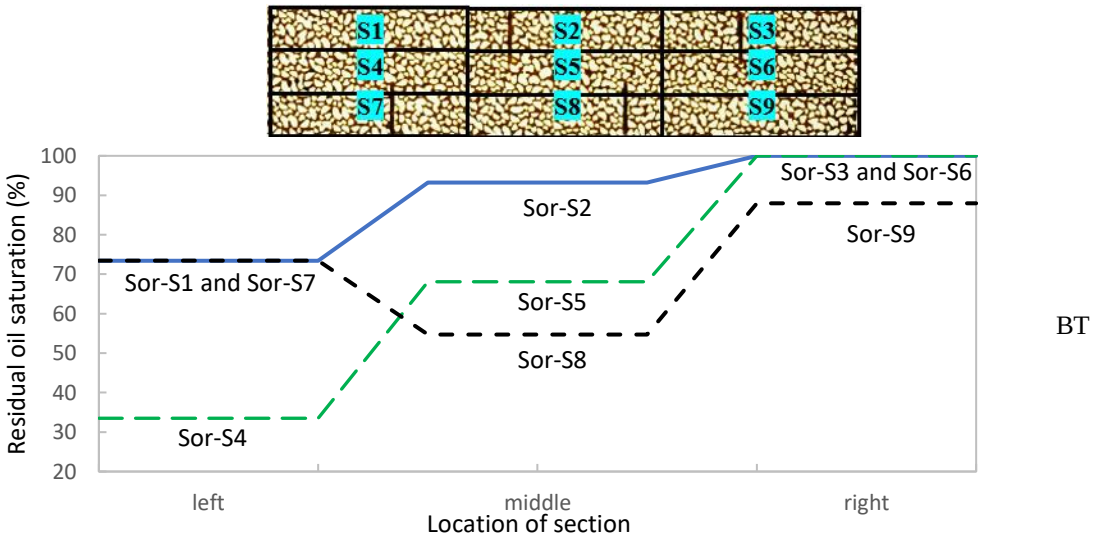

BT

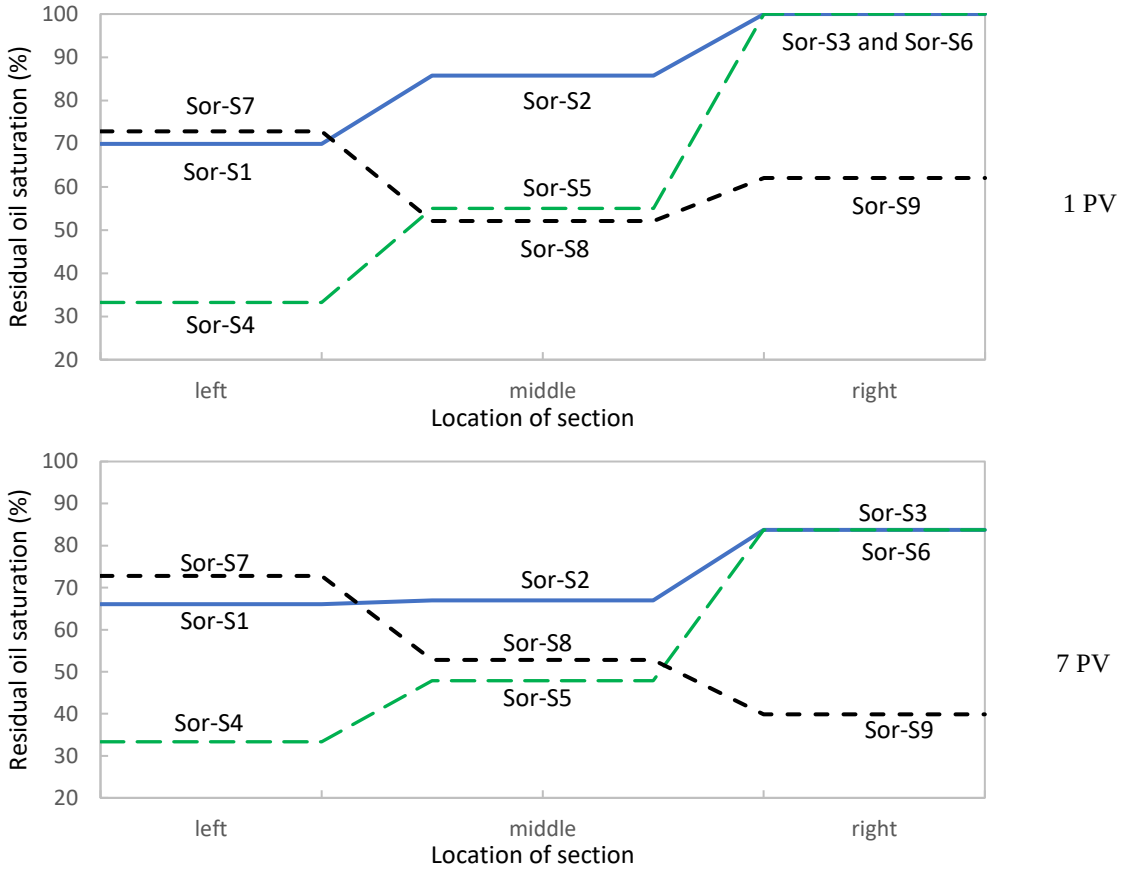

Figure 5–22: S_{or} in vertical fracture micromodel, sections S1 to S9 at BT, 1 PV, and 7 PV

Sectional analysis of the effect of gravity on oil displacement in homogeneous and heterogeneous micromodels revealed that fluid displacement was influenced by the orientation of micromodels (with and without gravity). However, the presence of fracture (horizontal and vertical fractures) was important to determine the fluid flow pattern.

5.3. Effect of CWI

In this section, the results of secondary and tertiary CWI are compared to simple water flooding to understand the performance of CWI on vertical sweep efficiency and oil recovery in both homogeneous and heterogeneous porous media.

5.3.1. Homogeneous Micromodel

The effect of carbonated water injection (secondary and tertiary CWI) compared to water flooding on the recovery factor in the homogeneous micromodel is shown in Figure 5-23. It was found that water breakthrough in secondary CWI takes a little longer for secondary CWI (0.32 PV) compared to water flooding (0.3 PV) due to the controlled mobility of oil by carbonated water than water. Water began to exhibit more viscous fingering behavior than carbonated water. The calculation showed that the dissolution of CO_2 in oil reduces the oil viscosity from 6.82 cP to 6.23 cP.

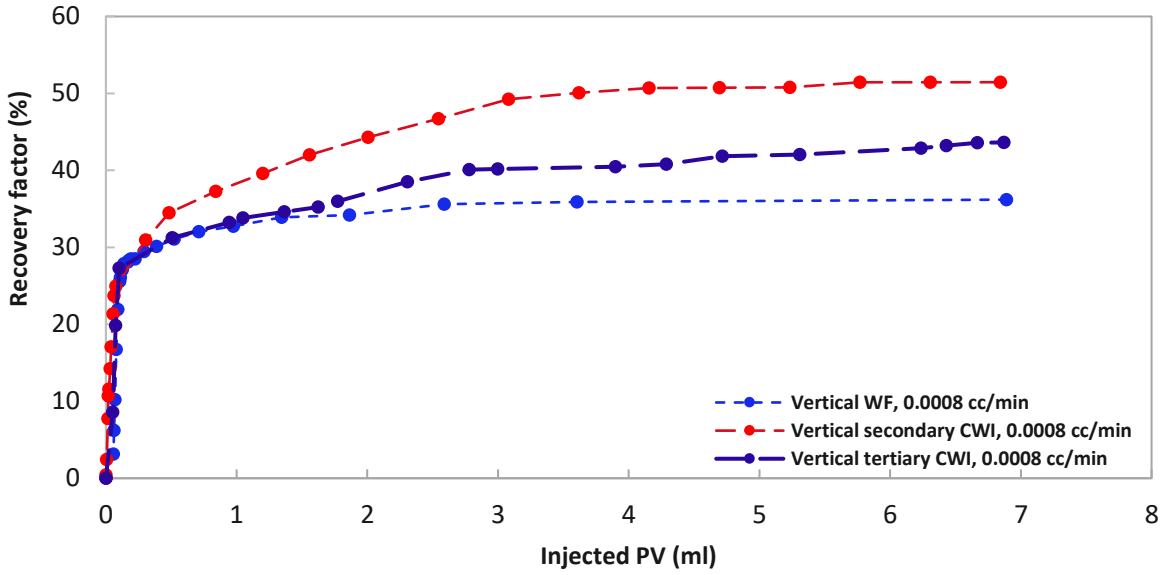

Figure 5–23: RF of water flooding, secondary and tertiary CWI in the homogeneous micromodel

Overall, secondary CWI was more effective at increasing the recovery factor at each time interval after breakthrough while the recovery factor for water flooding was lower than secondary CWI at breakthrough. The higher incremental oil recovery occurred after breakthrough for secondary and tertiary CWI compared to water flooding, the reason for that might be due to the CO_2 transfer from carbonated water to oil ($\delta_{CO2-oil} = 0.096$ mol CO_2/mol oil compared to $\delta_{CO2-water} = 0.0128$ mol CO_2/mol water) and more stable frontal displacement of carbonated phase (μ_{oil} changed from 6.82

cP to 6.23 cP, discussed in section 2.3.4). After 1 PV injection, the recovery factor for secondary CWI and water flooding reached 38.5 ± 0.03% and 32.7 ± 0.05%, respectively.

The oil recovery increased more in secondary CWI (34.2 ± 0.04% to 53.0 ± 0.02%) compared to water flooding (29.4 ± 0.02% to 36.2 ± 0.03%) post breakthrough, resulting in significantly different oil recovery at 7 PV. It was observed that from the beginning of secondary CWI, the carbonated water phase displaced the oil in the lower part of the micromodel due to the effect of gravity, and the displacement pattern almost remained constant until breakthrough. By-passed zones were not formed during CWI compared to water flooding. Pore-scale displacement was almost completed in the swept area due to the mobility control. However, there is a curvature in the front displacement caused by gravity effect (Figure 5-24). The secondary CWI, after breakthrough, the vertical displacement of oil was considerably enhanced, and the recovery factor increased.

Tertiary CWI was conducted to understand the performance of CWI in a pre-water flooded reservoirs. The ultimate oil recovery value for the water flooding was obtained at 33.5 ± 0.07% after 1.5 PV of water injection and then CWI commenced. By injection of 0.2 PV carbonated water, the recovery factor reached 34.9 ± 0.06%. CWI after 1 PV injection resulted in 40.1 ± 0.08%. The color of the water in-place began to change from dark blue to light blue (Figure 5-24, tertiary CWI). Initially, local oil distribution did not vary due to prior mixing (dilution) of rich phase CO_2 (carbonated water) and poor phase CO_2 (water) compared to the interaction of carbonated water and oil. Additionally, in tertiary CWI, gravity was unimportant as it did not affect the selected path by carbonated water in the pre-water flooded porous media.

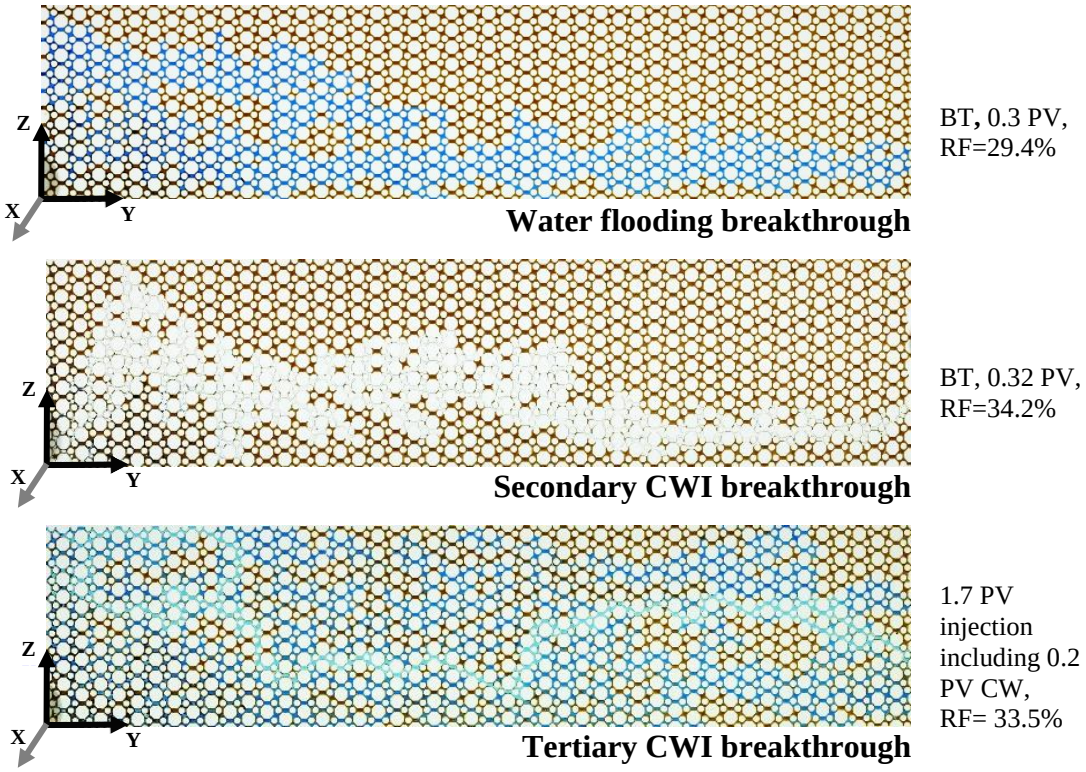

Figure 5–24: BT in WF, and secondary and tertiary CWI in the vertical homogeneous micromodel

Analysis of the results at 7 PV (Figure 5-25 and Table 5-2) demonstrated that higher pore volume injection of carbonated water causes more interaction between the carbonated water and oil phases, which resulted in a higher CO_2 transfer to the oil phase (Riazi et al., 2011; Seyyedi et al., 2017). For this reason, in the current study, oil production as a result of viscosity reduction (μ_{oil} changed from 6.82 cP to 6.23 cP, discussed in section 2.3.4), and oil swelling ($\delta_{CO2-oil} = 0.096$ mol CO_2/mol oil), occurred gradually during the course of secondary and tertiary CWI. During each experiment, the differential pressure increased until breakthrough as there was a two-phase flow of water and oil progressing in the core and an increase in water/CW saturation. The maximum differential pressure occurred at breakthrough and continued to decrease until the production was stabilized. Secondary CWI showed a lower pressure drop compared to water flooding. The lower differential pressure in the secondary CWI was less than that in the seawater flooding due to CO_2

transfer from the carbonated seawater to the oil and viscosity reduction (Appendix A, Figure A-19). Mobility is the ratio of relative permeability to viscosity of oil.

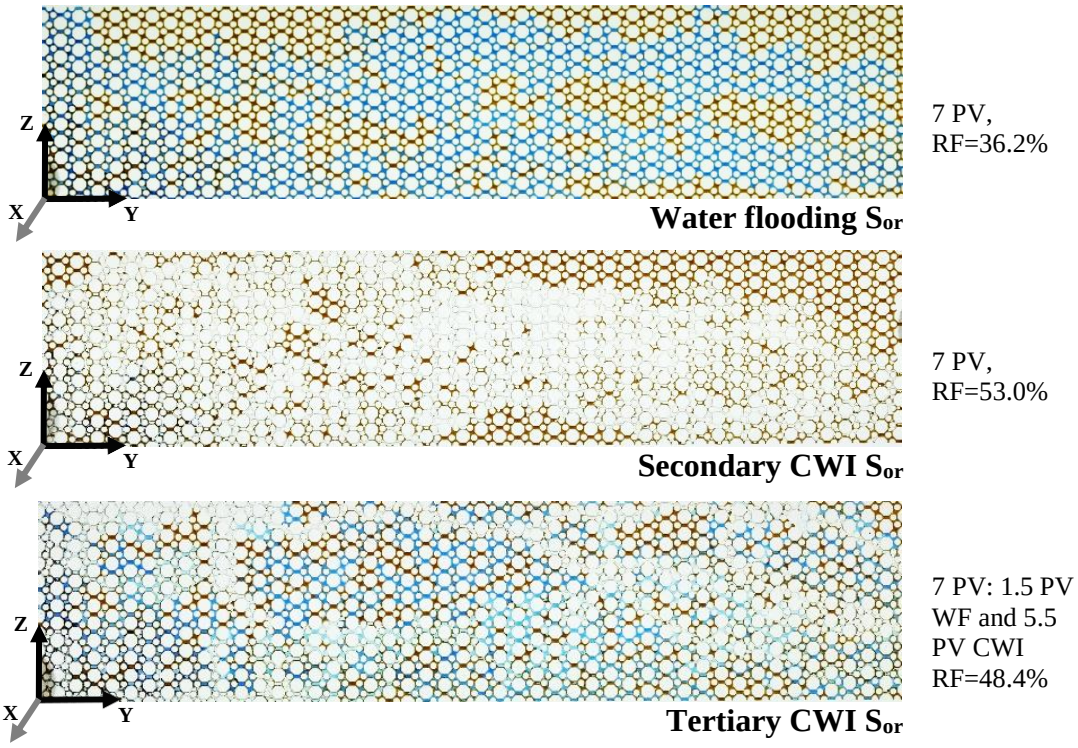

Figure 5–25: S_{or} in WF, and secondary and tertiary CWI in the vertical homogeneous micromodel

It is believed that dissolution of CO_2 in oil enhances the mobility of oil by reducing the oil viscosity, interfacial tension between oil and carbonated water, and oil swelling. When the viscosity is reduced the mobility is increased and oil swelling increases the relative permeability of the oil. Analysis the results of micromodel experiments at 21°C and 2.1 MPa showed that dissolved CO_2 in water is low which caused improvement in oil displacement by longer injection of carbonated water. We found that there were no considerable by-passed zones after 7 PV, especially in secondary CWI and tertiary CWI, due to the homogeneity of the micromodel.

Table 5-2: RF of WF, and secondary and tertiary CWI in the vertical homogeneous micromodel

Exp.	BT (PV)	RF (%) (BT)	RF (%) (0.8 PV)	RF (%) (1 PV)	RF (%) (1.2 PV)	RF (%) (2 PV)	RF (%) (3 PV)	RF (%) (7 PV)
WF	0.3	29.4	32.3	32.7	33.4	33.9	35.7	36.2
SCWI	0.32	34.2	36.7	38.5	40.7	42.4	49.3	53.0
SCWI^r	0.31	33.5	35.8	39.7	39.8	43.6	50.0	52.0
TCWI	1.7	34.9	38.5	40.1	40.2	42.9	43.8	48.4

WF: water flooding, SCWI: secondary CWI, TCWI: tertiary CWI, ^{r}: replicate, BT: breakthrough, PV: pore volume, RF: oil recovery factor

5.3.2. Heterogeneous Micromodels

To evaluate the impact of heterogeneity and the orientations of fractures on the performance of CWI, several schemes were implemented in both heterogeneous types of micromodels (horizontal fractures and vertical fractures). This section includes the results of simple water flooding, secondary CWI, and tertiary CWI. Secondary and tertiary CWI were conducted at the same flowrate of simple water flooding, 0.0024 ml/min. The ultimate oil recovery factors of 36.3 ± 0.04%, 42.3 ± 0.07%, and 40.1 ± 0.08% were achieved in water flooding, and secondary and tertiary CWI in the horizontal fracture micromodel compared to the same schemes with the recovery factors of 38.8 ± 0.08%, 48.9 ± 0.05%, and 47.8 ± 0.02% in the vertical fracture micromodel (Figure 5-26 and Table 5-3).

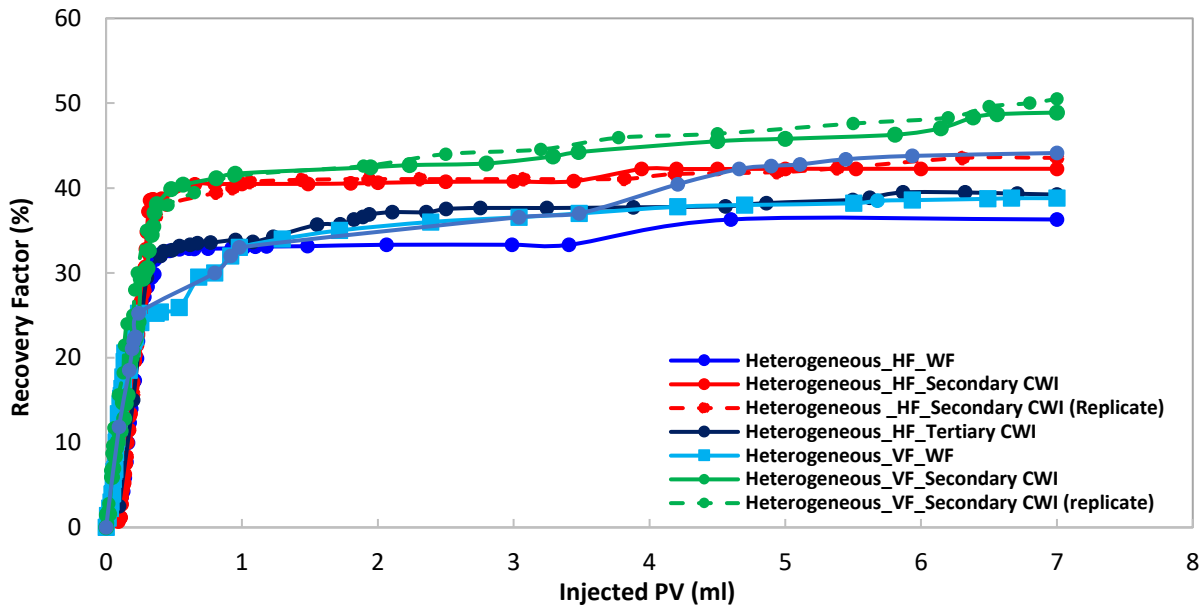

Figure 5–26: RF in WF, and secondary and tertiary CWI in the vertical heterogenous micromodels

Breakthrough in the horizontal fracture micromodel occurred at 0.31 PV and 0.34 PV in water flooding and secondary CWI, respectively (Figure 5-27). After 1 PV injection, recovery factor for water flooding and secondary CWI reached 33.0 ± 0.04% and 40.5 ± 0.02%, respectively. There was a change in the recovery factor (32.1 ± 0.03% to 36.3 ± 0.04%) of water flooding compared to secondary CWI (38.6 ± 0.04% to 42.3 ± 0.02%) from breakthrough to 7 PV. However, for the vertical fracture micromodel, breakthrough occurred at 0.24 PV and 0.37 PV in water flooding and secondary CWI, respectively (Figure 5-28). After 1 PV injection, the recovery factor for water flooding and secondary CWI reach 33.0 ± 0.06% and 41.5 ± 0.03%, respectively. The recovery factor changed from 25.2 ± 0.08% to 38.8 ± 0.08% and from 38.1 ± 0.06% to 48.9 ± 0.07% from breakthrough to 7 PV for water flooding and secondary CWI, respectively.

During water flooding and secondary CWI, the presence of fractures first channeled the carbonated water to fractures and then to the matrix, due to the high permeability of fractures. However, the

oil displacement in the lower part of the porous media progressed as well due to gravity, which did not allow the fluid to flow crosswise equally in the vertical fracture micromodel. In tertiary CWI, water was initially flooded to the micromodel. We could not report any actual breakthrough for tertiary CWI. The change in water color showed the injected carbonated water (colorless) was mixing (miscibility) with water (dark blue). Initially, oil saturation and local distribution of oil did not vary due to prior mixing of rich phase CO_2 (CW) and poor phase CO_2 (water) compared to the transfer of CO_2 from the carbonated water phase to the oil phase (2 PV water and 0.12 PV carbonated water, tertiary CWI). Ultimate oil recovery for the initial water flooding was obtained at 33.4 ± 0.07% and 35.3 ± 0.05% for the horizontal and vertical fracture micromodels at 2.12 PV.

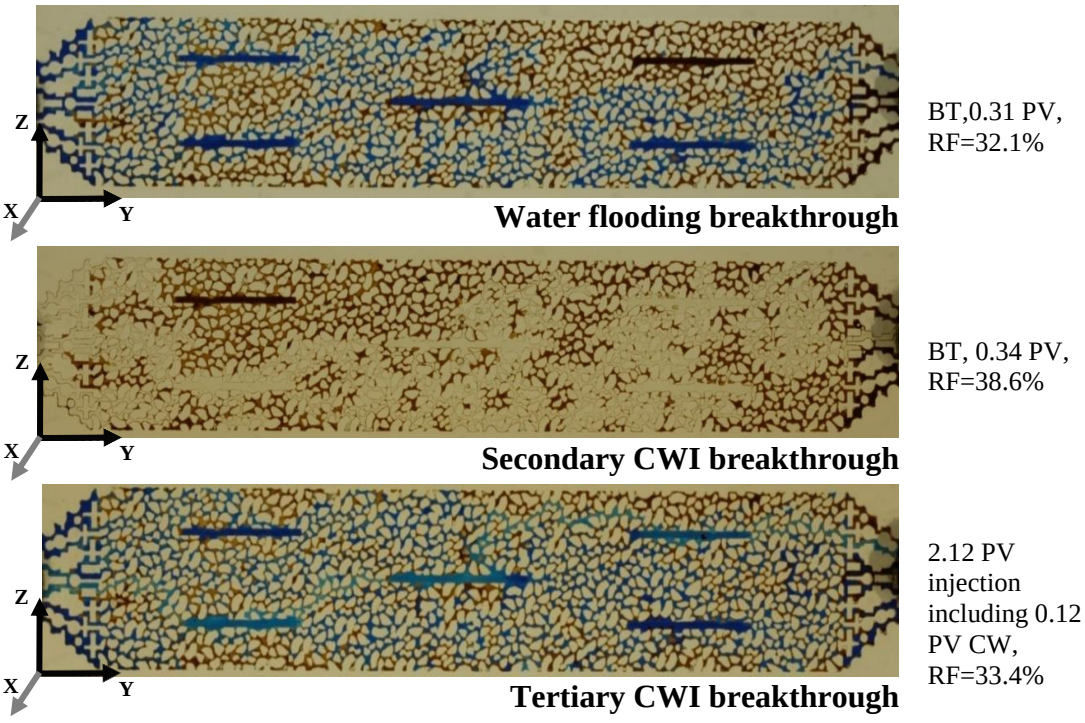

Figure 5–27: BT in WF, and secondary and tertiary CWI in the horizontal fracture micromodel (vertically oriented micromodels)

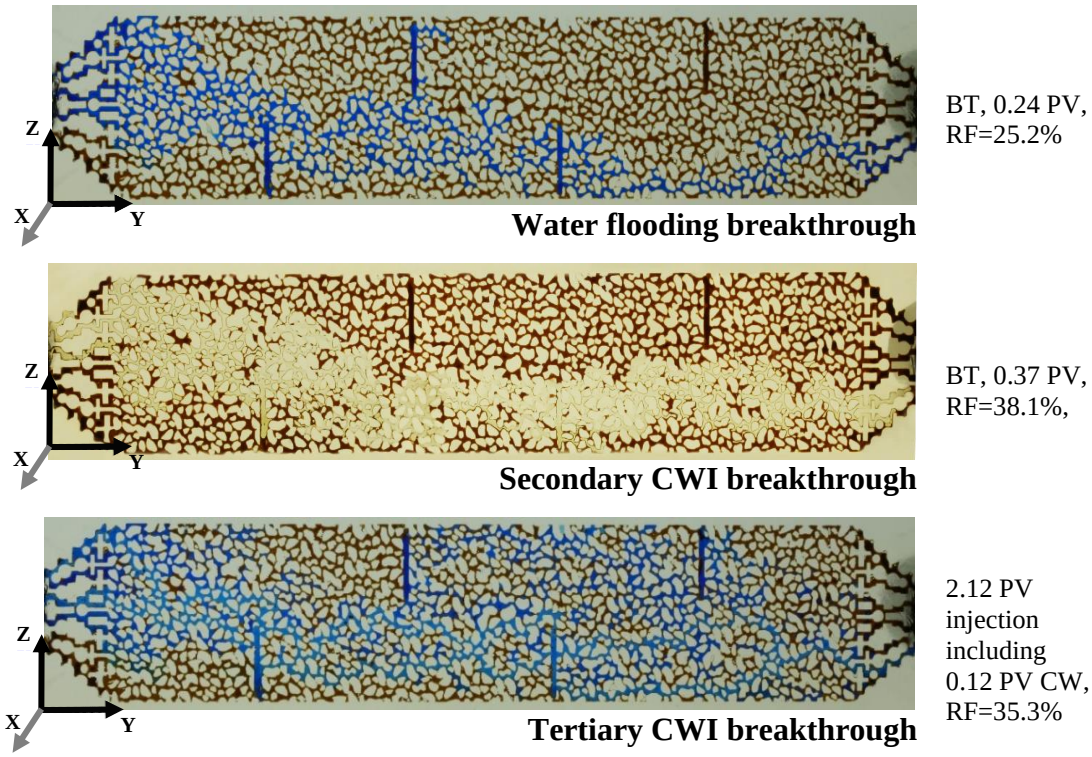

Figure 5–28: BT in WF, and secondary and tertiary CWI in the vertical fracture micromodel (vertically oriented micromodels)

It was observed that there was a significant difference between recovery factors at breakthrough and 7 PV injections for simple water flooding and secondary CWI in both horizontal and vertical fracture patterns. This evidence demonstrated the effect of fractures that caused an unstable water displacement, which resulted in differences between recovery factor at breakthrough and 7 PV. In secondary CWI, the effect of CO_2 solubility in oil and interaction between fracture and matrix improved the recovery factor at 7 PV compared to breakthrough. Fractures greatly slowed down the fluid flow in the matrix. As soon as full saturation occurred in fracture, the local oil distribution in the matrix was observed between fractures. There were un-swept areas due to the effect of gravity and heterogeneity of the porous media. The vertical fractures acted as distributors along the vertical direction. Moreover, vertical fractures connected the lower and upper parts of the micromodel to aid the injected fluid to displace the oil. This phenomenon helped the carbonated

water reach the upper part of the porous media and improve the vertical sweep efficiency of secondary CWI compared to horizontal fractures (Figures 5-29 and 5-30).

In tertiary CWI, the presence of vertical fractures transferred the carbonated water to the water flooded parts causing CO_2 interaction with the oil all over the porous media. By continuing CW injection, the previous pathways became more concentrated with carbonated water and the oil displacement occurred in the matrix and fracture. Another stream of carbonated water appeared in other directions and extended the invaded area. It was found that the gravity force was not able to push the carbonated water phase downward. The solubility of CO_2 in oil caused oil swelling (SF =1.014 cm^3/cm^3, $\delta_{CO2-oil}$ =0.096 mol CO_2/mol oil, discussed in section 2.3.4) and local oil viscosity reduction (6.82 cP to 6.23 cP). We believe that the oil remobilization in a fractured porous media is the main factor that helps to displace the oil toward production in tertiary CWI.

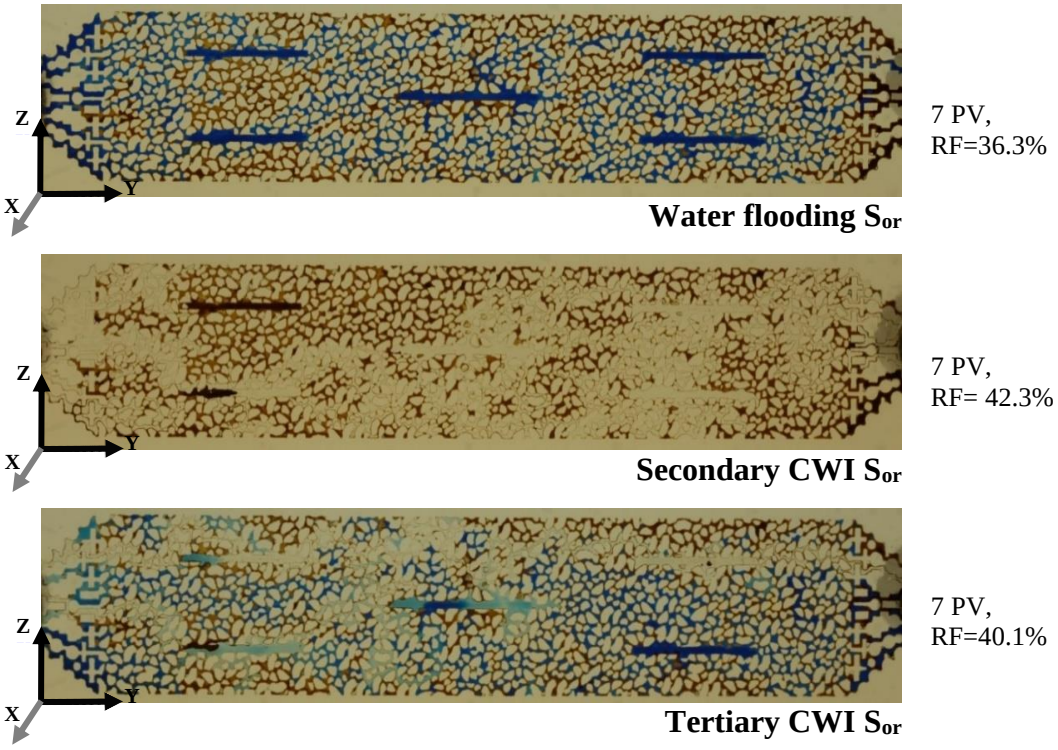

Figure 5–29: S_{or} in WF, and secondary and tertiary CWI in the horizontal fracture micromodel (vertically oriented micromodels)

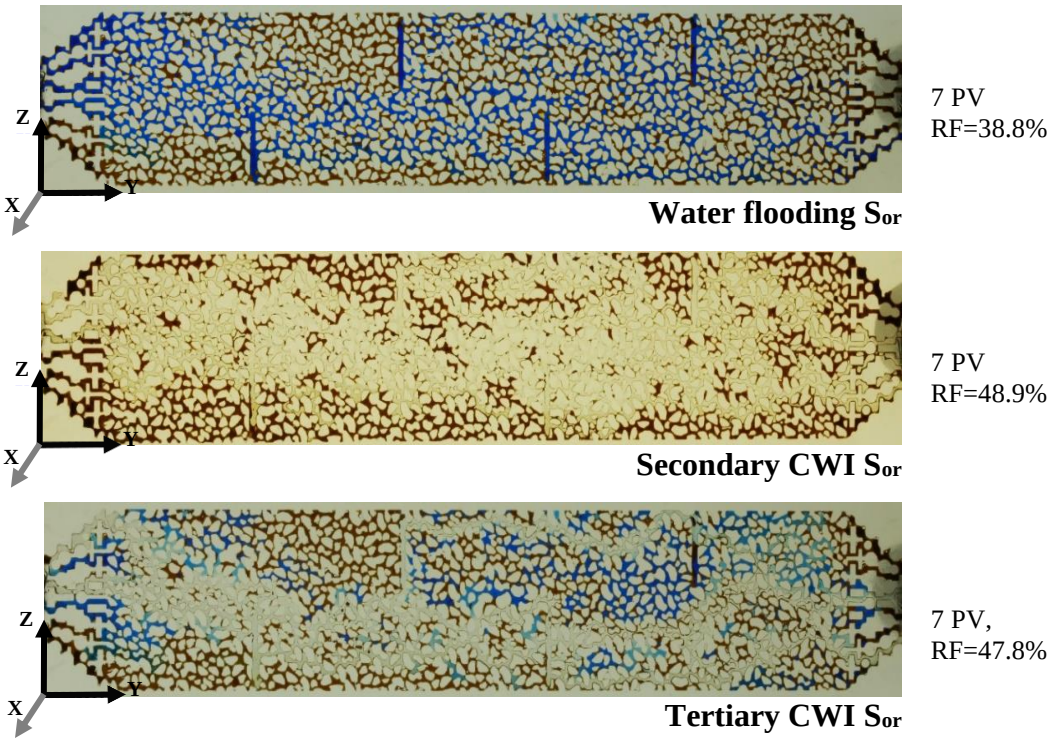

Figure 5–30: S_{or} in WF, and secondary and tertiary CWI in the vertical fracture micromodel (vertically oriented micromodels)

Table 5-3: RF of WF, secondary and tertiary CWI in heterogeneous micromodels (VRT)

Exp.	Fracture Orientation	BT (PV)	RF (%) (BT)	RF (%) (0.8 PV)	RF (%) (1 PV)	RF (%) (1.2 PV)	RF (%) (2 PV)	RF (%) (3 PV)	RF (%) (7 PV)
Horizontal Fracture Micromodel									
WF	H	0.31	32.1	32.9	33.0	33.1	33.3	33.3	36.3
SCWI	H	0.34	38.6	40.5	40.5	40.5	40.6	40.8	42.3
SCWI^r	H	0.37	36.7	38.9	40.6	40.7	40.7	41.0	43.6
TCWI	H	2.12*	33.4**	37.5	37.6	37.6	37.8	38.6	40.1
Vertical Fracture Micromodel									
WF	V	0.24	25.2	30.0	33.0	33.7	35.4	36.6	38.8
SCWI	V	0.37	38.1	40.5	41.5	41.8	42.6	42.9	48.9
SCWI^r	V	0.35	35.0	38.9	41.5	41.8	42.6	43.5	50.5
TCWI	V	2.12*	35.3**	36.6	36.9	37.1	40.4	42.8	47.8

WF: water flooding, SCWI: secondary CWI, TCWI: tertiary CWI, ^{r}: replicate, *: pore volume that carbonated water steam appears, **: recovery factor at the end of water flooding course in TCWI, BT: breakthrough.

5.4. Effect of Flowrate

Carbonated water injection experiments showed that gravity affects the fluid flow pattern. Initially oil displacement occurred in the lower part of the porous media and later oil was displaced all over the micromodel. In this section, the effect of flowrate on the performance of CWI in the presence of gravity is explained. The effect of production rate in secondary CWI was examined using two flowrates, 0.0008 (1.57 ft/d) and 0.004 (7.87 ft/d) ml/min in the homogeneous micromodel, and 0.0008 ml/min and 0.0024 ml/min in the heterogeneous horizontal fracture micromodel.

5.4.1. Effect of Flowrate in Homogeneous Micromodel

In the homogeneous micromodel, the recovery factor gradually increased within a higher flowrate of 0.004 ml/min and continued even after 7 PV compared to a lower flowrate of 0.0008 ml/min.

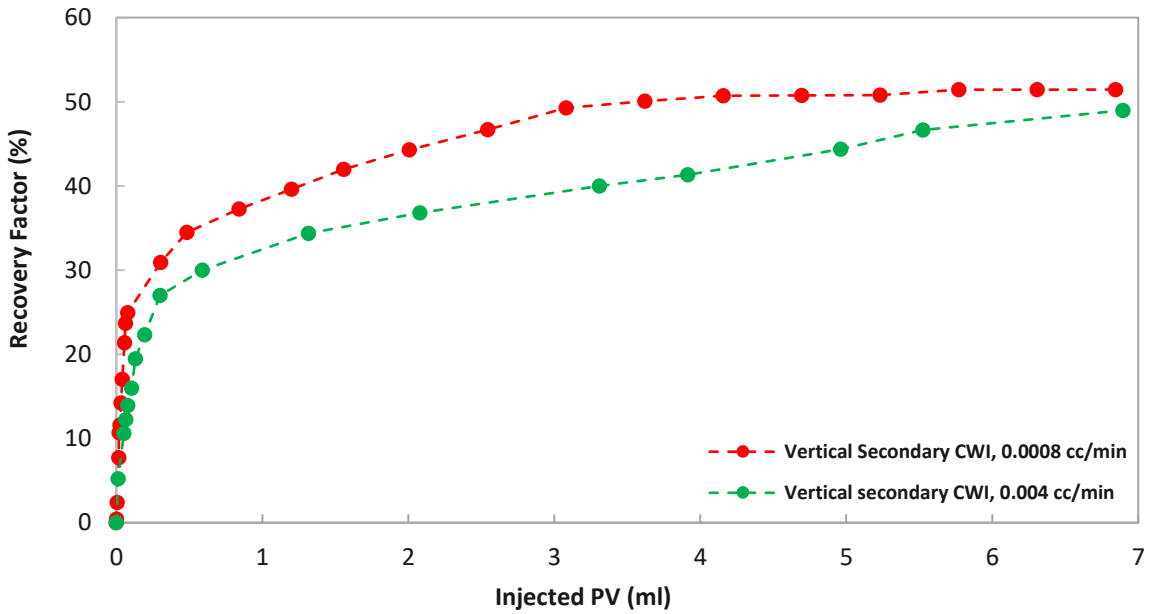

Figure 5–31: Effect of flowrate on oil recovery factor in the homogeneous micromodel

Although the recovery factor in secondary CWI with a flowrate of 0.004 ml/min was less than that in 0.0008 ml/min, the higher flowrate caused an increasing trend in oil recovery and production continued up to 7 PV. The production for a longer period as the recovery continued to increase

(the plateau is not happening in Figure 5-31). Because CO_2 transfer is a time-dependent process, CWI with an optimized flowrate could be beneficial for a reservoir-scale to continue production for so many years.

Secondary CWI at a high flowrate of 0.004 ml/min was conducted in a vertically-oriented micromodel. At the end of oil flooding, the inlet and outlet pressures were stabilized to 287 psi (1.98 MPa) and 285 psi (1.96 MPa), respectively. Initially, the carbonated water phase sped up and fingers began to form which resulted in an unequal oil displacement in the vertical direction. However, the carbonated water fingers tended to follow the lower part of the micromodel up to breakthrough due to the dominant effect of gravity (Figure 5-32). The lower fingers continued to move forward, meanwhile, the upper fingers slowed down until the breakthrough occurred at 0.28 PV with the recovery factor of 27.4 ± 0.03% compared to 0.32 PV with the recovery factor of 34.2 ± 0.04% in the scheme with a flowrate of 0.0008 ml/min. Fingers started to develop, and by-passed zones were formed. Recovery factor at 7 PV of carbonated water approached to 47.1 ± 0.05%.

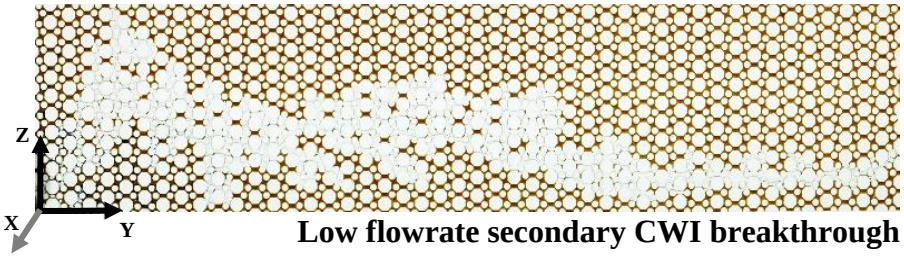

BT, 0.32 PV,
RF=34.2%

Low flowrate secondary CWI breakthrough

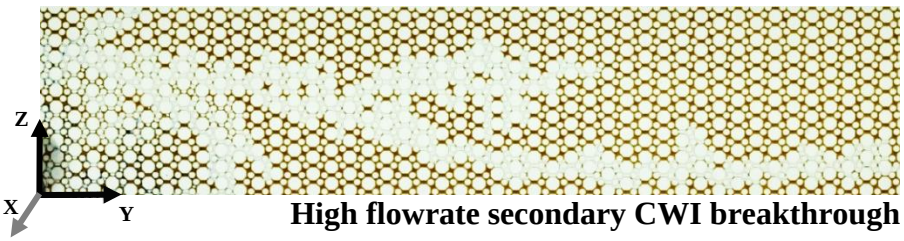

BT, 0.28 PV,
RF=27.4%

High flowrate secondary CWI breakthrough

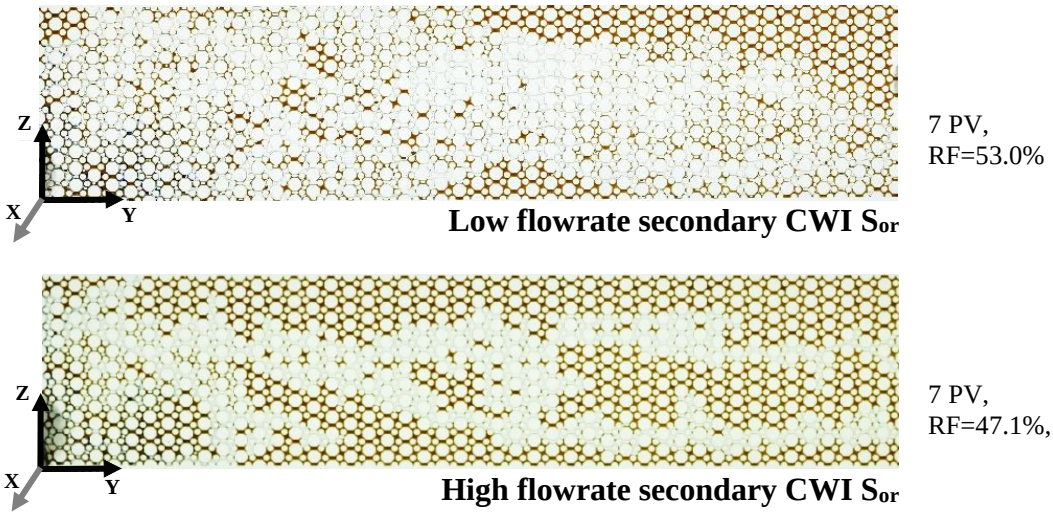

Figure 5–32: BT and S_{or} in secondary CWI, 0.0008 and 0.004 ml/min in the homogeneous micromodel

Table 5-4: RF at different flowrates in the homogeneous micromodel

Exp.	Rate (ml/min)	BT (PV)	RF (%) at BT	RF (%) (0.8 PV	RF (%) (1 PV)	RF (%) (1.2 PV)	RF (%) (2 PV)	RF (%) (3 PV)	RF (%) (~7 PV)
SCWI	0.0008	0.32	34.2	36.7	38.5	40.7	42.4	49.3	53.0
SCWI^r	0.0008	0.30	33.5	35.8	39.7	39.8	43.6	50.0	52.0
SCWI	0.004	0.28	27.4	31.3	32.8	33.3	38.5	38.6	47.1

SCWI: secondary CWI, ^{r}: replicate, BT: breakthrough, PV: pore volume, RF: oil recovery factor

5.4.2. Effect of Flowrate in Heterogeneous Micromodel

In the horizontal fracture micromodel, secondary CWI was tested using two flowrates of 0.0008 and 0.0024 ml/min. Breakthrough occurred at 0.34 PV and 0.30 PV for lower flowrate of 0.0008 ml/min and 0.0024 ml/min which resulted in the recovery factors of 38.6 ± 0.04% and 33.5 ± 0.07%, respectively. Recovery factor increased very gradually at 0.0008 ml/min, however, it continued production even after 7 PV. The ultimate recovery factor was obtained 39.8 ± 0.06% compared to 42.3 ± 0.07% at the higher flowrate of 0.0024 ml/min (Figure 5-33 and Table 5-5). Although the recovery factor in the scheme with a flowrate of 0.0008 ml/min was less than the one with 0.0024 ml/min, the lower flowrate helped the production to continue for a longer period.

Because lower flowrate improved the fracture-matrix interaction as fractures are a good source of oil and pathway for oil conduction. CO_2 transfer is a time-dependent process which CWI could be beneficial for a fractured reservoir production to produce oil for so many years with a low production rate but continues production.

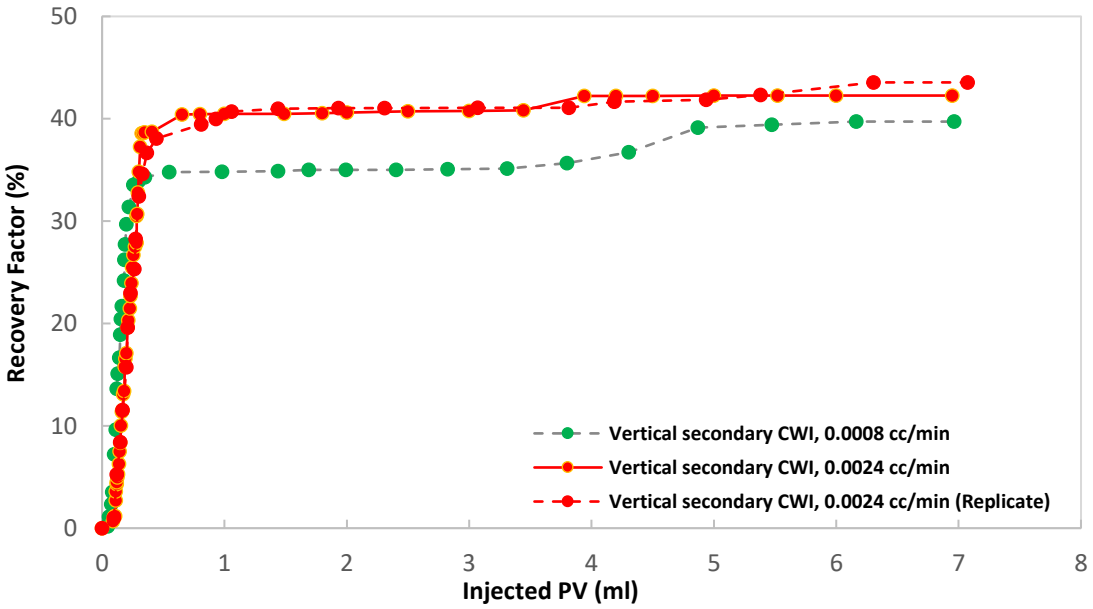

Figure 5–33: RF for different flowrates in the horizontal fracture micromodel

As is shown in Figure 5-34 (lower flowrate, 0.0008 ml/min), initially, the carbonated phase started to sweep the oil downward due to the high permeability of fractures and gravity force. It should be noted that displacement took place at the lower part of the micromodel and tended to move forward until breakthrough.

Continuing the injection of the carbonated water phase at a low flowrate (0.0008 ml/min) caused the oil in the matrix and fracture located in the lower part of the micromodel to be displaced due to the gravity effect and a low production rate. The oil saturation changed very slowly with the lower production rate, while high oil saturation was trapped in the upper part of the porous media

at 7 PV. Thus, we conclude that a combination of low flowrate and parallel fractures are responsible for controlling the mobility and oil recovery.

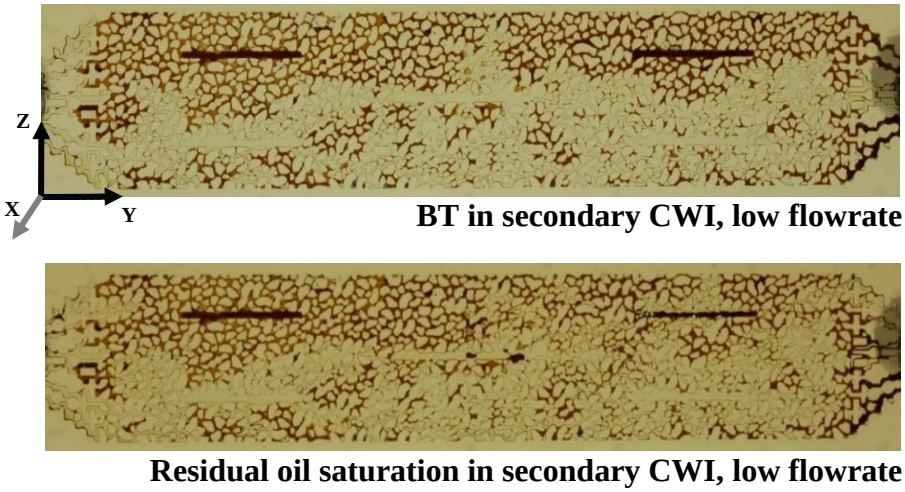

Figure 5–34: BT and S_{or} in secondary CWI at 0.0008 ml/min in the horizontal fracture micromodel

Table 5-5: RF at different flowrates in the horizontal fracture micromodel

Exp.	Rate (ml/min)	BT (PV)	RF (%) at BT	RF (%) (0.8 PV)	RF (%) (1PV)	RF (%) (1.2 PV)	RF (%) (2 PV)	RF (%) (3 PV)	RF (%) (7 PV)
SCWI	0.0024	0.34	38.6	40.5	40.5	40.7	40.6	40.8	42.3
SCWI^r	0.0024	0.37	36.7	39.4	40.7	40.8	40.9	41.0	43.6
SCWI	0.0008	0.30	33.5	34.8	34.8	34.9	35.0	35.0	39.5

SCWI: secondary CWI, ^{r}: replicate, BT: breakthrough, PV: pore volume, RF: oil recovery factor

5.5. Extended CWI

In secondary and tertiary CWI, there were areas in the upper and lower parts of the micromodel (homogeneous and heterogeneous) which were not displaced due to the effect of gravity and heterogeneity of the porous media. The recovery factor was low at different pore volumes due to an early breakthrough and the slow nature of CO_2 transfer from water to oil.

The solubility of CO_2 at this pressure and temperature is very low, so we decided to continue the injection for higher pore volumes. Extended injection of CWI in both secondary and tertiary CWI

was examined. The results of oil recovery in secondary CWI for homogeneous and heterogenous micromodels up to higher pore volume injections (10 PV for homogenous and 17.1 PV for heterogeneous micromodels) showed that longer injection was beneficial in continuous oil recovery due to a greater CO_2 transfer from the carbonated water phase to the oil phase.

In the homogeneous micromodel, a higher flowrate of 0.004 ml/min was continued up to 10 PV which resulted in an additional recovery factor of 9%. In the heterogenous micromodel with horizontal fractures, a lower flow rate of 0.0008 ml/min showed a different displacement pattern from 7 PV to 17.1 PV compared to a higher flowrate of 0.0024 ml/min. The extended secondary CWI demonstrated the effectiveness of long-term CWI by an additional recovery of 4.4% within the lower flowrate scheme (0.0008 ml/min) in horizontal fractures, and 3.2% and 10.1% within the higher flowrate scheme (0.0024 ml/min) for horizontal fracture and vertical fracture micromodels, respectively. The presence of vertical fractures caused the carbonated water stream to displace the center part of the micromodel. Hence from 7 PV to 17.1 PV injection, the displaced area started widening along the vertical line (Figure 5-35).

Although in general, by-passed zones in secondary CWI are fewer than in water flooding, some local by-passed zones were observed in both secondary and tertiary CWI schemes. In the horizontal fracture micromodel, extended CWI injection with the lower flowrate of 0.0008 ml/min improved the displacement pattern and resulted in fewer by-passed zones compared to the higher flowrate of 0.0024 ml/min. This difference in oil displacement pattern in both secondary and tertiary CWI schemes illustrated the competing interactions between fractures and gravity force in fluid flow pattern and vertical sweep efficiency.

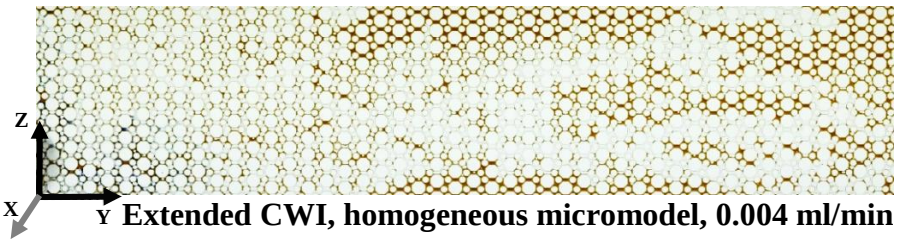

10 PV,
RF=57.5%

Extended CWI, homogeneous micromodel, 0.004 ml/min

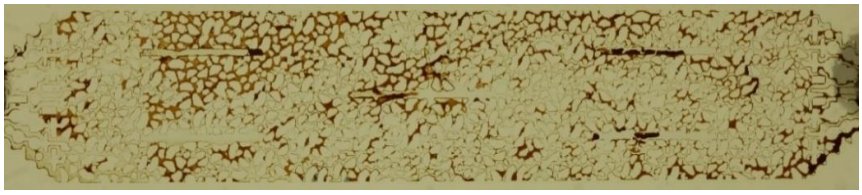

17.1 PV,
RF=43.9%

Extended CWI, horizontal fractures, 0.0008 ml/min

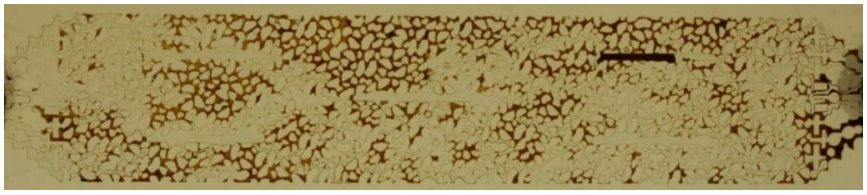

17.1 PV,
RF=45.5%

Extended CWI, horizontal fractures, 0.0024 ml/min

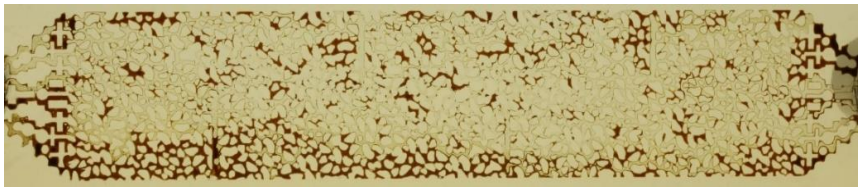

17.1 PV,
RF=59.0%

Extended CWI, vertical fractures, 0.0024 ml/min

Figure 5–35: Extended secondary CWI in the homogeneous and heterogeneous micromodels

The CO_2 transfer, presence of fractures, and gravity force were competing with each other to change the oil saturation. In tertiary CWI, as soon as carbonated water (white) mixed with the water phase (dark blue), and the water in-place started to change color, the CO_2 transfer mechanism was activated, and CO_2 interacted with the oil. Extended injection of carbonated water was helpful to recover the trapped oil (in fractures and matrix). The oil droplets preferred to join to each other and move forward to the fracture. There were flooded parts which never received CO_2 because the tackle water stream was cut off from the main CO_2 streams. This event prevented some parts of the trapped oil from being recovered by carbonated water in tertiary CWI. The horizontal fractures

left more by-passed zones compared to vertical fractures even after 17.1 PV injection (Figure 5-36). The ultimate recovery factor of 58.3 ± 0.04% at 10 PV for the homogeneous micromodel, and 42.2 ± 0.08% and 68.1 ± 0.03% at 17.1 PV were obtained for the horizontal fractures and vertical fracture micromodels, respectively.

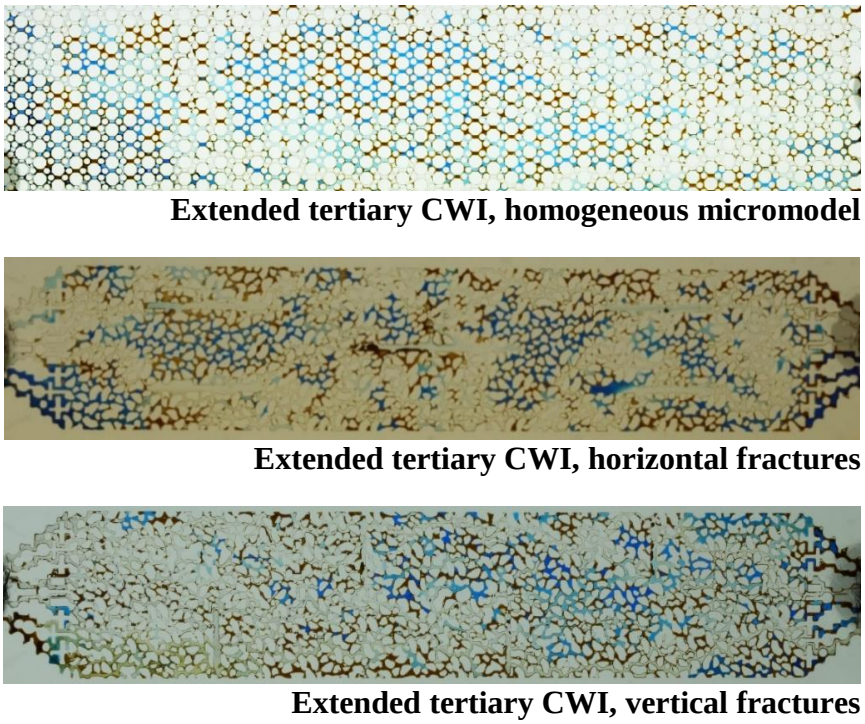

Figure 5–36: Extended tertiary CWI in the homogeneous and heterogeneous micromodels

5.6. Mechanism Study

Micromodel studies ae an excellent tool for examining the pore-scale mechanisms of oil recovery in a porous medium. In this study, mechanisms in simple water flooding, and secondary and tertiary CWI were monitored. Note that in the following figures, the oil phase is brown, the water is dark blue, the carbonated water phase is white, and the diluted water by carbonated water is light blue. There are several mechanisms causing oil trapping in water flooding and secondary CWI. The oil trapping mechanisms in the flooded zones are function of fluid and rock properties and their interactions. In my experiment, the main event that occurred was oil trapping in throats, dead-

ends, and pore bodies mainly in the form of by-passed oil in the small pore bodies and narrow throats. This is because of the size of the pore bodies and throats, where a throat is smaller than a pore body, a higher capillary pressure is built in the pore body as the injected fluid (water or CW) enters into the throats, which is shown in Figure 5-37. However, in the secondary CWI, the saturation of trapped oil in narrow throat was less than that in water flooding. Because the interfacial tension between oil and water decreases in the presence of CO_2 (Yang et al., 2004).

Interfacial tension between oil and displacing fluid plays an important role in recovering the trapped oil. Interfacial reduction causes an increase in capillary number by orders of magnitude, which enhances the oil recovery significantly. Honarvar et al., (2017) studied the interfacial tension between carbonated water and oil at different temperatures and pressures using an oil sample with 31.6 ºAPI and a brine with salinity of 35,079 ppm. The IFT of oil/brine and oil/carbonated brine were obtained to be 17.12 and 12.17 mN/m at 1,000 psi (6.9 MPa) and 178 °F (81°C). The results showed that increasing the temperature from 40 to 100°C and increasing the pressure from 1,000 to 2,500 psi (6.9 to 17.2 MPa) reduced the IFT between oil and carbonated brine. By increasing temperature, the IFT between carbonated brine and oil changed from 16.59 to 10.37 mN/m. And by increasing the pressure, the IFT between the same carbonated brine and oil reduced from 12.71 to 10.64 mN/m. Although the micromodels were water-wet, the capillary pressure between the water and oil in narrow throats was high and therefore the majority of the water phase flowed on the wall of larger pores and snap-off occurred (Blunt, 1998; Lenormand et al., 1983; Roof, 1970). Laidlaw and Wardlaw (1983), Lenormand, et al. (1983), and Roof (1970) reported that snap-off occurred in the porous media with aspect ratios (Pore radius to throat radius) of 1.5, 2.0, 2.3, and 3.65. Considering the aspect ratio ranging 1.65 to 3.08 in the current study, the snap-off oil trapping

mechanism occurred. This was visually captured and is shown in Figure 5-38. However, snap-off was less visible in the secondary CWI due to the ability of carbonated water to overcome the interfacial tension in narrow pores and throats. Hence, the carbonated water distributed evenly in most of the pore and throat. It should be noted that the connectivity between the carbonated water strings was stronger than that between the water strings. Nevertheless, the carbonated water solution maintained its continuity within pore bodies and necks and displaced the oil under the influence of displacement by capillary pressure.

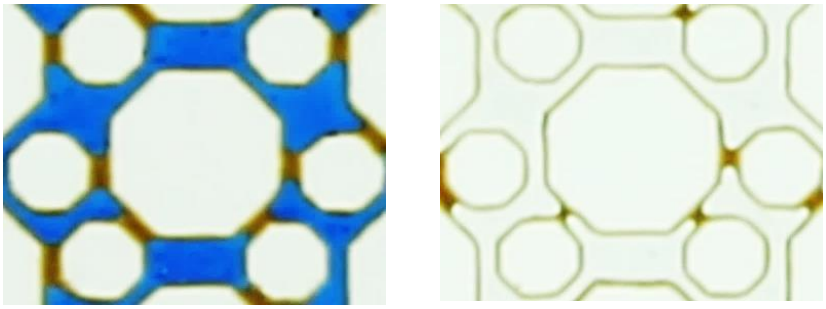

a) trapped oil in narrow throats in at the end of water flooding (7 PV)

b) trapped oil in narrow throats at the end of secondary CWI (7 PV)

Figure 5–37: Pore phenomena in narrow throats during, (a) WF and (b) secondary CWI

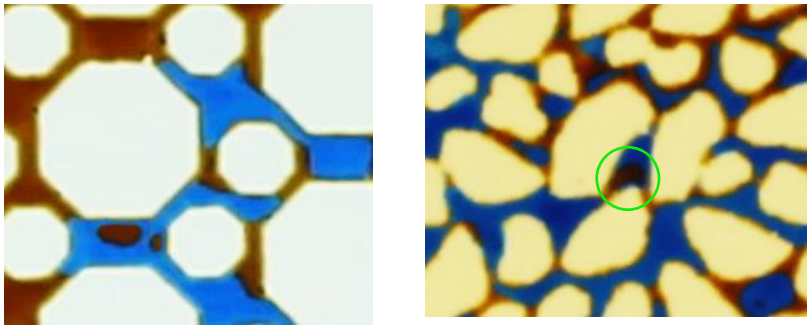

a) snap-off phenomenon at the end of water flooding (7 PV)

b) trapped oil in dead-end at the end of water flooding (7 PV)

Figure 5–38: Pore mechanisms in WF and secondary CWI, (a) snap-off and (b) dead-end

Oil trapping in dead-ends was another common trapping mechanism that was observed (Figure 5-39). Although the higher capillary pressure in dead-ends also caused oil trapping in dead-ends in both water flooding and secondary CWI, the lower interfacial tension between oil and carbonated water improved dead-end oil recovery (Figure 5-39). After breakthrough, it was easier for the

carbonated water stream to diffuse into narrow throats and dead-end pores. Figure 5-39 (a-c) depicts the sequences of a trapped oil extraction in a dead-end. By continuing injection, the tongue of the carbonated water phase entered into the dead-end and deformed the trapped oil ganglia at 3 PV. The deformation of oil ganglia was continued by carbonated water and was displaced at 17.1 PV. Figure 5-39 (a'-c') is another example of dead-end oil extraction by secondary CWI at the same pore volume injections.

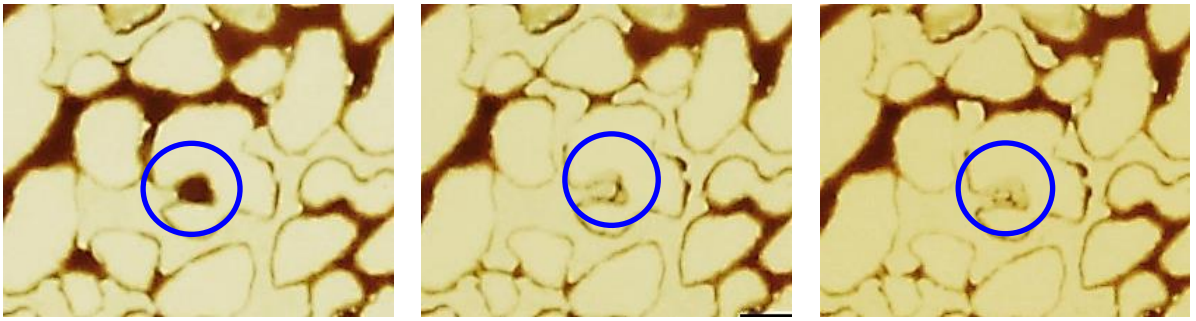

a) 0.28 PV | b) 3 PV | c) end of extended secondary CWI (17.1 PV)

a') 0.28 PV | b) 3 PV | c') end of extended secondary CWI (17.1 PV)

Figure 5–39: Oil extraction from a dead-end pore during secondary CWI (two examples)

In some parts of the porous media, oil covered the surface of the grains. However, by continuing the injection, the thickness of the oil film surrounding the grain was gradually disappeared due to the dissolution of CO_2 in the oil. The dissolution of CO_2 in oil resulted in lower interfacial tension between oil and carbonated water and also reduced the oil viscosity (from 6.82 cP to 6.23 cP, discussed in section 2.3.4), which are the most likely reasons for the observation for the reduction

of oil film saturation (Figure 5-40). It should be noted that, the micromodel was fabricated from soda lime glass plates, the glass micromodels are normally water-wet. However, it was believed that due to different stages in fabrication processes including laser engraving and chemical etching, the wettability of the glass in some parts may change from water-wet to intermediate or oil-wet. The effect of roughness on the wettability of the glass is important (Martinez, 2002; Yoshimitsu et al., 2002). Experiments on the roughness of silicon dioxide (the main component of soda lime glass) shows that as a surface is made rougher it will be more repellent to water (Soeno et al., 2004). It should be noted that in my experiments, there is no connate water saturation. Although the micromodels were cleaned by alcohol, toluene, and acetone after fabrication and each test, some part of the porous media remained intermediate-wet which might be due to the roughness and impurity of the glass in some parts.

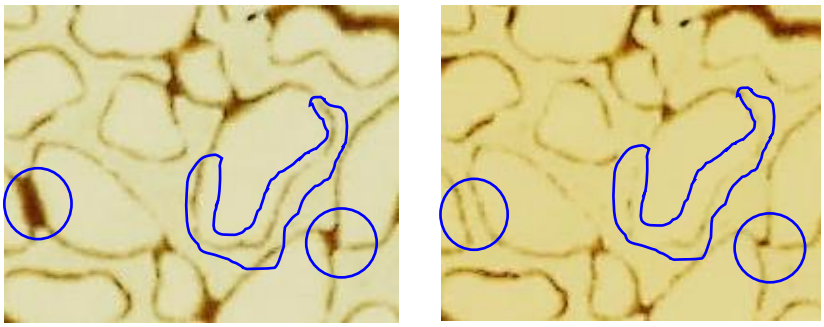

a) 0.34 PV b) 17.1 PV

Figure 5–40: Oil removal around grains during secondary CWI

CWI is an immiscible process, and diffusion of CO_2 from the water phase to the oil phase is the principal mechanism for recovering oil from dead-ends (Riazi et al., 2011). We believe that oil viscosity and interfacial tension reduction due to CO_2 diffusion in oil might be the main mechanisms behind the reduced residual oil saturation. By an overall overview of the entire micromodel in water flooding, it was determined that there was not a large number of full displaced pore and neighbor throats which confirmed the poor sweep microscopic efficiency of the water

flooding. However, as is shown in Figure 5-41, the final stage of secondary CWI after 7 PV which frequently took place in different parts of the micromodel, full displacement occurred. In other words, carbonated water removed oil from the walls of pores and throats which enhanced the microscopic recovery factor.

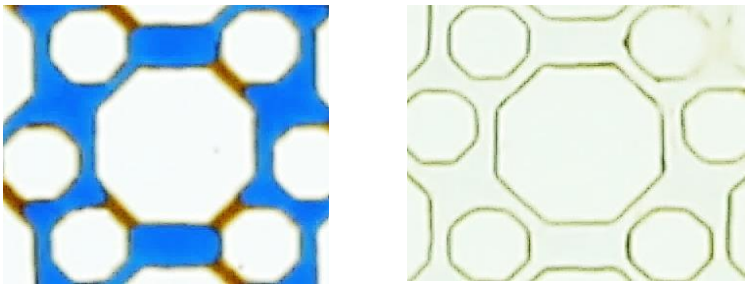

a) ultimate displacement by WF b) ultimate displacement by SCWI

Figure 5–41: Pore phenomena during WF and secondary CWI after 7 PV, oil (brown), white-hexagonal (grain), and blue (water)

In tertiary CWI, initially, water was flooded into the micromodel which caused both oil displacement and oil trapping in pore bodies and throats. Afterwards, the injection of the carbonated water began, the color of water in-place started to change from dark blue to light blue. By mixing water and carbonated water, the concentration of CO_2 in water in-place started to increase. However, the pore-scale oil saturation did not vary, because we believe that the dilution-mixing of rich phase CO_2 (carbonated water) and poor phase CO_2 (water) is a prior mechanism to the solubility of CO_2 in oil. In tertiary CWI, water acted as a barrier for CO_2 transfer from the carbonated water phase to the oil phase. As soon as the concentration of CO_2 in the pre-water flooded zones increased, the mechanisms of oil recovery were activated. In other words, CO_2 could reach the interface of water and oil and then transfer into the oil phase. The solubility of CO_2 in oil is responsible for oil swelling, and oil viscosity reduction. These mechanisms also assist with oil displacement and remobilization (Riazi et al., 2011). Figure 5-42 shows the oil recovery by tertiary CWI in pre-displaced area by water. We believe that oil redistribution might be the main

mechanism that took place during the tertiary CWI. It should be mentioned that for recovering all the trapped oil, a long-term CWI was required, which was discussed in section 5.5.

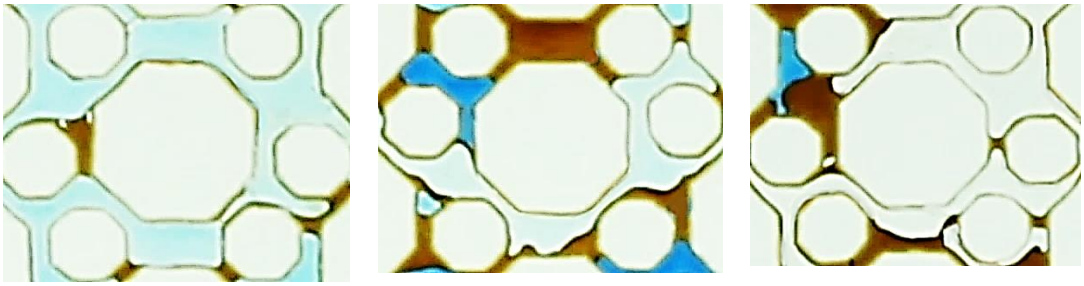

a) water dilution by CW (2.12 PV)

b) trapped water droplet in throats and pore bodies (3 PV)

c) oil removal around the grains by by CW (7 PV)

Figure 5–42: Pore phenomena in tertiary CWI, oil (brown), white-hexagonal (grain), white (CW), and light blue (diluted water with CW)

In water flooding, the presence of fractures led to an uneven distribution of the water phase in the matrix from a macroscopic point of view (discussed in section 5.2.3.2) which caused low microscopic displacement efficiency. The presence of fractures influences the flow of fluids in a reservoir. Fractures have high permeability which causes low differential pressure based on Darcy's formula at a constant flowrate. Fractures carry most of the water, and therefore reduce the buildup of large differential pressures across the porous media. As already discussed in this thesis, fractures (especially horizontal fractures) created an easy path for the injected water to displace the oil and move it toward the production port which resulted in an early breakthrough. However, due to the difference in the nature of water and oil with respect to viscosity (high viscosity ratio), water caused some trapped oil to remain in fractures as well as in the matrix (Figure 5-43).

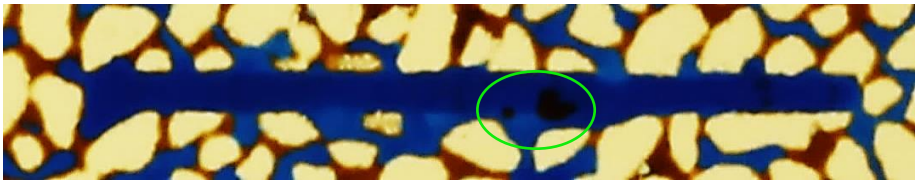

Figure 5–43: Trapped oil in a fracture after water flooding (3PV)

Although secondary CWI displaced most of the oil in fractures due to high permeability and viscous displacement, oil trapping occurred from the inlet to the middle body of the fracture (Figure 5-45). Contrary to water flooding, the main mechanism in solvent injection is diffusion than only viscous displacement (Da Silva and Belery, 1989; Das and Butler, 1998). By starting the step of carbonated water injection, the trapped oil ganglia started to spread out and remobilize. Dilution of oil continued due to CO_2 transfer to the oil from carbonated water phase It was believed that the solubility of CO_2 in oil caused oil swelling ($\delta_{CO2-oil} = 0.096$ mol CO_2/mol oil compared to $\delta_{CO2-water} = 0.0128$ mol CO_2/mol water, and swelling factor =1.003) which resulted in oil viscosity reduction and finally oil sweeping. Figure 5-44 shows how the ganglions A and B, and C began to be diluted and transformed to stretched droplets. Thereafter, carbonated water stream in the fracture helped the trapped oil to be remobilized and produced from the fracture. The oil remobilization took place in the fracture, due to the oil ganglion surrounded by a big source of CO_2 from carbonated water.

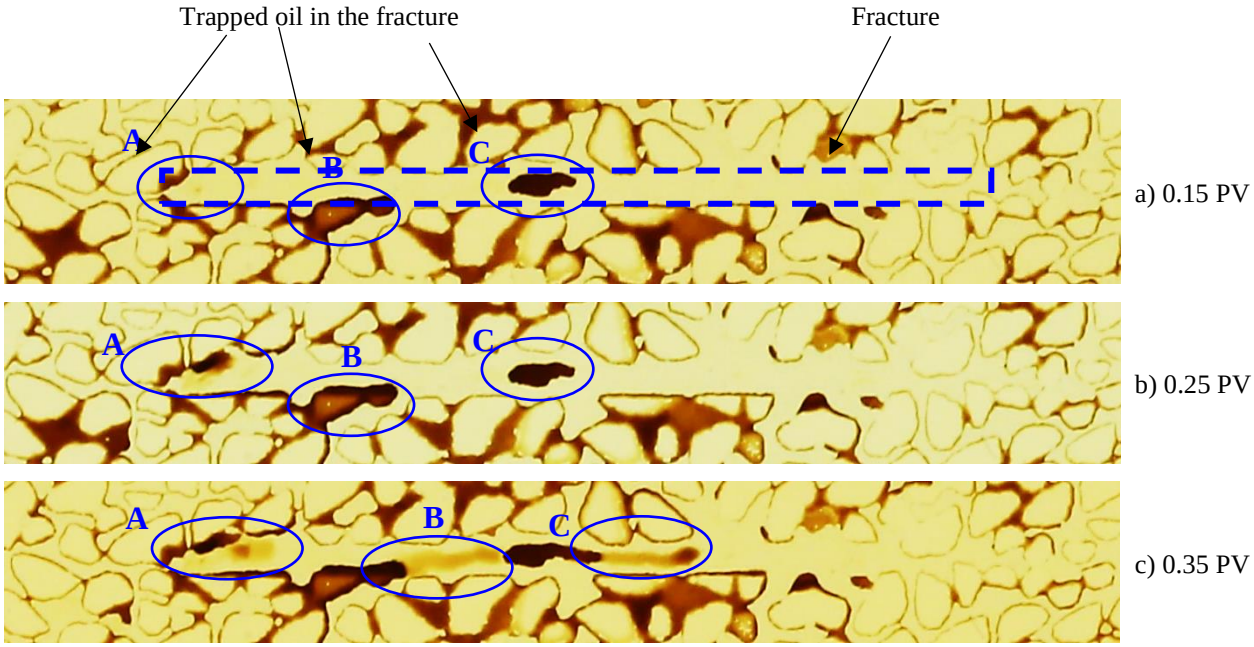

Figure 5–44: Trapped oil recovery in a fracture during secondary CWI

It was found that fractures (highlighted by the blue lines) play an important role in oil displacement in a fractured porous media (Figure 5-45). It was shown that the fractures play an important role in collecting and transporting oil to matrix. Fluid flow moved towards the fractures due to the high permeability of fractures. The water or carbonated water and oil moved from matrix pores upstream of the fracture into the fracture and outward into the matrix again downstream of the fracture. The oil from different pores appeared to accumulate in the fracture entering the porous matrix again (Figure 5-45 a-c and Figure 5-45 d-i).

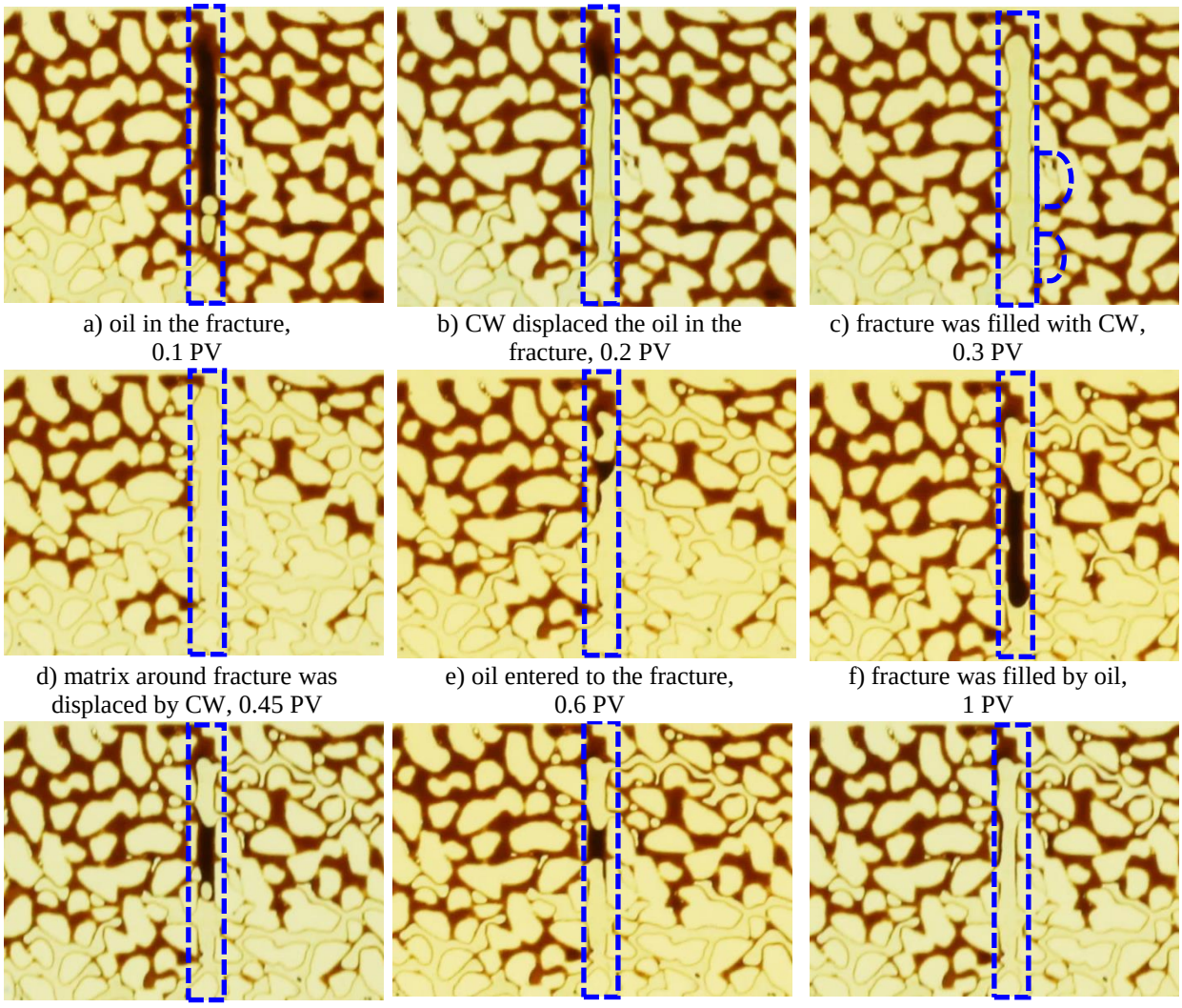

a) oil in the fracture, 0.1 PV

b) CW displaced the oil in the fracture, 0.2 PV

c) fracture was filled with CW, 0.3 PV

d) matrix around fracture was displaced by CW, 0.45 PV

e) oil entered to the fracture, 0.6 PV

f) fracture was filled by oil, 1 PV

g) oil left the fracture, 1.2 PV

h) saturation of oil was continuously decreased in the fracture, 2 PV

i) fracture was filled by CW, 2.4 PV

Figure 5–45: Fracture conduction during secondary CWI

In tertiary CWI in the heterogeneous fracture micromodel, the concentration of CO_2 was increased in the water by continuing injection of carbonated water. When the content of CO_2 in the oil phase increased as the fluid inside the fracture changed to completely white, the oil viscosity lowered and because the system was under flow, the CO_2 rich oil phase was displaced by the continuous carbonated water stream. Figure 5-46 represents the matrix-fracture interaction during tertiary CWI. As was illustrated, the residual oil around the fracture was in the form of trapped oil in pore bodies and throats. As long as water (blue) was mixed with carbonated water phase and changed to lighter blue, the saturation of oil around fractures was diminished (follow the green circle).

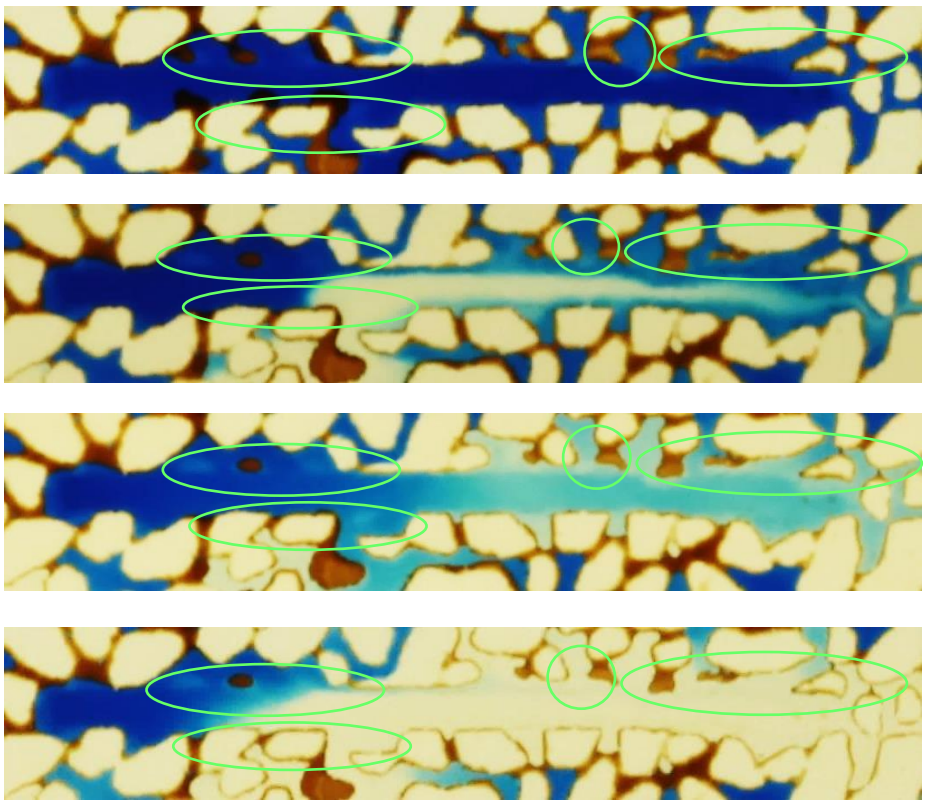

a) 2 PV, end of water flooding

b) 4 PV injection including 2 PV, CW

c) 8 PV injection including 6 PV, CW

d) 17.1 PV injection including 15.1 PV CW

Figure 5–46: The matrix-fracture interaction during tertiary CWI

5.7. Summary of CWI Experiments in Micromodels

The main objective of this study was to discuss and answer the following research question: ***what is the effect of CWI, as an EOR method, on oil production and vertical oil displacement in both homogeneous and heterogeneous porous media*****?**

The effect of gravity on water flooding in the homogeneous and heterogeneous micromodels showed that the presence of fractures in porous media impacted the effect of gravity on fluid flow patterns and caused an increase in the numbers of un-swept zones. The effect of gravity was neglected in the horizontally-oriented micromodel, which helped water to distribute all over the porous media.

The results of recovery factor for water flooding at BT, 1 PV, and 7 PV in the horizontally (without gravity) and vertically (with gravity) -oriented homogeneous, horizontal fracture, and vertical fracture micromodels are depicted in Figure 5-47. The comparison of the recovery factor profile from BT to 1 PV and then to 7 PV for all three patterns (homogeneous, horizontal and vertical fracture) shows that the higher recovery factor occurs in horizontal flooding compared to vertical flooding. For example, at BT, a higher recovery factor of 37.1 ± 0.04%, 34.3 ± 0.05%, and 38.6 ± 0.1% were achieved in horizontally-oriented micromodels compared to 29.4 ± 0.02%, 32.1 ± 0.03%, and 25.2 ± 0.08% in vertically-oriented micromodels for homogeneous, horizontal fracture, and vertical fracture patterns, respectively.

Monitoring the oil saturation profiles at 1 PV revealed that the same increasing trend of recovery factor was observed in horizontal flooding compared to vertical flooding (41.3 ± 0.03% vs 32.7 ±

0.05% in homogeneous, 37.6 ± 0.04% vs 33.0 ± 0.07% in horizontal fracture, and 43.6 ± 0.02% vs 33.0 ± 0.03% in vertical fracture micromodels).

A higher ultimate oil recovery factor of 42.7 ± 0.02%, 38.6 ± 0.08%, and 43.7 ± 0.1% were achieved in horizontally-oriented micromodel compared to 36.2 ± 0.03%, 36.3 ± 0.04%, and 38.8 ± 0.08% in vertically-oriented micromodels for homogeneous, horizontal fracture, and vertical fracture patterns, respectively.

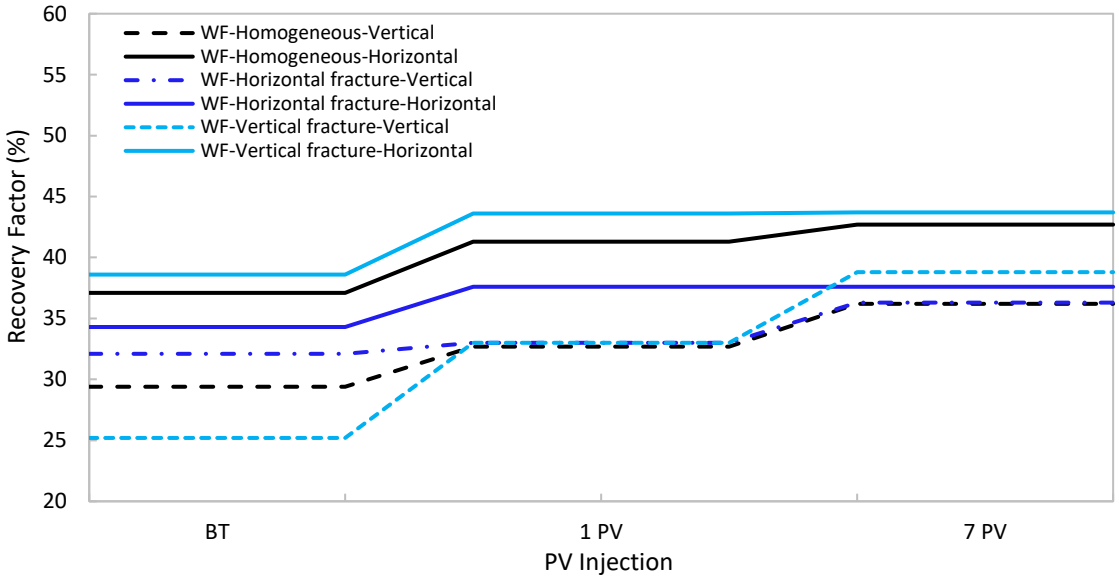

Figure 5–47: RF of WF in vertical and horizontal flooding; effect of gravity

The effect of CWI (secondary and tertiary) compared to water flooding on the recovery factor in the homogeneous and heterogeneous micromodels showed that water breakthrough in secondary CWI took a little longer. For example, 0.3 PV in WF compared to 0.32 PV in secondary CWI for the homogeneous micromodel and 0.31 PV in WF compared to 0.34 PV in secondary CWI for the horizontal fracture micromodel. Another example was the value measured at 0.24 PV in water flooding and 0.37 PV in secondary CWI for the vertical fracture micromodel.

Figure 5-48 illustrates the comparison of different scheme (water flooding, secondary and tertiary CWI) in homogeneous, horizontal fracture, and vertical fracture patterns. The change in recovery factor from BT to 1 PV for all the patterns showed that the highest change (25.2 ± 0.08% to 33.0 ± 0.06%) occurred in the vertical fracture micromodel compared to homogeneous (29.4 ± 0.02% to 32.7 ± 0.05%) and horizontal fracture (32.1 ± 0.03% to 33.0 ± 0.04%) micromodels.

In the homogeneous micromodel, the ultimate recovery factor changed for water flooding (29.4 ± 0.02% to 36.2 ± 0.03%) compared to secondary CWI (34.2 ± 0.04% to 53.0 ± 0.02%) from BT to 7 PV. In the horizontal fracture micromodel, the recovery factor changed (32.1 ± 0.03% to 36.3 ± 0.04%) for water flooding and secondary CWI (38.6 ± 0.04% to 42.3 ± 0.02%) from breakthrough to 7 PV, respectively. In the vertical fracture micromodel, the recovery factor changed from breakthrough to 7 PV for water flooding (25.2 ± 0.08% to 38.8 ± 0.08%) and secondary CWI (38.1 ± 0.06% to 48.9 ± 0.07%), respectively.

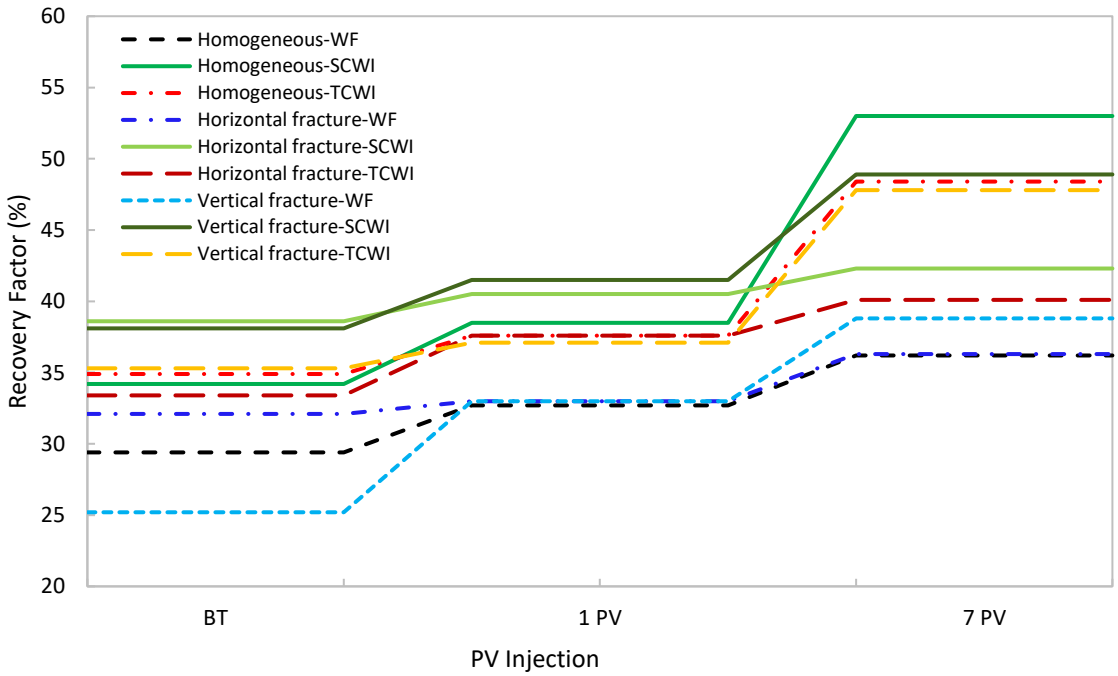

Figure 5–48: RF of WF in vertical and horizontal flooding; effect of scheme

In tertiary CWI, it was observed that there was a significant difference between recovery factors at breakthrough and 7 PV injections for simple water flooding and secondary CWI in both horizontal and vertical fracture patterns. This evidence demonstrated that fractures caused an unstable displacement which resulted in a difference between recovery factor at breakthrough and 7 PV. As soon as full saturation occurred in the fracture, the local oil distribution in the matrix was observed between fractures. There were un-swept areas due to the effect of gravity and heterogeneity of the porous media. When compared to horizontal fractures, the presence of vertical fractures helped the carbonated water to improve the vertical sweep efficiency of secondary CWI. It was believed that the solubility of CO_2 in oil caused oil swelling ($\delta_{CO2-oil}$ = 0.096 mol CO_2/mol oil and swelling factor =1.003) as well as oil viscosity reduction (6.82 cP to 6.23 cP). Oil remobilization in a fractured porous media was the main factor that helped to displace the oil toward production in tertiary CWI. Although the amount od CO_2 was low at micromodel experimental conditions, longer injection of carbonated water resulted in higher CO_2 transfer from water to oil phase and improve the displacement efficiency.

Secondary CWI at two flowrates of 0.004 and 0.0024 ml/min was conducted in homogeneous and horizontal fracture micromodels, respectively. In the homogeneous micromodel, with a flowrate of 0.004 ml/min, breakthrough occurred earlier at 0.28 PV compared to the scheme with a flowrate of 0.0008 ml/min, where breakthrough occurred at 0.32 PV. In contrast, in the horizontal fracture micromodel, breakthrough occurred earlier (0.32 PV) at a lower flowrate of 0.0008 ml/min compared to that (0.34 PV) with the higher flowrate of 0.0024 ml/min, respectively.

The results of recovery factor for secondary CWI at BT, 1 PV, and 7 PV are depicted in Figure 5-49. The recovery factor changed from 34.2 ± 0.04% to 38.5% ± 0.03 at 0.0008 ml/min compared to 27.4 ± 0.03% to 32.8 ± 0.05% at 0.004 ml/min in the homogeneous pattern from BT to 1 PV. The results illustrated that in the horizontal fracture micromodel, the change in recovery factor from BT to 1 PV at lower flowrate of 0.0008 ml/min (33.5 ± 0.07% to 34.6 ± 0.08%) was less than that at higher flowrate of 0.004/min (38.6 ± 0.04% to 40.5% ± 0.02).

In the homogeneous micromodel, the ultimate recovery factors of 53.0 ± 0.02% and 47.1 ± 0.05% were obtained for 0.0008 ml/min and 0.004 ml/min, respectively. In the horizontal fracture micromodel, the ultimate recovery factors of 39.8 ± 0.06% and 42.3 ± 0.07% were achieved for 0.0008 ml/min and 0.0024 ml/min, respectively. In comparison to the homogeneous micromodel, a higher flowrate may be more beneficial to recover the by-passed zones.

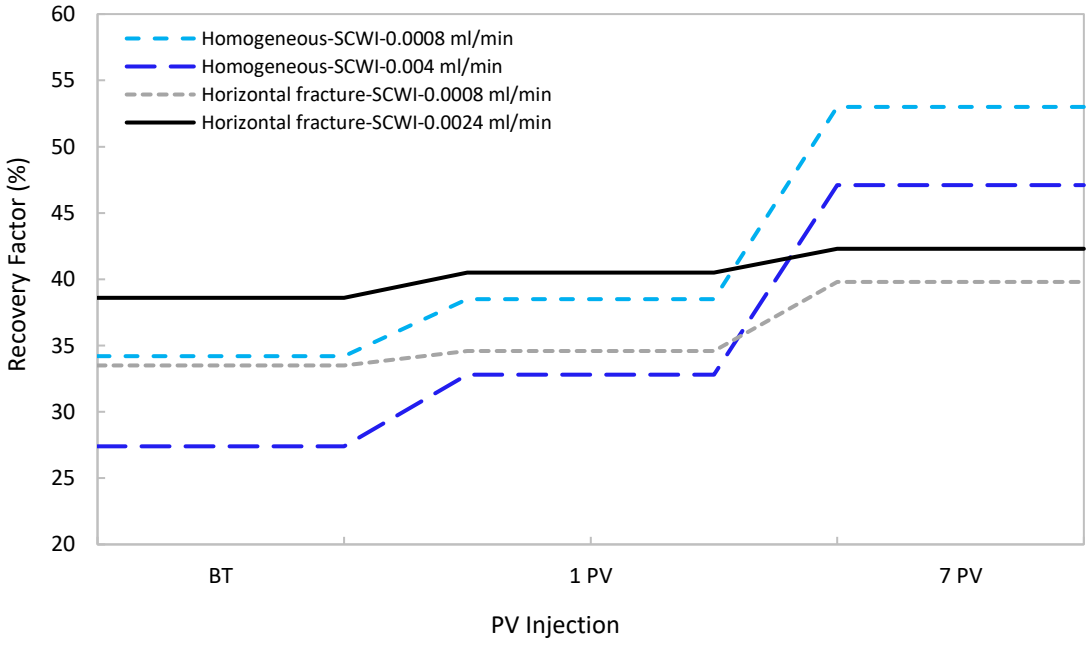

Figure 5–49: RF of WF in vertical and horizontal flooding; effect of flowrate

The extended injection of CWI in both secondary and tertiary CWI was examined in the homogeneous micromodel, which resulted in a 9.0% additional recovery factor. Extended secondary CWI demonstrated the effectiveness of long-term CWI by an additional recovery of 4.4% with the lower flowrate of 0.0008 ml/min in the horizontal fractures, and 3.2% and 10.1% with the higher flowrate of 0.0024 ml/min for the horizontal fracture and vertical fracture micromodels, respectively. The extended injection of carbonated water was helpful in recovering the trapped oil (in fractures and matrix). The horizontal fractures left more by-passed zones compared to the vertical fractures even at 17.1 PV injection. The ultimate recovery factor of 58.3 ± 0.04% at 10 PV for the homogeneous micromodel, and 42.2 ± 0.08% and 68.1 ± 0.03% at 17.1 PV were obtained for horizontal fracture and vertical fracture micromodels, respectively.

The calculation of SSE (sum of square of errors) based on the replicated experiments showed 0.42, 2.60 for water flooding in homogeneous and vertical fracture micromodel experiments. Additionally, SSE for secondary CWI were calculated to be 1.62, 1.99, and 2.47 for the homogeneous, horizontal fracture, and vertical fracture micromodel experiments. Table 5-6 summarizes the results of the micromodel experiments. The quantity of SSE shows that in the homogeneous micromodel experiments, the results were more in agreement with each other. In the heterogeneous micromodels, SSE is higher than homogeneous micromodel which might be due to the effect of heterogeneity of the porous media that determines the fluid flow displacement efficiency.

Table 5-6: Summary of the homogeneous, and horizontal and vertical fracture micromodel experiments

Exp.	ORT	Rate (ml/min)	BT (PV)	RF (%) at BT	RF (%) (0.8 PV)	RF (%) (1 PV)	RF (%) (1.2 PV)	RF (%) (2 PV)	RF (%) (3 PV)	RF (%) (7 PV)
Homogeneous-WF										
WF	V	0.0008	0.30	29.4	32.3	32.7	33.4	33.9	35.7	36.2
WF^r	V	0.0008	0.28	29.5	32.1	32.8	33.5	34.1	34.6	35.6
WF	H	0.0008	0.35	37.1	40.0	41.3	41.4	42.5	42.5	42.7
Heterogenous-Horizontal Fracture-WF										
WF	V	0.0024	0.31	32.1	32.9	33.0	33.1	33.3	33.3	36.3
WF	H	0.0024	0.36	34.3	37.3	37.6	37.6	37.6	37.6	37.6
Heterogenous-Vertical Fracture-WF										
WF	V	0.0024	0.24	25.2	30.0	33.0	33.7	35.4	36.6	38.8
WF^r	V	0.0024	0.27	27.3	32.2	33.6	34.0	35.2	37.4	39.0
WF	H	0.0024	0.35	38.6	43.6	43.6	43.6	43.7	43.7	43.7
Homogeneous-SCWI										
SCWI	V	0.0008	0.32	34.2	36.7	38.5	40.7	42.4	49.3	53.0
SCWI^r	V	0.0008	0.31	33.5	35.8	39.7	39.8	43.6	50.0	52.0
SCWI	H	0.0008	0.46	43.6	46.0	46.6	47.2	48.5	51.4	53.2
SCWI	V	0.004	0.28	27.4	31.3	32.8	33.3	38.5	38.6	47.1
Heterogenous-Horizontal Fracture-SCWI										
SCWI	V	0.0008	0.32	33.5	34.8	34.6	34.8	34.9	35.0	39.8
SCWI	V	0.0024	0.34	38.6	40.5	40.5	40.5	40.6	40.8	42.3
SCWI^r	V	0.0024	0.37	36.7	38.9	40.6	40.7	40.7	41.0	43.6
SCWI	H	0.0024	0.47	47.7	55.4	57.0	58.4	62.3	65.2	67.6
SCWI^r	H	0.0024	0.48	45.7	53.8	54.8	57.7	61.1	62.3	66.3
Heterogenous-Vertical Fracture-SCWI										
SCWI	V	0.0024	0.37	38.1	40.5	41.5	41.8	42.6	42.9	48.9
SCWI^r	V	0.0024	0.35	35.0	38.9	41.5	41.8	42.6	43.5	50.5
SCWI	H	0.0024	0.44	40.0	41.9	42.0	43.6	44.4	50.8	57.0

Homogeneous-TCWI								
TCWI	V	0.0008	1.7	At the end of WF (1.5) and 0.2 CW, 1.7 PV, RF=34.9%	40.2	42.9	43.8	48.4
Heterogenous-Horizontal Fracture-TCWI								
TCWI	V	0.0024	2.12	At the end of WF (2 PV) and 0.12 CW, 2.12 PV, RF=33.4%	37.6	37.8	38.6	40.1
Heterogenous-Vertical Fracture-TCWI								
TCWI	V	0.0024	2.12	At the end of WF (2 PV) and 0.12 CW, 2.12 PV, RF=35.3%	37.1	40.4	42.8	47.8

WF: water flooding, SCWI: secondary CWI, TCWI: tertiary CWI, ^{r}: replicate, H: horizontal, V: vertical, BT: breakthrough, PV: pore volume, RF: oil recovery factor

5.8. Gravity Stable Scheme

In the gravity stable displacement, the micromodel was placed vertically. Injection of water/carbonated water began from the bottom side of the micromodel and oil was produced from the top side. Initially, the micromodel was saturated with oil and then injection pressure was gradually increased to 305 psi (2.1 MPa) and the production rate was at 0.0024 ml/min. Afterward, the flooding was performed up to 7 PV.

5.8.1. Simple Water Flooding

Figure 5-45 illustrates the simple water flooding in the gravity-stable orientation. It was observed that water displaced the oil upward and in a nearly stable pattern. Gravity stable displacement aided water flooding to move slowly and displaced the oil gradually. By continuing simple water flooding up to 0.4 PV, the water stream displaced the oil upward, however, the displaced area was limited to the center part of the micromodel and water was not able to distribute crosswise (Figure 5-45a). By continuing injection, the oil in the un-swept areas adjacent to the side walls of the micromodel were pushed upward. Although the injected water displaced the oil in the lower part of the micromodel, water fingers began to form in the upper part of the micromodel, resulting in breakthrough at 0.6 PV with a recovery factor of 60.3 ± 0.04% (Figure 5-45b). as well, gravity stable displacement gave a stable frontal displacement along the micromodel even after breakthrough. Therefore, a few by-passed zones were formed before breakthrough. Water injection continued up to 2 PV and a recovery factor of 68.8 ± 0.06% was obtained. More injection of water up to 7 PV did not change the recovery factor. It became clear that trapped oil was mostly in the form of local trapping in the pores and throats. There were zones next to the side walls of the micromodel that could not be recovered by more injection. However, recovery factor improved an additional of 8.5% after breakthrough.

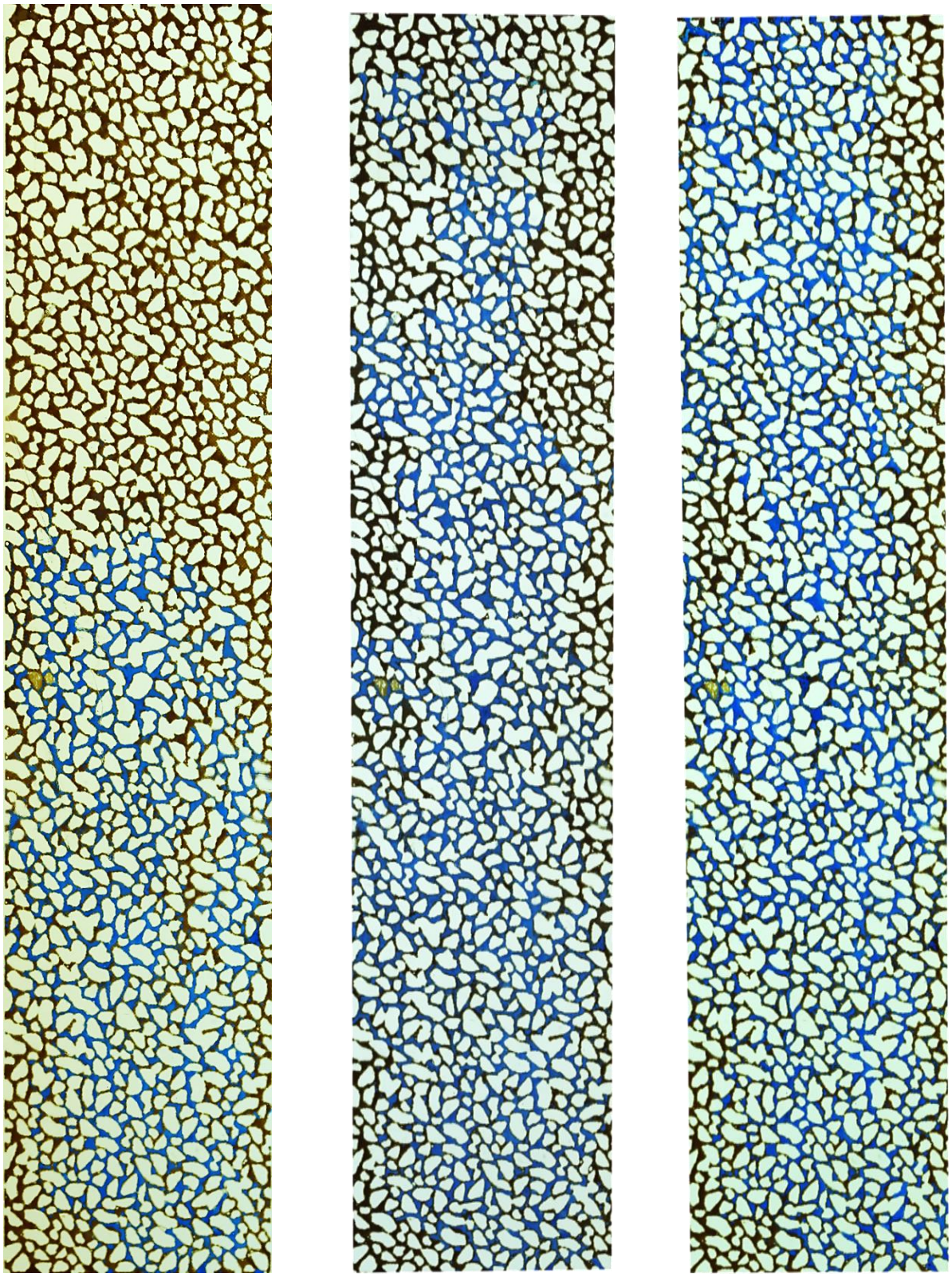

a) 0.4 PV, RF=44.2% b) 0.6 PV, BT, RF=60.3% c) 7 PV, RF=68.8%

Figure 5–50: Simple water flooding in gravity-stable orientation

5.8.2. Secondary CWI

Injection of carbonated water started from the bottom side of the micromodel and oil was produced from the top side. Carbonated water had a higher density of 1.003 g/cm^3 than oil, 0.877 g/cm^3. Carbonated water injection was performed up to 7 PV until no more oil production was observed. Different stages of flooding are displayed in Figure 5-46.

It was observed that carbonated water entered into the model across the bottom side and sweeping the oil very stably upward all over the displaced area. Controlled mobility and gravity effect reinforced the carbonated water phase to distribute evenly along the front. However, as observed in Figure 5-46a, the side wall effect began to appear at 0.4 PV. Along the frontal displacement, the un-swept oil adjacent to the side walls was mobilized and the oil saturation was reduced. Therefore, favorable oil displacement all around the carbonated water bank delayed the breakthrough to 0.69 PV resulting on oil recovery factor of 70.0 ± 0.04% (Figure 5-46b). CO_2 transfer from carbonated water to the oil phase improved the trapped oil extraction in pore-scale and dead-ends. Mobility control due to the dissolution of CO_2 in oil and reduced oil viscosity (from 4.50 cP to 3.76 cP) plus the effect of gravity provided a stable frontal displacement along the micromodel and resulted in a recovery factor of 72.6 ± 0.08% at 2 PV (Figure 5-46c). It was observed that, there was not any by-passed zones along the height of micromodel (Z-direction) resulting in an ultimate oil recovery factor of 79.1 ± 0.04% at 5 PV. Interaction of carbonated water with oil caused oil swelling and oil viscosity reduction, which removed the trapped oil from narrow pore bodies and throats.

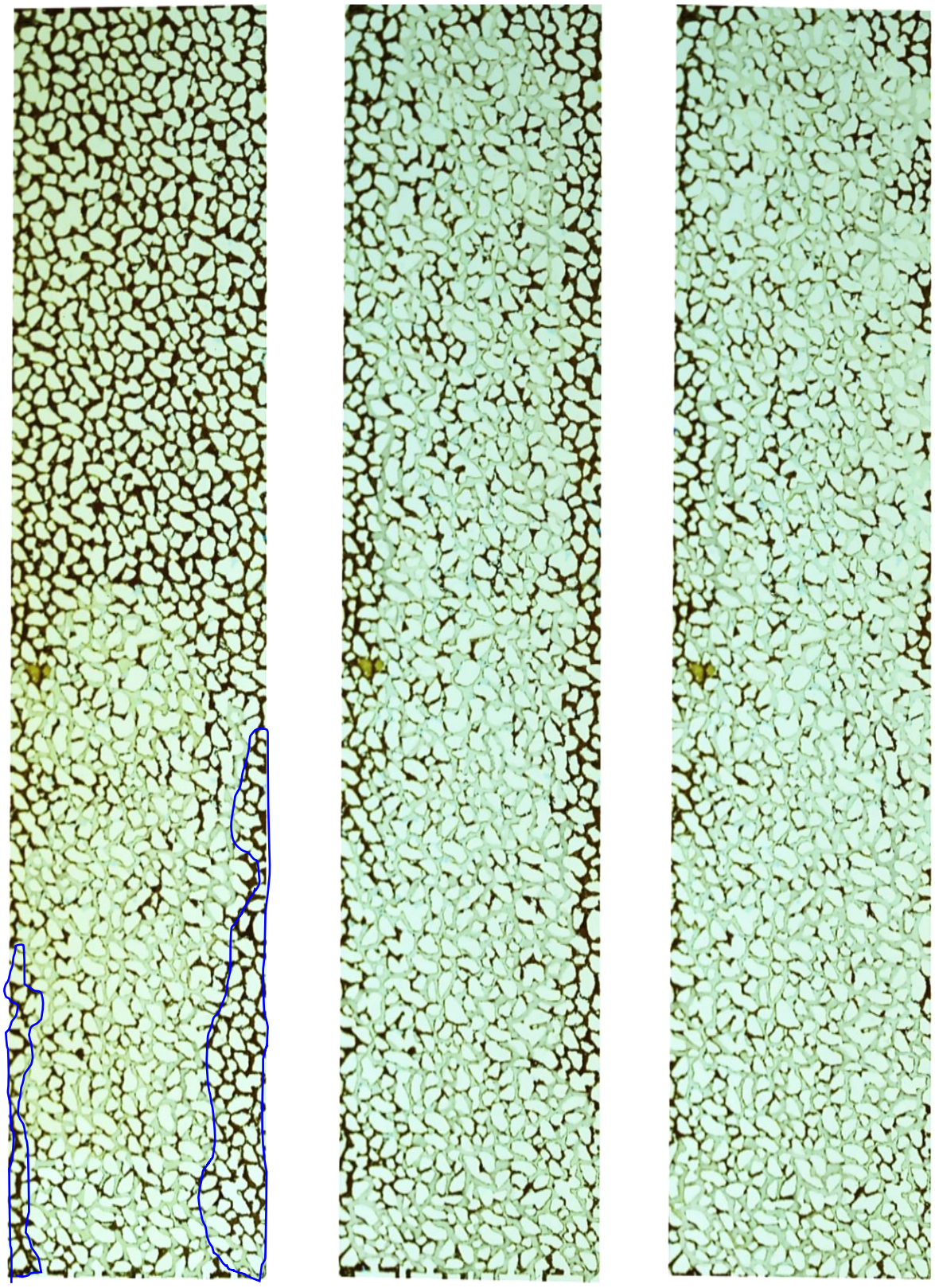

a) 0.4 PV, RF=42.4% b) 0.69 PV, BT, RF=70% c) 5 PV, RF=79.1%

Figure 5–51: Secondary CWI in gravity-stable orientation

Chapter 6 **Core Flooding Results and Simulation**

The chapter is based on a paper that was submitted as described below:

Carbonated Water Injection (CWI): Core-scale Study of CWI and its Application under Reservoir Conditions using a Light Oil Sample *(2018) is submitted, Journal of Industrial and Engineering Chemistry Research (ACS Publication), October, Mahdavi, S. and James, L.A.*

6.1. Overview

In this chapter, the result of carbonated water injection at the core-scale is reported. Offshore oil reservoirs in Eastern Canada have light oil with 22 to 36 °API and high permeability sandstone rocks (https://www.nr.gov.nl.ca/nr/invest/energy.html). Enhanced oil recovery (EOR) for offshore is challenging due to the cost of facilities and well modifications and constrained space. Despite the recent downturn in prices, the demand for oil continues to increase. To meet this demand, it is important that oil exploration and drilling continues, as current alternative energy sources are unable to fully replace fossil fuels. Newfoundland offshore fields are located 310 to 350 km off the coast. The availability of injection gas and transportation facilities required for EOR processes are limiting factors (Thomas, et al., 2010).

CO_2 captured from the electrically generated flue gas could be used in EOR techniques such as CWI, CO_2-WAG, or CO_2 enriched natural gas WAG where less CO_2 is necessary. CWI and CO_2-WAG are two EOR techniques that require less quantity of CO_2 and may be applicable in offshore reservoirs.

To comprehensively study the impact of CWI on the oil recovery factor, a series of core flooding experiments were designed. A mechanistic study of CWI in the presence of gravity (Chapter 5) demonstrated the ability of carbonated water to enhance oil recovery at 2.1 MPa (305 psi) and 21°C (69.8 °F). It was found that the sweep efficiency and trapped oil phase mobilization were affected by the carbonated water phase, which led to oil extraction from dead-ends and narrow throats. Typically, immobile disconnected oil is not recovered from narrow throats and pore bodies.

To investigate the impact of CWI on oil recovery at local reservoir conditions, core flooding experiments were designed at 85°C (185 °F) and 31 MPa (4,500 psi) using Cleveland Berea sandstone cores. Four schemes including seawater flooding, secondary CWI, tertiary CWI, and CO_2-WAG were studied in a vertically-oriented core holder. Two of the experiments were replicated. The density of the dead crude oil was 0.877 g/cm^3 and the viscosity was 6.82 cP at ambient conditions and 4.5 at experimental conditions. Seawater flooding was performed using seawater from the Atlantic Ocean (35,987 ppm salinity). Carbonated water was prepared using seawater, which is practical for offshore field. The solubility of CO_2 in seawater was measured to be 0.0188 mol CO_2/mol H_2O (details of setup and preparation in section 4.2.1)

The results of the core flooding experiments were simulated using a compositional model built in CMG-GEM™ (Computer Modeling Group Limited, Canada, version 2014.10). The model was constructed to mimic the core flooding experiments.

6.2. Core Flooding Experiments

The core flooding experiments give a more realistic indication of the amount of additional oil that can be recovered for the EOR method of choice. Table 6-1 summarizes the experimental design.

Table 6-1: Core flooding experimental design

Experiment	Rock	L (cm)	D (cm)	Porosity (%)	PV (ml)	Permeability (mD)	S_{wc}
Seawater flooding	Sandstone, Berea	9.80	3.0	20.0	14.5	380.6	0.27
Secondary CWI		10.88	3.0	22.0	16.9	381.6	0.28
Tertiary CWI		11.80	3.0	21.2	17.4	314.3	0.32
CO_2-WAG		10.88	3.0	19.5	15.0	360.3	0.30

L: length, D: diameter, PV: pore volume, and S_{wc}: connate water saturation

In this section, the experimental results of seawater flooding, secondary carbonated seawater injection (SCWI), Tertiary carbonated seawater injection (TCWI), and CO_2-WAG schemes are presented. The experiments were carried out at a pressure and temperature of 31 MPa (4,500 psi) and 85°C (185 °F), respectively to mimic one of the offshore NL conditions. After placing the core sample in the core holder and setting the back pressure to 31 MPa (4,500 psi), the temperature of the oven was increased step by step. When the temperature was stabilized at 85°C, the oil injection flowrate and the overburden pressure were gradually raised. Although the core samples were at connate water saturation, we initially performed oil flooding to raise the pressure of the system to the operating pressure condition (4,500 psi). After stabilizing the differential pressure to 1.58 psi (0.01 MPa) at the flowrate of 0.2 ml/min, the system was ready to start each of the flooding experiments. The flowrate of 0.2 ml/min was selected based on Darcy's flow (1 ft/day) with a corresponding capillary number of 3.5×10^{-6} (section 4.4.3).

The recovery factor, water-oil ratio (WOR), gas-oil ratio (GOR), and differential pressure for each flooding experiment were measured and shown in the following figures. The presented recovery

factor and cumulative WOR were obtained using the volumes of water to oil determined by a graduated cylinder, and the amount of gas to calculate the GOR was quantified by a gasometer (discussed in Chapter 4). Differential pressure between the inlet and the outlet of the core was recorded during each experiment by two pressure transducers.

The results of core flooding experiments are depicted in Figure 6-1. In seawater flooding, the breakthrough occurred at 0.39 PV resulting in a recovery factor of 47.1 ± 1.3% (average of three replicates by WF, and tertiary CWI and CO_2-WAG). The high permeability of the sandstone core samples might be the reason for an early breakthrough (Bailey et al., 2000), which in this experiment was 380.6 mD. Another reason for an early breakthrough could be large permeability contrast in sandstone rocks. A series of experiments on comparing CO_2 injection in chalk (porosity, 40 to 48% and permeability, 6.5 mD) and sandstone (porosity, 20 to 25% and permeability, 600 to 900) rock samples at experimental conditions of 9 to 14 MPa and 50 to 80ºC was conducted by Hamouda and Alipour Tabrizi (2013). A lower recovery factor of 38 to 52% for the sandstone was found compared to 45 to 60% for the chalk due to higher permeability contrast in the sandstone rock sample.

As observed, the breakthrough for secondary CWI occurred at 0.45 PV with a recovery factor of 50.4 ± 1.4%. Secondary CWI recovered more oil compared to simple water flooding for the same pore volume injection. In water flooding, oil recovery continued to increase after breakthrough to reach 59.7 ± 0.6% at 1.08 PV. The recovery factor at 1 PV for secondary CWI was 68.1 ± 0.6%. In secondary CWI, the increase in oil recovery continued up to 4.25 PV which resulted in a recovery factor of 74.8 ± 1.2%. Carbonated water injection was continued to 8 PV for observation.

The higher recovery factor of secondary CWI compared to seawater flooding might be due to late breakthrough and reduced viscosity of the oil from 4.50 cP to 3.76 cP under the CO_2 solubility in oil which was obtained 0.448 mol CO_2/mol oil (0.076 g CO_2/g oil and swelling factor, 1.162 cm^3/cm^3) at 85°C and 31 MPa. It should be mentioned that CO_2 solubility in seawater was measured to be 0.0188 mol CO_2/mol seawater (0.0459 g CO_2/g seawater) as was discussed in section 4.2.1.1. The reduced oil viscosity improves the mobility of oil causing piston-like displacement. Gravity stable recovery displacement (vertical core) and the homogeneous sandstone rock sample controlled the stable displacement during flooding. Viscosity of the carbonated seawater (0.438 cP) compared to seawater (0.364 cP) at 85°C and 31 MPa (4,500 psi) helped improve the displacement.

CO_2 solubility in oil is higher than water and seawater (Rojas and Farouq Ali, 1988; Mosavat et al., 2014). Hence, CWI is injected and comes in contact with the oil, the CO_2 partitions into the oil. The partitioning coefficient for CO_2 between seawater and oil was calculated using CMG-WinProp to be 29.3 (% mol CO_2 in oil/% mol CO_2 in seawater) using the mole fraction of CO_2 in oil and seawater at the experimental conditions.

It was found that seawater flooding and secondary CWI ended up with the oil recovery factors of 59.7 ± 0.6% and 74.8 ± 1.2%, respectively. This shows that secondary CWI significantly improved the recovery factor. The differential pressure dropped when the breakthrough took place. As oil production continued, the pressure of the system dropped. Secondary CWI showed a lower pressure drop compared to seawater flooding. The maximum pressure drop during secondary CWI was 9.35 psi while it was 9.90 psi for seawater flooding. The differential pressure increased until breakthrough as there was a two-phase flow of water and oil progressing in the core and an increase

in water saturation. The pressure drop was reduced after breakthrough as the water reached the outlet of the core and continued to decline until oil production was stabilized. The differential pressure in the secondary CWI was less than that in the seawater flooding due to CO_2 transfer from the carbonated seawater to the oil and viscosity reduction.

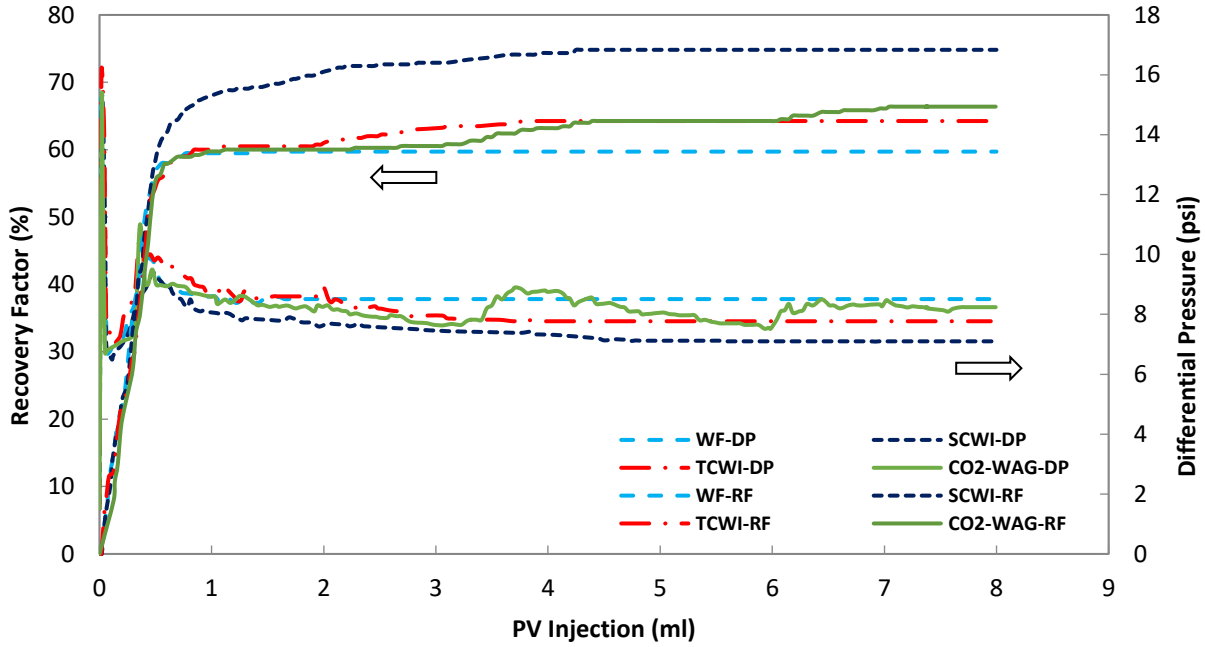

Figure 6–1: RF and DP of WF, and secondary and tertiary CWI, and CO_2-WAG

Table 6-2: Comparison of recovery factor at different pore volume

Test	BT (PV)	RF (BT)	RF (0.8 PV)	RF (1 PV)	RF (2 PV)	RF (3 PV)	RF (4 PV)	RF (8 PV)
Seawater flooding	0.39	47.1	58.5	59.4	59.7	59.7	59.7	59.7
Secondary CWI	0.45	50.4	66.4	68.1	71.5	72.9	74.3	74.8
Secondary CWI (r)	0.48	52.1	65.7	69.2	72.8	73.0	74.5	74.6
Tertiary CWI	0.39	45.5	59.1	60.5	61.7	63.2	64.2	64.2
CO_2-WAG	0.40	46.1	58.9	60.0	60.0	60.5	63.2	66.4

Tertiary CWI was performed in order to investigate the potential of CWI for enhancing oil recovery in a pre-water flooded reservoir. After setting up the core in the core holder and pressurizing the system, initially, the core was flooded with seawater (Atlantic seawater, 35,987

ppm) which resulted in 60.5% at 1 PV. As shown in Figure 6-1, after the injection of 2 PV of seawater, the recovery plateau was achieved and based on the seawater flooding experiment we knew that there would not be any more produced oil by increasing the injection pore volume. Subsequently, seawater flooding was stopped, and the injection of carbonated seawater was started with the same flowrate as seawater flooding (0.2 ml/min). Carbonated water was injected for 6 PV and an ultimate oil recovery of 64.2% was found compared to seawater flooding, 59.7%.

The differential pressure across the core indicated the maximum pressure difference of 10.5 psi at breakthrough and it reached 7.77 psi at 8 PV. CO_2 alternating water flooding (CO_2-WAG) was performed as a tertiary mode. It was carried out with a pre-water flooding stage (1.4 PV) to understand the application of CO_2-WAG in a pre-water flooded reservoir. The CO_2-WAG slug ratio of 1 PV water: 2 PV CO_2 and the WAG cycle of 2 was adopted after waterflooding. The reason for choosing this WAG slug ratio is because the recovery factor did not increase under water flooding after 1.4 PV, the higher quantity of CO_2 may be dissolved in both water-in-place and oil to recover the trapped oil. Different WAG cycle and WAG slug ratio has been suggested in literature. Although optimization of WAG parameters is required, in this work, we selected the WAG slug ratio of 1 PV water: 2 PV CO_2 to examine the effect WAG process.

The reason to select this WAG cycle was because the CO_2 cycle did not show a considerable increase in recovery factor and the plateau of recovery factor occurred, hence the injection was stopped after 2 cycle of water and CO_2 injection and also to be able to compare the results of different schemes (WF and CWI) up to 8 PV. In the WAG cycle, we selected the water flooding rate (0.2 ml/min) and the gas injection rate (0.06 ml/min): The former was selected as the same as

the flowrate value in the seawater flooding scheme, and the latter was calculated based on the amount of dissolved CO_2 in seawater (0.06 ml/min). The reason for choosing theses flowrates was because we wanted to compare the results of all schemes. Choosing the same injection flowrate for water cycle, automatically determined the gas injection flowrate. In the pre-water flooding stage, breakthrough was observed at 0.38 PV.

As is illustrated in Figure 6-2, the ultimate oil recovery of pre-seawater flooding in tertiary CO_2-WAG was obtained almost the same (60.0 ± 0.2%) at 1 PV and 1.4 PV and was succeeded by the CO_2 cycle. An additional 0.8% of oil was recovered during the first CO_2 injection cycle. In water flooding, oil is primarily trapped in large pores due to the water-wet nature of the core whereas in the first gas injection cycle the increase in the recovery factor was insignificant (Figure 6-2 and Table 6-2). However, the next cycle of water flooding increased the recovery factor from 60.8% to 63.8% and the trend of the first CO_2 cycle was replicated in the second one.

Figure 6-2 shows that oil production only occurred during the seawater cycle and not during the CO_2 cycle. This might be due to the role of CO_2 in the CO_2-WAG cycle, which created a more favorable mobility ratio through dissolution in oil. This also reduces the interfacial tension, thereby allowing the displacement of oil in small pore throats that are not accessible to seawater under normal circumstances after which seawater is used for sweeping and producing of oil (Righi, et al., 2004; Kulkarni and Rao, 2005). This then resulted in better microscopic displacement efficiency and a higher recovery factor. The ultimate oil recovery of CO_2-WAG approached to 66.4%. It should be noted that the ultimate recovery factor for secondary CWI, tertiary CWI, and water flooding was obtained to be 74.8%, 64.2%, and 59.7%, respectively.

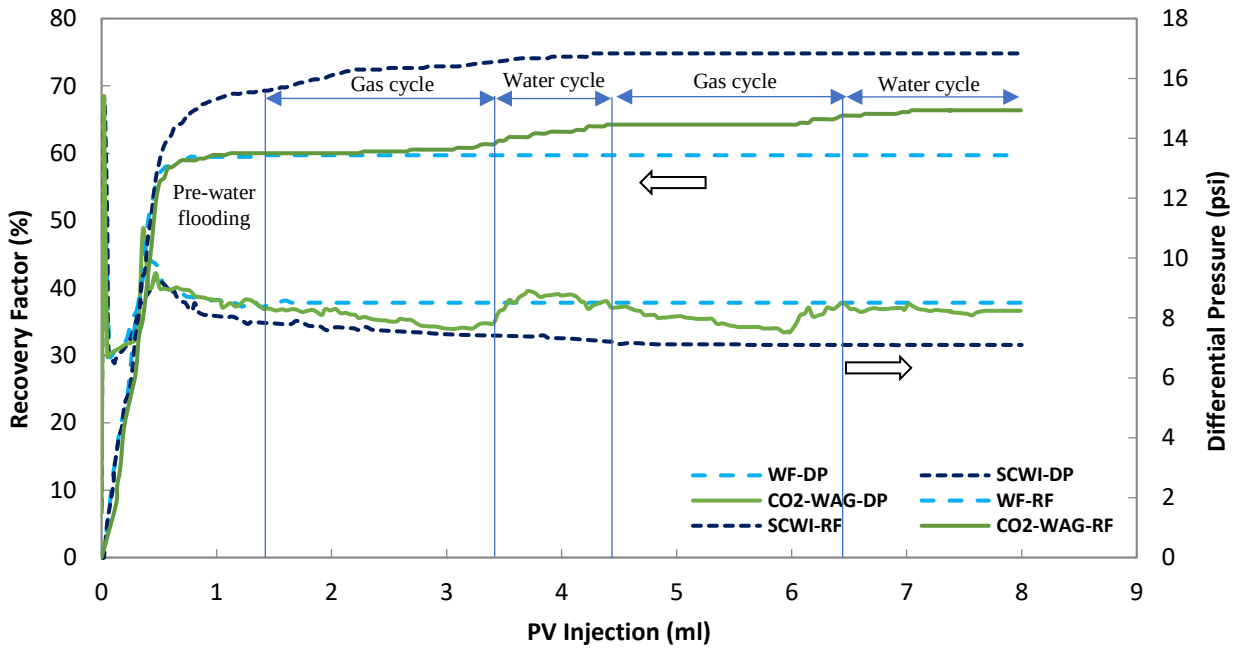

Figure 6–2: Results of recovery factor for water flooding (WF), secondary CWI, and CO_2-WAG

In each flooding experiment, the produced fluids after the core were directed to the back-pressure regulator into a high precision graduated cylinder and a gasometer. The presented cumulative WOR was obtained using determined volumes of water to oil from a graduated cylinder, and cumulative GOR was calculated using the amount of gas quantified by a gasometer (Figures 6-3 to 6-6).

The results of water to oil ratio and gas to oil ratio for all the schemes are described below. As is observed in Figures 6-3 and 6-4, water was produced after a period of oil production (zero water production) and water breakthrough occurred at 0.39 PV in the seawater flooding scheme compared to 0.45 PV in secondary CWI. Later water production in secondary CWI is due to CO_2 transfer from the carbonate water phase to the oil phase and reduced oil viscosity. The cumulative produced water in seawater flooding after 8 PV was 17.0 cm^3 compared to 15.2 cm^3 in secondary CWI.

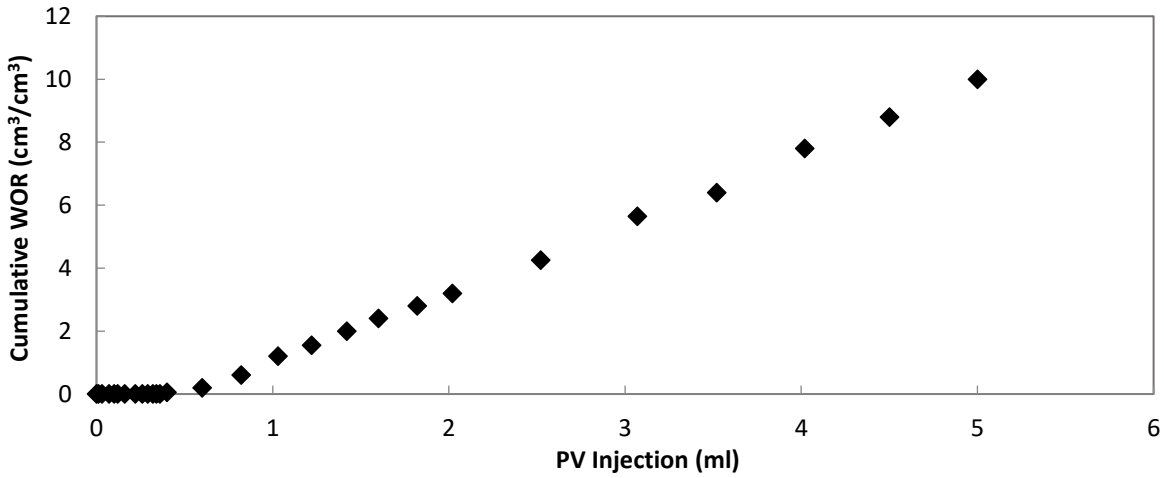

Figure 6–3: Experimental results of cumulative WOR for seawater flooding

Gas production for secondary and tertiary CWI processes are shown in Figures 6-4 and 6-5. As is depicted in Figure 6-4, there was not any produced gas until 0.52 PV in secondary CWI due to CO_2 transfer from the carbonated water phase to oil phase. It was believed that before gas breakthrough, the oil was getting saturated with CO_2 and most of the content of CO_2 in the water phase was transferred to the oil in place. Gas breakthrough in tertiary CWI occurred at 2.18 PV compared from the beginning of the experiment (2 PV seawater flooding and 0.18 carbonated water flooding).

In tertiary CWI, the gas breakthrough was observed earlier than in secondary CWI, because as was observed in micromodel experiments (Figures 5-24, 5-27, and 5-28, tertiary CWI in homogeneous and heterogeneous micromodels), the carbonated water stream is immediately mixed with water in place and moves forward to the production port. The water in place provided an easy path to take the CO_2 out of the porous media. The presence of water in place from the course of seawater flooding also tackled the carbonate water stream to be in contact with oil. Hence, the gas breakthrough in tertiary CWI occurred faster than secondary CWI. The volume of produced gas to

oil in secondary and tertiary CWI at ambient conditions (20ºC and 14.7 psi) was reached 535.0 cm^3 and 348.2 cm^3 at 8 PV injection.

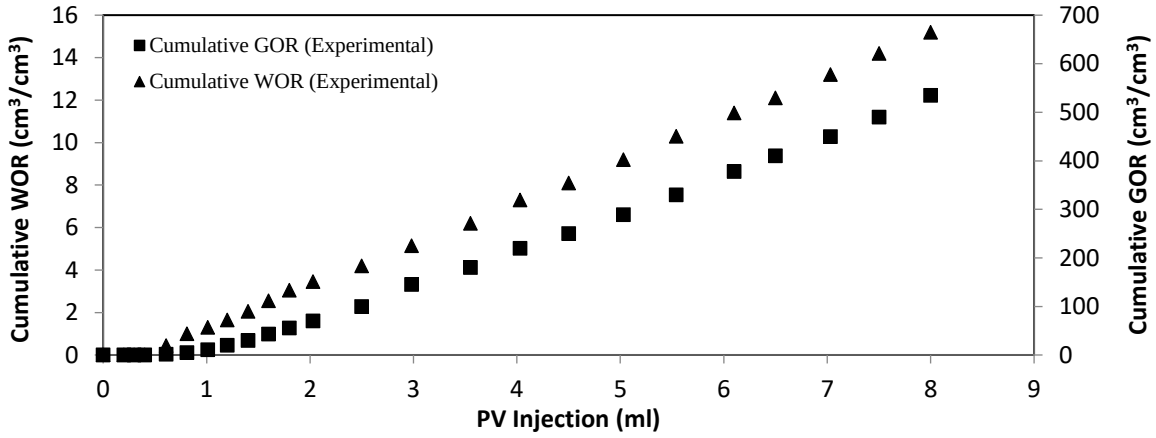

Figure 6–4: Experimental results of cumulative WOR and GOR for secondary CWI

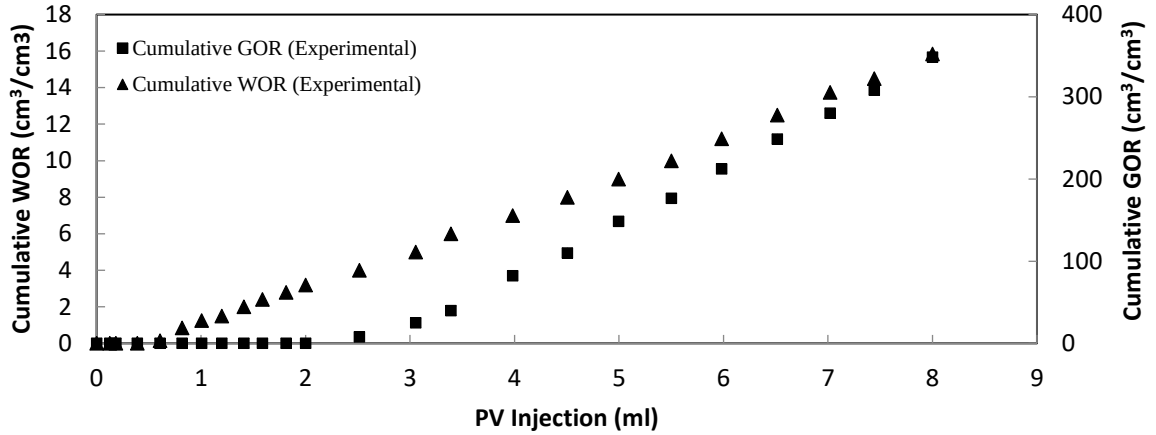

Figure 6–5: Experimental results of cumulative WOR and GOR for tertiary CWI

In CO_2-WAG, the water breakthrough was observed at 0.4 PV and production continued to increase until 1.4 PV, when the water flooding was stopped and gas cycle began for 2 PV. As is depicted in Figure 6-6, gas breakthrough occurred at 3.5 PV and the gas production continued to increase. However, the cumulative amount of gas increased very slowly. After the injection of 1 PV water from 3.4 PV to 4.4 PV, the second cycle of gas injection began for 2 PV until 6.4 PV. Following the GOR curve showed that gas injection was gradually produced up to 6.4 PV due to

possible gas dissolution in oil and water in place. Then GOR dramatically increased as the recovery curve showed no more oil production under gas injection cycle. The cumulative WOR and GOR were obtained 5.6 cm^3 and 253.0 cm^3, respectively.

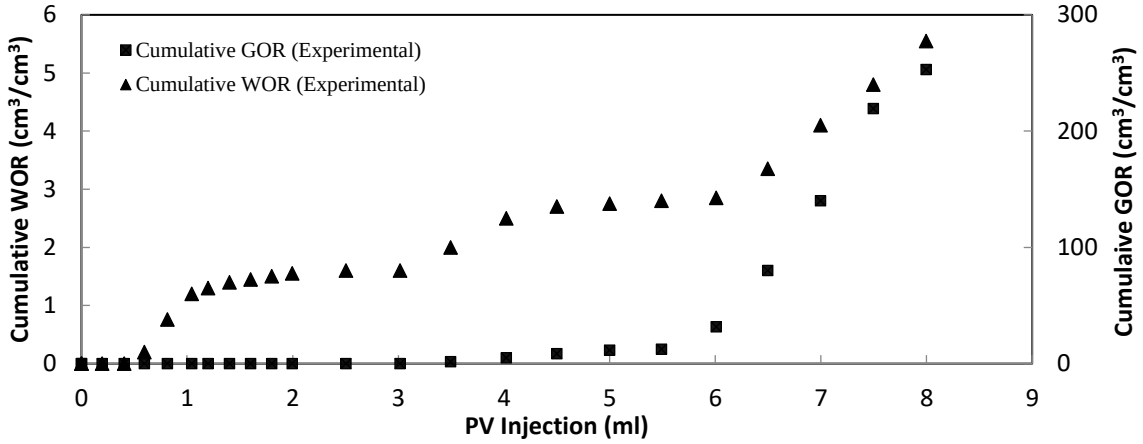

Figure 6–6: Experimental results of cumulative WOR and GOR for CO_2-WAG

The comparison of cumulative WOR and GOR for water flooding, secondary and tertiary CWI, and CO2-WAG are shown in Figures 6-7 and 6-8.

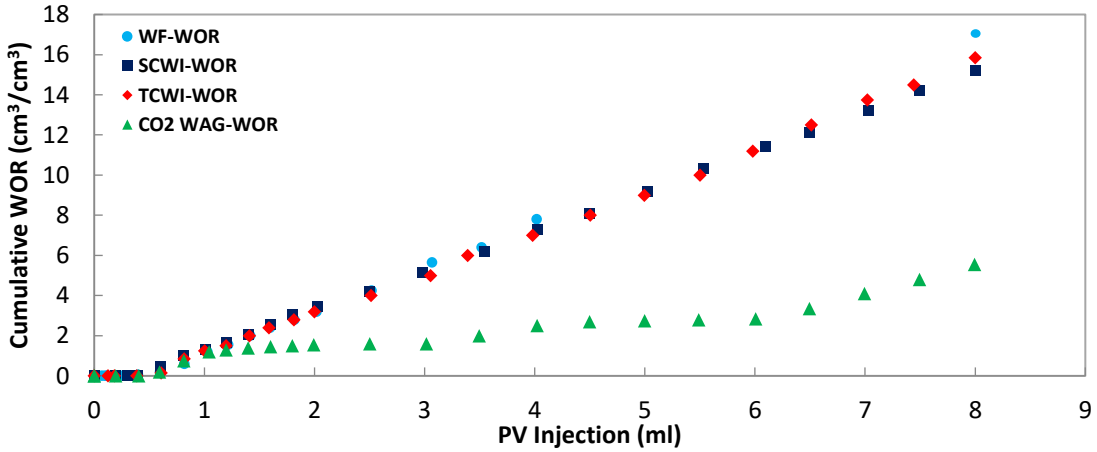

Figure 6–7: Comparison of cumulative WOR for WF, secondary and tertiary CWI, and CO_2-WAG

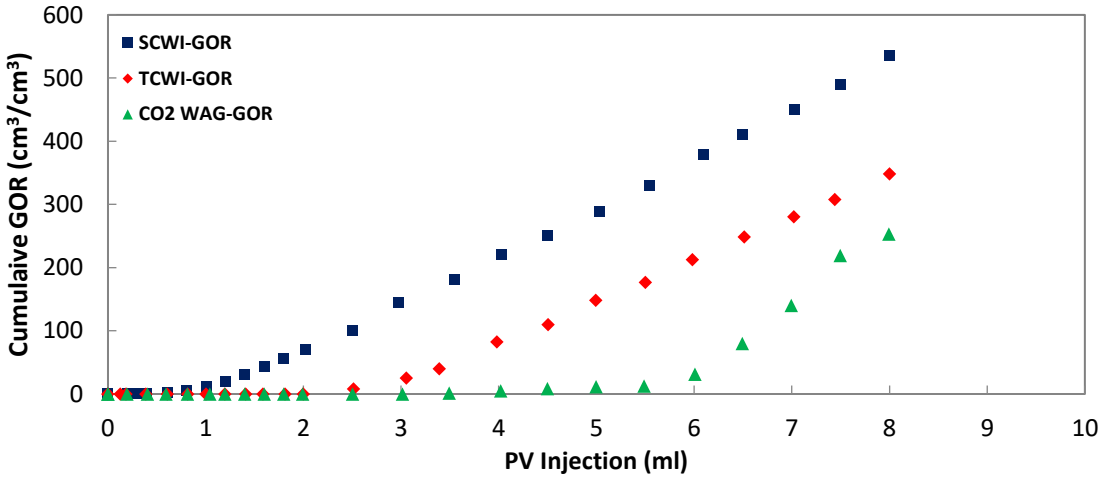

Figure 6–8: Comparison of cumulative GOR for secondary and tertiary CWI, and CO_2-WAG

6.3. Simulation Study

This section was carried out to assess the suitability of CWI to be implemented in improving oil recovery in a simulated sandstone core. Every simulation consisted of a fluid model to use an equation of state to predict the fluid behavior and a reservoir model to assign the rock properties. In this section, a simulation study of core flooding experiments is reported. The CMG simulator (computer modeling group) was described to simulate the simple seawater flooding, secondary CWI, tertiary CWI, and CO_2-WAG recovery processes at 85°C (185 °F) and 31 MPa (4,500 psi). The CMG-WinProp™ module was used to simulate the fluid model, and CMG-Builder™ was used to build the porous media model. The results of the reservoir model (fluid model and porous media model) were imported to the CMG-GEM™ compositional simulator to predict the core flooding experimental results.

6.3.1. Compositional Fluid Model

6.3.1.1. Fluid Model

In this study, CMG-WinProp™ was used to simulate the phase behavior and determine the PVT properties of dead oil, carbonated water, and carbonated seawater. A fluid model was built to identify the phase behavior of fluids. To match the fluid used experimentally, a light oil with the molecular weight of 257 g/mol, density of 0.877 g/cm^3, and viscosity of 6.82 cP, CO_2 as the injected gas, and seawater with the salinity of 35,987 ppm were used.

To build the fluid model, the Peng Robinson (PR) equation of state was selected to predict the phase behavior of liquids. It was developed to calculate liquid physical properties and was proven to be stronger than the Soave Redlich Kwang (SRK) equation in the prediction of liquid densities (Peng and Robinson, 1976). Note that the oil sample was a dead oil sample. To build a fluid model for a dead oil sample, the density, the viscosity, and the oil compositions are required (to build a live oil sample, the constant composition, the differential liberation, and the other PVT tests may be required to regress the results).

As shown in Table 6-3, the hydrocarbon analysis is from C6 to C30$^+$. It is very time consuming to simulate a reservoir model with 26 components is very time consuming especially in a compositional EOR process such as carbonated water injection. The initial calculated density of the oil sample was 0.745 g/cm^3. In order to modify the calculated density by an equation of state, a volume shift was added, which improved the density to 0.880 g/cm^3. However, this number still differed from the experimental value, 0.877 g/cm^3. After lumping, a fluid with 7 pseudo components was selected. Lumping was performed using the Whitson method (1983). The final density of 0.887 g/cm^3 was obtained with the pseudo components reported in Tables 6-3 and 6-4.

Table 6-3: Physical properties of pseudo components

Pseudo components	Mole (%)	P_c (atm)	T_c (k)	ω	MW (g/mol)	SG
C6-C8	7.78	29.507	564.689	0.34207	104.620	0.744
C9-C11	23.55	25.073	620.840	0.43515	133.327	0.781
C12-C15	22.84	19.995	689.843	0.57917	181.169	0.819
C16-C18	10.78	16.422	747.324	0.72053	235.631	0.849
C19-C22	10.12	14.202	786.408	0.83075	280.209	0.867
C23-C26	6.70	12.175	826.832	0.95070	329.209	0.886
C27-C30$^+$	18.21	8.659	1014.333	1.24648	584.226	0.979

Table 6-4: Table: Binary interaction coefficients between lumped components

	C6-C8	C9-C11	C12-C15	C16-C18	C19-C22	C23-C26	C27-C30$^+$
C6-C8	0.00000	0.00088	0.00449	0.00950	0.01415	0.01838	0.03289
C9-C11	0.00088	0.00000	0.00140	0.00462	0.00804	0.01132	0.02330
C12-C15	0.00449	0.00140	0.00000	0.00094	0.00275	0.00481	0.01346
C16-C18	0.00950	0.00462	0.00094	0.00000	0.00048	0.00150	0.00734
C19-C22	0.01415	0.00804	0.00275	0.00048	0.00000	0.00029	0.00410
C23-C26	0.01838	0.01132	0.00481	0.00150	0.00029	0.00000	0.00222
C27-C30$^+$	0.03289	0.02330	0.01346	0.00734	0.00410	0.00222	0.00000

There are three viscosity correlations in the CMG-WinProp^{TM} module; the Jossi, Stiel and Thodos (JST) model (Reid et al., 1977), the Pedersen corresponding state model (Pedersen et al. (1984)), and the Modified Pederson (Pedersen and Fredenslund, 1987). The JST model (Reid et al., 1977) is valid for low pressure mixtures and the Pederson et al. (1984) gives a better prediction for liquids, oil with light and medium specific gravity. The Modified Pedersen (1987) showed improved results for mixture viscosities up to 10 cP. Each model has a set of default coefficients, which may be modified during regression to match experimental viscosity data. In this study, the Modified Pederson correlation was selected. The initial estimation of viscosity using the default coefficient was reported to be 9.82 cP. By changing the coefficient of the correlation, the viscosity of 6.82 cP was obtained, which approximated the experimental data. Finally, the phase envelope of the crude oil sample was depicted: oil is single phase at 85°C and 31 MPa (Figure 6-9).

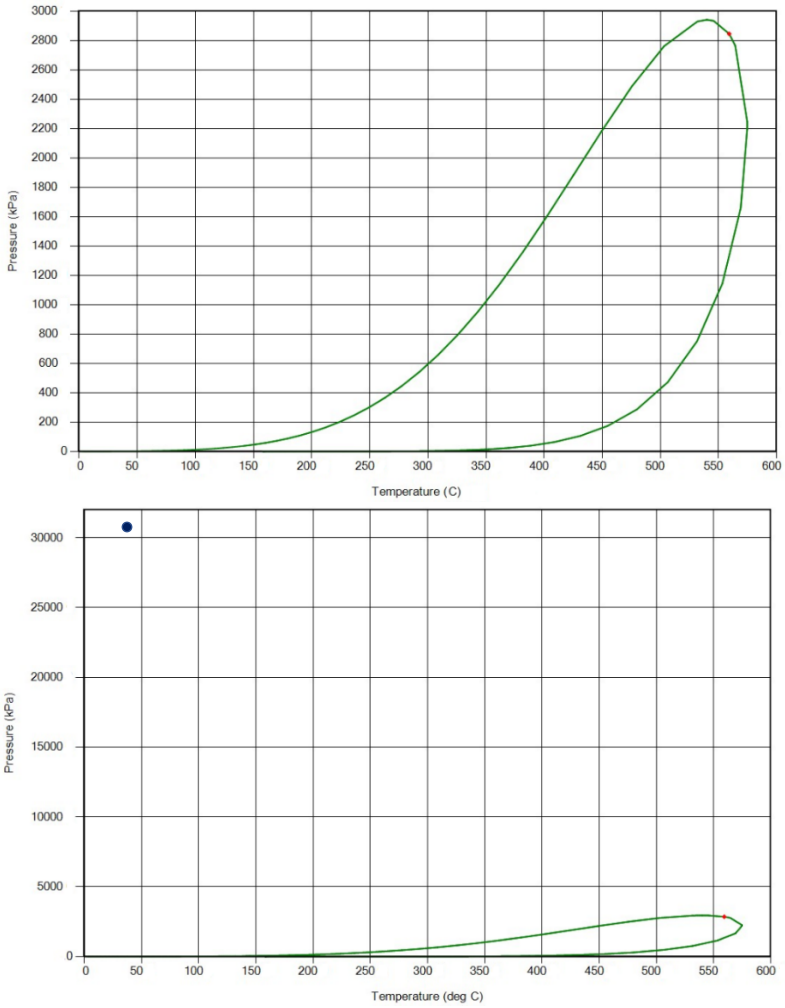

a)

b)

Figure 6–9: Phase envelope of the oil used in this study, a) 0 to 3 MPa and b) 0 to 34 MPa

6.3.1.2. Solubility Model

In this study, a solubility model using CMG-Win Prop™ and the compositional GEM simulator was selected to model the solubility of CO_2 in both the aqueous phases (water and seawater). A solubility model is required to simulate the solubility of gas in the processes that the injection phase is soluble in oil (e.g. CO_2). CMG-WinProp™ supports the calculation of solubility and the swelling factor of CO_2 and light hydrocarbons components in the aqueous phase using Henry's law. This feature was enabled by selecting the flash type OGW (Oil-Gas-Water) in the OGW/EOS multiphase flash form.

6.3.1.2.1. CO_2 Solubility in Water and Seawater

First, the Henry's law constant was estimated using WinProp's internal model (Harvey, 1996). There are two correlations available in WinProp to calculate the Henry's law constant: the Harvey's method (1996), and the Li-Nghiem's method (1986). Henry's law constants can be entered by the user or calculated internally using correlations to fit experimental solubility data. The component reference Henry's constants are Henry's constant at a specified reference pressure (H_i°) and molar volume at infinite dilution (v_i^∞) which can be adjusted to match experimental data. Henry's constant at any pressure and temperature is written as below:

$$\ln H_i = \ln H_i^\circ + v_i^\infty (p - p_i^\circ)/RT \quad (1)$$

where the superscript " ° " refers to the reference condition.

The effect of salt on the gas solubility in the aqueous phase is modeled either by the salting-out coefficient or the scaled-particle theory, depending on the component. The brine salinity is used to adjust the internally estimated Henry's constants for the CO_2 solubility in brine. In this study, the salinity of 0.035987 weight fraction was entered to the model. In the next step, the fitting parameters of Henry's law solubility model were regressed and a file containing the GEM fluid model keyword specifications was generated. Parameters in the internal Henry's model are Ref. Henry column (component Henry's constant), $V_{inf.}$ (molar volume at infinite dilution) and $P_{ref.}$ (reference pressure for Henry's constant). Tables 6-5 and 6-6 show the calculated physical properties of carbonated water and carbonated seawater.

Table 6-5: Physical properties of the carbonated water at 21°C (69.8 °F) and 2.1 MPa (305 psi)

Prop.	MW (*) (g/mol)	ρ (*) (g/cm^3)	μ (**) (mPa.s)	$\delta_{CO2/W}$ (*) (mol %)	$\delta_{CO2/W}$ (m) (mol %)	$\delta_{CO2/W}$ (**) (mol %)
Value	18.34	1.003	1.008	0.0128	0.0124	0.0128

(*) CMG-WinProp, (**) Correlation which was discussed the section 4.2, (m) measured by this work

Table 6-6: Physical properties of the carbonated seawater at 85°C (185 °F) and 24 MPa (3,500 psi)

Prop.	MW (*) (g/mol)	ρ (*) (g/cm^3)	μ (**) (mPa.s)	$\delta_{CO2/SW}$ (*) (mol %)	$\delta_{CO2/SW}$ (m) (mol %)	$\delta_{CO2/SW}$ (**) (mol %)
Value	19.01	1.0152	0.438	0.0180	0.0188	0.0182

(*) CMG-WinProp, (**) Correlation which was discussed the section 4.2, (m) measured by this work

6.3.2. Reservoir Model

We conducted simulation of EOR processes with CMG-GEM^{TM}, which is a 3-dimensional, multicomponent, multiphase, and compositional simulator that considers important mechanisms such as composition changes of reservoir fluids, swelling of oil and viscosity changes. After preparing the fluid model using WinProp, the reservoir core model was constructed. In this study, a reservoir grid model was constructed using GEM-Builder^{TM}. The grid system was a 3-dimensional cube model. A cube model containing dimensions that replicated the laboratory experimental model was undertaken to evaluate the performance of seawater flooding, secondary CWI, tertiary CWI, and CO_2-WAG.

The property of the model including, orientation, dimensions, and rock properties with porosity, permeability, and compressibility were defined as the same as the laboratory core flooding experiments. The reason why we used the Cartesian grid model was because the flow in a Cartesian grid is linear which is similar to the flow in a core flooding experiment. However, in general, the radial model simulates the flow in a radial direction which is not necessary for modelling a core flood experiment. If a Cartesian grid is used, the core dimensions needs to be converted while conserving volume since cores are in radial dimensions. The total numbers of grid blocks were 50 including 1 grid in I-direction, 1 grid in J-direction and 50 grids in K-direction (along the core). Table 6-7 shows the physical properties of the core model.

Table 6-7: Core model properties

L* (cm)	D (cm)	Porosity* (%)	Permeability* (mD)	Grid blocks	Grid Dimensions (LWH, cm^3), PV	Oil density (g/cm^3)	Oil viscosity (cP)	P (MPa)	T (°C)
9.8-11.8	3.0	19.5-22.0	314-381	1×1×50	2.69×2.69×L, (14.5 to 17.4 ml)	0.877	6.82	31	85

*: range of core sample property, LWH: length, width, height

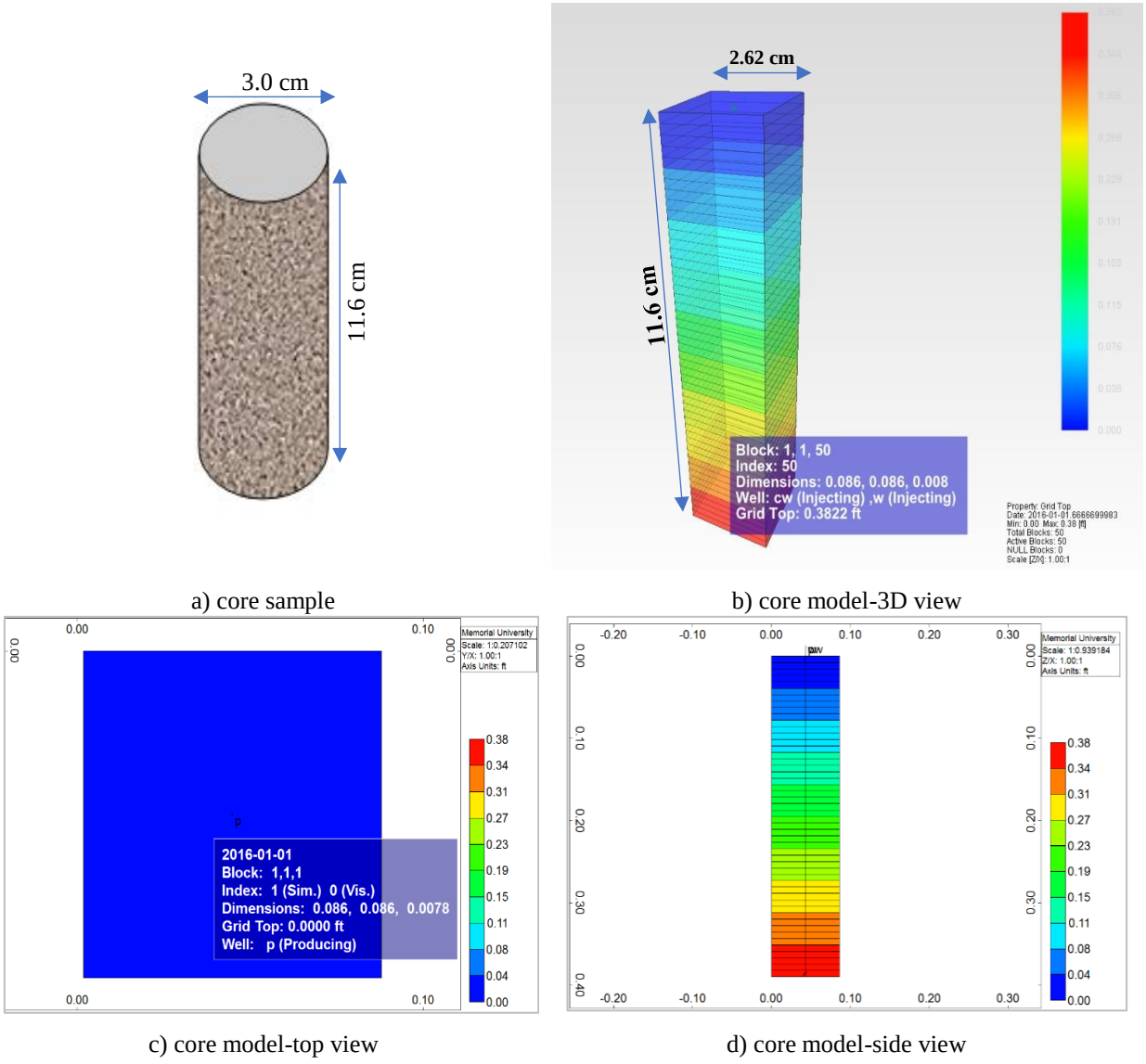

a) core sample

b) core model-3D view

c) core model-top view

d) core model-side view

Figure 6–10: Schematic of core sample (a) and 3D reservoir grid model (b-d)

Figure 6-10 shows the core model in different views. It should be noted that the dimensions followed the same dimensions of the core sample and also similar physical properties were

assigned to the core model. The grid model was considered a homogeneous model as was a sandstone core sample. The core model built in CMG followed the exact setup as the experiment, that is, injector well at the bottom and producer at the top of the cylindrical core.

6.3.2.1. Rock-Fluid Properties

The relative permeability curves are the most uncertain parameters in every simulation. To regress the experimental results, the end-point relative permeabilities are the uncertain parameters (Honarpour and Mahmood, 1988). The relative permeability curves are important for entering information into the simulator for each rock type and scheme. The simulation of oil displacement by any of the processes: water flooding, carbonated water injection, and CO_2-WAG, initially required two-phase relative permeabilities. In three-phase oil/water/gas experiments, two-phase water/oil and oil/gas relative permeabilities (Corey model) were used to calculate the three-phase oil relative permeabilities. Then the Stone II model in CMG-GEM was used to calculate the three-phase relative permeability. As an initial input, the end-point oil relative permeability (k_{ro}) at connate water saturation (S_{wc}) and the end-point water relative permeability at residual oil saturation were adopted for a sandstone rock and the same oil sample from Cao et al. (2015).

The relative permeability for water flooding was generated and incorporated in the simulation. The primary simulation results for recovery factor and cumulative produced fluids showed an acceptable trend as the adopted relative permeability graph was for the same sandstone rock and oil samples. The only difference was higher permeability of the used rock sample (780 mD) compared to our rock sample (380 mD).

6.3.2.2. Model Regression

In the Corey model, there are four exponents (n_w and n_o) to calculate the relative permeabilities, which by default in the CMG-Builder Module have been set at 3 for a consolidated sandstone. However, they can vary to obtain a better agreement between the simulation results and experimental data. Since each test was conducted using a fresh core sample, following almost the same identical rock type, porosity and permeability, the exponents (n_w, n_{ow}, n_g, n_{og}) for relative permeability correlations were regressed and held constant for all the experiments (Mosavat, 2015). These exponents are used to construct the relative permeability curves for both water-oil and oil-gas systems (Table 6-8).

Table 6-8: Corey exponents for relative permeability

Exponent	n_w for k_{rw}	n_{ow} for k_{row}	n_{og} for k_{rog}	n_g for k_{rg}
Value	3.2	2.5	3	2.9

The end-point relative permeabilities were modified for each individual experiment to match the experimental results (Mosavat, 2014; Tunnish et al., 2018). The connate water and residual saturations were obtained from experiments and entered in the relative permeability calculations in CMG-Builder/rock-fluid. The ultimate recovery factor of 67.6% was obtained (Figure 6.13), by modifying the end-point relative permeability using the Corey model set to our experimental residual oil and connate water saturations (Figure 6-11). The tuning of the relative permeability curve changed the predicted ultimate recovery factor to 59.4% compared to the experimental value of 59.7%. Therefore, each experiment has a specific set of relative permeability curves. The generated relative permeability curves for each experiment are depicted in the following figure.

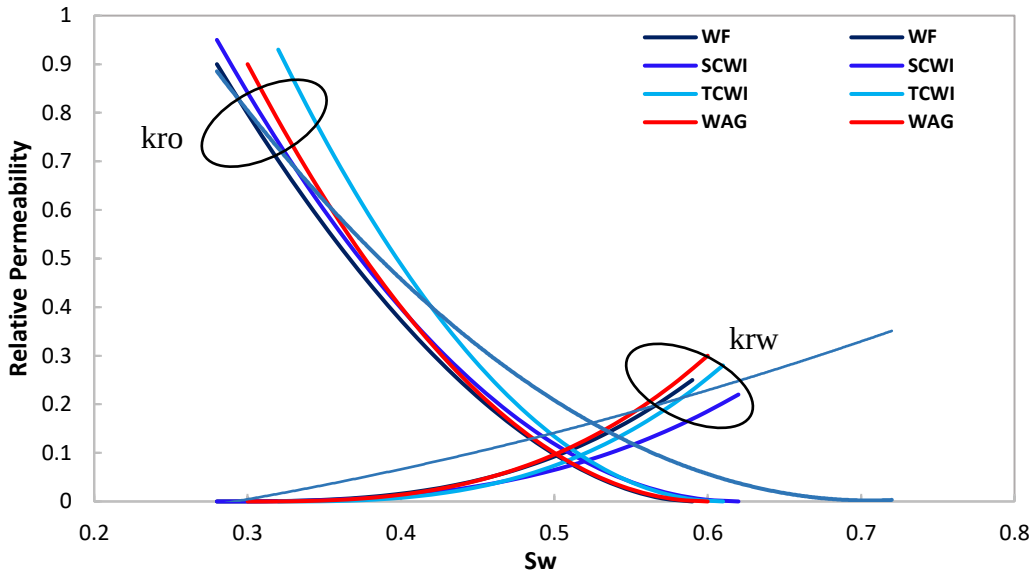

Figure 6–11: Generated K_r for WF, and secondary and tertiary CWI , CO_2-WAG, and Cao et al., 2015

Initially, secondary and tertiary CWI were simulated using relative permeability curves from water flooding. The end-point saturation in water relative permeability curves were replaced by the end-point saturation from the experiment. To modify the relative permeability curves, end-point relative permeabilities were changed. The results of core flooding experiments before and after regression are reported in Figures 6-11 to 6-18.

Initially, CO_2-WAG was simulated using the relative permeability curves from water flooding. The initial end-point gas-oil relative permeability was estimated based on Derakhshanfar et al. (2011) and then it was regressed for CO_2-WAG process based on our experimental end-point saturation. It should be noted that entering the gas-oil relative permeabilities to CWI injection process did not affect the predicted results as we did not have free gas in these processes.

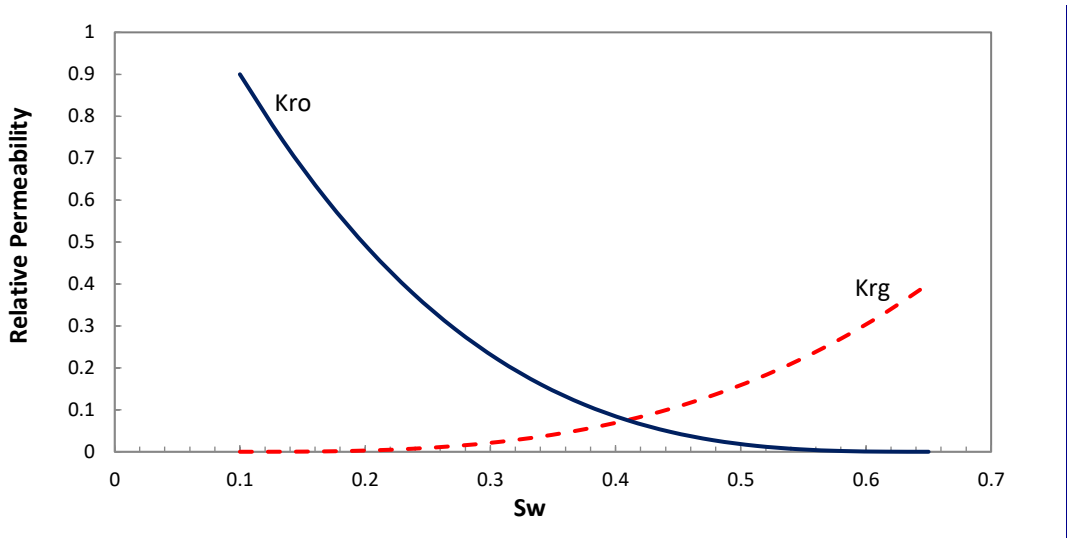

Figure 6–12: Relative permeability curves for CO_2-WAG

After constructing the grid model, it was imported to the CMG-GEM module. Oil recovery, produced oil/water, and oil/gas ratios at different injected pore volumes were obtained by the simulation and compared with the experimental results

6.3.3. Simulation Results

The comparison of core flooding experiments and simulated results under similar conditions are shown in Figures 6-11 to 6-18. The bottom hole pressure for the production well was considered 4,500 psi (31 MPa) and the injection rate was 0.2 ml/min corresponding to 3.46×10^{-6} m/s (1 ft/day).

6.3.3.1. Seawater Flooding

The results before and after regression for recovery factor and WOR are shown in Figures 6-14 and 6-15. As illustrated, the ultimate recovery factor before regression was 8.7%, which is higher than the experimental value. As mentioned before, the original relative permeability curves were

adopted from Cao et al. (2015) with the same oil and the same rock sample (sandstone) with higher permeability. The end-point residual oil saturation (from experiment) was used in the Corey model to calculate and modify the end-point relative permeability (k_{ro}) at residual oil saturation. The simulation results after match gave a better recovery factor and cumulative WOR compared to the experimental data. The breakthrough before match obtained at 0.52 PV with the recovery factor of 61.7%. However, after matching the breakthrough was improved to be at 0.41 PV with the recovery factor of 50.3% (experimental value: 0.39 PV with recovery factor of 47.1%). As it is illustrated in Figure 6-13 and 6-14, ultimate oil recovery factor was achieved with a very good agreement with the experimental value of 59.7%.

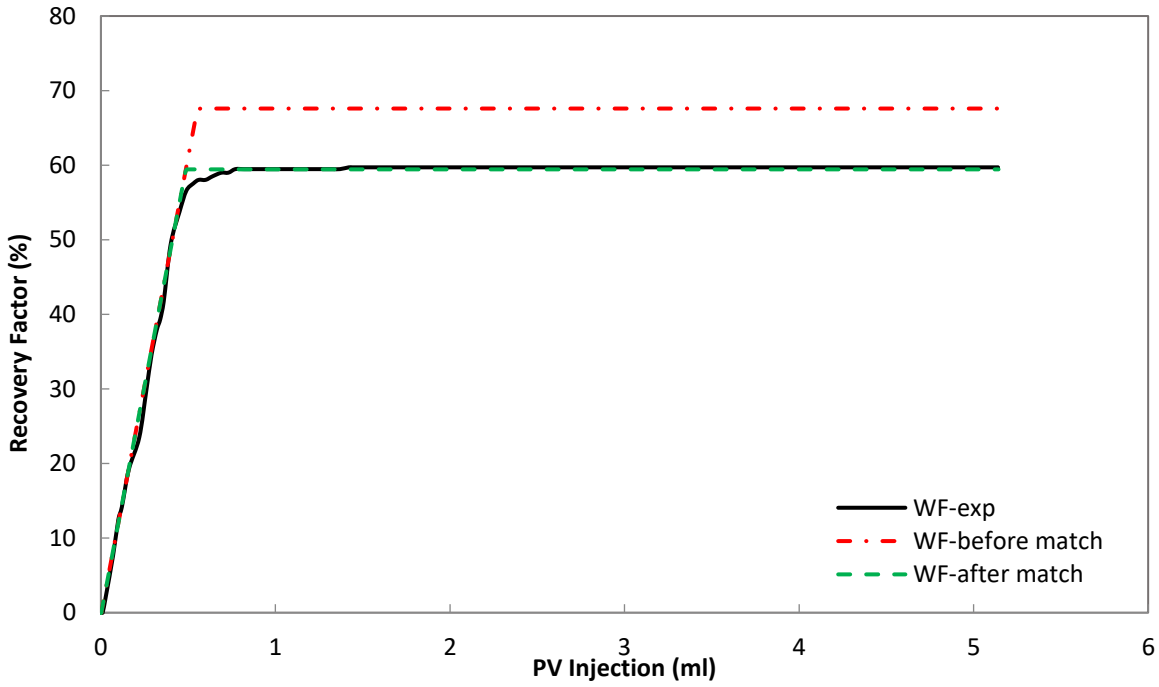

Figure 6–13: Experimental and simulation results of oil recovery for seawater flooding

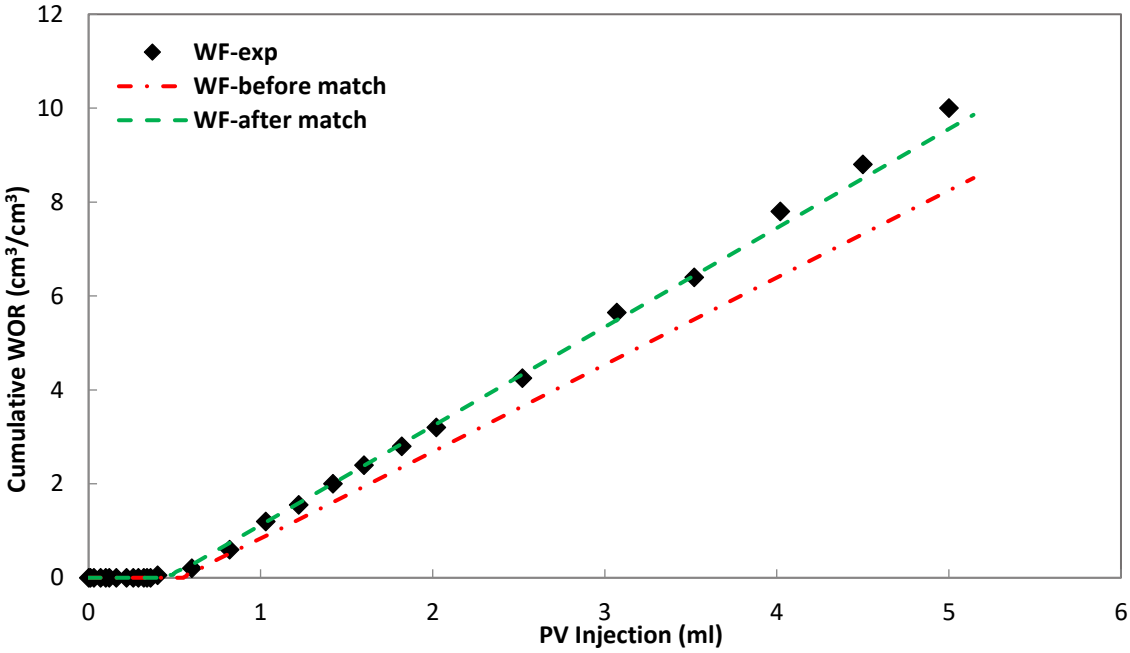

Figure 6–14: Experimental and simulation results of cumulative WOR for seawater flooding

6.3.3.2. Secondary and Tertiary CWI

Secondary CWI as shown in Figures 6-15 and 6-16, resulted in a higher recovery factor than seawater flooding. Although there was some discrepancy between the experimental results and the simulation due to the back-pressure operation, the ultimate recovery factor was matched. The injection rate was the same as seawater flooding, 0.2 ml/min. The result of ultimate oil recovery before matching showed a 5.0% difference compared to the experimental value. By modifying the end-point oil saturation in the relative permeability curves obtained from the experiment, a better match was achieved for recovery factor, cumulative WOR, and cumulative GOR. The breakthrough before match obtained at 0.53 PV with a recovery factor of 66.2%. However, after regression the breakthrough was improved to 0.47 PV with the recovery factor of 61.5% (experimental value: 0.45 PV with recovery factor of 59.9%). The ultimate recovery factor for secondary CWI before and after regression were obtained 78.9% and 73.8% at 8 PV, respectively (experimental value: 74.8%).

In tertiary CWI, water flooding was simulated for 2 PV and then carbonated water injection began with the same flowrate of 0.2 ml/min. As depicted in Figure 6-17, the ultimate recovery factor for tertiary CWI were obtained 74.6%, 65.7% before and after regression (experimental value: 64.3%). The results of cumulative water/oil and gas/oil ratios are depicted in Figure 6-18.

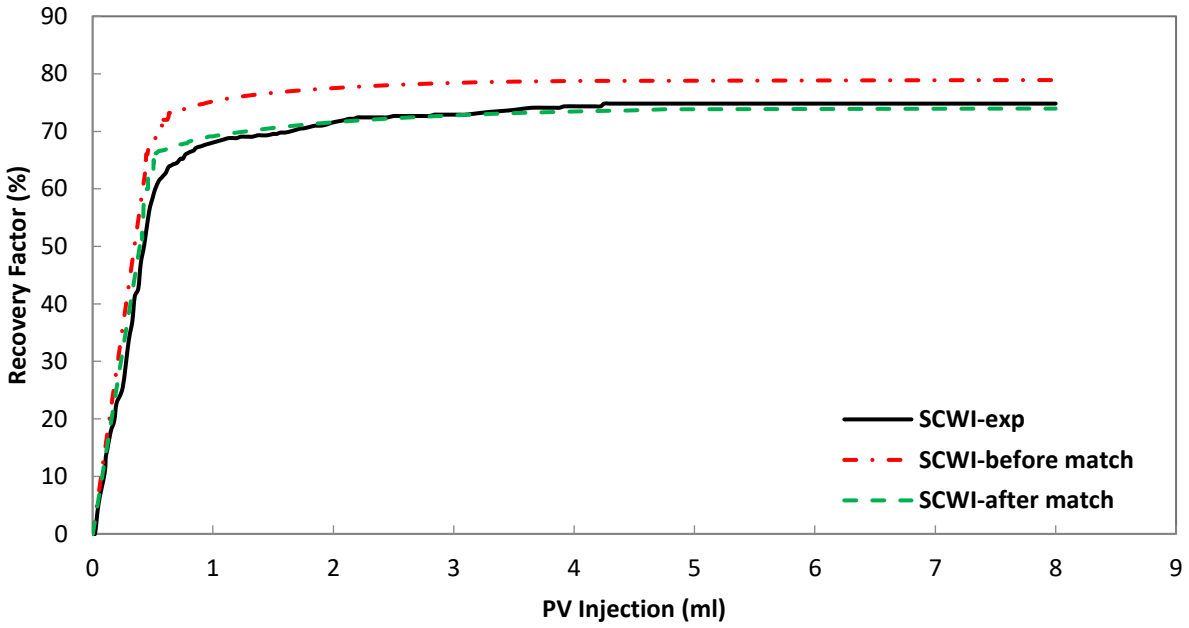

Figure 6–15: Experimental and simulation results of oil recovery for secondary CWI

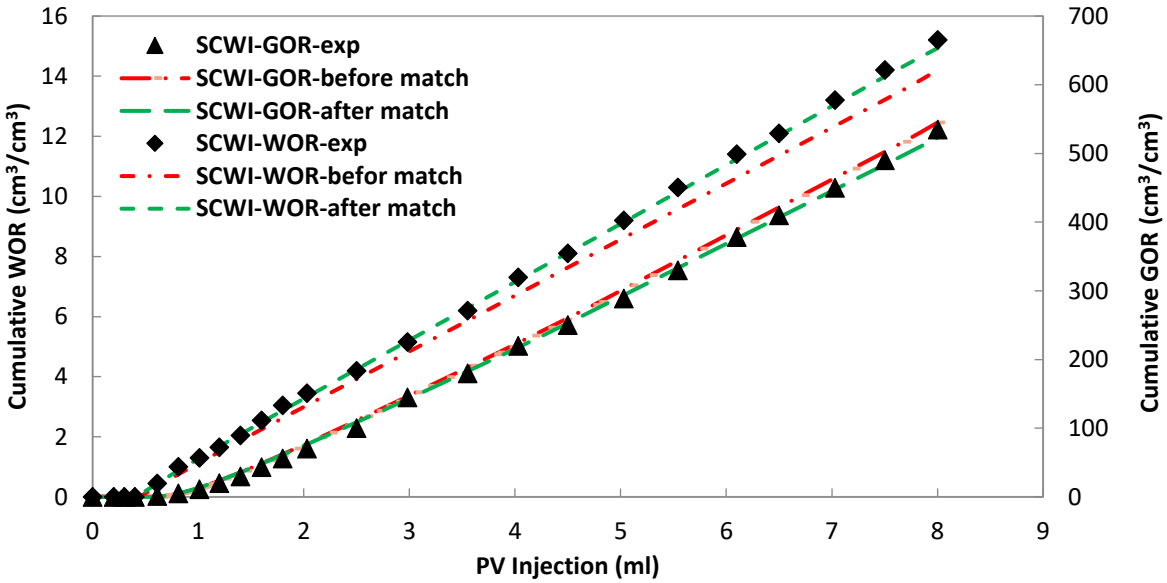

Figure 6–16: Experimental and simulation results of cumulative WOR and GOR for secondary CWI

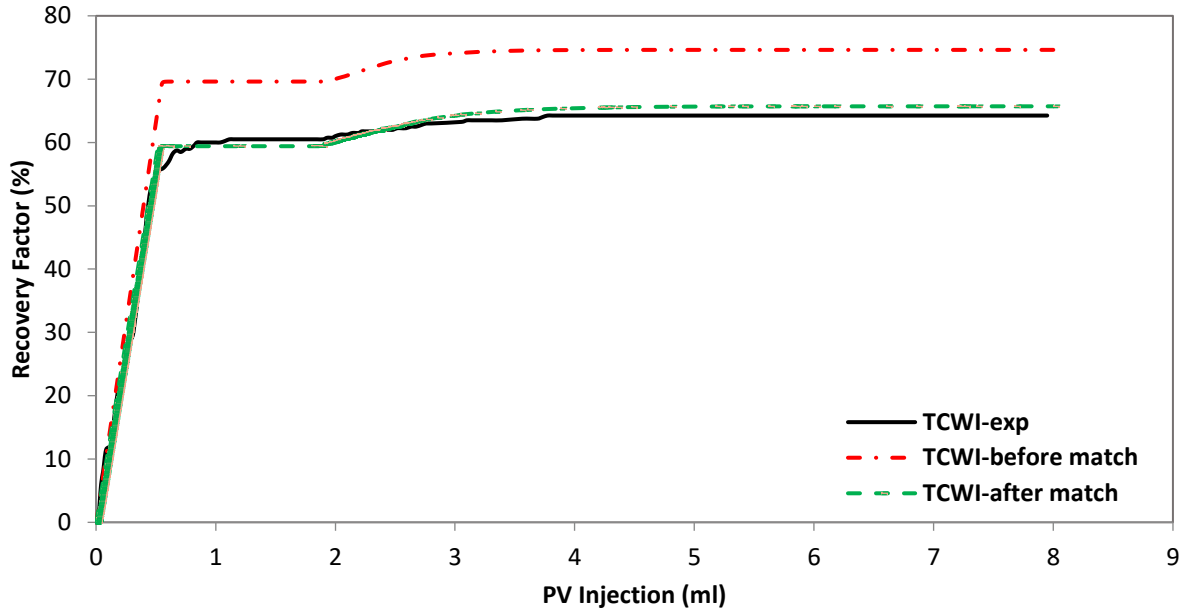

Figure 6–17: Experimental and simulation results of oil recovery for tertiary CWI

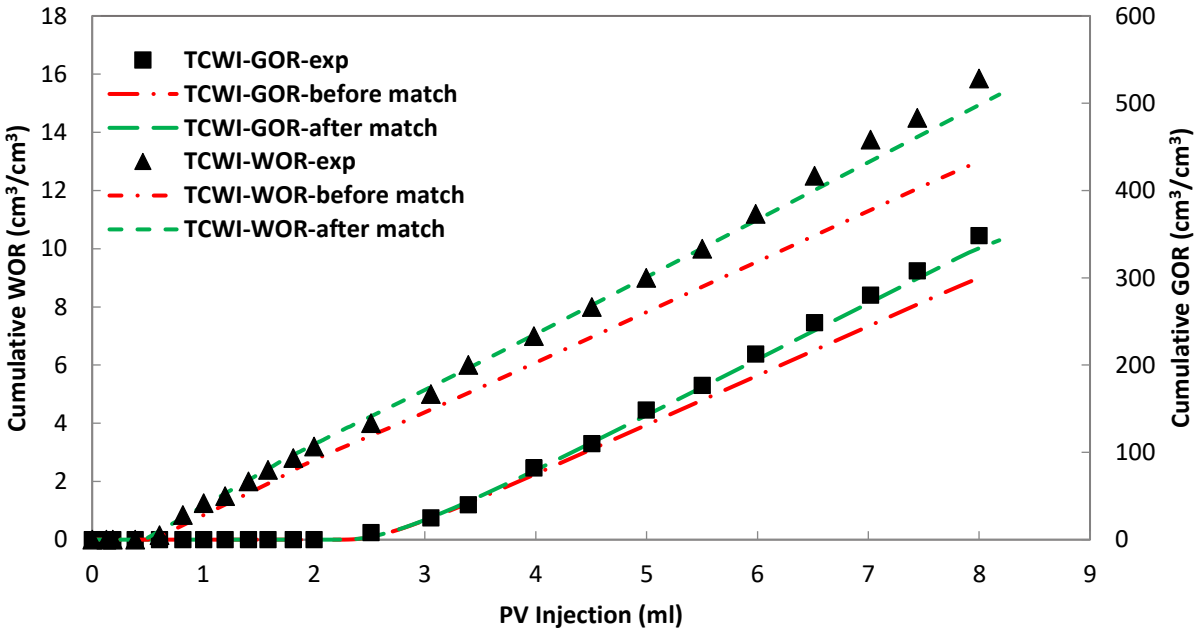

Figure 6–18: Experimental and simulation results of cumulative WOR and GOR for tertiary CWI

6.3.3.3. CO_2-WAG

The comparison of experimental and simulation results of CO_2-WAG is shown in Figures 6-19 and 6-20. The injection rate was the same as seawater flooding, 0.2 ml/min in water cycle. The gas flowrate which was previously explained in section 6.2, was chosen based on the solubility of CO_2 in seawater. As explained in section 6.3.2.1, the relative permeabilities were modified. The results before matching showed a 7.0% difference compared to the experimental data. By modifying the end-point relative permeability a better prediction was achieved for the recovery factor, cumulative WOR, and cumulative GOR. The breakthrough before match obtained at 0.49 PV with a recovery factor of 58.8%, however, after regression, the breakthrough was improved to 0.42 PV with a recovery factor of 47.9% (experimental value: 0.4 PV with recovery factor of 44.1%).

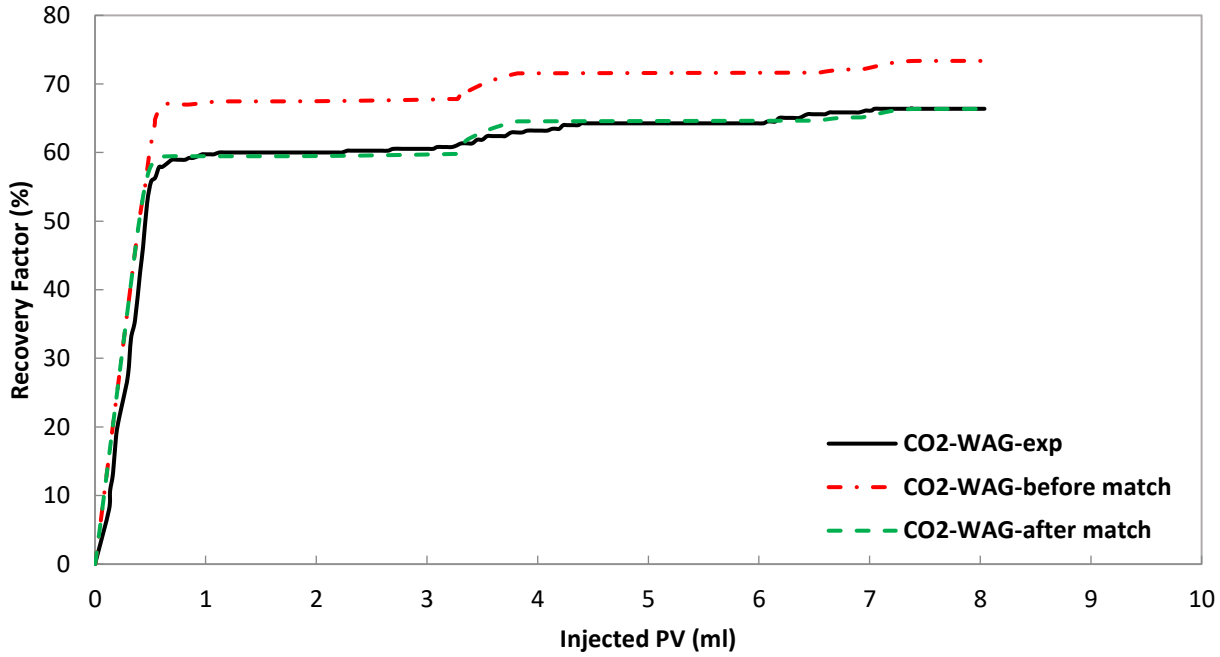

Figure 6–19: Experimental and simulation results of oil recovery for CO_2-WAG

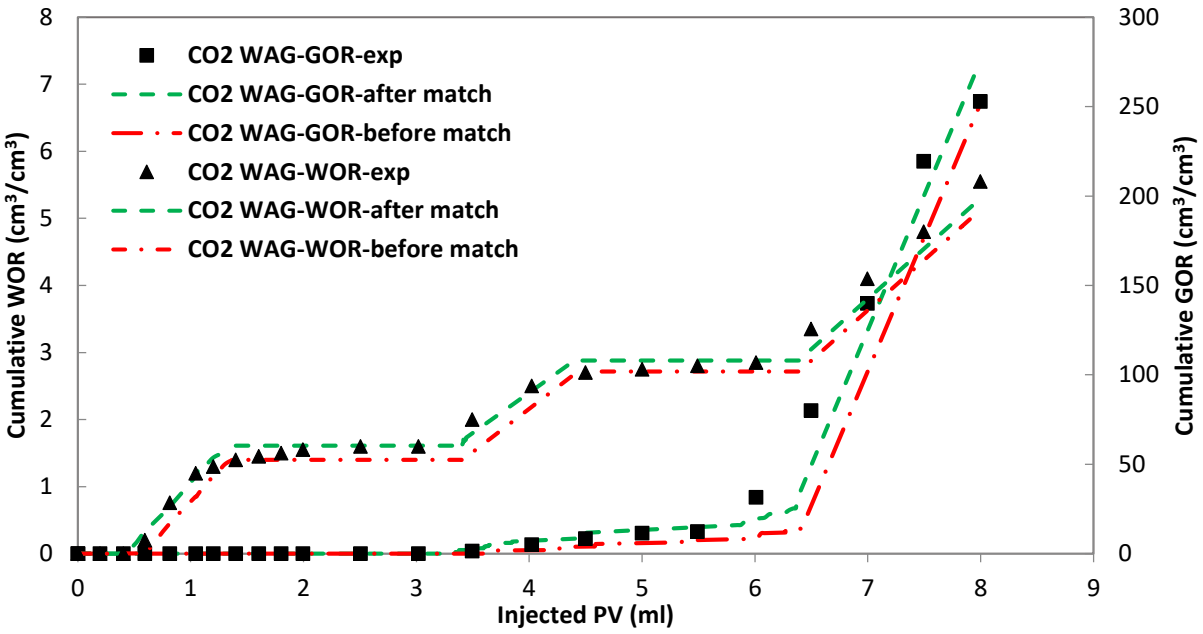

Figure 6–20: Experimental and simulation results of cumulative WOR and GOR for CO_2-WAG

6.4. Summary of the Core Flooding

To investigate the impact of CWI at reservoir conditions, core flooding experiments using Cleveland Berea sandstone cores were designed at 85°C (185°F) and 31 MPa (4,500 psi). The following four schemes were implemented: seawater flooding, secondary CWI, tertiary CWI, and CO_2-WAG. A local oil sample with a gravity of 29.8 °API and a viscosity of 6.82 cP was used. Simple water flooding was performed using seawater from the Atlantic Ocean with a salinity of 35,986 ppm. Carbonated water was prepared using seawater as well (section 4.2.1).

The results of core flooding experiments showed that both secondary and tertiary CWI improved oil recovery in comparison to seawater flooding. The breakthrough of water in CWI took place later than that in seawater flooding. The viscosity of oil in contact with carbonated seawater was calculated to reduce from 4.50 cP to 3.76 cP. Secondary CWI showed a delay in breakthrough and a significant improvement in the oil recovery. Moreover, the trend in oil recovery curve showed

that secondary CWI continued to produce oil for a longer period. CO_2-WAG flooding also improved the recovery factor significantly. The experimental results showed that secondary CWI obtained the recovery factors of 66.4% and 69.0% at 0.8 PV and 1.2 PV, respectively. The highest recovery factor of 74.8% was obtained at 8 PV injection. CO_2-WAG and tertiary CWI resulted in 58.9% and 59.1% at 0.8 PV and 60.0% and 60.5% at 1.2 PV, respectively. The ultimate recovery factors of 66.4% and 64.2% were obtained at 8 PV injection for CO_2-WAG and tertiary CWI, respectively. Sohrabi et al. (2012) examined the application of CWI at 13.7 MPa (2,000 psi) and 38°C (100 °F) in a horizontal core flooding using a sandstone core with a porosity of 22% and a permeability of 1,370 mD, and a light oil (20 °API). It was reported that the breakthrough for water flooding and secondary CWI occurred at about the same time. The ultimate oil recovery reached 60.0% at 2.5 PV for water flooding (no more production at higher PV was reported) and 69.2% at 8 PV for secondary CWI (synthetic seawater with the salinity of 35,380 ppm). An additional recovery factor of 9.2% was obtained.

Table 6-9: Summary of the results of core flooding experiments

Test	BT (PV)	RF (BT)	RF (0.8 PV)	RF (1 PV)	RF (2 PV)	RF (3 PV)	RF (4 PV)	RF (8 PV)
Seawater flooding	0.39	47.1	58.5	59.4	59.7	59.7	59.7	59.7
Secondary CWI	0.45	50.4	66.4	68.1	71.5	72.9	74.3	74.8
Secondary CWI (r)	0.48	52.1	65.7	69.2	72.8	73.0	74.5	74.6
Tertiary CWI	0.39	45.5	59.1	60.0	61.7	63.2	64.2	64.2
CO_2-WAG	0.40	46.1	58.9	60.0	60.0	60.5	63.2	66.4

Shakiba et al. (2016) studied CWI in a series of horizonal core flooding experiments using an oil with 28 °API at 40°C (104 °F) and 13.7 MPa (2,000 psi). The rock sample was carbonated with a porosity and a permeability of 24.0% and 11.6 mD, respectively. The results showed that higher oil recovery of 88.4% at 5 PV for secondary CWI and 72.2% at 7 PV for tertiary CWI compared

to 32% at 2.4 PV for water flooding. Compared to tertiary CWI, the secondary CWI resulted in 15.8% additional oil recovery.

In CWI, the oil recovery was mainly due to displacement prior to breakthrough. As more carbonated water was injected, it began to interact with the oil which resulted in trapped oil extraction. The trapped oil behind the front receives CO_2 form the CW phase and become mobilized. Several mechanisms are attributed to the additional oil recovery factor in carbonated water injection processes. CO_2 is gradually transferred to oil resulting in swelling and reduction in oil viscosity, which improves the mobility. The recovery factor was improved due to a higher solubility of CO_2 in the oil than that in seawater. The solubility of CO_2 in water, seawater, and oil were calculated to be 0.0188 mol CO_2/mol seawater and 0.448 mol CO_2/mol oil, respectively (discussed in sections 2.3.4 and 4.2.1.1)

When the carbonated seawater contacted the oil, it became richer in CO_2, especially as the oil ganglia started to swell, and the redistribution of oil took place. In secondary CWI, the direct contact between oil and carbonated seawater reinforced the CO_2 transfer. In tertiary CWI, the same mechanisms as secondary CWI were activated, however, due to the water barrier and the dilution effect, carbonated seawater was less effective over time. Globally, many sandstone oil reservoirs have already been water flooded. In offshore reservoirs, water flooding is the most feasible method, therefore, the application of a process such as carbonated seawater injection, that is compatible with the water flooding is promising.

The contribution of this work was building a model and tune it using experimental data to be able to predict the fluid production of one of the local oil reservoirs. The results of core flooding experiments were simulated using a compositional model which was built by CMG-GEM^{TM} (version 2014. 10, Computer Modeling Group Limited, Canada). The model was constructed to mimic the core flooding experiments. Initially, there were some differences between simulated and experimental results. However, by modifying the end-point relative permeabilities, a good agreement between the simulation and experimental results was obtained. The outcome of the simulation part was a tuned model that could predict the recovery factor, GOR, and WOR at reservoir pressure and temperature for different schemes (seawater flooding, and secondary and tertiary CWI, and CO_2-WAG). By having this model, we will be able to predict the fluid production of this reservoir at different schemes, for example, carbonated water injection at different CO_2 concentration, temperatures and pressures, schemes (e.g. CWI with soaking time).

Chapter 7 **Conclusions and Recommendations**

7.1. Conclusions

In summary, this investigation compares the use of carbonated water injection (CWI) as a secondary or tertiary recovery method compared to water flooding and CO_2 WAG. Specifically, CWI is shown to outperform waterflooding at the pore scale (from micromodel studies) in the presence of gravity even when horizontal or vertical fractures (heterogeneities) are present. At offshore Newfoundland conditions, core flooding experiments resulted in secondary CWI outperforming tertiary CWI, CO_2 WAG, and waterflooding at any injection time (pore volumes injected). Repeat experiments and core scale simulation studies confirm the results. Carbonated water injection can be considered a technically feasible EOR method. The novelty of this research was to investigate the performance of water flooding and CWI in the presence of gravity using homogeneous and heterogeneous (fractured) porous media. Water flooding and carbonated water injection (CWI) were studied at both the pore-scale and core-scale. Furthermore, the effect of water flooding and CWI on vertical displacement (gravity effect) was investigated (Figure 4-1).

The first phase of this research investigated the phenomena in pore-scale displacement which occurs in the presence of CWI in glass micromodels (homogeneous, horizontal fracture, and vertical fracture). We fabricated glass micromodels that could withstand the maximum pressure of 5 MPa (720 psi) without overburden pressure. A series of experiments in the homogeneous and heterogeneous (fractured) micromodels were designed at 2.1 MPa (305 psi) and 21°C (69.8 °F) using a local oil sample (29.8 °API). The oil saturation profile, sweep efficiency, pore-scale mechanisms, and trapped oil mobilization were analyzed during the experiments. The results of

different schemes, including water flooding, and secondary and tertiary CWI in the homogeneous and heterogeneous micromodel experiments showed the following:

1. The effect of gravity in both water flooding and secondary CWI was verified in all the geometries (homogeneous, horizontal fracture, and vertical fracture). However, fractures competed the effect of gravity force and affected the vertical and horizontal sweep efficiencies. The presence of vertical fractures strongly affected the fluid flow pattern and improved the vertical sweep efficiency. These findings demonstrated that vertical fractures acted as distributors along the vertical line. Moreover, vertical fractures connected the lower and upper parts of the micromodel to aid the injected fluid for displacing the oil. Although the by-passed zones were formed in the vertical fracture micromodel, the carbonated water swept the upper part of the micromodel as well as the lower part to enhance the vertical sweep efficiency (Figure 5-19 and Table 5-1).
2. An earlier breakthrough was observed in the presence of gravity in both water flooding and secondary CWI compared to the horizontally-oriented micromodels (Figure 5-7, 5-15, and 5-16). The gravity force directed the flow of water and carbonated water toward the lower part of micromodels and the saturation of oil remained mostly unchanged in the upper part of micromodels until breakthrough.
3. In the homogeneous micromodel with the presence of gravity, the recovery factor changed (29.4 ± 0.02% to 36.2 ± 0.03%) for water flooding compared to secondary CWI (34.2 ± 0.04% to 53.0 ± 0.02%) from breakthrough to 7 PV, respectively (Figure 5-19).
4. In the horizontal fracture micromodel with the presence of gravity, the recovery factor changed (32.1 ± 0.03% to 36.3 ± 0.04%) for water flooding and secondary CWI (38.6 ± 0.04% to 42.3 ± 0.02%) from breakthrough to 7 PV, respectively (Figure 5-19).

5. In the vertical fracture micromodel, with the presence of gravity, the recovery factor changed from breakthrough to 7 PV for water flooding (25.2 ± 0.08% to 38.8 ± 0.08%) and secondary CWI (38.1 ± 0.06% to 48.9 ± 0.07%), respectively (Figure 5-19).
6. Prior to the breakthrough, oil recovery occurred mainly due to displacement and generally there was not a considerable difference in the recovery factor between the different schemes. However, as more carbonated water was injected, CO_2 from the injected carbonated water was transferred to the oil resulting in a lower oil viscosity and oil swelling.
7. Carbonated water had a greater capacity than water to be evenly distributed in pore bodies and channels both with and without the effect of gravity. Hence, unlike simple water flooding, CWI enhanced the vertical and horizontal sweep efficiencies compared to simple water flooding (Figure 5-41).
8. The oil recovery factor after breakthrough in secondary CWI in the vertically-oriented homogeneous micromodel was increased gradually compared to the horizontally-oriented micromodel. Despite this, in horizontal fracture micromodel the difference in oil recovery between vertically-oriented and horizontally-oriented micromodels was not high due to the high permeability of fractures.
9. In both heterogeneous micromodels, the horizontally and vertically-oriented fractures significantly affected the fluid flow in simple water flooding and secondary CWI. By-passed zones were formed in the areas adjacent to and between fractures in both above-mentioned micromodels.

10. In the micromodel including horizontally-oriented fractures, the presence of fractures determined the flow pattern, especially in vertical flooding. Secondary CWI showed more stable front displacement than simple water flooding and later breakthrough.
11. Secondary CWI resulted in an additional oil recovery of 5.8%, 7.5%, and 8.5% at 1 PV, and 16.8%, 6% and 10.1% at 7 PV compared to water flooding in the homogeneous, horizontal fracture, and vertical fracture micromodels in the presence of gravity, respectively.
12. As was observed in the visual study (micromodel study) the interaction of carbonated water and oil resulted in better oil recovery in narrow pores, narrow throats, and dead-ends (Figures 5-37, 5-39, and 5-40). Oil swelling and a favorable mobility ratio allowed the displacement of oil in small pores and throats that were not accessible to water.
13. Tertiary CWI was not affected by gravity during the course of CWI. An additional recovery factors of 12.2%, 3.8%, and 9% were achieved in the homogeneous, horizontal, and vertical fracture micromodels (Figures 5-23 and 5-26, and Tables 5-2 and 5-3).
14. The effect of the production rate on secondary CWI was examined using the following production rates: 0.0008 ml/min and 0.004 ml/min in the homogeneous micromodel and 0.0008 ml/min and 0.0024 ml/min in the horizontal fracture micromodel. The recovery factor gradually increased for the higher flowrate and continued to increase at higher PV injections (Figures 5-31 and 5-33).
15. In the homogeneous micromodel, the recovery factor of 47.1% for the scheme with the flowrate of 0.0008 ml/min was lower (53.0%) with 0.004 ml/min at 7 PV. However, the recovery factor increased gradually for the higher flowrate of 0.004 ml/min and approached to 57.5% at 10 PV. In the horizontal fracture micromodel, the recovery factor

of 39.5% for the scheme with the flowrate of 0.0008 ml/min was lower compared to 42.3% for the scheme with 0.0024 ml/min due to the presence of horizontal fractures (Tables 5-4 and 5-5).

16. A longer injection of secondary CWI (17.1 PV) resulted higher recovery factor of 43.9% (0.0008 ml/min, horizontal fracture), 45.5% (0.0024 ml/min, horizontal fracture), and 59.0% (0.0024 ml/min, vertical fracture) in all the geometries (Figures 5-35 and 5-36).
17. Additional recovery factors of 22.1%., 5.9%, and 29.3% were obtained in the extended tertiary CWI schemes for homogeneous, horizontal fracture, and vertical fracture micromodels, respectively (Figures 5-35 and 5-36).
18. CO_2 transfer is a time-dependent process; hence, CWI was beneficial for long-term reservoir production, especially for heterogeneous vertical fracture porous media.

In the second phase of this research, the impact of CWI on the oil recovery factor in core flooding was investigated. A series of core flooding experiments were designed at a local reservoir under the conditions of 85°C (185 °F) and 31 MPa (4,500 psi) using Cleveland Berea sandstone cores. Four schemes including seawater flooding, secondary carbonated seawater injection, tertiary carbonated seawater injection, and CO_2-WAG were implemented in a vertically-oriented core holder.

1. Experimental results showed that secondary CWI obtained the highest recovery factor of 74.8% at 8 PV injection. CO_2-WAG and tertiary CWI obtained 66.45% and 64.2% ultimate recovery factor. The recovery factor was improved due to a higher solubility of

CO_2 in oil compared to water phase. Seawater flooding showed the lowest recovery factor of 59.7% among the other schemes (Figure 6-1).

2. The breakthrough of water in CWI took place later than that in plain seawater injection due to solubility of CO_2 in oil which reduced the viscosity of oil.
3. A comparison of the trend in the oil recovery curve showed that secondary CWI continued to increase the recovery factor for a longer period. CO_2-WAG flooding also significantly improved the recovery factor compared to seawater flooding. The dissolution of CO_2 in oil helped to recover oil due to swelling as well as favorable mobility ratio by allowing the displacement of oil in small pores and throats that were not accessible to seawater flooding.
4. The results of the core flooding experiments were simulated using a compositional model which was built by CMG-GEM^{TM} (version 2014. 10, Computer Modeling Group Limited, Canada). There were some discrepancies between simulated and experimental results due to the small size of the model. However, a good agreement between the experimental results and the simulation was obtained with the regression of end-point relative permeabilities (Figures 6-11 to 6-18).

7.2. Recommendations for Future Work

The following recommendations are proposed to better investigate the application of CWI:

1. Better vertical sweep efficiency depends on the fluid flow distribution, which is a function of heterogeneity and flowrate. The study of different flowrates of carbonated water in a heterogeneous porous media is suggested to avoid the formation of by-passed zones and overcome the effect of gravity.

2. The application of different schemes, such as carbonated water injection with soaking time, especially in heterogeneous fractured reservoirs to avoid early breakthrough and higher incremental oil recovery is proposed. Because the CO_2 transfer, from water phase to oil phase, is a time-dependent process and it is an important factor in oil recovery during matrix/fracture interaction.
3. The effect of CWI in fractured reservoirs, especially carbonated mixed-wet porous media, must be visually investigated using dead-oil and live oil samples. The wettability of porous media is another factor that is affected by carbonated water injection due to the presence of ions in carbonated reservoirs. The presence of light hydrocarbons in a light oil sample may impact the amount of CO_2 solubility.
4. The effect of CWI using live oil sample is suggested considering the effect of dissolved gas on the solubility of CO_2 in oil.
5. CWI showed a high potential to recover oil from narrow pores and throats. Therefore, the application of CWI using different types of geometries may help to visually understand the effects of wettability and pore size distribution.
6. Facility consideration of offshore EOR including CO_2 capture, injection, monitoring, and risk analysis.
7. The simulation of CWI in a field-scale is suggested to understand the applicability of CWI in reservoir scale with respect to water to oil and gas to oil production.

References

Allen, J. and Sun, S.Q. (2003). Controls on Recovery Factor in Fractured Reservoirs: Lessons Learned from 100 Fractured Fields, SPE ATCE, Denver, USA, 84590-MS.

Araujo, S. V., Vargas, J. A. and Trevisan, O.V. (2013). Diffusion Coefficient of CO_2 in Light Oil under Reservoir Conditions using X-Ray Computed Tomography. *Offshore Technology Conference*, Brazil, OTC 24454.

Abedini, A. and Torabi, F. (2014). On the CO_2 Storage Potential of Cyclic CO_2 Injection Process for Enhanced Oil Recovery. *Fuel*, 124, 14-27.

Alotaibi, F.M., Zhou, Z. and Kokal, S.L. (2015). Laboratory Evaluation of Different Mode of Supercritical CO_2 Miscible Flooding for Carbonate Rocks, SPE Annual Technical Symposium and Exhibition, Al-Khobar, SPE 177986.

Al-Rawajfeh, A. (2004). *Modeling and Simulation of CO_2 Release in Multiple-Effect Distillers for Seawater Desalination* (PhD Thesis). Martin-Luther-University, Halle-Wittenberg, Halle, Germany.

Akinfiev, N. N. and Diamond, L. W. (2010). Thermodynamic Model of Aqueous CO_2-H_2O-NaCl Solutions from -22 to 100°C and from 0.1 to 100 MPa. *Fluid Phase Equilibria*, 295, 104-124.

Anderson, W. G. (1986). Wettability Literature Survey Part 2-Wettability Measurement. *Journal of Petroleum Technology*, 1246-1262.

Araktingi, U.G. and Orr Jr, F. M. (1993). Viscous Fingering in Heterogeneous Porous Media. *SPE Advanced Technology Series*, SPE 18095.

Aguilera, R. (1980). *Naturally Fractured Reservoirs*. Tulsa, Oklahoma, U.S.A: Pennwell Corp.

Azin, R., Mahmoody, M., Jafari Raad, S.M. and Osfouri, S. (2013). Measurement and Modeling of CO_2 Diffusion Coefficient in Saline Aquifer at Reservoir Conditions. *Central European Journal of Engineerin*g 3(4), 585-594.

Bagalkot, N. and Hamouda, A. A. (2017). Experimental and Numerical Method for Estimating Diffusion Coefficient of the Carbon Dioxide into Light Components, *Industrial & Engineering Chemistry Research (ACS Publications)*, 56, 2359-2374.

Bailey, B., Crabtree, M., Tyrie, J., and et al. (2000). Water Control, *Oil Field Reviews*. 12(10), 30-51.

Baker, R., (1998). Reservoir Management for Waterfloods-Part II. *Journal of Canadian Petroleum Technology*, 37 (1).

Bamberger, A., Sieder, G., and Maurer, G. (2000). High-Pressure (Vapor Plus Liquid) Equilibrium in Binary Mixtures of (Carbon Dioxide plus Water or Acetic Acid) at Temperatures from 313 to 353 K. *Journal of Supercritical Fluids*, 17, 97-100.

Barclay, T. H. and Mishra, S. (2016). New Correlations for CO_2-Oil Solubility and Viscosity Reduction for Light Oils. *Journal of Petrol Explor Prod Technol*, 6, 815-823.

Barenbaum, A. A., Zakirov, S. N., Zakirov, E. S., Klimov, D. S., and Serebryakov, V. A. (2015). Physical and Chemical Processes During the Carbonated Water Flooding in the Oilfields. *SPE Russian Petroleum Technology Conference*, Russia, SPE 176729-M.

Basov, N. G., Danilychev, V. A., Popov, Y. M., and Khodkevich, D. D. (1970). Laser Operating in the Vacuum Region of the Spectrum by Excitation of Liquid Xe by an Electron Beam. *Journal of Experimental and Theoretical Physics*, 12, 329.

Bavière M. (1991). Basic Concepts in Enhanced Oil Recovery Processes, United Kingdom: Published for SCI, Elsevier Applied Science, London and New York.

Belgrave, J.D.M. and Win, T. (1993). Vertical Sweep Efficiency and Oil Recovery from Gas Injection in Heterogeneous Horizontal Reservoirs. *Western Regional Meeting*, Anchorage, Alaska, U.S.A, SPE 26085.

Blunt, M. J. and Scher, H. (1995). Pore-level Modeling of Wetting. *Physical Review Journals*, E52, 6357.

Bourbiaux, B. J. (2009). Understanding the Oil Recovery Challenge of Water Drive Fractured Reservoirs. *International Petroleum Technology Conference*, Doha, Qatar, IPTC-13909-MS.

Brownell, L.E. and Katz, D.L. Flow of Fluids Through Porous Media, Part II, Simultaneous Flow of Two Homogeneous Phases. Chemical Engineering Progress, 43, 601-612.

Buchgraber, M., Al-Dossary, M., Ross, C. M., and Kovscek, A. R. (2012). Creation of a dual-porosity micromodel for pore-level visualization of multiphase flow. *Journal of Petroleum Science and Engineering*, 86-87, 27-38.

Burton, M. and Bryant, S. L. (2007). Eliminating Buoyant Migration of Sequestered CO_2 through Surface Dissolution: Implementation Costs and Technical Challenges. *SPE Annual Technical Conference and Exhibition*, California, U.S.A, SPE 110650.

Campbell B. T. and Orr, Jr F. M. (1985). Flow Visualization for CO_2/Crude-Oil Displacements. *SPE Annual Conference and Exhibition*, Mexico, SPE 11958.

Cao, J., Liu, X., James, L., and Johansen, T. (2015). Analytical Interpolation Methods for Dynamic Immiscible Core Flooding at Constant Differential Pressure, *International Symposium of the Society of Core Analysts*, Canada, SCA2015-039.

Carcoana, A. (1992). *Applied Enhanced Oil Recovery*. U.S.A, Englewood Cliffs, Prentice-Hall.

Chatzis, I. (1982). *Photo Fabrication Technique of 1-D Glass Micromodels*, Petroleum Recovery Research Center. New Mexico Institute of Mining and Technology, Report 82-12, 1-6.

Chatzis, I. and Dullien, F. A. L. (1983). Dynamic Immiscible Displacement Mechanisms in Pore Doublets: Theory Versus Experiment. *Journal of Colloid and Interface Science*, 91(1), 199-222.

Chatzis, I. and Morrow, N. R. (1981). Correlation of Capillary Number Relationships for Sandstone. *Annual Technical Conference and Exhibition*, San Antonio, U.S.A, SPE 10114.

Chen, J. D. and Wilkinson, D. (1985). Pore-Scale Viscous Fingering in Porous Media. *Journal of Physics Review Letters*, 55, 1982-1986.

Christensen, R. J. (1961). Carbonated Water Flood Results-Texas and Oklahoma. *Society of Petroleum and Engineers of AIME, 6300 North Central Expressway*, Dallas, U.S.A, SPE 66.

Chuoke, R. L., van Meurs, P., and van der Poel, C. (1959). The Instability of Slow, Immiscible, Viscous Liquid-Liquid Displacements in Permeable Media. *Petroleum Transactions, AIME*, 216, 188-194.

Conn, C. A., Ma, K., Hirasaki, G. J., and Biswal, S.L. (2014). Visualizing Oil Displacement with Foam in a Microfluidic Device with Permeability Contrast. *Lab on Chip*, 14, 3968.

Cotter, W. H. (1962). Twenty-Three Years of Gas Injection into A Highly Undersaturated Crude Reservoir. *Journal of Petroleum Technology* 14 (4), 361-365.

Crawford, H. R., Niell, G. H., Crawford, P. B. (1963). Carbon Dioxide-A Multipurpose Additive for Effective Well Stimulation. *Journal of Petroleum Technology*, 237-244, SPE-571-PA.

Dake, L. P. (1978). *Fundamentals of Reservoir Engineering*. U.S.A: Elsevier Science.

Darvish, G. R. (2007). *Physical Effects Controlling Mass Transfer in Matrix Fracture System during CO_2 Injection into Chalk Fractured Reservoirs* (PhD Thesis). NTNU University, Norway.

Da Silva, F. L. and Belery, P. (1989). Molecular Diffusion in Naturally Fractured Reservoirs, A Decisive Recovery Mechanism. *SPE Annual Technical Conference and Exhibition*, San Antonio Texas, U.S.S, SPE 19672.

Das, S. K. and Butler, R. M. (1998). Mechanism of the Vapor oil Extraction Process for Heavy Oil and Bitumen. *Journal of Petroleum Science and Engineering*, 21 (1-2), 43-59.

Davis Jr., J. A., Jones, S. C. (1968). Displacement Mechanisms of Micellar Solutions. *Journal of Petroleum Technology*, 20 (12), 1415-1428, SPE 1847.

Delshad, M., Fathi Najafabadi, N., and Sepehrnoori, K. (2009). Scale up Methodology for Wettability in Fractured Carbonates. *SPE Reservoir Simulation Symposium*, Texas, USA, SPE 118915.

Derakhshanfar, M., Nasehi, and M, Asghari, K., (2012). Simulation Study of CO_2-assisted Water Flooding for Enhanced Heavy Oil Recovery and Geological Storage. *Carbon Management Technology Conference*, Florida, USA, SPE 151183.

De Ruiter, R. A., Nash, L. J., and Singletary, M. S. (1994). Solubility and Displacement Behavior of a Viscous Crude with CO_2 and Hydrocarbon Gases. *SPE Annual Technical Conference and Exhibition*, New Orleans, U.S.A, SPE 20523.

Dhima, A., de Hemptinne, J. C., and Jose, J. (1999). Solubility of Hydrocarbons and CO_2 Mixtures in Water under High Pressure. *Ind. Eng. Chem. Res*, 38, 3144-3161.

Diamond, L. W., Akinfiev, N. N. (2003). Solubility of CO_2 in Water from -1.5 to 100°C and from 0.1 to 100 MPa: Evaluation of Literature Data and Thermodynamic Modeling. *Fluid Phase Equilibria* 208(1-2), 265-290.

Ding, M. and Kantzas, A. (2004). Capillary Number Correlations for Gas-Liquid Systems. *5th Canadian International Petroleum Conference*, Calgary, Canada, SPE 2004-062.

Development of Global Carbon Dioxide Emissions and Concentration in Atmosphere (2017). Retrieved from www.volker-quaschning.de/datserv/CO_2/index_e.php.

Doorwar, S. and Mohanty. K. K. (2015). Fingering Function for Unstable Immiscible Flows. *SPE Journal*. 22(1), 19-31, SPE 173290.

Dong, Y., Ishizawa, C., Lewis, Ed., and Dindoruk, B. (2011). C*arbonated Water flood: What We Observed in Sand-Pack Experiments, International Symposium of the Society of Core Analysis*, Austin, Texas, USA, SCA2011-34

Duan, Z., Moller, N., Greenberg, J., and Weare, J. H. (1992a). The Prediction of Methane Solubility in Natural Waters to High Ionic Strength from 0 to 25°C and from 0 to 1600 bar. *Geochimica and Cosmochimica Acta*, 56, 1451-1460.

Duan, Z. and Sun, R. (2003). An Improved Model Calculating CO_2 Solubility in Pure Water and Aqueous NaCl Solutions from 273 to 533 K and from 0 to 2000 bar. *Chemical Geology Journal*, 193, 257-271.

Duan, Z., Sun, R., Zhu, C., and Chou, M. (2006). An Improved Model for the Calculation of CO_2 Solubility in Aqueous Solutions Containing Na+, K+, Ca^{2+}, Mg^{2+}, Cl^-, and SO_4^{2-}. *Marine Chemistry Journal*, 98 (2), 131-139.

Dullien, F.A.L. (1979). Porous Media Fluid Transport and Pore Structure. *Academia Press*.

El-Dessouky, H. T. and Ettouney, H. M. (2002). Fundamentals of Salt Water Desalination. *Elsevier Science*.

El Ela, M. A., Sayyouh, H., El Tayeb E. S. (2014). An Integrated Approach for the Application of the Enhanced Oil Recovery Projects. *Journal of Petroleum Science Research*, 3(4).

Emera, M. K., Sarma, H. K. (2006). A Genetic Algorithm-Based Model to Predict CO_2-oil Physical Properties for Dead and Live Oil. *7th Canadian International Petroleum Conference, 57th Annual Technical Meeting*, Calgary, Canada, Paper 2006-197.

Emera, M. K., Sarma, H. K. (2007). Prediction of CO_2 Solubility in Oil and the Effects on the Oil Physical Properties. *Energy Sources, Part A: Recovery, Utilization, and Environmental Effects*, 29(13), 1233-1242.

Enick, R. M., Klara, S. M. (1990). CO_2 Solubility in Water and Brine under Reservoir Condition. *Chemical Engineering Communications Journal*, 90, 23-33.

Er, V, Babadagli, T. and and Xu, Z. (2010). Pore-Scale Investigation of the Matrix-Fracture Interaction During CO_2 Injection in Naturally Fractured Oil Reservoirs. *Energy Fuels*, 24, 1421-1430.

Sripal, E. and James. L. (2016). Application of an Optimization Method for Restoration of Core Samples for SCAL Experiments. *Society of Core Analysis*, U.S.A, SCA2016-002.

European Technology for Zero Emission Fossil Fuel Power Plants, Platform for The Costs of CO_2 Transport, 2010.

Fathi, S. J., Austad, T., and Strand, S. (2010). Smart Water as a Wettability Modifier in Chalk: The Effect of Salinity and Ionic Composition. *Energy Fuels*, 24, 2514-2519.

Fathollahi, A. and Rostami, B. (2015). Carbonated Water Injection: Effects of Silica Nanoparticles and Operating Pressure. *The Canadian Journal of Chemical Engineering*, 93(11), 1949-1956.

Firoozabadi, A. (2000). Recovery Mechanisms in Fractured Reservoirs and Field Performance. *Journal of Canadian Petroleum Technology*, 39(11), 13

Fyfe, W. S., Price, N. J., and Thompson, A. B. (1978). Fluids in the Earth's Crust, *Elsevier*.

Oceanography 101, Gases dissolved in seawater. (2017). Solubility of Gases Compared to CO_2. Retrieved from http://geologycafe.com/oceans/chapter7.html .

Gomari, K.A.R., Karrousi, O., and Hamouda A. A. (2006). Mechanistic Study of Interaction between Water and Carbonate Rocks for Enhanced Oil Recovery. *SPE Europec/EAGE Annual Conference and Exhibition*, Austria, SPE 99628.

Ghasemzdeh, A., Momeni, A., and Vatani., A. (2011). Application of Miscible CO_2 Injection to Maximize Oil Recovery in One of Iranian Unsaturated Oil Reservoirs, Simulation and Optimization Study. *SPE Enhanced Oil Recovery Conference*, Malaysia, SPE 144476.

Green, D. W. and Willhite, G. P. (1998). *Enhanced Oil Recovery*. U.S.A: *Society of Petroleum Engineers*.

Grigg, R. B. (1995). Dynamic Phase Composition, Density, and Viscosity Measurements during CO_2 Displacement of Reservoir Oil. *SPE International Symposium on Oil Field Chemistry*, San Antonio, USA, SPE 28974.

Grogan, A.T. and Pinczewski, W.V. (1987). The Role of Molecular Diffusion Processes in Tertiary CO_2 Flooding. *Journal of Petroleum Technology*, SPE-12706-PA.

Gu, F. (1998). Solubility of Carbon Dioxide in Aqueous Sodium Chloride Solution under High Pressure. *Journal of Chemical Engineering of Chinese Universities*, 12(2), 118-1231.

Guo, P., Wang, Zh., Shen, P., and Du, J. (2009). Molecular Diffusion Coefficients of the Multicomponent Gas-Crude Oil Systems under High Temperature and Pressure. *Industrial and Engineering Chemistry Research*, 48(19).

Gupta, S. P. and Greenkorn, R. A., (1974). An Experimental Study of Immiscible Displacement with an Unfavorable Mobility Ratio in Porous Media. *Water resources*, 10(2), 371-374.

Haghighi M., Xu, B., and Yortsos, Y.C. (1994). Visualization and Simulation of Immiscible Displacement in Fractured Systems Using Micromodels: I. Drainage. *Journal of Colloid and Interface science*, 166, 168-179.

Hamouda, A. A. and Alipour Tabrizy, V. (2013). The Effect of Light Gas on Miscible CO_2 Flooding to Enhance Oil Recovery from Sandstone and Chalk Reservoirs. *Journal of Petroleum Science and Engineering*, 108, 259-266.

Hamouda, A. A., Chukwudeme, E. A., and Mirza, D. (2009). Investigating the Effect of CO_2 Flooding on Asphaltenic Oil Recovery and Reservoir Wettability. *Journal of Energy & Fuels*, 23, 1118-1127.

Han, L. and Gu, Y. (2014). Optimization of Miscible CO2 Water-Alternating-Gas Injection in the Bakken Formation, *Journal of Energy and Fuel*, 28, 6811-6819.

Harvey, Allan H. (1996). Semi Empirical Correlation for Henry's Constants over Large Temperature Ranges. *AIChE Journal*, 42(5), 1491-1494.

Hatiboglu, C. U. and Babadagli, T. (2005). Visualization Studies on Matrix-Fracture Transfer Due to Diffusion. *6th Canadian International Petroleum Conference, 56th Annual Technical Meeting*, Calgary, Canada, Paper 2005-077.

Hickok, C. W., Christensen R. J., and Ramsay, H. J. (1960). Progress Review of the K&S Carbonated Waterflood Project. *Journal of Petroleum Technology*, SPE 1474-G.

Hickok, C. W. and Ramsay, H. J. (1962). Case Histories of Carbonated Waterfloods in Dewey-Bartlesville Field. *SPE Secondary Recovery Symposium*, Texas, U.S.A, SPE 333-MS.

Hilfer, R. (1996). Transport and Relaxation Phenomena in Porous Media. *Advances in Chemical Physic*s, 92, 299-424.

Hirasaki, G. J. (1991). Wettability: Fundamentals and Surface Forces. *SPE/DOE Enhanced Oil Recovery Symposium*, Tulsa, U.S.A, SPE 17367.

Holm, L. W. (1959). Carbon Dioxide Solvent Flooding for Increased Oil Recovery. *Oil Recovery Conference of the Permian Basin Section of the Society of Petroleum Engineers*, Texas, USA, SPE 1250G

Holm, L. W. and Josendal, V. A. (1974). Mechanisms of Oil Displacement by Carbon Dioxide. *Journal of Petroleum Technology*, 26(12),1427-1438.

Honarvar, B., Azdarpour, A., Karimi, M., Rahimi, A., Afkhami Karaei, M., Hamidi, H., Ing, J., and Mohammadian, E. (2017). Experimental Investigation of Interfacial Tension Measurement and Oil Recovery by Carbonated Water Injection: A Case Study Using Core Samples from an Iranian Carbonate Oil Reservoir. *Journal of Energy Fuels*, 31 (3), 2740-2748.

Hou, S. X., Maitland, G. C., and Trusler, J.P.M. (2013). Measurement and Modeling of the Phase Behavior of the (Carbon Dioxide + Water) Mixture at Temperatures from 298.15 K to 448.15 K, *The Journal of Supercritical Fluids*, 73, 87-96.

Hull, C. (1986). Apparatus for Production of Three-Dimensional Objects by Stereolithography. U.S. Patent 4,575,330.

Ilievaa, P., Kilzer, A., and Weidner, E. (2016). Measurement of Solubility, Viscosity, Density and Interfacial Tension of the Systems Tristearin and CO_2 and Rapeseed oil and CO_2, *Journal of Supercritical Fluids*, 117, 40-49.

International Energy Agency. (2017). Deep Energy Transformation Needed by 2050 to Limit Rise in Global Temperature. Retrieved from https://www.iea.org.

International Energy Outlook (2016). Retrieved from www.eia.gov/outlooks/ieo/world.cfm# us policies.

International Energy Agency, World Energy Outlook. (2006). Retrieved from http://mcensustainableenergy.pbworks.com/w/page/30058012/ Energy%20 Demand.

International Energy Agency. (2014). Publications, Scenarios and Projections. Retrieved from https://www.iea.org/publications/scenariosandprojections.

Javadpour, F. and Fisher, D. (2008). Nanotechnology-Based Micromodels and New Image Analysis to Study Transport in Porous Media. *Journal of Canadian Petroleum Technology*, 47(2), 30-37.

Johnson, W. E. (1952). Lab Experiments with Carbonated Water and Liquid Carbon Dioxide as Oil Recovery Agents. *Producer Monthly*, 15.

Juanes, R. and M. J. Blunt (2006). Analytical Solutions to Multiphase First-Contact Miscible Models with Viscous Fingering. *Transport in Porous Media*, 64(3), 339-373.

Jung, J. Y., Lee, J. W., and Kang,Y. T. (2012). Synthesis of Silica Nanofluid and Application to CO_2 Absorption, *Journal of Mechanical Science and Technology*, 26(8), 2285-2290.

Kamari, E., Shadizadeh, S. R., and Rashtchian, D. (2012). Effect of Fracture Geometrics on Breakthrough Time in Immiscible Displacement Process through Strongly Oil Wet Fractured Porous Media: Experimental Investigation. *Energy Sources Journal, Part A: Recovery, Utilization, and Environmental Effects*, 34(10), 867–876.

Kang, P. S., Se Lim, J., and Huh, C. (2016). Screening Criteria and Considerations of Offshore Enhanced Oil Recovery, *Energies*, 9, 44.

Kavousi, A., Torabi, F., Chan, C. W., and Shirif, E. (2014). Experimental Measurement and Parametric Study of CO_2 Solubility and Molecular Diffusivity in Heavy Crude Oil Systems, *Fluid Phase Equilibria*, 371, 57-66

Kechut, N. I., Sohrab, M., and Jamiolahmady, M. (2011). Experimental and Numerical Evaluation of Carbonated Water Injection (CWI) for Improved Oil Recovery and CO_2 Storage, *SPE EUROPEC/EAGE Annual Conference and Exhibition*, Austria, SPE 143005-MS.

Khatib, A. K., Earlougher, R. C., and Kantar, K. (1981). CO_2 Injection as an Immiscible Application for Enhanced Recovery in Heavy Oil Reservoirs. *SPE California Regional Meeting*, California, U.S.A, SPE 9928.

Kiepe, J., Horstmann, S., Fischer, K., and Gmehling, G. (2002). Experimental Determination and Prediction of Gas Solubility Data for CO_2 + H_2O Mixtures Containing NaCl or KCl at Temperatures Between 313 and 393 K and Pressures up to 10 MPa, *Industrial and Engineering Chemistry Research*, 41, 4393-4398.

Karadimitriou, N. K. and Hassanizadeh, S. M. (2012). A Review of Micromodels and Their Use in Two-Phase Flow Studies. *Soil Science Society of America*.

Klins, M. A. and Farouq Ali, S. M. (1982). Heavy Oil Production by Carbon Dioxide Injection, Journal of Canadian Petroleum Technology, 5, 64-72.

Koschel, D., Coxam, J. Y., Rodier, L., and Majer, V. (2006). Enthalpy and Solubility Data of CO_2 in Water and NaCl (aq) at Conditions of Interest for Geological Sequestration. *Fluid Phase Equilibria*, 247(1-2), 107-120.

Kulkarni, M. M. (2005). *Multiphase Mechanism and Fluid dynamics in Gas Injection Enhanced Oil Recovery Processes* (PhD Thesis). Louisiana State University, U.S.A.

Kulkarni, M. M. and Rao, D. N. (2004). Is Gravity Drainage an Effective Alternative to WAG? *AIChE Annual Meeting*, Austin, Texas, U.S.A.

Lago, M., Huerta, M., and Gomes, R. (2002). Visualization Study during Depletion Experiments of Venezuelan Heavy Oils using Glass Micromodel. *Journal of Canadian Petroleum Technology*, 4(1).

Laidlaw W. G. and Wardlaw N. C. (1983). A Theoretical and Experimental Investigation of Trapping in Pore Doublets, *Canadian Journal of Chemical Engineering*, 61(5), 719-727.
Lake L. W. (1989). *Enhanced oil Recovery*. U.S.A: Prentice-Hall, Englewood Cliffs.

Laroche, C., Vizika, O., Kalaydjian, F. (1999). Wettability Heterogeneities in Gas Injection; Experiments and Modeling. *Petroleum Geoscience*. 5(1), 65-69.

Lenormand, R., Zarcone, C., and Sarr, A. (1983). Mechanisms of the Displacement of one Fluid by Another in a Network of Capillary Ducts. *Journal of Fluid Mechanics*, 135, 337-353.

Lenormand, R. and Zarcone, C. (1984). Role of Roughness and Edges during Imbibition on Square Capillaries. *59th Annual Technical Conference and Exhibition of the Society of Petroleum Engineers of AIME*, Houston, Texas, SPE 13264.

Lenormand, R., Touboul, E., and Zarcone, C. (1988). Numerical Models and Experiments of Immiscible Displacements in Porous Media. *Journal of Fluid Mechanics*, 189, 165-187.

Leverett, M. C. (1938). *Flow of Oil-Water Mixtures through Unconsolidated Sands* (PhD Thesis). Massachusetts Institute of Technology, Houston, Texas, U.S.A.

Li, Z., Dong, M., Li, S., and Dai, L. (2004). Densities and Solubilities for Binary Systems of Carbon Dioxide plus Water and Carbon Dioxide plus Brine at 59ºC and Pressures to 29 MPa. *Journal of Chemical and Engineering Data*, 49 (4), 1026-1031.

Li, F. F., Yang, S. L., Chen, H., Zhang, X., Yin, D. D., He, L. P., and Wang, Z. (2015). An Improved Method to Study CO_2-Oil Relative Permeability under Miscible Conditions. *Journal of Petroleum Exploration and Production Technology*, 5, 45-53.

Lide, D. R. (1990). CRC Handbook of Chemistry and Physics, 71 Edition. Boca Raton, Ann Arbor, Boston, *CRC Press*.

Lohrenz, J., Bray, B., and Clark, C. (1964). Calculating Viscosities of Reservoir Fluids from Their Composition. Journal of Petroleum Technology, 16(10), 1171-1176.

Luo, H. and Kantzas, A. (2008). Investigation of Diffusion Coefficients of Heavy Oil and Hydrocarbon Solvent Systems in Porous Media, *SPE Symposium on Improved Oil Recovery*, Tulsa, Oklahoma, U.S.A, SPE 113995.

Lu, W., Guo, H., Chou, I.M., Burruss, R.C., and Li, L. (2013). Determination of Diffusion Coefficients of Carbon Dioxide in Water Between 268 and 473 K in a High-Pressure Capillary Optical Cell with in Situ Raman Spectroscopic Measurements. Geochimica et Cosmochimica Acta 115, 183-204.

Mahdavi, S. and James, L. (2016). Pore Scale Investigation of Carbonated Water Injection with and without Gravity, *International Symposium of the Society of Core Analysts*, Colorado, USA. SCA2016-037.

Mahdavi, S. and James, L. (2017). Investigation of Water Flooding and Carbonated Water Injection (CWI) in a Fractured Porous Media. *International Symposium of the Society of Core Analysts*, Vienna, Austria, SCA2017-058.

Mahmudi, M., Mahdavi, S., and James, L. (2018). A Quick and Low-Cost Method to Fabricate Glass Micromodel Networks. *Journal of Microsystem Technologies*, 24(5), 2419-2427.

Majlaton, N. I. (2012). *A Visual Study of CO_2 Injection at the Pore Scale using Micromodels* (MSC Thesis). University of Bergen, Norway.

Manique, E. J., Muci, V. E., and Gurfinkel, M. E. (2006). EOR Field Experiences in Carbonate Reservoirs in the United States, *SPE/DOE Symposium on Improved Oil Recovery*, Tulsa, USA, SPE 100063.

Martin, J. W. (1951). Additional Oil Production through Flooding with Carbonated Water, *Producers Monthly*, 15(9).

Martin, F. D., and Taber, J. J. (1992). Carbon Dioxide Flooding. *Journal of Petroleum Technology*, 44 (4), 396-400, SPE 23564.

Martin, J. W., Tuckahoe, N. Y. (1959). *Process of Recovering Oil from Oil Fields Involving the Use of Critically Carbonated Water*, U.S Patent 2875833.

Martinez, N., (2009). *Wettability of Silicon, Silicon Dioxide, and Organosilicate Glass* (MSc Thesis). University of North Texas, U.S.A.

Mattax, C. C. and Kyte, J. R. (1961). Ever See a Water Flood? *Oil Gas Journal*. 59, 115-128.

Mattax, C. C. and Kyte, J. R., (1962). Imbibition Oil Recovery from Fractured, Water-Drive Reservoir, *SPE Journal*, 2(2), 177-184, SPE-187-PA.

McKeller, M. and Wardlaw, N. C. (1983). A Method of Making Two-Dimensional Glass Micromodels of Pore Systems. *Journal of Canadian Petroleum Technology*, 21(4), 39-41.

McLachlan, C.N.S. and Danckwerts, P. V. (1972). Desorption of Carbon Dioxide from Aqueous Potash Solutions with and without the Addition of Arsenite as a Catalyst. *Trans. Inst. Chem. Eng*., 50, 300-309.

Miller, J. S. and Jones, R. A, (1981), A laboratory study to determine physical characteristics of heavy oil after CO_2 saturation, *SPE/DOE Enhanced Oil Recovery Symposium*, Tulsa, USA, SPE 9789.

Mohammadi, S., Maghzi, A., Ghazanfari, M. H., Masihi, M., Mohebbi, A., Kharrat, R. (2012). On the Control of Glass Micromodel Characteristics Developed by Laser Technology, *Journal of Energy Sources, Part A: Recovery, Utilization, and Environmental Effects*, 35(3), 193-201.

Mohd Noh, M. G., Hor, W. V., Jalani, M. Y., and Masoud, M. A. (2014). Optimizing energy Footprint for Offshore Separation, Transportation and Storage, *Offshore Technology Conference*, Malaysia, OTC-25051-MS.

Moritis, G. (2004). EOR Continues Unlock Oil Resources, Report on enhanced Oil Recovery, *Oil and Gas Journal*, 102(14), 45-65.

Mosavat, N. and Torabi, F. (2014). Experimental Evaluation of the Performance of Carbonated Water injection (CWI) under Various Operating Conditions in Light Oil Systems. *Fuel*, 123, 274-284.

Mosavat, N. (2014). *Utilization of Carbonated Water Injection (CWI) as a Means of Improved Oil Recovery in Light Oil Systems: Pore-Scale Mechanisms and Recovery Evaluation* (PhD Thesis). Regina University, Canada.

Mosavat, N. and Torabi, F. (2016). Micro-Optical Analysis of Carbonated Water Injection in Irregular and Heterogeneous Pore Geometry. *Fuel*, 175, 191-201.

Morrow, N., Chatzis, I., and Taber, J. (1988). Entrapment and Mobilization of Residual Oil in Bead Packs, *SPE Reservoir Engineering Proceedings*, Las Vegas, U.S.A, SPE 14423.

Muñoz, E. R., Winter, A., and Trevisan, O. V. (2015). Wettability Alternation in Limestone and Dolomite with Brines and CO_2, *Proceedings of the ASME 2015 34th International Conference on Ocean, Offshore and Arctic Engineering*, OMAE2015, St. John's, Newfoundland, Canada.

Nasehi Araghi, M. and Asghari, K. (2010). Use of CO_2 in Heavy-Oil Waterflooding. *SPE International Conference on CO_2 Capture, Storage and Utilization*, New Orleans, Louisiana, USA, SPE 139672-MS.

Nevers, N.D. (1964). A Calculation Method for Carbonated Water Flooding. *SPE Production Research Symposium*, 4(1), 9-20, SPE 569-PA.

Nguyen, V.H., Sheppard, A. P., Knackstedt, M.A., and Pinczewski, W.V. (2006). The Effect of Displacement Rate on Imbibition Relative Permeability and Residual Saturation, *Journal of Petroleum Science and Engineering*, 52, 54-70.

Nguyen, T.V, Tock, L., Breuhaus, P., Maréchal, F., and Elmegaard, B. (2016). CO_2-Mitigation Options for the Offshore Oil and Gas Sector. *Journal of Applied Energy* 161, 673-694.

Orr Jr. F. M., Yu, A. D., and Lien, C. L. (1980). Phase Behavior of CO_2 and Crude Oil in Low-Temperature Reservoirs. *SPE/DOE Symposium on Enhanced Oil Recovery*, Tulsa, U.S.A, SPE 8813.

Orr Jr. F.M., (2009). Onshore Geologic Storage of CO_2. *Science*, 325(5948), 1656-1658325.

Park, S., Kim, H., Kim, K., Lee, J., and Lho, D. S. (1999). Spectroscopic Measurement of the Acid Dissociation Constant of 2-naphthol and the Second Dissociation Constant of Carbonic acid at Elevated Temperatures. *Physical Chemistry Chemical Physics*, 1, 1893-1898.

Pedersen, K. S., Fredenslund, A., Chirstensen, P. L., and Thomassen, P. (1984). Viscosity of Crude Oils. Chemical Engineering Science, 39, 1011-1016.

Pedersen, K. S., Fredenslund, A., (1987). An Improved Corresponding States Model for Prediction of Oil and Gas Viscosities and Thermal Conductivities. Chemical Engineering Science, 42(1), 182-186.

Peksa, A. E., Karl-Heinz A. A., Zitha, P.L.J. (2013). Molecular Diffusion of CO_2 from Carbonated Water (CW) into the Oil-Experimental Observations. *SPE Asia Oil and Gas Conference*, Indonesia, SPE 165902.

Peng, D. Y., and Robinson, D. B. (1976). A New Two Constant Equation of State, *Industrial and Engineering Chemistry Research Fundamentals*, 15, 59-64.

Perez, J. M., Poston, S. W., and Sharif, Q. J. (1992). Carbonated Water Imbibition Flooding: An Enhanced oil Recovery Process for Fractured Reservoirs. *SPE/DOE 8th Symposium on Enhanced Oil Recovery*, Tulsa, Oklahoma, U.S.A, SPE 24164.

Perkins, T.K.J. and Johnston, O.C. (1963). A Review of Diffusion and Dispersion in Porous Media. *Society of Petroleum Engineering Journal*, 70-84, SPE 480.

Picha, M. S. (2007). Enhanced Oil Recovery by Hot CO_2 Flooding. *15th Middle east Oil and Gas Show*, Bahrain, SPE 105425.

Pooladi-Darvish, M. and Firoozabadi, A. (1998). Experiments and Modelling of Water Injection in Water-wet Fractured Porous Media. *49th Annual Technical Meeting on the Petroleum Society*, Calgary, Canada, SPE 98-55.

Puntervold, T. and Austad, T. (2007). Injection of Seawater and Mixtures with Produced Water into North Sea Chalk Formation: Impact on Wettability, Scale Formation, and Rock Mechanics

Caused by Fluid-rock Interaction. *SPE/EAGE Reservoir Characterization and Simulation Conference*, Abu Dhabi, UAE, SPE 11237.

Qasem, F. H., Sami Nashawi, I., Gharbi, R., Mir, M. I. (2008). Recovery performance of partially fractured reservoirs by capillary imbibition, *Journal of Petroleum Science and Engineering*, 60, 39-50.

Quake, S. R. and Scherer. A. (2000). From Micro to Nanofabrication with Soft Materials. *Science* 290(5496), 1536-1540.

Rapoport, L.A. and Leas, W.J. (1953). Properties of Linear Waterfloods, Trans AIME, *Journal of Petroleum Technology*, 198, 139-148.

Reid, R. C., Prauznitz, J. M., and Sherwood, T. K. (1977). The Properties of Gases and Liquids. 3rd Edition, *McGraw-Hill*, New York.

Renner, T. A. (1988). Measurement and Correlation of Diffusion Coefficients for CO_2 and Rich-Gas Applications. *SPE Reservoir Engineering* Journal, 3(2), 517-523.

Riazi, M. (2011). *Pore Scale Mechanisms of Carbonated Water Injection in Oil Reservoirs* (PhD Thesis). Herriot-Watt University, England.

Riazi, M., Sohrabi, M., and Jamiolahmady, M. (2011). Experimental Study of Pore-Scale Mechanisms of Carbonated Water Injection, *Journal of Transport in Porous Media*, 86, 73-86.

Righi, F. E., Royo, J., Gentil, P., Castelo, R., Del Monte, A., and Bosco, S. (2004). Experimental Study of Tertiary Immiscible WAG Injection. *SPE/DOE symposium on Improved Oil Recovery*, Oklahoma, U.S.A, SPE, 89360-MS.

Rojas, G. A., Farouq Ali S. M. (1988). Dynamics of Subcritical CO_2/Brine Floods for Heavy-Oil Recovery. SPE Reservoir Engineering, SPE 13598 PA.

Roof, J. G. (1970). Snap-Off of Oil Droplets in Water-Wet Pores. *Society of Petroleum Engineering Journal*, 10, 85, SPE, 2504-PA.

Rose, W. (2001). Modeling Forced versus Spontaneous Capillary Imbibition Processes Commonly Occurring in Porous Sediments. *Journal of Petroleum Science and Engineering*, 30, 155-166.

Saidi, A. M., (1987). Reservoir Engineering of Fractured Reservoirs, *Total Edition Press*.

Seyyedi, M., Sohrabi, M., and Farzaneh, A. (2015). Investigation of Rock Wettability Alteration by Carbonated Water through Contact Angle Measurements, *Energy Fuels*, 29, 5544-5553.

Seyyedi, M., Mahzari, P., and Sohrabi, M. (2017). An Integrated Study of the Dominant Mechanism Leading to Improved Oil Recovery by Carbonated Water Injection, *Journal of Industrial and Engineering Chemistry*, 45, 22-32.

Shakiba, M., Riazi, M., and Ayatollahi, Sh. (2015). Oil Recovery and CO_2 Storage through Carbonated Water Injection Process; Experimental Investigation on an Iranian Carbonate Oil Reservoir. *1st National Conference on Oil and Gas Fields Development*, Tehran, Iran.

Shakiba, M., Ayatollahi, Sh., And Riazi, M. (2016). Investigation of oil recovery and CO_2 storage during secondary and tertiary injection of carbonated water in an Iranian carbonate oil reservoir, *Journal of Petroleum Science and Engineering*, 137, 134-143.

Shenawi, S. H. and Wu, C.U. (1994). Compositional Simulation of Carbonated Waterfloods in Naturally Fractured Reservoirs. *SPE/DOE 9th Symposium on Improved Oil Recovery*, Tulsa, Oklahoma, U.S.A, SPE 27741.

Shu, G., Dong, M., Chen, S., and Luo, P. (2014). Improvement of CO_2 EOR Performance in Water-Wet Reservoirs by Adding Active Carbonated Water, *Journal of Petroleum Science and Engineering*, 121, 142-148.

Simon, R. and Graue, D. J. (1964). Generalized Correlations for Predicting Solubility, Swelling and Viscosity Behavior of CO_2-Crude Oil Systems, *39th Annual Fall Meeting*, Huston, U.S.A, SPE 917.

Sohrabi, M., Nor Idah Kechut, Riazi, M., Jamiolahmady, M., Ireland, S., and Robertson, G. (2012). Coreflooding Studies to Investigate the Potential of Carbonated Water Injection as an Injection Strategy for Improved Oil Recovery and CO_2 Storage. *Transport Porous Media Journal*, 91, 101-121.

Span, R. and Wagner, W. (1996). A New Equation of State for Carbon Dioxide Covering the Fluid Region from the Triple-Point Temperature to 1100 K at pressures up to 800 MPa. *Journal of Physical Chemistry*, 25, 1509.

Span, R., Gernert, J., and Jäger, A. (2013). Accurate Thermodynamic-Property Models for CO_2-rich Mixtures. *Energy Procedia*, 37, 2914-2922.

Soeno, T., Inokuchi, K., and Shiratori, S. (2004). Ultra-Water-Repellent Surface: Fabrication of Complicated Structure of SiO_2 Nanoparticles by Electrostatic Self-Assembled Films. *Applied Surface Science*, 237, 539-543.

Sohrabi, M., Emadi, A., Farzaneh, A., and Ireland, S. (2015). A Through Investigation of Mechanisms of Enhanced Oil Recovery by Carbonated Water Injection. *SPE Annual Technical Conference and Exhibition*, Texas, U.S.A, SPE 175159.

Sripal, E. and James, L. (2016). Application of an Optimization Method for Restoration of Core Samples for SCAL Experiments, *International Symposium of the Society of Core Analysts*, Colorado, USA.

Srivastava, R. K., Huang, S. S., and Dong, M. (2000). Laboratory Investigation of Weyburn CO_2 Miscible Flooding. *Journal of Canadian Petroleum Technology*, 39(2).

Stoll, W. M., Hofman, J. P., Faber, M. J., and van den Hoek, P. J. (2007). Toward Field-Scale Wettability Modification-The Limitations of Diffusive Transport. *SPE Reservoir Evaluation & Engineering*, 11(3), SPE 107095.

Sündermann, Landolt-Börnstein, J. (1986). Numerical Data and Functional Relationships in Science and Technology. *Group V: Geophysics and Space Research, Oceanography*, Springer, 3a Berlin.

Taber, J. J., Martin, F. D., and Serigth R. S. (1997). *EOR Screening Criteria Revisited-Part 1: Introduction to Screening and Enhanced Recovery Field Projects*. *SPE/DOE Symposium on Enhanced Oil Recovery*, Tulsa, Oklahoma, U.S.A, SPE 36385.

Tang G. Q. and Koscek, A. (2011). High Resolution of Imaging of Unstable Forced Imbibition in Brea sandstone. *Transport in porous media*, 86 (2), 617-634.

Terry, R. E. (2001). Enhanced Oil Recovery. *In Encyclopedia of Physical Science and Technology 3rd Edition, Academic Press*, 18, 503-518.

Thomas, F. B., Holowach, N., Zhou, X., Bennion, D. B., and Bennion, D.W. (1964). Miscible or Near-Miscible Gas Injection, Which Is Better? *SPE/DOE, 9th Symposium on Improved Oil Recovery*, Tulsa, Oklahoma, U.S.A, SPE 2781.

Thompson, L. F., Willson, C. G., and Bowden, M. J. (1983). *Introduction to Microlithography. ACS Symposium. Ser. 219. American Chemical Society*, Washington, DC.

Thompson, L. F., Willson, C. G., and Bowden, M. J. (1994). Introduction to Microlithography. *2nd Edition, American Chemical Society*, Washington, DC.

Tunnish, A., Shirif, E., and Henni, A. (2018). History Matching of Experimental and CMG-STARS Results. *Journal of Petroleum Exploration and Production Technology*, https://doi.org/10.1007/s13202-018-0455-2.

Unatrakarna, D., Asgharia, K., and Condora, J. (2011). Experimental Studies of CO_2 and CH_4 Diffusion Coefficient in Bulk Oil and Porous Media, *Energy Procedia*, 4, 2170-2177.

Upadhyaya, A. (2001). *Visualization of Four-Phase Flow Using Micromodels* (MSC Thesis). Stanford University, California, U.S.A.

Van Dijkum, C. E. and Walker, T. (1991). Fractured Reservoir Simulation and Field Development Natih Field, Oman. *SPE Annual Technical Conference and Exhibition*, Texas, U.S.A, SPE 22917.

Wegner, M. W. and Christie, J. M. (1983). Chemical Etching of Deformation Substructures in Quartz. Physical Chemistry of Minerals, 9(2), 67-78.

Verma, Mahendra K. (2010). Fundamentals of Carbon Dioxide-Enhanced Oil Recovery (CO_2-EOR)-A Supporting Document of the Assessment Methodology for Hydrocarbon Recovery Using CO_2-EOR Associated with Carbon Sequestration. *U.S. Department of the Interior, U.S. Geological Survey*.

Welker, J. R. and Dunlop, D. D. (1963). Physical Properties of Carbonated Oils, *Journal of Petroleum Technology*, 15(8), 873-876, SPE-567-PA.

Wendland, M., Hasse, H., and Maurer, G. (1999). Experimental Pressure-Temperature Data on Three- and Four-Phase Equilibria of Fluid, Hydrate, and Ice Phases in the System Carbon Dioxide-Water, *Journal of Chemical Engineering Data*, 44, 901-906.

McKee, B. N. (2007). *Carbon Capture and Storage: a WEC, Interim Balance*. World Energy Council Cleaner Fossil Fuels Systems Committee, United Kingdom.

Yang, D. and Gu, Y. (2004). Interfacial Interactions of Crude Oil-CO_2-Brine Systems Under Reservoir Conditions, *SPE Annual Technical Conference and Exhibition*, Houston, Texas, USA, SPE 90198.

Yang, D. and Gu, Y. (2008). Determination of Diffusion Coefficients and Interface Mass-Transfer Coefficients of the Crude Oil-CO_2 System by Analysis of the Dynamic and Equilibrium Interfacial Tensions. Industrial & Engineering Chemistry Research, 47(15), 5447-5455.

Yoshimitsu, Z., Nakajima, A., Watanabe, T., and Hashimoto, K. (2002). Effects of Surface Structure on the Hydrophobicity and Sliding Behavior of Water Droplets. *Langmuir*, 18(15), 5818-5822.

Yousef, A.A., Al Saleh, S., and Al-Jawfi, M. (2011). Smart Water Flooding for Carbonated Reservoirs, Salinity and Role of Ions. *SPE Middle East Oil and Gas Show and Conference*, Manama, Bahrain, SPE 141082.

Zarghami, Sh., Boukadi, F., and Al-Wahaib, Y. (2017). Diffusion of Carbon Dioxide in Formation Water as a Result of CO_2 Enhanced Oil Recovery and CO_2 Sequestration, Journal of Petroleum Exploration and Production Technology, 7(1), 161-168.

Appendix A: Micromodel Images

Micromodel images of all the explained experiments at Chapter 5 are shown below.

Simple Water Flooding in the Absence of Gravity in the Homogeneous Micromodel

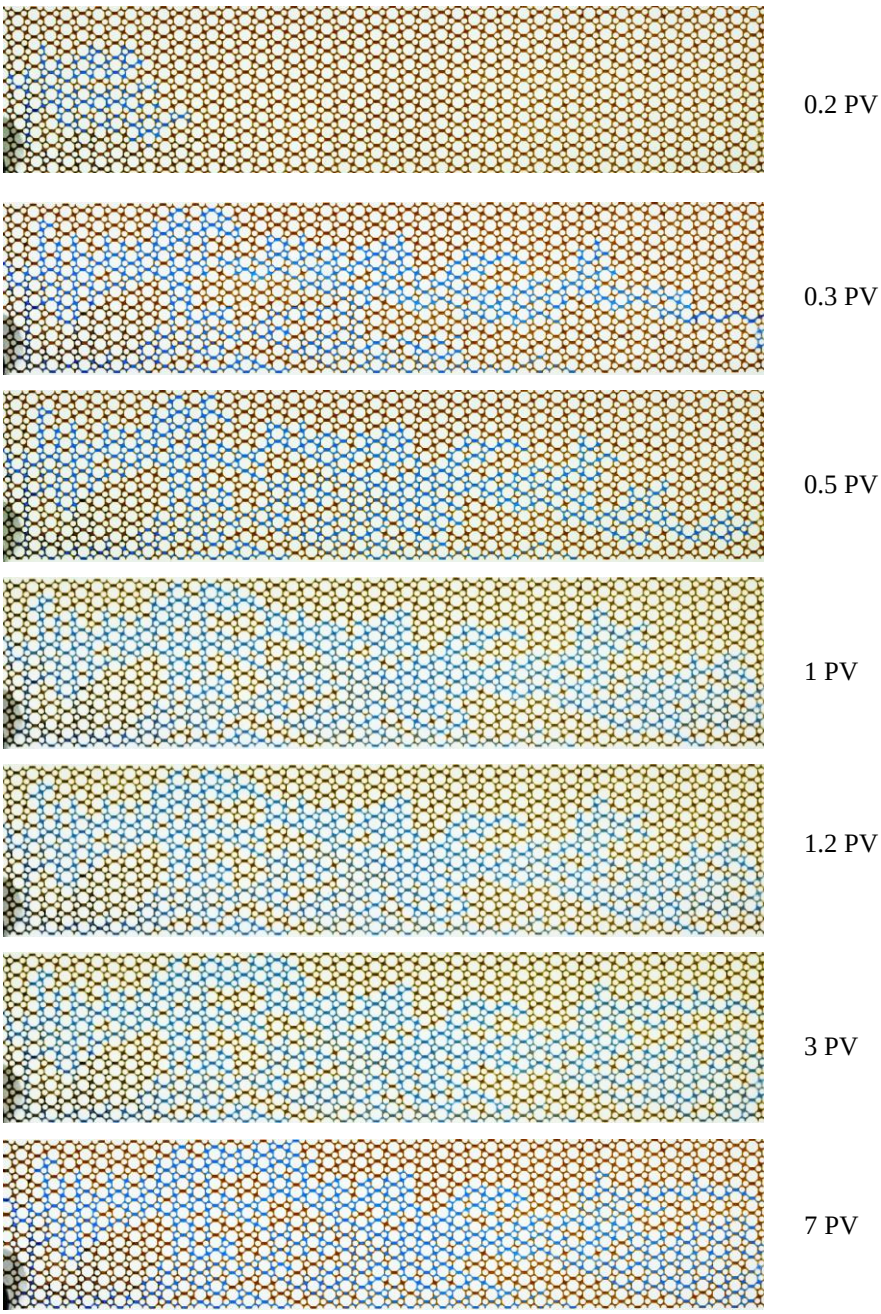

Figure A–1: Simple water flooding in the absence of gravity in the homogeneous micromodel

Simple Water Flooding in the Absence of Gravity in the Homogeneous Micromodel

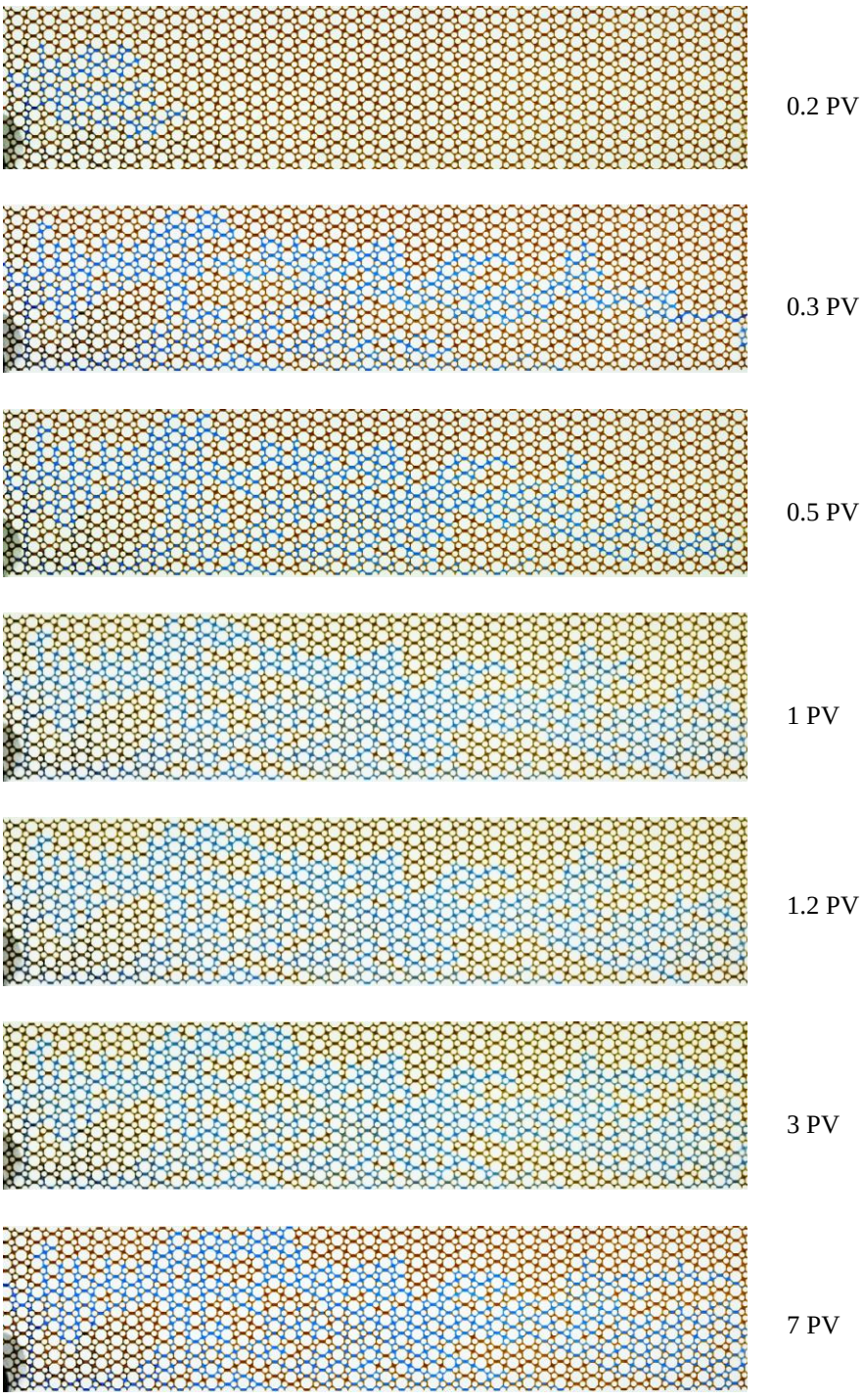

Figure A–2: Simple water flooding in the absence of gravity in the homogeneous micromodel

Simple Water Flooding in the Presence of Gravity in Horizontal Fracture Micromodel

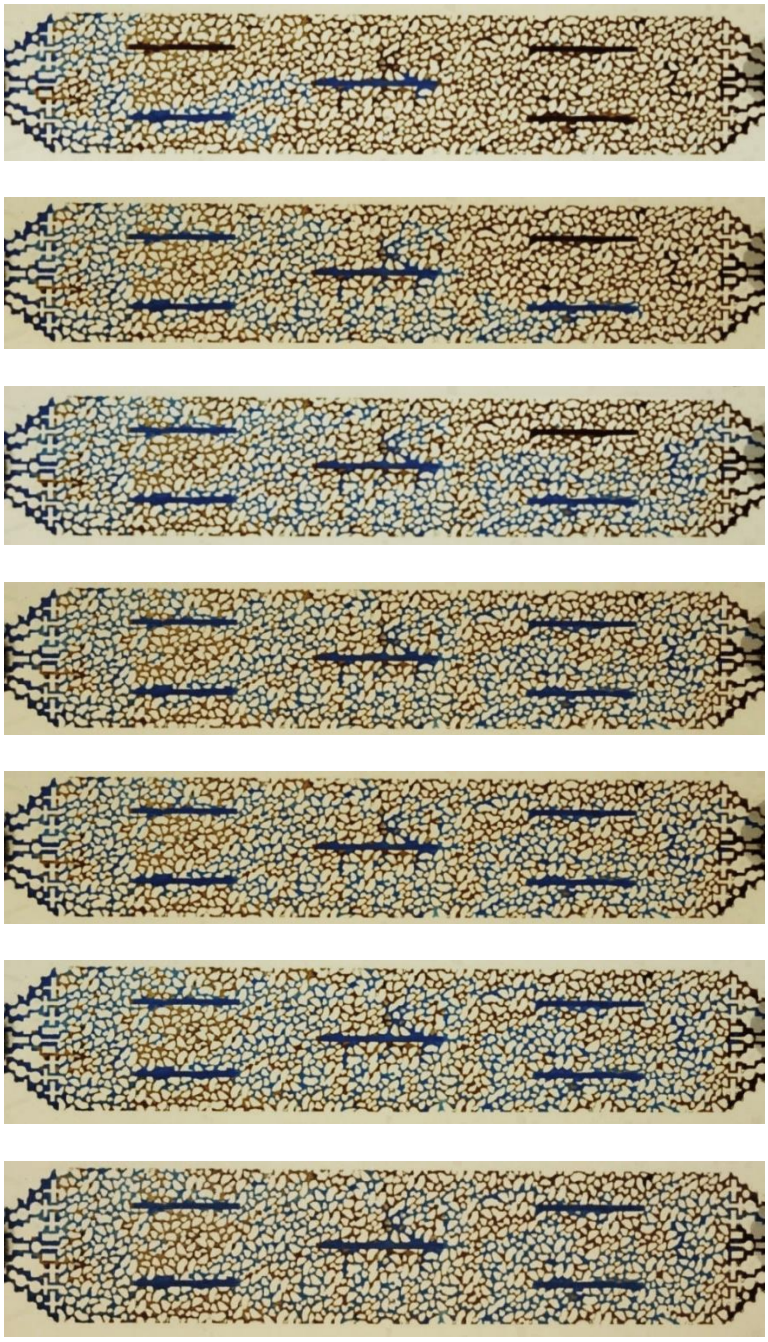

Figure A–3: Simple water flooding in the presence of gravity in the horizontal fractures micromodel

Simple Water Flooding in the Absence of Gravity in the Horizontal Fracture Micromodel

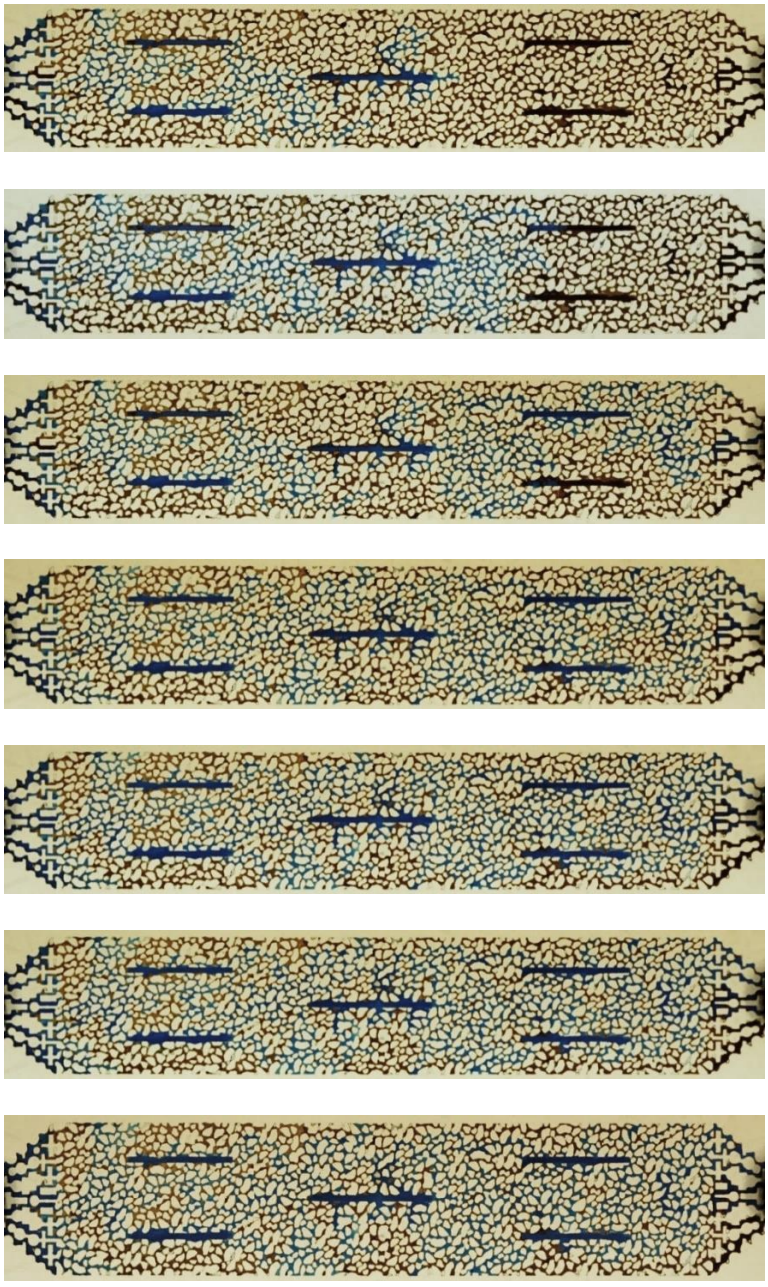

Figure A–4: Simple water flooding in the absence of gravity in the horizontal fracture micromodel

Water Flooding in the Presence of Gravity in the Vertical Fracture Micromodel

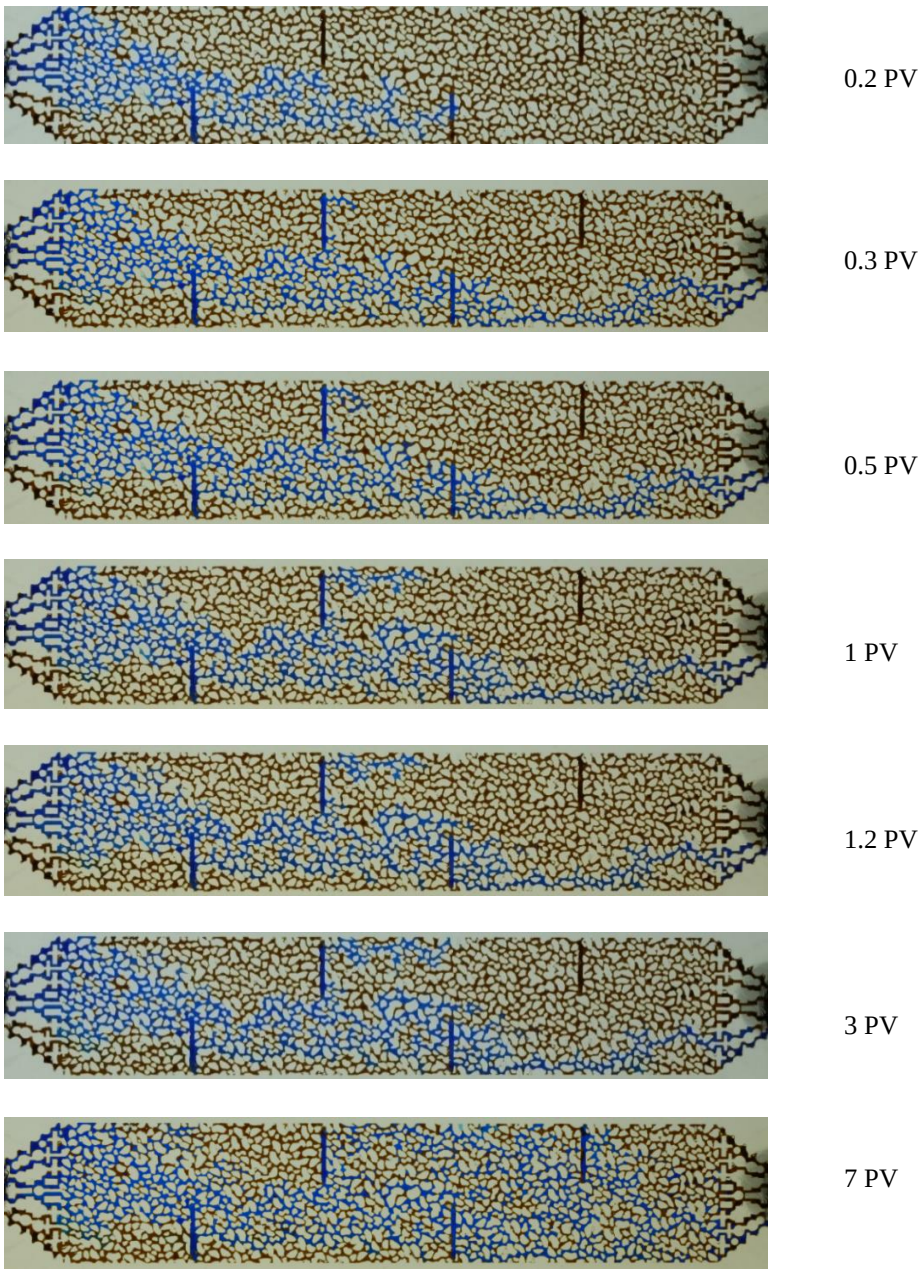

Figure A–5: Simple water flooding in the presence of gravity in the vertical fracture micromodel

Simple Water flooding in the Absence of Gravity in the Vertical Fracture Micromodel

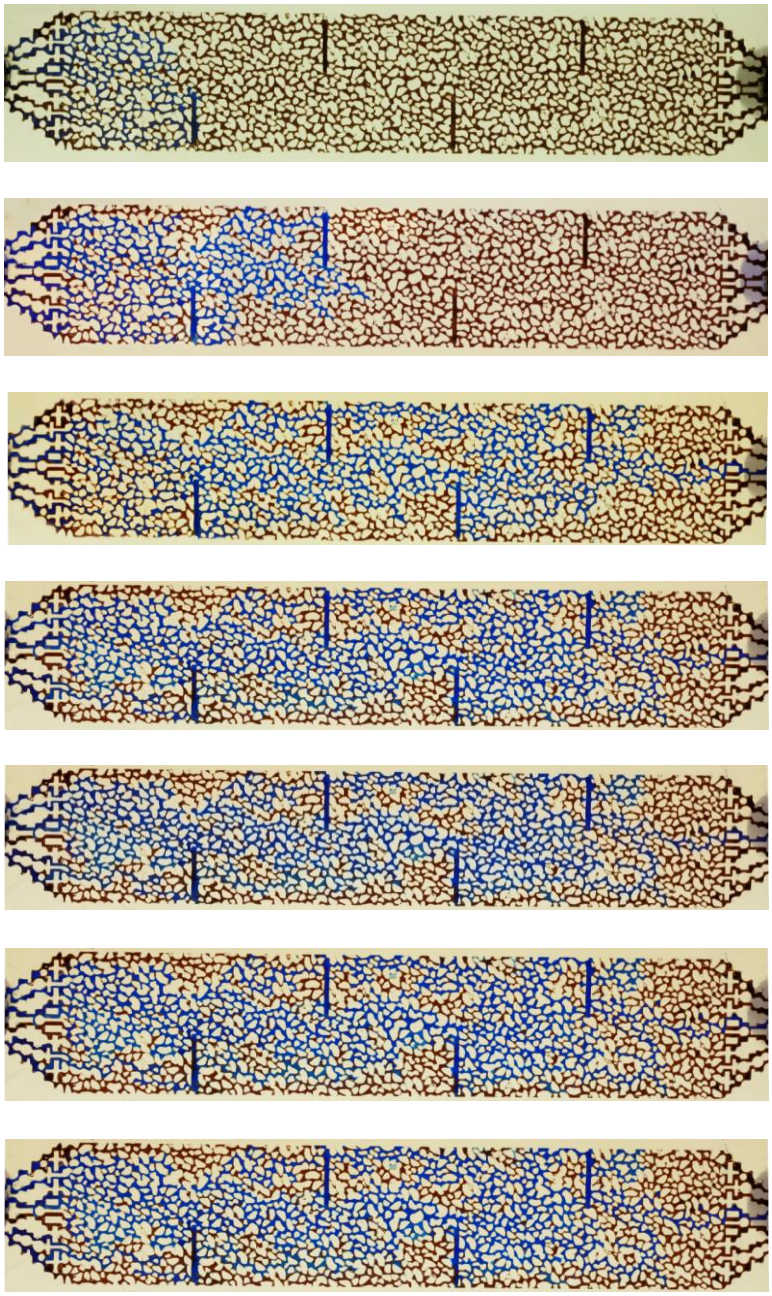

Figure A–6: Simple water flooding in the absence of gravity in the vertical fracture micromodel

Secondary CWI in the Presence of Gravity in the Homogeneous Micromodel

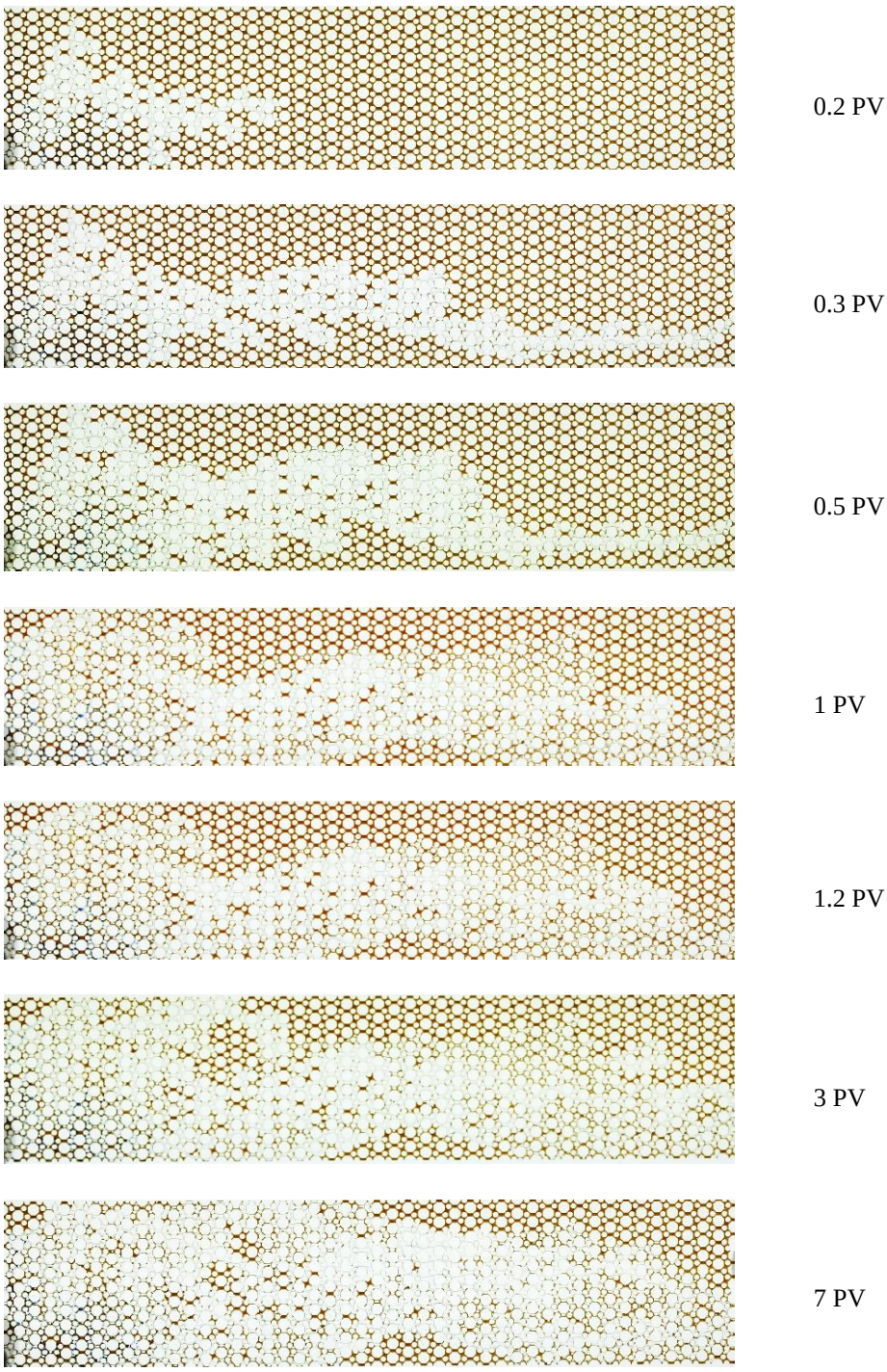

Figure A–7: Secondary CWI in the presence of gravity in the homogeneous micromodel

Secondary CWI in the Absence of Gravity in the Homogeneous Micromodel

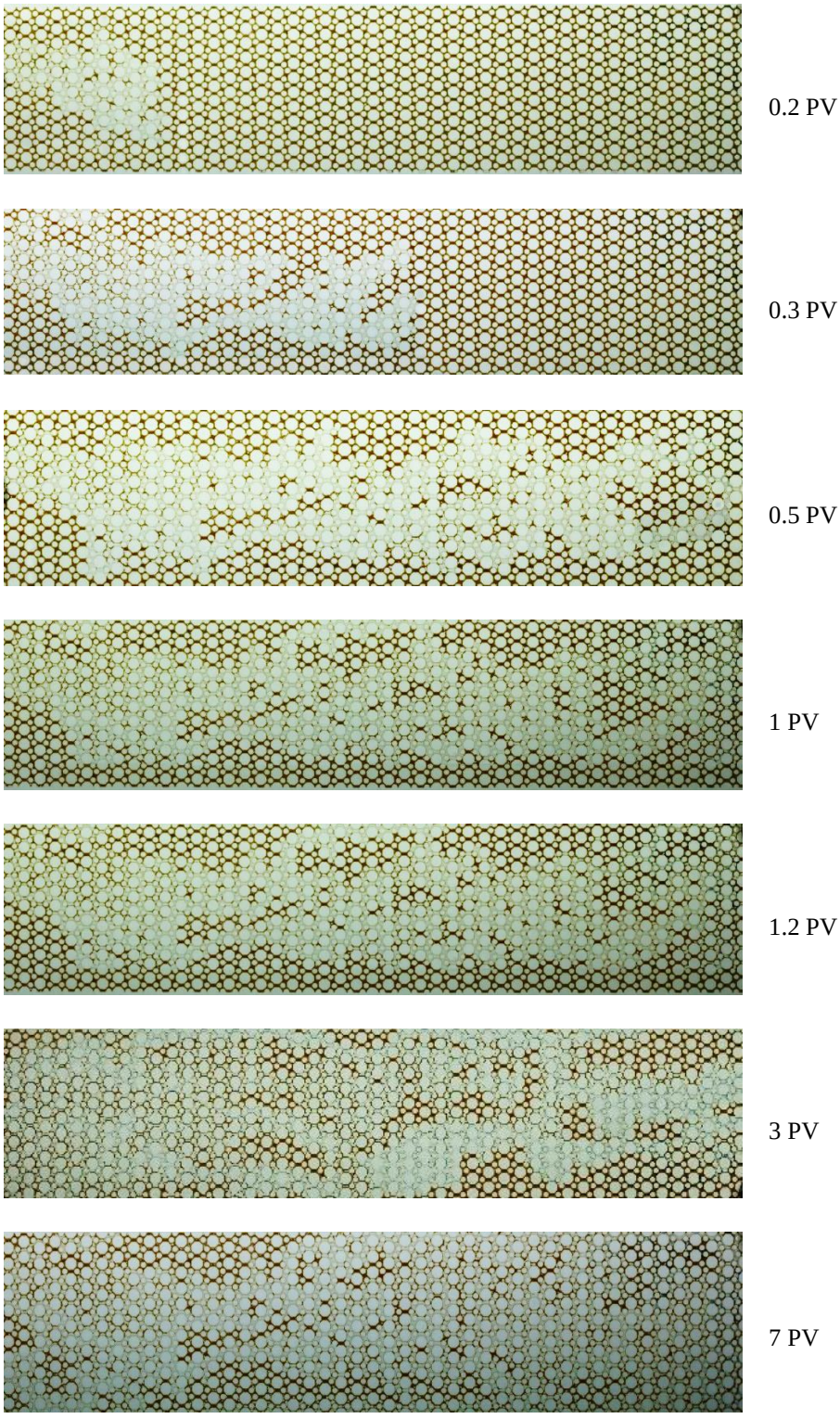

Figure A–8: Secondary CWI in the absence of gravity in the homogeneous micromodel

Secondary CWI in the Presence of Gravity in the Homogeneous Micromodel at High Flowrate (0.004 ml/min)

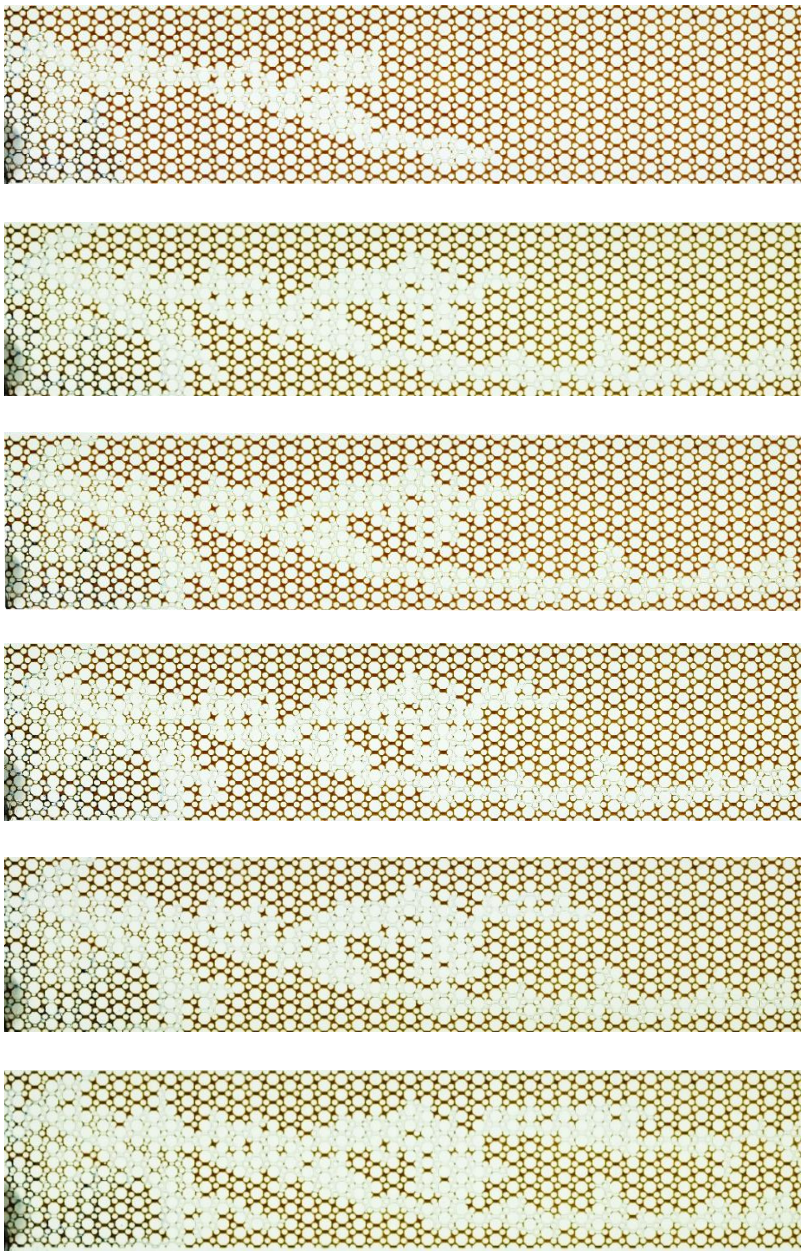

Figure A–9: Secondary CWI in the presence of gravity in the homogeneous micromodel, 0.004 ml/min

Secondary CWI in the Presence of Gravity in the Horizontal Fracture Micromodel

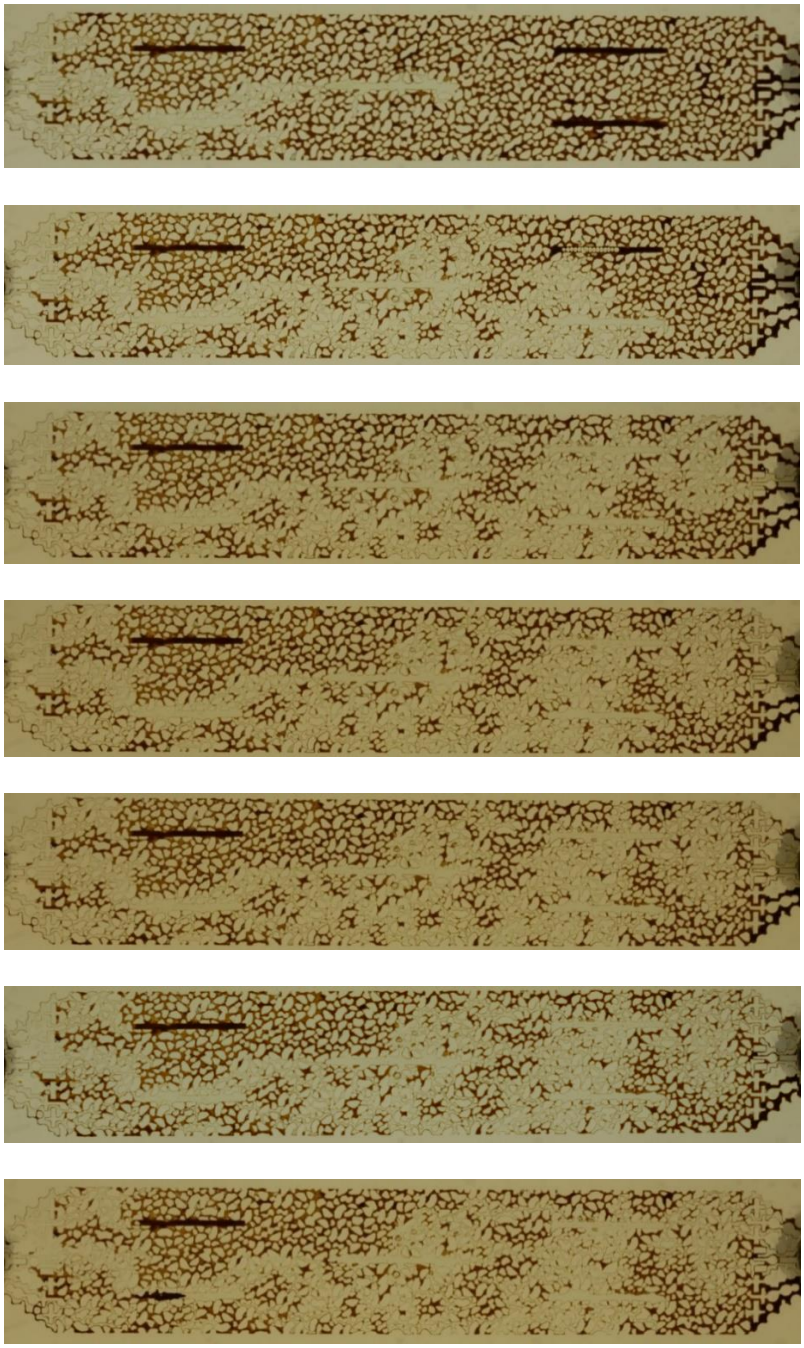

Figure A–10: Secondary CWI in the presence of gravity in the horizontal fracture micromodel

Secondary CWI in the Absence of Gravity in the Horizontal Fracture Micromodel

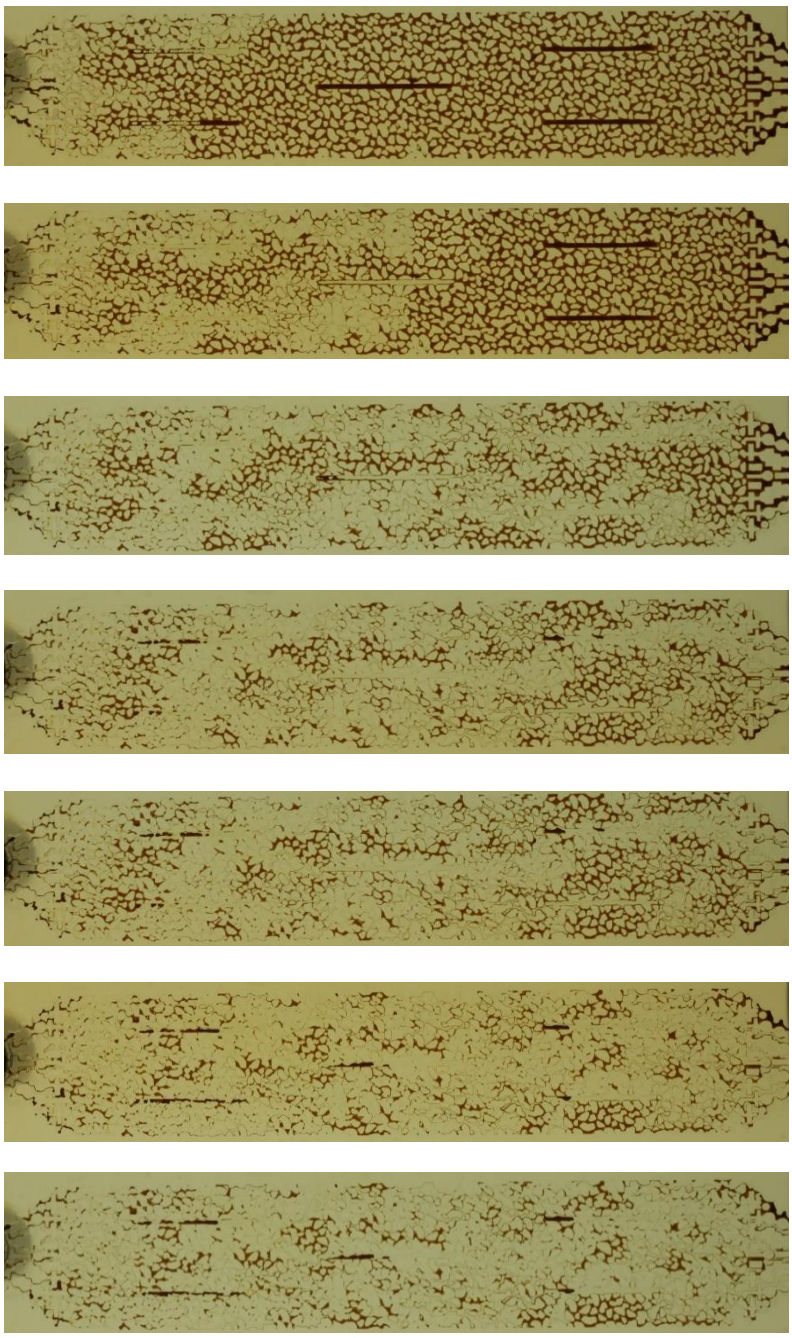

Figure A–11: Secondary CWI in the absence of gravity in the horizontal fracture micromodel

Secondary CWI in the Presence of Gravity in the Horizontal Fracture Micromodel at Low Flowrate (0.0008 ml/min)

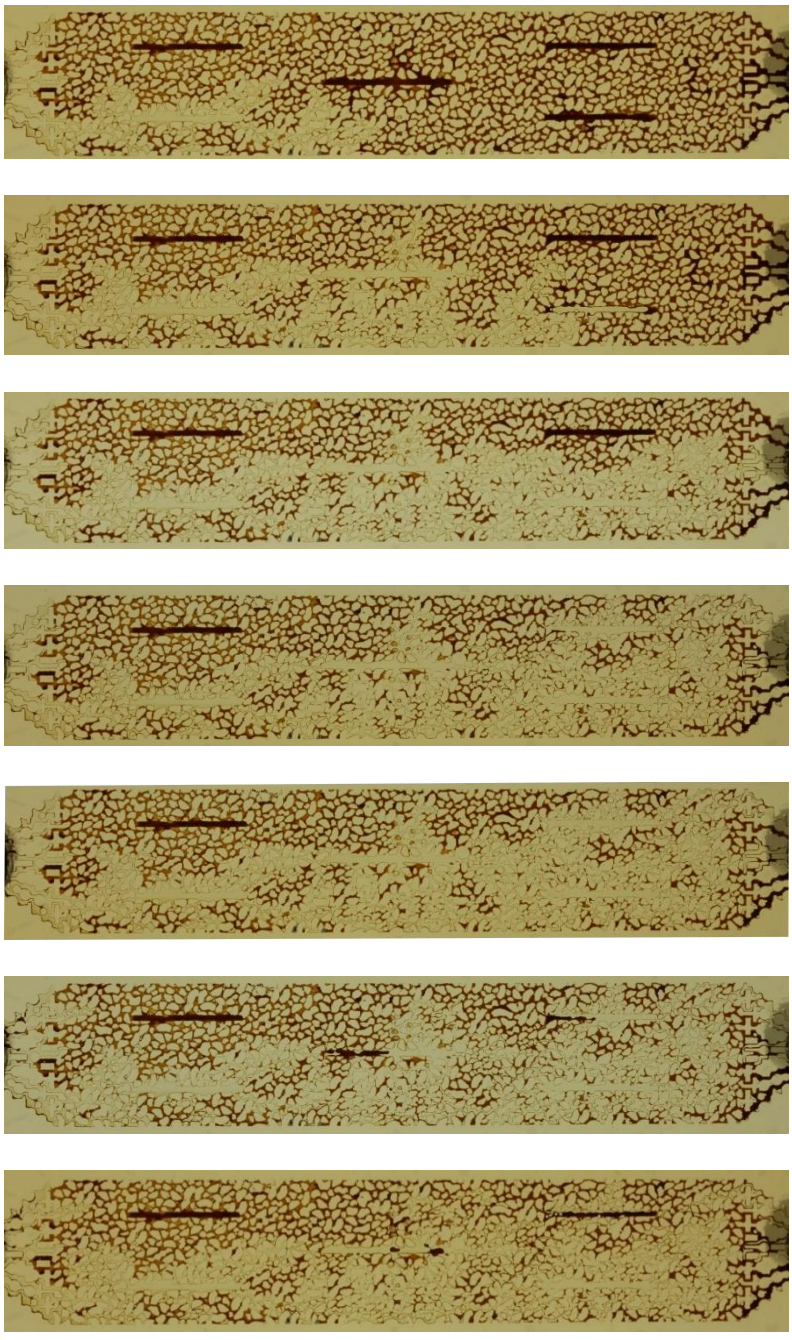

Figure A–12: SCWI flooding in the presence of gravity in the horizontal micromodel at low flowrate (0.0008 ml/min)

Secondary CWI In the Presence of Gravity in the Vertical Fracture Micromodel

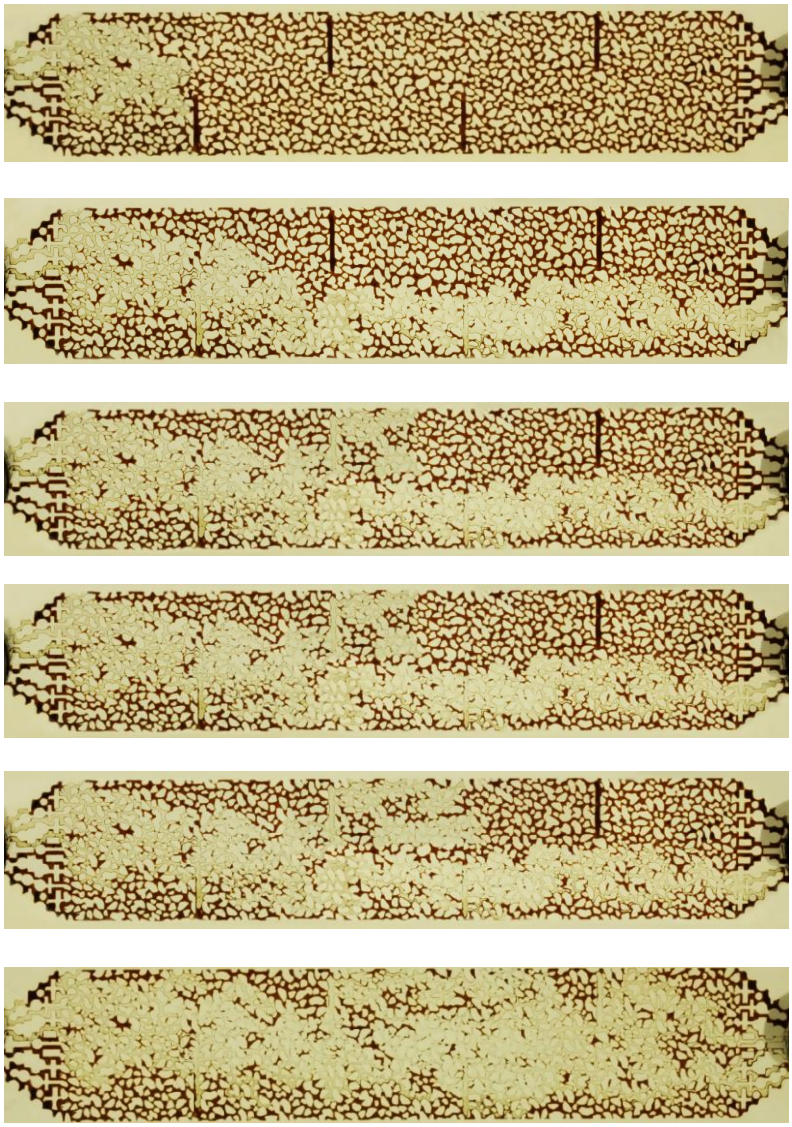

Figure A–13: Secondary CWI in the presence of gravity in the vertical fracture micromodel

Secondary CWI In the Absence of Gravity in the Vertical Fracture Micromodel

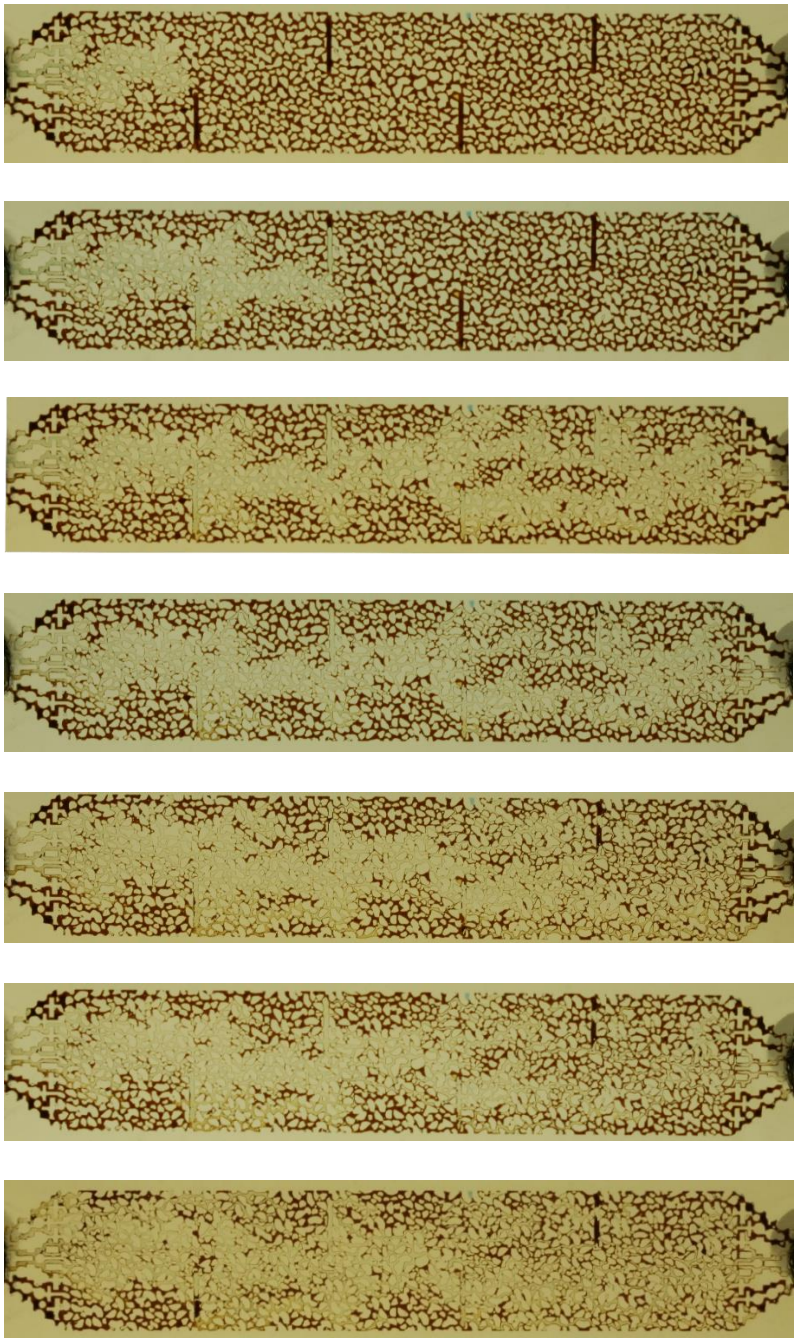

Figure A–14: Secondary CWI in the absence of gravity in the vertical fracture micromodel

Tertiary CWI in the Presence of Gravity in the Homogeneous Micromodel

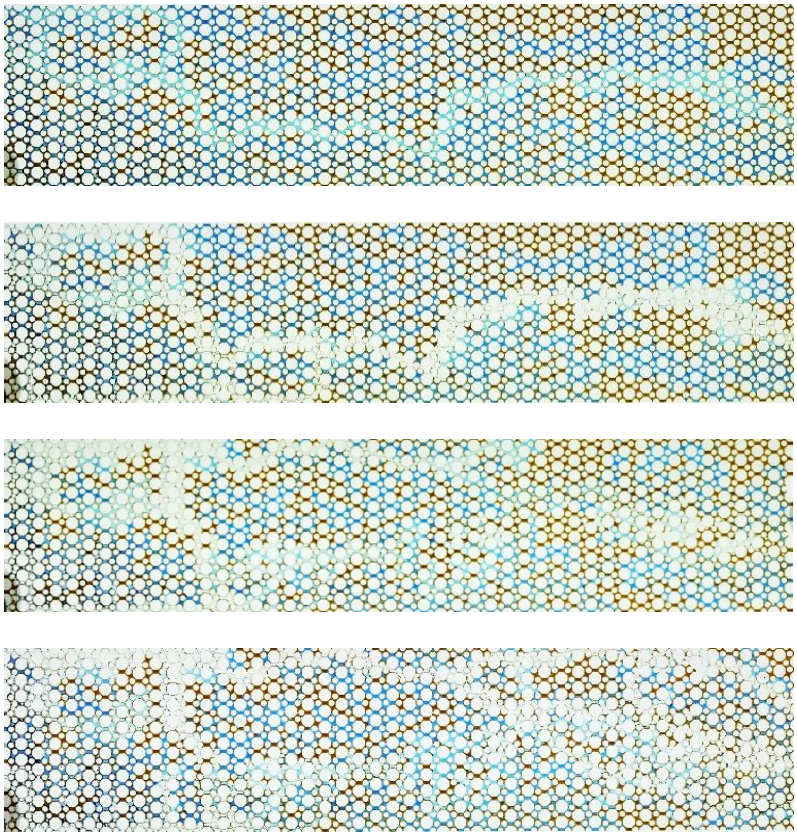

Figure A–15: Tertiary CWI in the presence of gravity in a homogeneous micromodel

Tertiary CWI in the Presence of Gravity in the Horizontal and Vertical Fracture Micromodels

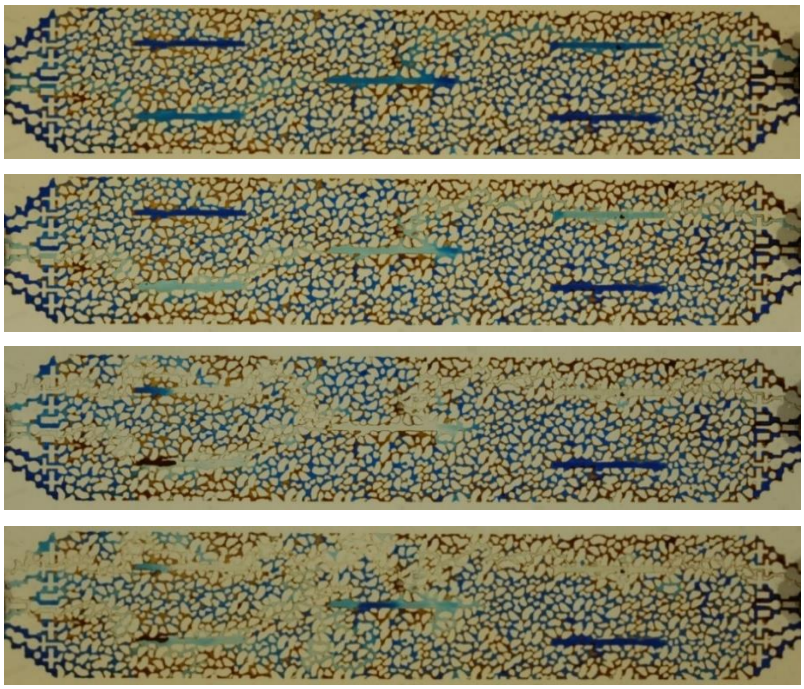

2.12 PV injection including 0.12 PV CW

3.12 PV injection including 1.12 PV CW

5.12 PV injeciton including 3.12 PV CW

7.12 PV injeciton including 5.12 PV CW

Figure A–16: Tertiary CWI in the presence of Gravity in the horizontal fracture micromodel

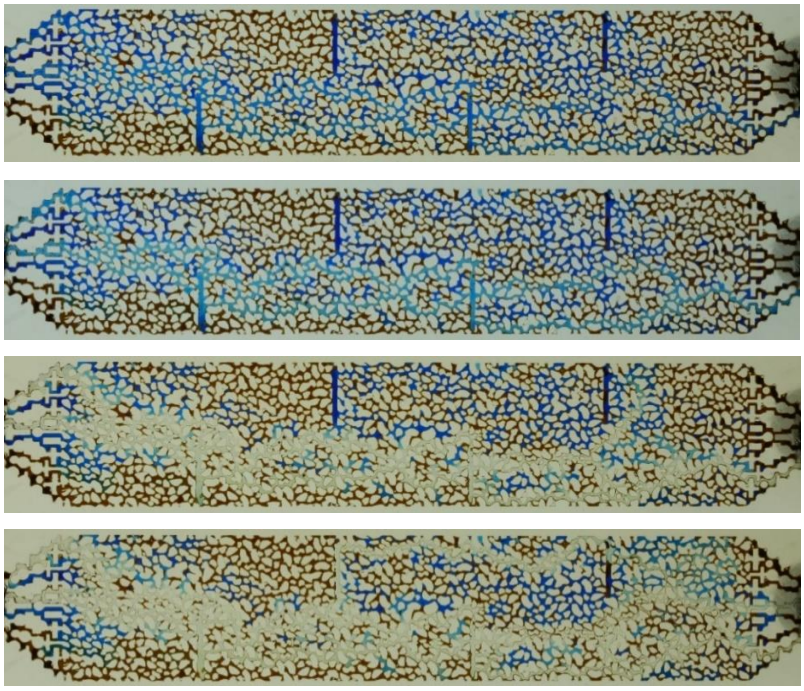

2.12 PV injection including 0.12 PV CW

3.12 PV injection including 1.12 PV CW

5.12 PV injections including 3.12 PV CW

7.12 PV injections including 5.12 PV CW

Figure A–17: Tertiary CWI in the presence of gravity in the vertical fracture micromodel

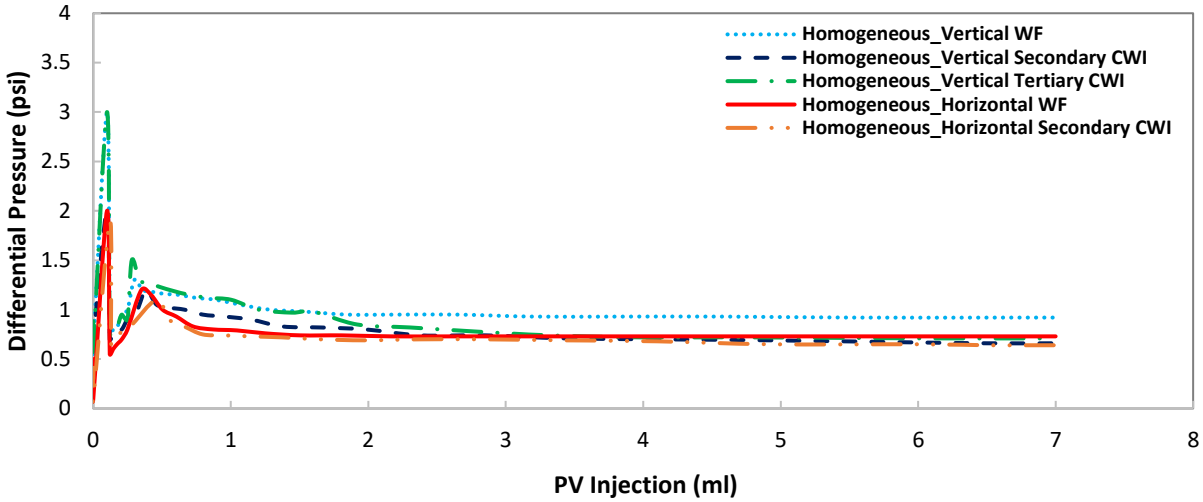

Figure A–18: Differential pressure for homogeneous micromodel experiments

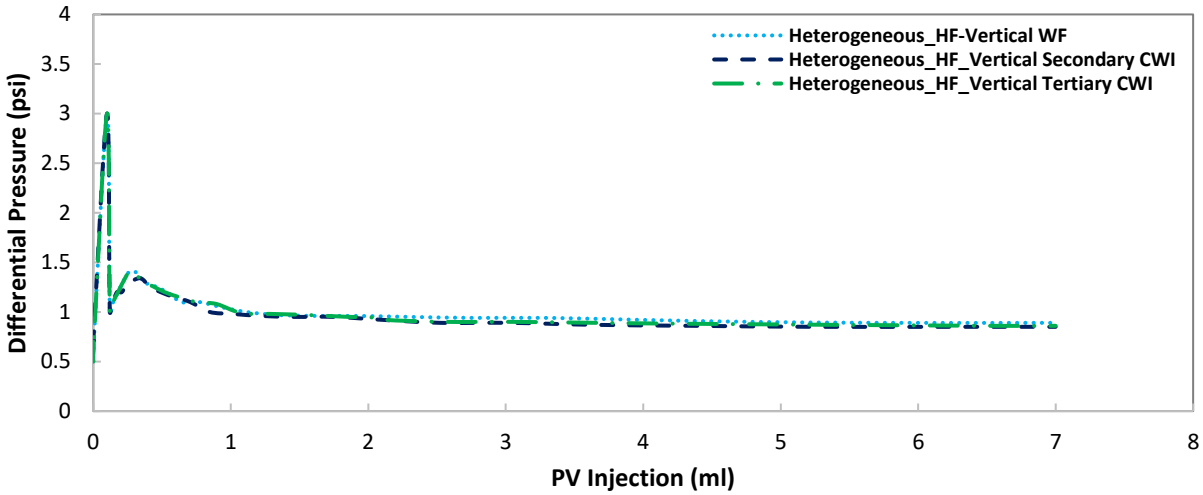

Figure A–19: Differential pressure for horizontal fracture micromodel experiments

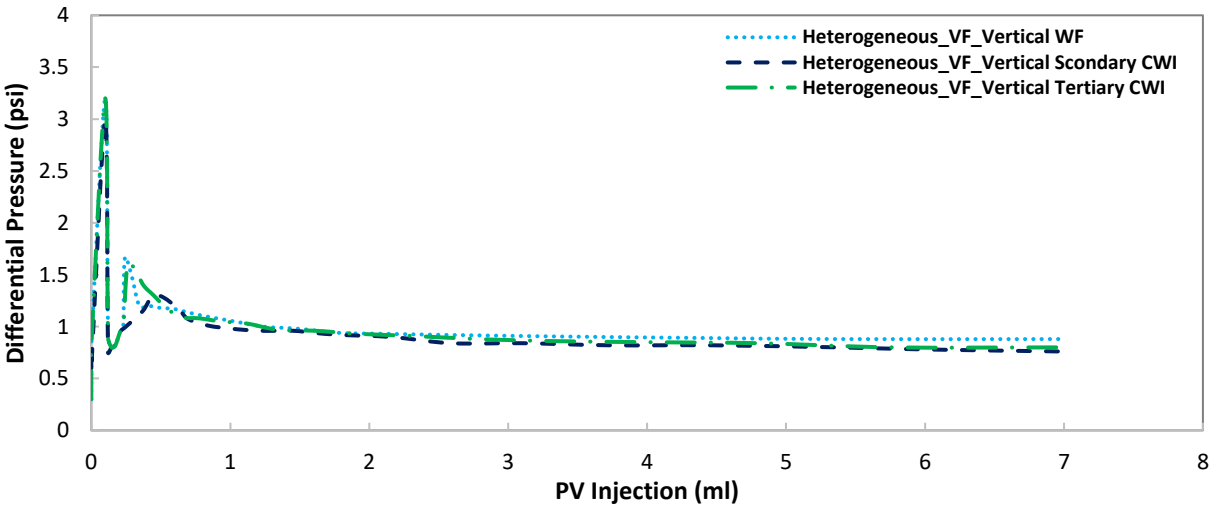

Figure A–20: Differential pressure for vertical fracture micromoel experiments

Appendix B: Image Analysis and Saturation Measurements

Although the main purpose of micromodel experiments is to qualitatively analyze the information about fluid flow mechanisms, the results can also be quantitatively processed using image analysis techniques. In this research, the captured images during the experiments were analyzed using an in-house image analysis software, which was written by image processing functions available in LabVIEW. The image processing program works in six steps: i) initialization, ii) monochrome plane extraction, iii) background correction, iv) segmentation, v) particle analysis, and vi) calculation.

In the initialization step, a set of captured images at different pore volumes was loaded to the software. It should be noted that during the experiment the position of the camera should be constant to have consistent conditions for all the pictures and the light source should have a diffuser to distribute the light evenly all over the micromodel. After loading the images, one of the images was selected and cropped to delete the extra region around the pattern. Then, this coordination was applied to all the images.

In the monochrome plane extraction step (second step), the initial color image (RGB) was displayed in RGB color space. The RGB color image was transformed into other color spaces by utilizing linear or nonlinear transformation techniques. The purpose of transformation is to differentiate between the fluid phases and the background. The output of this step was a histogram, which describes the frequency of each phase as opposed to its intensity. Additionally, matching intensity intervals (also called cluster) with each current fluid phase region (oil phase, water phase, and grain phase) during the micromodel visualization were highlighted in histograms. Therefore,

based on visual observation of histograms, the possible representative monochrome plane from the extracted components of pre-defined color systems (RGB and HSI-based systems) was selected and assigned for further segmentation of the flowing phases in the micromodel. If a histogram performed a distinguishable peak (high contrast) and had a smooth shape (low noise) then the corresponding region was adequately addressed by setting parameters.

If there was uneven luminosity in the image, the background was corrected in the non-uniform background correction step (third step) by changing different filters. The result of three previous processes was a gray image, which is the input of step iv to be segmented. Segmentation consisted of assigning thresholding functions to recognize different phase regions (oil, water, and grain). All three steps ii) monochrome plane extraction, iii) background correction, iv) segmentation were repeated for each of the phases of oil, water, and grain to select the appropriate settings for selected functions with respect to intensity range, threshold method and the equivalent gray plane. After configuring the controlling parameters, all the images in the initialized global cluster will be recalled and processed in batch mode to generate binary images for step 5 (particle analysis). In the last step, the quantitative analysis was reported in terms of saturation (percentage).

Appendix C: Core Flooding Data

Seawater Flooding Experiment

Time	Cum. volume injected (ml)	Cum produced oil (ml)	Cum. produced water (ml)	P_{in} (psi)	P_{out} (psi)
2:18 pm	0.00	0.0	0.0	4804.37	4802.87
2:21	0.78	0.7	0.0	4704.57	4689.57
2:25	1.59	1.5	0.0	4585.21	4578.51
2:30	2.58	2.5	0.0	4585.25	4578.25
2:35	3.60	3.5	0.0	4585.32	4578.22
2:40	4.42	4.3	0.0	4585.42	4578.12
2:49	6.38	6.2	0.0	4585.61	4577.21
2:55	7.59	7.4	0.0	4584.97	4575.47
3:00	8.41	8.2	0.0	4587.38	4577.58
3:05	9.59	9.4	0.0	4586.59	4577.36
3:08	10.09	9.7	0.1	4585.85	4576.85
3:11	10.69	9.7	0.7	4585.58	4576.68
3:18	12.00	9.8	2.0	4585.64	4576.78
3:24	13.35	9.8	3.3	4586.11	4577.46
3:34	15.38	9.8	5.3	4585.54	4576.78
3:40	16.53	9.8	6.5	4585.66	4577.02
3:46	17.69	9.8	7.7	4585.64	4577.01
3:59	20.32	9.8	10.3	4585.15	4576.50
4:05	21.43	9.8	11.4	4586.27	4577.42
4:12	22.94	9.9	13.0	4586.27	4577.42
4:16	23.62	9.9	13.6	4585.83	4577.32
4:28	26.04	9.9	16.0	4585.71	4577.20
4:59	32.16	9.9	22.2	4585.64	4577.13
5:18	36.05	9.9	26.1	4585.51	4577.00
6:18	48.20	9.9	38.2	4585.45	4576.94
7:18	60.00	9.9	50.3	4585.33	4576.82
8:20	72.50	9.9	62.3	4585.53	4576.70
9:15	84.40	9.9	74.5	4585.41	4577.20
10:18	96.50	9.9	86.7	4586.27	4577.42
11:18	108.9	9.9	99.0	4584.47	4575.96
00:20 am	120.0	9.9	111.1	4585.20	4576.69

Secondary CWI Experiment

Time	Cum. volume injected (ml)	Cum. produced oil (ml)	Cum. produced water (ml)	P_{in} (psi)	P_{out} (psi)
1:20 pm	0.00	0.0	0.0	4798.30	4800.00
2:20	12.13	10.6	2.4	4570.27	4579.27
2:25	13.09	10.7	3.4	4639.00	4650.00
2:31	14.27	10.8	4.6	4573.93	4579.93
2:35	15.06	10.8	5.5	4573.77	4579.87
2:43	16.67	10.9	7.1	4578.87	4569.87
2:48	17.62	11.0	8.0	4578.80	4569.90
2:58	19.64	11.1	10.1	4578.73	4569.88
3:11	22.22	11.2	12.7	4578.67	4569.77
3:24	24.89	11.3	15.4	4578.60	4569.87
3:34	26.91	11.4	17.4	4578.54	4569.90
3:57	31.43	11.5	21.9	4578.47	4569.92
4:16	35.34	11.6	25.8	4578.41	4569.91
4:43	40.69	11.8	31.0	4578.34	4569.97
5:00	44.06	11.8	34.7	4578.27	4569.99
5:13	46.61	11.8	37.0	4578.21	4569.96
5:20	48.00	11.9	39.7	4578.14	4569.64
5:38	51.68	12.0	42.0	4578.07	4569.85
6:10	58.13	12.0	48.5	4578.01	4569.86
6:33	62.75	12.1	53.0	4577.94	4569.84
7:01	68.26	12.1	58.6	4577.88	4569.75
7:36	75.28	12.2	65.5	4577.81	4569.73
7:49	77.97	12.2	68.2	4577.75	4569.69
8:14	82.94	12.3	73.2	4577.68	4569.64
8:43	88.67	12.3	78.9	4577.61	4569.60
9:07	93.51	12.3	83.6	4577.55	4569.50
9:28	97.79	12.4	87.9	4577.48	4569.48
9:53	102.78	12.4	92.8	4577.41	4569.49
10:01	104.36	12.4	94.4	4577.35	4569.46
10:20	108.00	12.4	98.0	4577.28	4569.48
10:49	113.90	12.5	103.9	4577.22	4569.35
11:46	125.28	12.5	115.2	4577.16	4569.30
00:36 am	135.38	12.6	125.2	4577.09	4569.24
1:15	143.02	12.6	132.8	4577.03	4569.19
1:54	150.82	12.6	140.6	4576.96	4569.13
2:20	156.00	12.7	145.7	4576.90	4569.08
2:48	161.63	12.7	151.3	4578.87	4569.87
3:47	173.59	12.7	163.2	4578.80	4569.90
4:15	178.71	12.7	168.3	4578.73	4569.88

Tertiary CWI Experiment

Time	Cum. volume injected (ml)	Cum. produced oil (ml)	Cum. produced water (ml)	P_{in} (psi)	P_{out} (psi)
1:17 pm	0.00	0.0	0.0	4796.57	4795.07
1:18	0.23	0.2	0.0	4805.00	4803.50
1:22	1.19	1.1	0.0	4578.67	4569.77
1:26	1.98	2.0	0.0	4578.60	4569.87
1:30	2.79	2.6	0.0	4578.54	4569.90
1:35	3.79	3.6	0.0	4585.71	4577.20
1:39	4.58	4.4	0.0	4585.64	4577.13
1:45	5.79	5.6	0.0	4585.51	4577.00
1:53	7.39	7.1	0.0	4585.45	4576.94
2:00	8.78	8.5	0.0	4585.33	4576.82
2:08	10.39	10.0	0.1	4585.71	4577.20
2:17	12.00	10.0	1.5	4585.55	4578.09
2:30	14.64	10.1	4.1	4572.44	4574.47
2:36	15.81	10.1	5.3	4572.19	4573.81
2:47	18.11	10.1	7.5	4572.36	4574.76
3:08	22.39	10.2	11.6	4572.20	4574.85
3:17	24.00	10.2	13.3	4585.83	4577.32
3:58	32.38	10.2	21.6	4585.71	4577.20
4:23	37.28	10.2	26.6	4585.64	4580.13
4:40	40.64	10.3	30.5	4585.51	4577.00
4:56	43.99	10.3	33.9	4585.83	4577.32
5:25	49.79	10.5	39.9	4585.70	4578.20
6:02	57.01	10.7	49.8	4581.38	4572.96
6:44	65.58	11.1	59.0	4581.03	4572.89
7:40	76.79	11.1	67.5	4581.02	4572.77
8:08	82.29	11.2	72.2	4580.66	4572.28
8:35	87.66	11.2	77.6	4579.96	4571.61
8:44	89.53	11.2	79.5	4581.80	4573.65
9:17	96.53	11.2	85.9	4581.65	4573.61
9:31	98.93	11.2	88.8	4580.62	4573.56
10:17	108.88	11.2	97.9	4581.80	4573.36
10:38	112.39	11.2	102.2	4581.72	4573.25
11:36	123.95	11.2	113.7	4581.79	4572.92
00:56 am	139.89	11.3	129.5	4581.03	4572.89
1:17	144.32	11.3	133.6	4581.02	4572.77
2:20	156.76	11.3	145.5	4580.66	4572.28
3:15	168.44	11.3	157.5	4579.96	4571.61
4:30	180.45	11.3	169.6	4581.80	4573.26
5:17	193.07	11.3	181.7	4580.67	4574.90

CO_2-WAG Experiment

Time	Cum. volume injected (ml)	Cum. produced oil (ml)	Cum. produced water (ml)	P_{in} (psi)	P_{out} (psi)
11:30 am	0.00	0.0	0.0	4809.57	4801.57
12:00	6.18	6.2	0.0	4699.57	4609.57
12:21	10.38	10.0	0.1	4809.57	4808.07
12:28 pm	11.78	10.0	1.4	4699.57	4684.57
12:43	14.74	10.0	4.3	4679.57	4667.57
1:24	22.96	10.0	12.5	4595.24	4588.54
1:35	25.07	10.0	13.5	4591.64	4584.84
1:44	26.84	10.0	13.5	4593.53	4586.53
1:51	28.36	10.0	13.6	4588.73	4581.63
2:05	31.02	10.0	13.6	4587.78	4580.48
2:12	32.86	10.0	13.6	4586.93	4578.61
2:24	34.93	10.0	13.6	4587.95	4579.65
2:36	37.20	10.0	13.7	4588.10	4579.85
2:50	40.02	10.0	13.7	4587.98	4579.69
3:00	42.08	10.0	13.8	4588.82	4580.57
3:19	45.97	10.0	13.8	4589.66	4581.38
3:30	48.00	10.0	13.8	4589.56	4581.27
3:50	52.13	10.0	13.8	4588.47	4580.27
4:12	56.49	10.0	13.9	4586.93	4578.61
4:39	61.90	10.1	13.9	4587.95	4579.65
5:11	68.27	10.2	13.9	4588.10	4579.85
5:35	73.16	10.3	14.9	4587.98	4579.69
5:45	75.13	10.5	16.7	4588.82	4580.57
6:01	77.16	10.6	18.6	4589.66	4581.38
6:17	81.46	10.8	22.7	4589.56	4581.27
6:30	84.07	10.9	25.1	4588.47	4582.27
6:32	84.43	10.9	25.1	4590.18	4588.94
7:00	90.03	10.9	25.2	4587.98	4579.69
7:35	97.06	10.9	25.3	4588.82	4580.55
8:15	105.12	10.9	25.4	4589.66	4581.43
8:50	112.50	10.9	25.4	4588.98	4579.99
9:30	120.09	10.9	25.5	4587.82	4580.55
10:40	134.1	10.9	25.7	4590.66	4582.43
11:30	144.80	10.9	25.8	4589.66	4581.43
00:14 am	152.84	11.0	34.0	4588.98	4579.99
1:52	172.59	11.2	52.7	4588.82	4580.55
2:23	178.61	11.2	58.6	4582.27	4582.27
2:30	180.00	11.2	60.0	4588.98	4579.99
3:30	192.87	11.2	72.0	4588.82	4580.78